Investigation of the human MG63 osteoblastic cell response to nanotubular surfaces

Ryan Berthelot

Thesis submitted to the University of Ottawa in partial fulfillment of the requirements for the

Doctor of Philosophy degree in Biomedical Engineering

Supervisor: Dr. Fabio Variola

Department of Biomedical Engineering

Faculty of Engineering

University of Ottawa

ACKNOWLEDGEMENTS

I extend my sincere gratitude to my advisor, Dr. Fabio Variola, for his unwavering support throughout this project. While the journey through uncharted territory can be both frustrating and time-consuming, I have always valued Dr. Variola's sound advice, especially in challenging circumstances. I also wish to thank all the members of the Variola Lab for their constant encouragement and readiness to assist whenever needed. My heartfelt thanks go to my parents and friends, whose unwavering support have been essential to my academic journey. To my loving partner, Sabrina Beauchamp, who has endured this journey alongside me, your patience and kindness have been, and will always be, deeply appreciated. My thanks to Professor Marianne Fenech, whose council, aid and advice came when I needed it most. I would also like to thank Dr. John Dutcher, who, throughout every period of my academic career, has helped me when I needed it most and has always been there to support me or provide a reference. To Dr. Suresh Neethirajan, who provided me so many opportunities to grow as a scientist. I would like to thank Dr. Jay Leitch for his guidance throughout my BSc and MSc degrees, and whose playful and critical methods of approaching and solving problems have stayed with me throughout my entire career. Lastly, to my friend Dr. David Lomboni, whose long conversations on our patio, or in the office, helped carry forward the momentum of my work and whose kind disposition and unrelenting work ethic provided much needed moments of inspiration, even in the worst of circumstances. To all I have mentioned above, I could not have accomplished this without the support of you all. Thank you.

ABSTRACT

Cells found within bone tissues, and in particular osteoblasts, are profoundly influenced by the nanotopographical features of their extracellular environment which play a critical role in orchestrating osteogenesis, cellular differentiation, and bone mineralization, via a wide range of mechanical and biochemical signals. Advances in materials science and nanotechnology have made possible to create substrates and interfaces with intricate nano-patterns that interact with cells at the molecular level, offering unprecedented opportunities to investigate the mechanisms that control cellular interactions with both natural and synthetic surfaces. The development of micro-and nano-engineered surfaces has been one of the main factors that has spurred the advances in bone tissue engineering. However, the development of more effective surfaces capable of predictively dictate a beneficial cellular response also requires a deep understanding of how to account for the complex and variable conditions of the native bone microenvironment. In this Thesis, nanotopographical and environmental variables were incorporated by investigating the role of cellular preconditioning in elevated glucose levels and the ability of optimized, single diameter titanium nanotubular surfaces to modify the preconditioned behavior via direct physicochemical cueing. In further pursuit of optimal parameters, the integration of high-throughput screening processes for evaluating these surfaces has aroused interest for the rapid identification of nanotopographical features that best support osteogenesis. Multivariable testing via nanotopographical gradients can help address this need, accelerating the development of effective surfaces and enhance our ability to rapidly tailor surface properties to specific real-world applications. As the field advances, the design and implementation of nanotopographical surfaces that can effectively direct osteoblast behavior will be pivotal in creating next-generation biomaterials. The future of bone tissue engineering lies in the ability to create specialized surface

designs with a nuanced understanding of cellular dynamics to achieve superior outcomes in bone health and regeneration.

The overarching goal of my doctoral work was to engineer nanotopographical surfaces with tailored structural complexities to elicit specific osteoblastic responses. This approach aims to optimize surface properties for enhanced bone tissue engineering applications, including promoting osteogenic differentiation, reducing experimental variability from both environmental and surface features, and creating high-throughput platforms for rapid biomaterial screening.

In the first study (Chapter 2), I investigated the combined influence of nanotopographical cues and environmental factors on human MG63 osteoblastic cell behavior. Using a triphasic anodization protocol, I created highly ordered single nanotube surfaces with varying tube diameters and compared these with a complex honeycomb architecture. I also modulated the glucose content in the culture medium to simulate normal and hyperglycemic conditions, incorporating a preconditioning step to ensure cells adapted to the altered environment. I then systematically analyzed cellular responses, including proliferation, migration, viability, and differentiation, under these different conditions to uncover potential synergistic or antagonistic effects between the nanotopographical features and environmental factors.

In the second study (Chapter 3), I explored the influence of hierarchical nanotubular gradients on cell response, focusing on the complexity of the two-tiered, honeycomb architecture. I used a bipolar anodization process to create these surfaces, which featured a gradient of increasing disorder end-to-end, transitioning from single tubes into complex honeycomb topography. The study assessed the impact of these nanotopographical variations on cellular responses, including proliferation, differentiation, and migration. My findings highlighted the significant role of nanotopographical complexity, particularly in promoting osteogenic differentiation. I developed a

high throughput testing process, aimed at shortening the time required to troubleshoot and optimize cell response, culminating in the extraction and synthesis of the most and least favorable surfaces, for further testing and validation of this process.

In the third study (Chapter 4), I investigated MG63 osteoblastic cell behavior on rationally selected titanium nanotubular surfaces that were extracted from the previously developed gradient anodization process. These surfaces validated the high-throughput approach by confirming cell responses across the two topographies and provided deeper insights into the interactions between cells and surfaces of different complexities. Lastly, I established a Raman confocal imaging protocol on opaque, light-sensitive titanium, identifying key biochemical features of single cells and bone-like mineral for future research, demonstrating the feasibility of this technique for further study.

RÉSUMÉ

Les cellules présentes dans les tissus osseux, et en particulier les ostéoblastes, sont profondément influencées par les caractéristiques nanotopographiques de leur environnement extracellulaire, qui jouent un rôle critique dans l'orchestration de l'ostéogenèse, de la différenciation cellulaire et de la minéralisation osseuse, via une large gamme de signaux mécaniques et biochimiques. Les avancées en science des matériaux et en nanotechnologie ont permis de créer des substrats et des interfaces avec des nano-modèles complexes qui interagissent avec les cellules au niveau moléculaire, offrant des opportunités sans précédent pour étudier les mécanismes contrôlant les interactions cellulaires avec des surfaces naturelles et synthétiques. Le développement de surfaces micro- et nano-ingénierées a été l'un des principaux facteurs ayant stimulé les avancées dans l'ingénierie des tissus osseux. Cependant, le développement de surfaces

plus efficaces, capables de dicter de manière prédictive une réponse cellulaire bénéfique, nécessite également une compréhension approfondie des conditions complexes et variables du microenvironnement osseux natif.

Dans cette thèse, les variables nanotopographiques et environnementales ont été intégrées en étudiant le rôle du préconditionnement cellulaire dans des niveaux élevés de glucose et la capacité de surfaces nanotubulaires en titane optimisées et de diamètre unique à modifier le comportement préconditionné via des signaux physicochimiques directs. Dans une quête continue des paramètres optimaux, l'intégration de processus de criblage à haut débit pour évaluer ces surfaces a suscité un intérêt pour l'identification rapide des caractéristiques nanotopographiques soutenant le mieux l'ostéogenèse. Des tests multivariables via des gradients nanotopographiques peuvent répondre à ce besoin, accélérant le développement de surfaces efficaces et renforçant notre capacité à adapter rapidement les propriétés de surface à des applications spécifiques dans le monde réel. À mesure que le domaine progresse, la conception et la mise en œuvre de surfaces nanotopographiques capables de diriger efficacement le comportement des ostéoblastes seront essentielles pour créer des biomatériaux de nouvelle génération. L'avenir de l'ingénierie des tissus osseux repose sur la capacité à créer des conceptions de surface spécialisées avec une compréhension nuancée des dynamiques cellulaires pour atteindre des résultats supérieurs en matière de santé osseuse et de régénération.

L'objectif global de mon travail doctoral était d'ingénier des surfaces nanotopographiques avec des complexités structurelles adaptées pour susciter des réponses ostéoblastiques spécifiques. Cette approche vise à optimiser les propriétés de surface pour des applications avancées d'ingénierie des tissus osseux, notamment la promotion de la différenciation ostéogénique, la

réduction de la variabilité expérimentale liée aux facteurs environnementaux et de surface, et la création de plateformes à haut débit pour un criblage rapide des biomatériaux.

Dans la première étude (Chapitre 2), j'ai étudié l'influence combinée des signaux nanotopographiques et des facteurs environnementaux sur le comportement des cellules ostéoblastiques humaines MG63. En utilisant un protocole d'anodisation triphasique, j'ai créé des surfaces de nanotubes simples hautement ordonnés avec des diamètres de tubes variables et les ai comparées à une architecture complexe en nid d'abeille. J'ai également modulé la teneur en glucose dans le milieu de culture pour simuler des conditions normales et hyperglycémiques, en incorporant une étape de préconditionnement pour garantir que les cellules s'adaptent à l'environnement modifié. J'ai ensuite analysé systématiquement les réponses cellulaires, notamment la prolifération, la migration, la viabilité et la différenciation, dans ces différentes conditions afin de découvrir des effets potentiellement synergiques ou antagonistes entre les caractéristiques nanotopographiques et les facteurs environnementaux.

Dans la deuxième étude (Chapitre 3), j'ai exploré l'influence des gradients nanotubulaires hiérarchiques sur la réponse cellulaire, en me concentrant sur la complexité de l'architecture en nid d'abeille à deux niveaux. J'ai utilisé un processus d'anodisation bipolaire pour créer ces surfaces, qui présentaient un gradient de désordre croissant d'une extrémité à l'autre, passant de nanotubes simples à une topographie complexe en nid d'abeille. L'étude a évalué l'impact de ces variations nanotopographiques sur les réponses cellulaires, notamment la prolifération, la différenciation et la migration. Mes résultats ont mis en évidence le rôle significatif de la complexité nanotopographique, en particulier dans la promotion de la différenciation ostéogénique. J'ai développé un processus de test à haut débit, visant à raccourcir le temps nécessaire pour résoudre les problèmes et optimiser les réponses cellulaires, culminant dans

l’extraction et la synthèse des surfaces les plus et les moins favorables pour des tests et validations ultérieurs de ce processus.

Dans la troisième étude (Chapitre 4), j’ai étudié le comportement des cellules ostéoblastiques MG63 sur des surfaces nanotubulaires en titane rationnellement sélectionnées, extraites du processus d’anodisation en gradient précédemment développé. Ces surfaces ont validé l’approche à haut débit en confirmant les réponses cellulaires sur les deux topographies et ont fourni des informations plus approfondies sur les interactions entre les cellules et les surfaces de complexités différentes. Enfin, j’ai établi un protocole d’imagerie confocale Raman sur du titane opaque et sensible à la lumière, identifiant des caractéristiques biochimiques clés des cellules uniques et des minéraux ressemblant à des os pour des recherches futures, démontrant la faisabilité de cette technique pour des études ultérieures.

STATEMENT OF ORIGINALITY

I, Ryan Berthelot, state that the content of this Thesis is entirely original. Research and corresponding manuscripts were done under the supervision of Dr. Fabio Variola, a professor at the University of Ottawa in the Department of Mechanical Engineering, cross-appointed to the Department of Cellular and Molecular Medicine. The research presented in this Thesis consists of one experimental research manuscript that is currently under review in Biomaterials Science (Chapter 2) and two in the preparation stage (Chapter 3 & 4). All co-authors' contributions are highlighted at the start of each chapter. Future directions of study are presented in Chapter 5.

Manuscripts included in this Thesis:

- Berthelot R.B., Variola F., "Investigating the interplay between environmental conditioning and nanotopographical cueing on the response of human MG63 osteoblastic cells to titanium nanotubes", under peer-review (accepted, minor revisions) in *Biomaterials Science*.

STATEMENT OF CONTRIBUTIONS

I, Ryan Berthelot, was the primary contributor to the research presented in this Thesis. I developed the protocols used for creating the tested biomaterials and carried out the majority of the material characterization. I was fully responsible for conducting the experimental aspects of the research including wide-field microscopy, cell culture experiments, Raman spectroscopy/microscopy, and the subsequent analysis of images and data. I also actively participated in writing the scientific papers included in this Thesis.

OVERVIEW AND RATIONALE

The integration of biomaterials, such as titanium, into human tissues posed significant challenges, particularly in the context of orthopedic and dental implants. Titanium is a material known for its high biocompatibility, however complications in achieving effective tissue integration are still prevalent. In parallel with traditional methods focusing on biochemical enhancements, much focus has been placed on the development of advanced materials, interfaces and nanostructured surfaces, like titanium nanotubes, to enhance this integration. These nanotopographical surfaces offer the potential to directly drive cellular behavior at the tissue-biomaterial interface, improving osteogenesis and the overall success of implants. Nanotubular surfaces can be precisely engineered through anodization to control nanotube diameter and spatial dynamics, both of which are crucial for eliciting desired cellular responses. However, variability between studies has led to inconsistent outcomes in the classifications of feature effectiveness, underscoring the need for more reliable methods to create and optimize these surfaces. In a similar fashion, standard *in vitro* assays often fell short of replicating the complex biochemical environments found *in vivo*, limiting the applicability of these studies to real-world scenarios. In this way, understanding how cells interacted with these surfaces under more physiologically relevant conditions is essential.

My doctoral research aimed to address these challenges by developing and optimizing titanium nanotubular surfaces that were both reproducible and effective in promoting desired cellular responses. By controlling exposure to simulated microenvironments and exploring gradient-based approaches to surface design, focusing on the effects of nanotube diameter and spatial dynamics, my work sought to improve *in vitro* models, ultimately aiming to contribute in the creation of more reliable and application-specific biomaterials in bone- and tissue-engineering.

SPECIFIC OBJECTIVES

Objective 1 (Chapter 2)

In the pursuit of understanding cell-surface interactions, particularly within the context of nanotubular structures and environmental factors, many studies have taken for granted that initial exposure post-seeding represents cellular behavior in more realistic environments. This assumption overlooks the dynamic and complex nature of environmental conditions *in vivo*, which could have a profound impact on cellular behaviors, potentially already exposed to variable levels of the antagonists in their natural state. My research challenged this assumption, asking whether the topographical cueing exerted by the nanotubes was constant regardless of the environment the surfaces are in or previous exposure the cells may have had to such antagonists. To explore these questions, we investigated the effects of high glucose levels, as a well-known, studied, and easily accessible chemical tool that modifies certain cellular behaviors in MG63 cells. By focusing on high glucose, my work aimed to demonstrate that the chemical environment could change how a specific nano-feature affects cells. This insight was key for a more comprehensive analysis of surfaces, where environmental variables had to be considered alongside topographical features. If a particular feature exerted consistent effects across different environments, it could pave the way for more focused studies to understand surface-cell interaction mechanisms. Moreover, from a long-term application perspective, such a feature might be expected to behave similarly *in vitro* and *in vivo*. The exploration into three different, interrelated tube diameters further emphasized not only the effect of single nanotubular diameters but also the effect of spacing and order across the nanotubular surface.

To this end, my first objective was to optimize multi-hierarchical and single diameter titanium nanotubes to generate consistent, highly ordered and reproducible titanium nanotubular substrates to elucidate MG63 cell response after preconditioning in low and high glucose. Ultimately, I aimed at determining whether direct physicochemical cueing could reverse the detrimental effects imprinted in cells via preconditioning in a high glucose environment and if positive cell response dynamics of nanoscale surface features are sensitive to the biochemical cellular environment.

Objective 2 (Chapter 3)

Understanding the complex nature of cellular responses to nanotopographical surfaces is crucial for advancing biomedical applications. Building on the optimization of highly ordered nanotubes prepared in my previous study, this component of my research explored titanium nanotubular gradients as a novel approach to studying cell-surface interactions. These gradients vary nanotube diameter and spatial dynamics, eliminating batch-to-batch variability and providing a detailed understanding of how these parameters influence cellular behaviors such as proliferation, migration, and differentiation. Nanotubular gradients encapsulate a range of diameters within a single substrate, allowing for a multidimensional analysis of cellular responses to varying nanotopographical stimuli. The ability to generate specific nanotube diameters through anodization voltage manipulation facilitates the transition from gradient studies to homogeneous single-diameter surfaces, streamlining the optimization process. This approach offers a valuable contribution to the field by accelerating the production of optimized surfaces via a high-throughput workflow for work *in vitro*.

In this way, my second objective was to explore the MG63 cellular response to novel surfaces consisting of gradients with variable titanium nanotube diameters, geometries and spatial

dynamics, providing an innovative approach to better understand the role of disorder in cell-surface interactions. By removing most of the batch-to-batch variation and leveraging the flexibility of anodization voltage manipulation, this study also aimed to create a production pipeline that pinpointed specific nanotube features eliciting optimal cellular responses, expediting the traditional, time-consuming process associated with consistently creating and optimizing nanotubular surfaces on different samples. To this end, the derived process was used to create the first optimized titanium honeycomb lattice, elucidating the role of variable tube geometry in the hierarchical structures and their influence on cell behavior, laying the groundwork to use the honeycomb geometry as a tool for controlling disorder on anodized surfaces.

Objective 3 (Chapter 4):

Rapid optimization and validation of biomaterial surfaces are critical in advancing tissue engineering, particularly for developing effective and application-specific biomaterials. As traditional methods of surface optimization are often time-consuming and prone to batch-to-batch variability, there is a growing need for efficient approaches that can quickly identify and validate optimal surface features. Additionally, label-free methods such as Raman microscopy offer a powerful means of exploring cell-surface interactions on complex systems like titanium nanotubular surfaces, providing deeper insights into the biochemical and mechanistic pathways that drive cellular behavior. By employing these techniques, researchers can more accurately predict how cells will respond to specific nanotopographical cues, thereby enhancing the design and functionality of biomaterials for regenerative medicine.

Building on my previous work, my third objective focused on validating and further exploring the effects of optimized nanotubular titanium surfaces, derived from a gradient, on the behavior of

MG63 cells. Emphasizing early osteogenic differentiation, my research utilized a combination of traditional immunofluorescence analysis, cell assays and Raman microscopy to gain a comprehensive understanding of how these surfaces influenced cellular response. The goal was to provide context into the mechanisms by which varying nanotopographical complexities impacted cellular adhesion, proliferation, and differentiation, and validate the results found in the gradient study. This study also aimed to assess mineral quality and identify key spectral features and biochemical markers indicative of early differentiation, using Raman microscopy to map their spatial distribution within bone-like nodules and single cells, respectively. The findings from this objective contributed to the development of a protocol for single cell Raman confocal microscopy on opaque, metallic surfaces. Ultimately, this research aims to hasten the transition between *in vitro* observations and practical applications, paving the way for more effective and application-specific biomaterials in tissue engineering and regenerative medicine.

LIST OF FIGURES

LIST OF TABLES

TABLE OF CONTENT

CHAPTER 1: INTRODUCTION

Nanostructured surfaces play a key role in controlling cellular events at the tissue-biomaterial interface by exerting direct beneficial cueing to adherent cells.[1–3] As a result, much effort by the scientific community has been invested in the design of nanostructured biomaterials in order to unveil the structure-function relationships between nanotopographical cues and cellular functions.[2] This study aims to investigate the cellular response and osteoinductive capabilities of nanotubular titanium surfaces.

Biomaterials used for implants have made significant strides in biocompatibility, but often fall short in facilitating effective tissue integration, leading to patient pain or discomfort and the potential removal and replacement of the implant, dramatically increasing the cost of the whole operation.[4,5] As a result, there has been a heavy emphasis on biochemical treatments (dexamethasone, B-glycerophosphate etc.) that do not have a great track record for success rates, are often costly, and require patients to undergo treatments for a prolonged period.[5,6] Knowing this, alternative methods have become of increasing interest in the pursuit of enhanced compatibility, particularly for orthopedic and dental implants, biocompatible materials like titanium have become the gold standard. The challenge lies in eliciting the formation of bone at the interface with the material, a critical factor for successful integration.

Metals and metal alloys have been used for implants for over 100 years. Titanium has been longstanding choice for these implants due to its high biocompatibility, low rejection rate and a chemical proclivity for forming an oxide layer which prevents corrosion.[7] In particular, the field has seen much interest in modifying the surface properties of titanium, especially at the nanoscale, to encourage osteoblast formation and advantageous behaviours.[8,9] Research has explored various

methods to modify titanium's properties, including physical and chemical alterations.[9–12] Anodization has emerged as an effective technique to produce semi-ordered nanotubular arrays over large titanium surfaces, with the diameters of the tube openings entirely tunable in relation to anodization times and the composition of the electrolyte used during anodization.[2,13–15] Nanotubes are hollow, cylindrical structures, with a circular opening having nano scale dimensions.[1,8] Titanium nanotubes have been widely studied as a frontrunner for the next step in biocompatible materials for bone implants.[2,15,16] Though results for these structures have been gathered over the last two decades, existing literature presents contradictory information, primarily due to variability from one nanotubular surface to the other.[1,2] This has led to more recent studies aiming to craft tunable gradients of increasing diameters allowing for much larger ranges for experimentation and optimization while decreasing batch-to-batch variability.[16–18] These characteristics have rightly produced a lot of interest surrounding these nanostructures.

There is an ongoing need to examine the effect and type of nanostructures being proposed to transfer technologies successfully and efficiently into actual medical application. Due to a lack of consideration for biochemical variables pertaining to the cellular microenvironment most *in vitro* assays cannot replicate the complex *in vivo* reality, a limitation that may impact the overall understanding of nanostructure effects.[19] In this, the impact of preconditioning in a high glucose environment on the behavior of MG63 cells is a central aspect of our investigation. Preconditioning cells in varied environments is a potent technique to modulate their responses to external stimuli, with possible influence on subsequent cellular behaviors such as adhesion, proliferation, and differentiation.[20–22] High glucose preconditioning is especially notable due to its relevance to conditions such as diabetes and prediabetes, where elevated glucose levels can considerably affect cellular functions and tissue responses to implanted biomaterials.[23] Observing the effects of high

glucose preconditioning on MG63 cells as they interact with titanium nanotubes can provide a more comprehensive understanding of their behavior in a high glucose or diabetic *in vivo* environment, elucidating their potential in rescuing cells in an antagonistic environment. This understanding is instrumental in refining our strategies for improving implant integration and success in patients with diverse physiological conditions.

While traditional methods of analysis and imaging have been invaluable for examining cell-surface interactions such as those previously mentioned, a more comprehensive understanding calls for advanced techniques. Raman microscopy emerges as a significant innovation in this field, offering a deeper view into the interaction of MG63 cells with titanium nanotubes. Raman imaging, with its capacity for label-free, non-invasive characterization of biological samples, provides unique advantages.[24] Through the generation of Raman spectra, essentially molecular fingerprints, it offers detailed insights into the biochemical composition of cells in their native state. Therefore, Raman imaging can shed light on the interaction and adaptation of MG63 cells to the nanotubular titanium surfaces at a molecular level, contributing valuable knowledge towards optimizing nanostructured surfaces for improved cellular response and tissue integration.

1.1 Osteogenesis and Mechanotransduction

Bone formation, or osteogenesis, is a critical aspect of the skeletal system, and osteoblasts play an integral role in this complex process. Maturing osteoblasts express proteins and enzymes crucial to bone matrix synthesis, such as alkaline phosphatase, collagen type I, and osteocalcin.[25] They are responsible for producing and secreting the osteoid—an unmineralized bone matrix composed mainly of collagen and other proteins. Subsequent mineralization involves the accumulation of hydroxyapatite crystals within the matrix, providing the bone's strength and rigidity. Some osteoblasts, once embedded within the mineralized bone matrix, further differentiate into osteocytes, which maintain bone homeostasis. Osteoblasts also play a key part in the continuous remodeling and maintenance of bone tissue throughout life. The dynamic balance between bone formation by osteoblasts and bone resorption by osteoclasts is essential for maintaining healthy bone structure and function.[26,27] In essence, osteogenesis begins with the recruitment and differentiation of mesenchymal stem cells into osteoblasts, followed by osteoid secretion, mineralization, and osteocyte formation. The understanding of osteoblast functions and interactions is pivotal for developing therapeutic strategies for bone disorders and advancing tissue engineering for bone graft substitutes.

1.1.1 Cellular Models

In the complex study of cell-surface interactions, particularly on titanium nanotubular surfaces, a selection of cell models including SaOs-2, MG63, and MC3T3, have been instrumental. Immortalized cell lines, though not fully representative of primary osteoblast cells, have become crucial in research due to their accessibility and consistent results.[28] SaOs-2 is a human osteosarcoma cell line that has been valuable for exploring various aspects of bone biology, including ALP activity and mineralization potential. MG63, another human osteosarcoma cell line,

is known for its ability to synthesize and regulate osteocalcin and specific integrin subunits, making it a prominent model for examining bone formation/regeneration and cell-surface interactions. MC3T3-E1, a mouse pre-osteoblast cell line, is often used to study osteogenic differentiation and has provided significant insights into the mechanisms of bone mineralization and proliferation.[28]

Comparatively examining SaOs-2, MG63, and MC3T3-E1 cells against primary human osteoblast (HOb) cells for their suitability as *in vitro* models for biomaterials testing, certain distinctions have emerged. SaOs-2 and MG63 cells showed a higher proliferation rate than HOb cells, with SaOs-2 and MC3T3-E1 revealing similarities in cell proliferation and mineralization with primary cells.[28,29] SaOs-2 cells demonstrated comparable ALP activity, mineralization potential, and gene regulation to HOb's, unlike MG63 cells. This ability for similar behavior to primary cells makes SaOs-2 a valuable tool for studying cellular differentiation and gene expression in a variety of environments. MG63 showed the least similarities with HOb's; however, these cells were shown to be reliable in recapitulating OC synthesis and regulation, and integrin subunit expression, making MG63 a vital part of the toolkit for exploring implant integration and bone regeneration mechaisms.[29,30] As for MC3T3-E1 cells, they have also proven to be a valuable model, particularly in studying the osteogenic differentiation process. The similarities in cell proliferation and mineralization with primary cells enhance their utility in biomaterial testing. [28]

The potential suitability of the MG63 cell line for studying cell-nanotopography response offers numerous avenues of specific and technical exploration, including their unique ability to synthesize and regulate OC and their specific integrin expression. MG63 cells also demonstrate a higher proliferation rate, unique sensitivity to nanotopographical features, and proven reliability in previous studies.[28,31] Additionally, MG63 cells have a significant amount of literature measuring

cellular response to elevated glucose levels, making them a useful indicator of cellular response in high glucose environments.[32–35] Therefore, despite of the trade off in ALP Activity and degree of mineralization, the specificity of their integrin response, fast proliferative abilities and comparability with literature, makes them a suitable candidate for testing osteoblast response to nanotopography in normal and elevated glucose environments. Such a multi-faceted approach can provide a more comprehensive understanding and could avoid misleading conclusions.

1.1.1.1 In vitro Assays: Human MG63 Cells, a Widely Used Model for Osteoblasts

Optimal osseointegration requires the formation of bone tissue at the interface with an orthopedic or dental implant. This process is vital for the long-term stability and success of implants in the human body. A well-characterized cellular model is essential for studying osseointegration and evaluating the compatibility of different biomaterials and nanostructure surfaces. In this context, MG63 cells, a human osteosarcoma cell line, have emerged as a popular model for investigating osseointegration *in vitro*.[30,33,34]

MG63 cells are derived from a human osteosarcoma, a type of malignant bone tumor. While the cells are cancerous in nature, they retain many of the characteristics of normal osteoblasts, the cells responsible for bone formation. MG63 cells exhibit a high proliferation rate, making them ideal for *in vitro* experiments. Furthermore, they express several osteoblastic markers, including alkaline phosphatase (ALP), osteocalcin, and type I collagen, which are crucial for bone formation and mineralization.[33,36] One of the primary advantages of using MG63 cells for osseointegration studies is their ability to closely mimic the behavior of osteoblasts, the primary cells involved in bone formation (*osteogenesis*) during osseointegration. They exhibit similar adhesion, proliferation, and differentiation characteristics on various biomaterial surfaces, providing a relevant model for understanding how materials interact with bone-forming cells. Additionally,

the rapid proliferation rate of MG63 cells enables the generation of large numbers of cells for experimentation in a relatively short amount of time.[30,31] This feature allows for high-throughput screening of materials candidates and putative surface treatments, accelerating the discovery of optimal materials for osseointegrated implants. Furthermore, compared to primary human osteoblasts, which can be challenging to isolate and maintain in culture, MG63 cells are readily available and easy to propagate. This cost-effectiveness makes them a practical choice for many laboratories studying osseointegration, and as a result, MG63 cells have been widely used in osseointegration research, leading to a substantial body of literature on their behavior and response to various materials and conditions.[30,33] This wealth of information provides valuable insights and a solid foundation for further experimentation, making MG63 cells a suitable choice for studying osseointegration of surfaces and materials.

1.1.2 Mechanotransduction and Subsequent Markers of Differentiation

The investigation of MG63 cell differentiation has been a pivotal aspect to understand *osteogenesis*. This differentiation process involves a series of orchestrated molecular events where specific proteins play significant roles at different stages. However, in order to comprehend how it is possible for nanoscale features to guide cellular behavior and osteoinductive properties at scales orders of magnitude larger than their own surface geometries, a detailed understanding of cell mechanical response and the resulting cascade of signaling molecules is required. Integrin-dependent signaling pathways play a crucial role in mechanotransduction, the process by which cells convert mechanical stimuli into biochemical signals. Integrins are transmembrane receptors that mediate cell adhesion to the extracellular matrix (ECM) and facilitate communication between the cell and its environment. The interaction between integrins and the ECM leads to the activation

of various signaling pathways, which govern essential cellular processes such as growth, survival, migration, and differentiation[1,37,38].

One of the key pathways in integrin-dependent mechanotransduction is the Focal Adhesion Kinase (FAK) pathway. FAK is a non-receptor tyrosine kinase that is constitutively associated with the β-integrin subunit. Upon integrin activation and clustering, FAK localizes at focal adhesions or early focal complexes, leading to its autophosphorylation. This event triggers the recruitment and activation of other signaling proteins, such as Src family kinases. FAK and Src work together to phosphorylate downstream signaling molecules, ultimately controlling cellular processes like growth, migration, and differentiation. Another important pathway involved in integrin-mediated mechanotransduction is the mitogen-activated protein kinase (MAPK) pathway, which includes extracellular signal-regulated kinases (ERK) 1 and 2. ERK1/2 are activated by FAK and Src in adherent cells, acting as mediators of both cellular differentiation and survival. The activation of ERK1/2 leads to the phosphorylation and activation of various transcription factors that regulate gene expression, ultimately influencing cell behavior. The phosphatidylinositol-3-kinase (PI3K) pathway is also involved in integrin-dependent signaling. Upon integrin activation, PI3K can be recruited to focal adhesions by interacting with FAK and Src. Once activated, PI3K generates phosphatidylinositol-3,4,5-trisphosphate (PIP3), a lipid second messenger that activates downstream effectors.[8,38,39] The critical role of integrin-dependent signaling pathways in mechanotransduction, extends to this pathway's influence on the production of osteogenic markers such as RUNX2, osterix (OSX), osteocalcin (OCN), and osteopontin (OPN), which are key to bone formation and remodeling.

OSX is a vital transcription factor for osteoblast differentiation and bone formation, with pathways like FAK and MAPK/ERK modulating OSX expression and aiding in the maturation of

pre-osteoblasts. OCN and OPN, non-collagenous proteins secreted by osteoblasts, play essential roles in bone development and remodeling. OCN, often considered as a late marker of osteoblast differentiation, plays an indispensable role in binding calcium ions and promoting the mineralization of the bone matrix.[8,38,40] As the cells transition into the late differentiation stage[41] Integrin-mediated activation of pathways such as MAPK/ERK and PI3K/Akt influences OCN production, leading to increased bone mineralization.[41] OPN is a constituent of the bone matrix and functions as a cell attachment protein. Its secretion suggests an active bone formation process. OPN has been found to mediate mechanotransduction, highlighting its role in cellular responses to substrate topography. Similarly, mechanical stimuli upregulate OPN in osteoblasts, with integrins and activated calcium channels contributing to this process.[38] These complex interactions within osteoblasts are integral to bone formation and adaptation.[14,38,42]

The early differentiation stage of MG63 cells into osteoblasts is typically marked by the expression of alkaline phosphatase (ALP), a glycoprotein enzyme critically involved in the mineralization process. ALP functions by promoting the release of phosphate groups, thereby facilitating hydroxyapatite crystal formation – a principal component of bone matrix. Upregulation of ALP is frequently associated with enhanced osteogenic differentiation, particularly in response to mechanical stimuli, affirming the mechanosensitive nature of osteoblasts.[1,33,38,40]

Recent investigations have spotlighted two principal agents of mechanotransduction instigated by ECM rigidity and cell shape, Yes-associated protein 1 (YAP1) and transcriptional coactivator with PDZ-binding motif (TAZ).[43,44] Governed by Rho GTPase activity and actomyosin contractility ensuing from cell adhesion to the ECM, these elements hint at additional mechanisms that sense or coordinate mechanical stimuli. Cellular- and ECM-mediated mechanical cues can lead to an intricate adhesome, influencing cellular phenotypes, and even modulating chromatin

organization and expression via tension within the cytoskeleton. These cues impact the downstream regulators of the Hippo signaling pathway, YAP1 and TAZ, with inactive pathways triggering proliferation via nuclear translocation. A prevailing model also suggests F-actin can increase the availability of active YAP1 by competing for binding sites on inhibitory protein angiomotin. With much left to investigate, it's evident that the interplay of cellular and ECM-mediated stress, both at the FAC–adhesome and through cytoskeletal dynamics, are fundamental in shaping cell biology.[43] The differentiation of MG63 cells into mature osteoblasts is a multifaceted process orchestrated by several key proteins, intricately linked to mechanotransduction. It underscores the need for an in-depth understanding of the role of substrate topography and mechanical forces in promoting osteogenesis.

1.1.2.1 Effect On Proliferation and Subsequent Markers

The proliferative status of MG63 cells when interfacing with nanotubes can be meticulously evaluated using several protein markers that reflect distinct aspects of the cell cycle. Ki-67, a nuclear protein expressed in all active phases of the cell cycle (G1, S, G2, and mitosis), is completely absent in quiescent cells (G0). Therefore, the detection of Ki-67 serves as a reliable indicator of the growth fraction of a cell population, and its abundance can shed light on the proliferative response of MG63 cells to nanotopographical cues from nanotubes.[45]

Integrin-dependent signaling pathways, as detailed above, are not only critical to mechanotransduction but also profoundly influence the expression of proliferative markers, namely Ki67, indicators of cellular proliferation. Ki67, a nuclear protein, is predominantly expressed in proliferating cells and serves as a reliable marker of cell proliferation. It's worth noting that the FAK pathway, which is activated upon integrin clustering, significantly contributes to cell proliferation.[38,46,47] FAK, by collaborating with other proteins such as Src family kinases,

phosphorylates multiple downstream signaling molecules. These phosphorylation events can activate various transcription factors, which subsequently upregulate the expression of Ki67. Consequently, cells exhibiting increased levels of Ki67 are indicative of a heightened proliferative state.[46] ERK1/2, activated in adherent cells by FAK and Src, can mediate cellular differentiation and survival. Their activation could potentially stimulate the transcription of genes related to cell proliferation, such as Ki67.[46,48]

Recently, studies have also explored the role of activated YAP1, operating as a transcriptional co-activator, orchestrating cellular behaviors, notably proliferation.[43,49] Their research unveiled a fascinating interplay between biomechanical strain and cell proliferation, gauged via the KI-67 marker, which appeared to mirror the activity pattern of nuclear YAP1. This suggested a causative correlation between strain, YAP1 activity, and cellular proliferation. Notably, the team's experiments with a U0126 inhibitor, implemented during a Western Blot against KI-67, underscored the pivotal role of YAP1. This was evident as the proliferation pattern persisted, pointing towards a minimal influence of ERK1/2 activity in this dynamic. The findings of Hutler-Hassler *et al.* 2017, resonate with earlier research, illustrating the absolute correlation between strain-responsive nuclear YAP1 activation and cell proliferation, including in contact-inhibited cells. Further validation of this hypothesis was achieved with the administration of verteporfin, resulting in a pronounced decrease in KI-67-labeled cells before YAP1 nuclear exclusion. This affirmed the decisive role of nuclear YAP1 in directing cell proliferation behavior, irrespective of biomechanical strain.[49]

Therefore, through the activation of signaling cascades such as the FAK, MAPK/ERK, and PI3K/Akt pathways, integrin-dependent mechanotransduction have a substantial influence on cellular proliferation, as evidenced by the expression of markers like Ki67. These pathways

regulate the dynamic processes of cell growth and survival, underscoring the interconnectedness of cellular adhesion, mechanotransduction, and proliferation. Protein markers such as this, provide a comprehensive portrait of the proliferative status of MG63 cells on nanotubes. Understanding their involvement in the proliferation response to nanotubes could reveal how mechanotransduction cues from the nanotube surfaces influence cell cycle progression and growth in osteoblast-like cells such as MG63. The underpinning molecular mechanisms and pathways that link surface topography to cell proliferation may be further unraveled by probing these key proliferation markers.

1.2 Engineering Biomaterials for Guiding Cell Behavior

Optimizing biomaterials for osseointegration is not confined to surface alterations but includes a rich assortment of strategies that contribute to implant success. Among these, coatings are a prominent method and involve techniques such as plasma spraying, where a heated plasma jet melts the coating material like hydroxyapatite to spray onto the implant surface. The rough texture obtained this way promotes bone cell adhesion.[50] Electrodeposition is another method, applying an electrical current to deposit materials like calcium phosphate or metallic nanostructures onto the surface for precise control over coating thickness and composition.[5] Sol-gel methods, a wet chemical technique, transform metallic or non-metallic substances into a colloidal solution, which is then used for silica or ceramic coatings.[9] These coatings, while offering various advantages, may suffer from issues of delamination or cracking under load, and their long-term stability must be critically evaluated.[50] Chemical modifications offer another spectrum of possibilities. Surface functionalization, where specific functional groups or bioactive molecules are attached to the surface, can direct biological responses such as osteoblast differentiation.[51] Plasma treatments alter surface energy, improving wettability and promoting protein adsorption, while self-assembled

monolayers create ordered molecular domains on surfaces to introduce reactive groups for attaching biomolecules.[52] However, precise control over these methods is crucial, as changes may only be superficial or temporary, and consistency in their application remains a vital consideration. Physical modifications provide a range of alternatives, from simple processes like blasting the surface with ceramic particles to create roughness, to more complex techniques such as texturing at the micro and nano-level. Laser texturing, for example, uses lasers to melt and rapidly cool the surface, forming desired patterns. The emergence of 3D printing or additive manufacturing has opened doors for customization in implant shapes and textures, including porous structures that can significantly support bone in-growth.[51]

1.2.1 Nanoscale Surface Modification

Shifting the focus to topographical modifications, they provide a compelling approach for improving osseointegration due to their ability to mimic the intricate nanoscale architecture of natural bone. Techniques for creating nanotopography include anodization, chemical vapor deposition, photolithography, electrospinning, and others. These methods allow for the design of nanostructured surfaces such as nanopits, nanopillars, nanorods, and nanotubes, all of which can significantly influence cellular interactions.[11,51] Common nanotopographical features can be generally categorized into nanopits (depressions on the material surface) and nanoprotrusions (raised features), with structures like nanotubes and nanowires combining various scales and geometries to emulate tissues. Nanopits, widely studied, have effects on cell adhesion based on size and depth. Generally, pits with inner areas smaller than 300 nm result in reduced cell adhesion.[1] Depths ranging from 10 to 20 nm promote cell adhesion, while those shallower than 100 nm decrease cell adhesion.[1,13,14] Research indicates that cells interact more with proteins adsorbed from the surrounding ECM rather than the nanostructures, affecting surface topography

and promoting cell filopodia's exploration within the pits.[1,43] Nanoprotrusions, elevated features with controlled dimensions, have shown consistent impact on cell adherence, with the importance of symmetry, spacing, and height increasingly recognized. Studies on varying these features have shown distinct effects on cell apoptosis[53], spreading, and osteoblast differentiation. [1,54,55] It has been observed that as nanoscale protrusions increase in height (greater than 70 nm), cell adhesion decreases.[1,13,55] One key advantage of topographical modification over coatings is the increased durability: nanotopographical features are less prone to cracking or peeling, promoting cell adhesion, proliferation, and differentiation, all critical for successful osseointegration.[9,51] For example, specific dimensions of nanopits and nanoprotrusions can guide cell growth and enhance bone tissue formation. However, there are also challenges associated with nanotopographical modifications, such as technical difficulty in achieving consistent nanotopography across complex three-dimensional implants, limitations related to size, shape, and spacing, and concerns about long-term stability in demanding physiological environments.[1,2,50,51]

Despite these challenges, the ability of nanotopographical modifications to emulate the natural bone environment at the nanoscale and their inherent durability compared to coatings makes them a promising approach for improving implant osseointegration. Research into the optimization of these techniques and the nanostructures they produce is a key area of focus in the pursuit of improved patient outcomes. By considering the intricate balance of size, shape, spacing, and geometry, along with understanding cellular interactions with proteins, nanotopography opens new doors for biomedical applications, fostering innovation in implant design and performance strategies.

1.2.1.1 Nanotopographical Gradients

Nanotopographical gradients, involving a continuous variation of surface topography, have garnered significant interest in the field of biomaterials due to their ability to provide valuable insights into the relationship between surface properties and cellular responses.[17,56–60] When compared to homogenous or single feature surfaces, nanotopographical gradients offer in fact a more comprehensive understanding of cellular behavior, as they enable researchers to examine the effects of variable surface topographies continuously spanning an array of diameters within a single sample (vs discrete sizes and multiple samples). We see the disadvantages of the single sample approach in research such as the study discussed above by Park *et al* 2007, who had demonstrated a reduction in adhesion, osteogenesis and proliferation of rat MSCs on titanium nanotubes with a pore size larger than 50 nm compared to a flat titanium control or a surface with a smaller pore size (~15 nm)[61], while some studies argue that larger pore sizes (79 and 150 nm) stimulate osteogenesis.[1,62] These discrepancies could also be due to the lack of focus of the order of the nanostructures as mentioned above.[2,3,8]

By reducing batch to batch sample variation due to all tube diameters existing on one surface created at a singular timepoint under the identical conditions, nanotopographical gradient offer a significant advantage in identifying optimal surface characteristics that promote desirable cellular responses, such as adhesion, proliferation, differentiation, or migration.[62] The use of nanotopographical gradients also allows for efficient screening of a broad range of surface topographies, accelerating the development of tailored biomaterials that enhance cell-material interactions. [93]An additional advantage of studying cellular response on nanotopographical gradients is the ability to identify critical thresholds in surface properties that trigger significant changes in cellular behavior.[18] Gaining an understanding of these thresholds can provide valuable

insights into the design of materials that promote specific cellular responses or inhibit unwanted behavior, such as inflammation or bacterial colonization.

An attempt to address the inconsistency of single feature surfaces was made by Wang *et al.* 2012, where an examination of rat MSCs' attachment and differentiation on a stable n-pSi topography gradient substrate (0-310 nm) was carried out.[59] A key discovery was the direct correlation between cell attachment and the n-pSi topography gradient, emphasizing the vital role played by ridge roughness. This pivotal relationship subsequently resulted in the creation of an inverse cell density gradient and ridge roughness gradient along the surface. A crucial part of the study was the discovery that osteogenesis in rMSCs was significantly enhanced on porous topography with ridge roughness less than 10 nm and numerous submicron pores. This was notably superior when compared to areas exhibiting higher roughness or flat silicon surfaces. Conversely, adipogenesis in rMSCs was found to be generally stimulated by the porous topography, independent of the feature size.[57] Previous work on aluminum gradients corroborates these findings of a general affinity for osteoblasts to gravitate towards rougher surfaces.[60] Despite these advantages, creating nanotopographical gradients of certain materials, such as titanium for nanotubes, can be quite challenging. The fabrication of well-defined gradients requires precise control over the surface properties and spatial variation of the material, which can be technically demanding and time-consuming. This difficulty has led to a limited number of studies utilizing this approach, the most relevant of which have come out only in the past few years,[17,18] with researchers often focusing on homogenous or single feature surfaces due to their simpler fabrication processes.[60]

1.2.2 Titanium Nanotubes

Nanotubes are hollow, cylindrical structures, with the circular opening having a dimension that can range from tens to hundreds of nanometers. In a manufacturing sense, nanotubes have received a lot of attention due to the cheap, reliable and scalable methods of synthesis. Titanium nanotubes have been widely studied as a forerunner for the next step in biocompatible materials for bone implants.[1,9,10,63]

1.2.2.1 Synthesis: Anodization

Methods involving anodization reliably produce semi-ordered arrays over large surfaces. What's more, the diameters of the tube openings are entirely tunable in relation to anodization times and the composition of the anodization electrolyte solution.[15] These characteristics have rightly produced a lot of intrigue surrounding these nanostructures, garnering significant interest due to their unique physical properties, such as increased surface area and biocompatibility. They show immense promise in promoting osseointegration by enhancing bone growth, fostering the differentiation and proliferation of cells, and potentially improving the longevity and success of orthopedic implants.

General synthesis of TiO_2 nanotubes use a cleaned titanium (foil or wire) substrate placed opposite of a platinum electrode. The titanium and the platinum metals are then connected to at the positive and negative terminals of a power supply, respectively, for anodization. Anodization is performed in an electrolyte solution (e.g. a common solution mixture combines anhydrous ethylene glycol, crystalline ammonium fluoride and deionized water).[15] The anodization can be done a single time on polished surfaces; however, unpolished titanium surfaces generally have to undergo multiple anodization steps in order to improve tube ordering. For example, our lab has established a protocol by which anodization is performed in two steps, varying voltage and time.[2]

Between the first and second step, the resulting oxide layer is removed from both sides by adhering tape to the oxide surface and peeling off the initial layer of titanium oxide nanotubes. The freshly peeled titanium substrate is then placed back into the holder to undergo a second round of anodization[2] The removal of the initial layer of nanotubes leaves behind shallow nanopits, that act as "seed points" for new nanotube growth in step two, greatly improving the degree of order.[2] Geometric parameters can be further tuned using parameters such as: voltage, time, electrolyte composition and electrolyte age.

The effect of voltage, time and nanotube diameter published by our team can be seen in Table 1.1. As the voltage increases, larger tube diameters form. The addition of more acid into the electrolyte solution increases the speed of reaction, however, this leads to an increase in tube defects and flaking in the titanium oxide layer. Lastly, fresh solution (unused) produces wider and deeper tubes, while aged solution (previously used) has opposite effect.[15] The reduction in tube widening with age is likely due to the increase of titanium ions in electrolyte solution forming bonds with the acid molecules during reaction. In the case of Gulati *et al.* 2015, the fluorine atoms from the ammonium fluoride crystals, combined with the newly released titanium ions to form TiF_6. This gradual removal of fluorine, changing the composition of the anodization fluid along with the evaporation of water at high voltages, is an alternative explanation to this phenomenon.[15]

Table 1.1. Effect of time and voltage on nanotube diameter.[2]

	Condition	20nm	50nm	90nm
Step 1	Voltage (V)	30	40	60
	Time (Min)	60	45	30
Step 2	Voltage (V)	30	40	60
	Time (Min)	5	25	10

1.2.2.2 Physicochemical Characterization

Titanium nanotubes, with their potential in biomedical implants and drug delivery systems, necessitate thorough characterization for application-specific optimization. Among various characterization techniques, my work has mainly relied on scanning electron microscopy (SEM), atomic force microscopy (AFM), and Raman spectroscopy, since this array of methods collectively provides information about micro- and nano-topography, chemical composition and crystallinity of the titanium dioxide layer.

SEM is, by far, the most prevalent nanoimaging technique for characterizing titanium nanostructures. The technique works by focusing a high-energy beam of electrons onto the sample surface, creating an image through the detection of secondary electrons. It provides a detailed examination of surface morphology, structure, and nanotube distribution. SEM can be coupled with energy-dispersive X-ray spectroscopy (EDX), which works by measuring the X-rays emitted by the sample under the electron beam, providing valuable insights into the elemental composition of the nanotubes, a factor critical for their performance.[64] AFM, another effective tool, operates by scanning a sharp probe across the sample surface, measuring forces between the probe tip and the sample to generate a high-resolution image of surface topography and mechanical properties. This method provides a tangible perspective of nanoscale features and the interaction of the nanotubes with their surroundings.[65] To complement these imaging methods, Raman spectroscopy, a non-destructive technique, illuminates the sample with a laser and measures the scattered light, which undergoes a shift in energy that corresponds to the vibrational modes of the molecules in the sample.[66] This technique effectively discerns molecular structure, vibrational properties, and chemical composition. Moreover, it is incredibly efficient in identifying crystallographic phases, detecting impurities and dopants, and scrutinizing surface modifications, while also being sensitive

to defects and disorder within the nanotubes, offering comprehensive insights into their characteristics.[66,67] In relation to titanium nanotubes, Raman spectroscopy can determine the crystallinity of the TiO2 layer (amorphous vs anatase vs rutile), which has been shown to affect cell response.[2,68,69]

In summary, SEM, AFM, and Raman spectroscopy present an accessible and effective combination for the comprehensive characterization of titanium nanotubes. This triumvirate of methods empowers researchers to understand and optimize the properties of titanium nanotubes for specific applications, facilitating their broader and more successful implementation.

1.2.2.3 Titanium Nanotubular Gradients

Titanium nanotubular gradients, with varying nanotube diameters or other topographical features, are increasingly recognized for their potential in osseointegration and implant development.[17,18,70] They allow for a comprehensive study of cellular response to different surface properties, enabling researchers to identify optimal characteristics promoting cell adhesion, proliferation, differentiation, and matrix deposition, with results less influenced by synthesis errors between samples. Moreover, these gradients more closely simulate natural tissue variations, providing a more biologically relevant environment for studying osteoblast behavior.[16–18,58] Despite these advantages, the fabrication of titanium nanotubular gradients presents several challenges. Creating well-defined gradients requires precise control over the surface properties and spatial variation of the material, which can be technically demanding and time-consuming.

For example, the titanium dioxide nanotubes with a gradient oxide layer were found by Li *et al.* 2020 to cover around 70% of the titanium foil surface.[18] This overpotential on the bipolar electrode's surface, which was at its greatest at the anodic edge and tapered toward the middle, resulted in nanotubes being primarily distributed in the anodic area. The tube diameter was noted

to decrease across the foil. SEM micrographs showed an orderly arrangement of the gradient TiO2 nanotube arrays, both pre- and post-annealing. Fluctuating outer diameters of the gradient nanotubes were also reported, ranging between approximately ~20 nm and ~350 nm. The wall thicknesses were recorded to vary from roughly ~5 nm to ~35 nm. The team observed nanotube lengths spanning from about ~0.2 μm to ~2.8 μm. Near the smallest nanotubes, the surface was relatively smooth. Additionally, Zhang *et al.* 2022 conducted a thorough investigation on the formation process of gradient coatings on titanium foils, emphasizing their analysis on the composition and morphology of the material. SEM micrographs from a top-view perspective displayed an evident gradient in TiO2 nanotubes across different voltages, with a pronounced effect observed at 100 and 120 V. The nanotubes, notably larger at the anode edge of the titanium foils, showed a steady decrease in diameter as the distance from the edge increased.[17] The researchers established a direct relationship between the nanotube diameter and the applied voltage. At an applied voltage of 120 V, the nanotubes exhibited an outer diameter of 120 nm, an inner diameter of 75 nm, and a wall thickness of 28 nm. However, these dimensions diminished with increasing distance from the anode edge. At a distance of 35 mm, the nanotubes nearly vanished, replaced by an array of small protrusions, a morphology that was similarly observed between 40 and 50 mm. The study by Zhang *et al.* 2022 revealed that the most substantial nanotubes formed close to the anode edges at varying applied voltages. The locations where the nanotubes ceased to exist and were substituted by smaller protrusions varied with the voltage. The TiO2 nanotube wall thickness demonstrated a consistent reduction from 100 V down to 50 V. At an applied voltage of 30 V, the nanotubes were absent, and a multitude of tiny protrusions became apparent even at a 2 mm distance. EDS element mapping at 120 V, to ascertain the elemental makeup of the nanotube surface, consisted predominantly of Ti, O, and F. As the distance from

the anode edge was amplified, the content of Ti elevated, while the concentrations of O and F receded. This gradient distribution was noted at other voltage levels as well. The team discovered distinct nanotubes at the interfaces of scratch marks on the anodized BPE titanium foils. These nanotubes, measuring approximately 5.8 μm in length at a distance of 2 mm from the anode edge, showed a length decrease as the distance expanded. Additionally, the nanotube length was found to be inversely proportional to the applied voltage. This finding was accompanied by the emergence of discrete cylindrical structures, as opposed to hollow tubular formations, in certain regions on the anodized surfaces.[17]

The mechanism for this synthesis was described by Krabbenborg *et al.* 2014, who detailed a specific form of electrochemical gradients, which arise from in-plane potential gradients, called bipolar electrochemical gradients. This approach contrasts to other configurations as it does not involve any conducting connections to either side of the electrode. Instead, the single bipolar electrode simultaneously acts as both the anode and the cathode. What is noteworthy is the presence of a potential gradient in the solution, while the bipolar electrode maintains a roughly uniform potential across its surface. This setup results in an in-plane varying potential difference between the bipolar electrode's surface and the solution. Once an adequate voltage is applied to the electrolyte solution that contains the bipolar electrode, this potential difference stimulates electrochemical reactions.[16] Interestingly, these reactions are most pronounced at the edges of the bipolar electrode. Li *et al.* 2020, referenced this specific bipolar electrochemistry mechanism, focusing on the factors that determine the size of nanotubes. The titanium foil serves as a bipolar electrode submerged in an electrolyte solution, while two platinum foils act as feeder electrodes. Once power is applied, a polarization potential that forms across the bipolar electrode, triggers simultaneous reduction and oxidation reactions.[18] A noteworthy outcome of this process, is the

generation of titanium dioxide nanotubes at the anodic pole of the bipolar electrode through a standard anodization process. Over time, this polarization potential reduces, causing a decrease in the dimensions of the nanotubes and leading to the creation of a gradient of titanium dioxide nanotubes. The researchers emphasized that a number of experimental parameters, including the type and concentration of the electrolyte, the applied potential, the duration of anodization, and the size of the bipolar electrode, can substantially influence the dimensions of nanotubes.[18] Previous studies have shown that the choice of electrolyte can impact the shape and size of nanotubes formed in a single electrochemistry anodization process.[16,18] In this study, a combination of ammonium fluoride, water, and glycerol was used as the electrolyte. By adjusting various parameters, they succeeded in generating gradient titanium dioxide nanotubes with a wide diameter range.[18]

1.3 Cellular Response to Titanium Nanotubes

1.3.1 Bioactive Properties of Titanium Nanotubes

Titanium and its alloys have long been the material of choice for various clinical applications, such as dental implants, bone and joint replacements, and cardiovascular implants.[11,71,72] The quality and characteristics of the interactions between cells and the implant surface is a critical factor in determining the success of these devices. Consequently, numerous studies have investigated the cellular response to titanium oxide nanotubes using various cell lines, including fibroblasts, chondrocytes, muscle cells, and mesenchymal cells.[1,9,13,73]

Similar to the trends mentioned above in Section 1.2.1 in nanoscale pits and protrusions, cellular responses to titanium nanotubes are highly sensitive to their diameter and interspacing. Research has shown that these parameters can significantly impact cell adhesion, growth, proliferation, and differentiation. To optimize osseointegration—the process by which an implant becomes

integrated within the surrounding bone tissue—researchers have been working diligently to determine the ideal structure and size of titanium oxide nanotubes. [1,8,13] Analysis of bone cell responses to titanium oxide nanotubes with varying diameters and architectures has been crucial in guiding the development of more effective implant materials. By identifying the optimal nanotube dimensions and structures that promote cell adhesion, growth, and differentiation, researchers aim to enhance the overall success and longevity of titanium-based implants.[15,74] Understanding the cellular response to titanium oxide nanotubes is an essential aspect of developing improved implant materials. By investigating how factors such as nanotube diameter and interspacing influence cell behavior, researchers can optimize implant design to promote osseointegration and ultimately improve patient outcomes.[5,6]

1.3.2 **Cell Proliferation and Spreading**

Cell proliferation refers to the increase in cell numbers over time resulting from the mitotic cycle while cellular spreading refers to the total area occupied at the cell-surface interface. Cellular proliferation and spreading are vital for osseointegration as they dictate the extent of interaction between the bone cells and the implant surface. An enhanced rate of cellular proliferation ensures a faster growth and maturation of bone cells around the implant, leading to a stronger bonding interface. Similarly, effective cellular spreading improves cell adhesion to the implant surface, further promoting differentiation the integration of the implant into the bone structure.[12,75]

To investigate the correlation between titanium nanotubes and cellular proliferation kinetics, Brammer et al. (2008) carried out a study where MC3T3-E1 mouse osteoblasts were cultured on vertically aligned TiO2 nanotubes. SEM imaging revealed the average dimensions of these nanotubes to have an outer diameter of about 100 nm, an inner diameter close to 70 nm, a wall thickness nearly 15 nm, and a height approximately 250 nm.[76] The dimension of 70 nm was chosen

as previous research highlighted its suitability for integrin function and activation, fitting within the desired range of 53 to 73 nm necessary for successful cell attachment.[77] The researchers noted a remarkable boost in cell adherence and proliferation on TiO2 nanotubes - around 300% to 400% - compared to standard titanium metal surfaces. This result could be attributed to the increased surface area, distinctive topography of the nanotubes, and enhanced hydrophilicity.[76] In another study, Park et al. (2007) investigated the proliferation and spreading of cells on TiO2 nanotubes with varying diameters (15, 20, 30, 50, 70, and 100 nm).[61] The nanotubes were prepared by anodization using a phosphate-fluoride electrolyte with voltages ranging from 1 to 20V. Green fluorescent protein (GFP)-labeled rat mesenchymal stem cells were seeded on the TiO2 nanotube layers with six different diameters, and polished smooth TiO2 layers were used as controls. Cell spreading and proliferation was found to be highest on the 15 nm. It was found that as tube diameter increased both features decreased. Interestingly, the cells formed lamellipodia and wide filopodia in contrast to the smooth surface. The 15 nm tubes were then tested for the osteoinductive ability, and it was found to have the greatest effect of differentiation compared to the smooth titanium control and higher tube diameters. This osteoinduction was quantified through staining of the mineralization of the stem cells with alizarin red and osteocalcin immunofluorescence. Additionally, FAK and ERK kinase expression was also found to be highest on 15 nm. In fact, 100 nm tube diameter showed an increased in apoptosis of the cells.[61] SEM and fluorescence microscopy revealed the formation of thick filopodia and lamellipodia in nanotubes ranging from 15 to 30 nm. As filopodial growth promotes cell spreading across nanotubes, cell adhesion and propagation were positively influenced by the presence of nanotubes. Impaired extension of filopodia was observed on cells seeded onto 100 nm nanotubes, indicating poor adhesion and proliferation. Overall, cell proliferation decreased with larger pore sizes.[61]

To further investigate the effects of spatial structural variables on cell-surface interaction, Steeves *et al.* 2020 developed a two-tiered honeycomb (HC) nanoarchitecture, consisting of smaller diameter (~20 nm) tubes nested in larger diameters (~100 nm).[2] Human MSCs were cultured and stained with DAPI on the nanotubular substrates, and time points within the first 48 hours were used to determine cell proliferation. Immunofluorescence microscopy was employed to observe substrate-induced variations. Initially (at 6 hours), more pronounced spreading was observed in the case of the honeycomb architecture compared to other nanotubular substrates. Ultimately, the highest cell area was seen in NT1 (20 nm) and HC (20 nm and 100 nm) architecture nanotubular surfaces. This finding suggests that the HC architecture led to more significant cell spreading and that the more elongated cell morphology resulted in an abundance of protrusions, an effect not observed on the larger 90 nm domains.[2]

1.3.3 Focal Adhesion Formation

The interaction of the cell with a material interface, ECM or other cells, is mediated by integrins. Integrins are responsible for the major cellular activities like migration, proliferation, differentiation, cell shape etc. A focal adhesion is a structure containing multiple proteins within it's structure and acts as the adhesive contact between the cell and ECM. The adhesion of the cell to the ECM activates the intercellular signaling cascades described in Section 1.1.2.[47,78] The focal adhesions emerge as diverse protein networks that provide structural integrity and dynamically link the ECM to intracellular actin filaments, directly facilitating cell migration and spreading. Over time, a functional focal adhesion will increase in size and complexity because of the recruitment of additional proteins such as vinculin and paxillin. In particular, many researchers use both vinculin and paxillin-targeting markers to evaluate the formation and quality of focal adhesions.[1,61] Park *et al.* 2007, demonstrated that the higher focal contact was observed in

nanotubes diameter smaller than 30nm. Such results also lead to a higher cell proliferation and differentiation in 15 nm diameter nanotubes as it provided the optimum length for focal adhesion and integrin clustering. In addition, tube diameters larger than 50 nm prevented integrin clustering, resulting in loss of focal adhesion complexes and thus reduced cell proliferation and differentiation.[61]

Another study carried out by Park *et al.* 2009 on human osteoblasts-like cells taken from human iliac bone marrow also demonstrated similar findings. Six different nanotube diameters ranging from 15 nm up to 100 nm were used as a substrate for cells that were stained for paxillin and fibronectin. Enhanced focal contacts and more significant deposition of fibronectin fibres were observed in the case of 15nm nanotubes compared to 100 nm nanotubes, ultimately showing that smaller diameter nanotubes enhance cellular adhesion. Furthermore, SEM images revealed that cells seeded onto 100 nm nanotubes were characterized by an impaired extension of filopodia, whereas they exhibit thick filopodia when seeded on to 15nm nanotubes.[79]

1.3.4 Osseointegration and Differentiation

The implant surface, which directly interacts with surrounding tissues, should be carefully engineered to improve the functional and structural fixation of the implant within the osseous tissue. A primary objective in bone tissue engineering is the development of highly osteoconductive implants that support bone growth by promoting osteoblast adhesion, proliferation, and bone extracellular matrix formation. To assess surface osteoconductivity, researchers often employ various cell lines at various stages along the osteo lineage such Saos-2, MG63, M3T3 or MSCs who's final cell fate has yet to be determined.[63,80]

In a recent study, anodized titanium nanotubes with varying diameters were utilized to evaluate the cellular response of Saos-2 cells, specifically focusing on ALP expression, a widely accepted

marker for early osteogenic differentiation. Saos-2 cells seeded on 30 nm and 80 nm titanium nanotube samples displayed significantly higher ALP expression compared to the flat titanium control, indicating enhanced differentiation of cells towards an osteogenic lineage.[80] MSCs are adult stem cells characterized by the ability of self-renewing and differentiating into different lineages such as chondrocytes, osteoblasts, fibroblasts, myocytes and endothelial cells. Such ability has boosted the use of MSCs in the biomedical field and namely regenerative medicine.[5,52,57,75] For this reason, many researchers have been attempting to unveil the effects of titanium nanotubes over the differentiation fate of MSCs. In particular, the ability to selectively guide the differentiation of MSCs toward osteogenic lines greatly impacts the field of bone tissue engineering. In an experiment focusing on the influence of nanoscale cues on hMSCs, also investigated cellular morphological alterations and differentiation marker response relative to the size of TiO2 nanotubes.[81] It was found that as the size of the nanotubes increased, so did the elongation ratio of the hMSCs. This contrasted with the isotropic configuration observed in smaller nanotubes and flat titanium. Larger nanotubes led to a marked elongation of hMSCs, a finding further corroborated through live cell imaging. This increased elongation on the larger nanotubes instigated a preferential shift towards osteogenic differentiation, as evidenced by immunofluorescent staining of osteogenetic protein markers OPN and OCN. Positive staining was specifically observed in hMSCs on 100 nm nanotubes but was absent on smaller nanotubes or flat titanium substrates. These observations were further substantiated by real-time PCR analysis which revealed upregulated osteoblast gene expression in hMSCs cultured on 70 and 100 nm TiO2 nanotubes. The highest level of up-regulation was exhibited by the 100 nm nanotubes, suggesting their potential utility in steering hMSCs differentiation into osteoblast-like cells. However, the 30-nm nanotube sample demonstrated an almost negligible degree of osteoblast gene expression.[81]

In a study conducted by Popat *et al.* 2007, TiO2 nanotubes with a length of 400 nm and diameter of 80nm were shown to enhance the osteogenic differentiation of MSCs. In particular, the authors evaluated using immunofluorescence to target the cellular expression of ALP, an early marker of osteogenic differentiation.[82] The results revealed a 50% increase in the ALP levels in cells seeded on nanotubular TiO2 compared to flat titanium surfaces, suggesting that the nanotube surface provides a better interface for osteogenic differentiation.[82] Similar results were obtained by Das *et al.* 2009, that demonstrate a higher ALP activity in osteoblasts on the nanotubular surfaces compared to control titanium surface, indicating that bone cells on nanoporous surface-initiated expressions of the mature osteoblastic phenotype.[83] Steeves *et al.* 2020, investigated the osteoinductive capabilities of nanotubular architectures through distribution and identification of Osterix/Sp7(OSX) protein. The nuclear localization of the OSX gene is essential in the commitment of pre-osteoblastic cells towards mature osteoblasts.[2] Surface-driven osteogenic differentiation was observed in all the varying nanotube architectures ranging from ~20nm (NT1), ~50nm (NT2) and ~90 nm (NT3), along with the two-tiered honeycomb surface (HC) consisting of smaller nanotubes(~20nm) and larger nanotubes (~100nm).[2] The introduction of nanotubular cues on TiO2 surface has been shown to not only enhance cell adhesion and proliferation but can also preferentially guide the differentiation of MSCs toward an osteogenic phenotype.[88]

1.3.5 Titanium Nanotube Gradient Cellular Response

Though titanium nanotubular gradients have been produced, there is much less depth in the biological and cellular responses to the topographical gradients. Song *et al.* 2018 constructed a structural gradient of titanium oxide nanotube arrays on medical titanium via pull-stop-pull and electrochemical anodization methods. Distinct characteristics including wettability translation, crystalline structure evolution, and the electrodeposition of octacalcium phosphate were studied,

as well as, *in vitro* testing which showed varied cell adhesion, extension, and propagation behaviors on the arrays for mouse MC3T3-E1 cells and different bacteria such as *E. coli* and *S. aureus*. The 60 nm diameter tubes were particularly bioactive for MC3T3-E1 cells, while certain bacteria preferred the 90 nm diameter topography.[70] In an expansion of this research, Li *et al.* 2020 used bipolar electrochemistry to create graded titanium nanotubes with diameters ranging from 20–350 nm. Investigations into protein adsorption and cellular behaviors revealed larger diameter TiO2 nanotubes had a higher protein adsorption capacity, whereas smaller nanotubes favored cell adhesion, proliferation, and differentiation; Annealed nanotubes with diameters over 180 nm adsorbed more serum proteins, and cell proliferation was more significant on the flat titanium and 20 nm diameter areas.[18] Cell differentiation was also influenced by nanotube dimensions, but ALP activity was similar for both as-prepared and annealed titanium nanotubes of the same size.[18] These results highlight the potential of using the titanium oxide nanotube gradients for high-throughput screening on medical titanium surfaces offering a deeper understanding of nanotube dimensions separate from sample to sample variation.

1.4 Environmental Mediation in Cell-Surface Interaction

While considerable focus has been placed on understanding how cells respond to these engineered surfaces, such as titanium nanotubes, less attention has been paid to the role of environmental conditions that exist beyond the surface.[84–86] The traditional approach *in vitro* often isolates the variable of surface topography while neglecting the complexities of the cell's natural microenvironment.[85–90] *In vivo*, cells reside within a dynamic system, where they are constantly exposed to a multitude of factors—such as nutrient gradients, mechanical forces, pH changes, and varying concentrations of metabolites—that influence their behavior.[11,43,86,88,91–93] In contrast, *in vitro* experiments frequently introduce cells to surfaces without considering these environmental

influences, assuming that surface characteristics alone are the primary determinant of cellular response.[84,85,87,94–99] For example, in the body, cells would have adapted to chronic stressors like low oxygen levels or high metabolic demands long before interacting with a surface.[21–23,94,100] By contrast, *in vitro* assays often initiate these stressors abruptly, failing to account for preconditioning effects that would more accurately mimic the *in vivo* situation.[22,84,85,88,89,94] This disconnect between in vitro models and the *in vivo* reality can lead to misinterpretation of results, where the observed cellular response might be a result of the sudden environmental change rather than an intrinsic response to the surface.

High glucose serves as a relevant and accessible example of an environmental factor that can mediate cell-surface interactions, particularly in the context of diabetes-related complications in bone regeneration.[19,23,86,88,94] By preconditioning cells in elevated glucose before introducing them to a nanotubular surface, it may be possible to more accurately assess the independent and combined effects of surface topography and environmental stressors.[19,98,101–105] This approach emphasizes the need for environmental mediation in cell-surface interaction studies, moving beyond the simple focus on surface properties to a more holistic view that incorporates the complexities of the *in vivo* microenvironment.

1.4.1 Diabetes and Hyperglycemic in vitro Models

In the field of biomaterial research, *in vitro* assays are commonly employed to explore the interaction between cells and various surface properties. However, traditional approaches often neglect the importance of the cellular microenvironment, focusing mainly on surface characteristics. One aspect that has been explored in this context is high glucose levels, a condition used to study diabetes, is known to affect MG63 proliferation and differentiation.[33–35,106,107] Second, while high glucose has been extensively researched for its influence on cellular behavior,

the aspect of preconditioning has often been overlooked. The current study aims to go beyond the traditional boundaries of surface-based analysis by implementing high glucose as a model to mimic physiological changes in the cellular environment. By choosing a modifier with known effects on specific cell types, our approach emphasizes the need for preconditioning to ensure that the cells display distinct behavior, which will be examined in the context of nanostructures. In doing so, we extend the investigation to broader cellular responses, such as those influenced by oxidative stress or hypoxia, instead of limiting the focus to diabetes-related factors. This research represents a shift in perspective, recognizing that if the goal is to imprint specific behavior in cells, there must be an assurance that this behavior is properly imprinted, regardless of the specific physiological conditions that might be present in patients. By focusing on HG and preconditioning, we aim to provide insights that can lead to tailored design of implants or biomaterials, thereby improving their interaction with the cellular microenvironment and contributing to a more nuanced understanding of cell-surface interactions.

1.4.1.1 Effects of Glucose on Proliferation and Differentiation of MG63 Cells

High glucose concentrations have been shown to impair cell proliferation and adhesion on implant surfaces, hindering the initial stages of osseointegration. Furthermore, these conditions negatively affect the differentiation of MG63 cells and osteoblasts, resulting in decreased expression of osteogenic markers such as ALP, OCN, and type I collagen. This impaired differentiation may compromise the bone-forming ability of osteoblasts, ultimately affecting osseointegration. [17,25] High glucose levels also inhibit the mineralization of the extracellular matrix produced by these cells, potentially due to the downregulation of genes involved in mineralization, leading to weaker bone-implant integration and reduced implant stability.[33] Another consequence of high glucose environments is the induction of oxidative stress in MG63 cells and osteoblasts,

causing the production of reactive oxygen species (ROS) and the activation of pro-inflammatory pathways. This oxidative stress may impair the function and survival of osteoblasts, further hindering the osseointegration process. Additionally, high glucose levels can alter the cellular response to implant materials, with osteoblasts exhibiting modified adhesion, proliferation, and differentiation on various biomaterial surfaces.[23,32,34,107]

In a study researching the effectiveness of metformin, high glucose levels were observed by Shao *et al.* 2014 to negatively impact the proliferation of osteoblasts and lead to reduced OCN and osteoprotegerin expressions. Interestingly, other common differentiation markers the levels, such as Collagen I and RANKL expressions remained stable. Additionally, high glucose conditions were linked with a decrease in intracellular ALP levels, a scenario effectively counteracted by metformin. Notably, metformin fully restored ALP downregulation by day 6, did so partially by day 12. The study showed the effectiveness of metformin in reducing the suppressive effects of high glucose on osteoblast proliferation and gene expression, especially during the early stages.[33] In a separate study by Linxi *et al.* 2015, MG63 cells were incubated in different glucose concentrations for a 24 hour period. The MTT measurement technique was adopted to track cell proliferation, and flow cytometry was used to examine cell cycles. Real time PCR Results indicated that minor glucose concentrations (5-8mM) had an insignificant effect on the proliferation of MG63 cells and other biological activities. However, a surge in glucose concentration (20-30mM) hindered MG63 cell proliferation, resulting in an increase in G1 phase cells, no change in S phase cells, and a decline in G2 phase cells. With a rise in glucose concentration, there was an enhancement in TNF related apoptosis inducing ligand and osteoprotegerin ligand expressions in MG63 cells, while osteoprotegerin expression exhibited a downward trend.[34]

These findings underscore the challenges associated with osseointegration in high glucose environments, such as those encountered in patients with diabetes. The damaging nature of elevated glucose levels to proliferative and differentiation markers *in vitro,* transfer *in vivo* in the form of poor wound healing and recovery.[23,108,109] Future research should focus on elucidating the molecular mechanisms underlying these effects and developing strategies to overcome these challenges. Potential approaches include optimizing implant surface properties, developing targeted drug delivery systems, and using growth factors and other bioactive molecules to enhance osseointegration in diabetic patients. Ultimately, a deeper understanding of the effects of high glucose environments on osseointegration will contribute to improved clinical outcomes for patients with diabetes requiring orthopedic or dental implants.

1.4.1.2 Preconditioning of MG63 Cells in High Glucose

Preconditioning MG63 cells in high glucose environments allows them to adapt to altered metabolic conditions. This adaptation leads to changes in the cells' behavior, such as alterations in gene expression, cellular signaling pathways, and metabolic processes, which can influence their response to implant materials.[20,21] It is possible that high glucose preconditioning provides a more relevant *in vitro* model for studying osseointegration by inducing cellular stress responses and molecular changes characteristic of the diabetic condition[94], but not the focus of this study. Though there has been a lot of work discussing the effects of high glucose after cells have been plated, there is a surprising lack of literature on the effects of preconditioning cells in antagonistic in elevated glucose environments. This is especially true in relation to nanotopographies influence on cell behavior.

When considering these studies, one finds that, in reference to whether or not cells were preconditioned throughout passaging prior to experimentation, studies definitively state there was

none[33,36,95,106,107], are unclear[34,110], or completed a short round of 24 hour or less pre-exposure before experimentation[111]. Preconditioning experiments outside osteoblastic lineages have a wide ranging degree of time points from single days to months.[94,100,112] In addition to this lack of information on preconditioning, many experiments involving the effects of high glucose on cellular differentiation are done over relatively short time periods (1-7 days), many showing similar results in TC culture plates or their respective surfaces.[23,33,35,36] Interestingly, when long-term studies are completed on osteoblasts, results can vary substantially when comparing 14-21 day timepoints to 7 days and earlier.[103,106] This may be due to the lack of sufficient timepoints in short term studies utilizing MG63, MC3T3 cells or SaOs-2 cells, as suggest in Czekanska *et al.* 2014.[28]

For example in a 2020 study, Takeno *et al.* utilized MC3T3-E1 cells, a mouse-derived osteoblastic cell line, to investigate the effect of high glucose on osteoblast maturation. They exposed cells to a glucose-rich medium (16.5 and 27.5 mM) over different intervals: continuously for 21 days, only for the initial 7 days (early stage), and only for the final 7 days (late stage). Findings showed that a 21-day high glucose exposure led to increased mineralization compared to the control (5.5 mM), with high glucose causing an elevation in the mRNA expression of ALP, OCN, RUNX2, and OSX on days 3 and 5. However, these osteoblastic markers decreased with prolonged high glucose exposure (14 and 21 days). Notably, early-stage HG enhanced mineralization, but late-stage high glucose had no significant effect. The team observed high glucose-induced upregulation in bone morphogenetic protein 4 expression. The study concluded that while HG may stimulate initial osteoblast differentiation, it can disrupt their maturation, with potential involvement of BMP-4-Smad signaling in HG-induced differentiation and mineralization of osteoblasts.[106] Similar plateaus and discrepancies occurred between days 7-21 in a 2022 study

by Valdez-Salas *et al*.,[103] investigating the role of osteoblasts in bone development, focusing on processes of cell proliferation, differentiation, and extracellular matrix mineralization, including calcium production and deposition. Utilizing the Alizarin Red S staining assay, the researchers studied MC3T3-E1 cells cultured on titanium nanotubes and the Ti6Al4V control surface under varied biochemical conditions over 7, 14, and 21 days of osteogenic differentiation. The team found escalating mineralization over time, with the nanotubes consistently stimulating calcified nodule creation. Despite observing a pattern similar to the control in the initial to the middle maturation phase, a significant surge in Alizarin levels was noted during the late phase for the nanotubes, suggesting a boost in nodule formation in this simulated micro-environment. Additionally, they found that the nanotextured surfaces seemed to foster swift initial bone mineralization, with a pronounced increase in the later stages. After 14 days of culture on these surfaces, collagen secretion from the MC3T3E-1 cells was observed, indicating collagen synthesis. Though there are studies that utilize preconditioning with other antagonists, preconditioning exposure to elevated glucose, are very rare. This opens potential space for research in preconditioning cells in high glucose and studying how the early exposure and acclimatization to elevated levels before introduction to a material or treatment may promote or further inhibit cell response. [103]

CHAPTER 2: Investigating the interplay between environmental conditioning and nanotopographical cueing on the response of human MG63 osteoblastic cells to titanium nanotubes

Ryan Berthelot [1-2], Fabio Variola[1-4,*]

[1] Faculty of Engineering, Department of Mechanical Engineering, University of Ottawa, Canada

[2] Ottawa-Carleton Institute for Biomedical Engineering (OCIBME), Ottawa, Canada

[3] Department of Cellular and Molecular Medicine, University of Ottawa, Canada

[4] Children's Hospital of Eastern Ontario (CHEO), Ottawa, Canada

1.5 Abstract

Titanium nanotubular surfaces have been extensively studied for use in biomedical implants due to their ability to promote relevant *in vitro* and *in vivo* phenomena associated with osseointegration, among other functions. However, despite the large body of literature on the subject, potential synergistic/antagonistic effects resulting from the combined influence of environmental effects and nanotopographical cueing remain poorly investigated. It is still unclear whether the nanotubes-induced variations in cellular activity are preserved across different biochemical contexts. To bridge this gap, this study systematically evaluates the combined influence of nanotopographical cues and environmental factors on human MG63 osteoblast-like cells. To this end, we capitalized on a triphasic anodization protocol to create nanotubular surfaces characterized by an average tube inner diameter of 25 nm (NT1) and 80 nm (NT2), as well as on a two-tiered honeycomb (HC) architecture, with minimal bifurcation. A variable glucose content was chosen as an environmental modifier due to its well-known ability to affect specific functions of MG63 cells. Alkaline phosphatase (ALP), viability/metabolic activity and proliferation were quantified to identify the suitable preconditioning window required for dictating a change in behaviour without significantly damaging cells. Successively, a combination of immunofluorescence, colorimetric assays, live cell imaging and western blots quantified viability/metabolic activity and cell proliferation, migration and differentiation as a function of the combined effects exerted by the nanostructured substrates and the glucose content. To achieve a thorough understanding of MG63 cell adaptation and response to nanotubular substrates and glucose content, a comparative analysis table that includes and systematically cross-analyzes all variables from this study was used for interpretation and discussion of the results.

1.6 Introduction

The drive to enhance bone tissue integration of both orthopedic and dental implants has homed in on titanium and its alloys, primarily due to their high mechanical strength, corrosion resistance and innate biocompatibility.[9,11,113] Many strategies have been posited to improve the osteoconductive potential of these biomedical devices by capitalizing on the well-documented *in vitro* and *in vivo* evidence that cells, and ultimately tissues, respond to specific surface properties of biomaterials.[113–116] Among these, nanotopography is generally recognized as a key influencer in regulating cellular events.[53,117,118] As a result, the employment of modification methods capable of precisely fabricating and customizing nanoscale features has rapidly emerged as an effective strategy to engineer cell-instructive substrates and biomedical implant surfaces.[115,119–121] In this context, nanotubes (NTs) generated by anodization of titanium and its alloys[9,63,73,122–124] have received considerable attention, ultimately becoming a widespread choice for both *in vitro* (e.g. nanostructured substrates to elucidate cell-surface interactions)[12,63,72,125–127] and *in vivo* (e.g. bone implants)[1,9,10,63,126] applications. In fact, in addition to the cost-effective, reliable and scalable methods of synthesis, the nanoscale topography of anodized surfaces can be precisely modulated to single out how specific morphological parameters affect cell fate decisions[54,61,128,129] and other functions (e.g. antibacterial properties, blood clotting).[130–133] Results from these studies established that the NTs' morphology plays a crucial role in dictating spreading, adhesion, proliferation and differentiation of commonly used cells in bone tissue research (e.g. mesenchymal stem cells, osteoblasts).[79,128,129] However, the identification of the optimal characteristics (e.g. diameter, spacing, wall thickness) that predictably elicits a specific cellular response is still a subject of controversy due to contradicting findings.[134] These inter-study discrepancies may in part derive from the specific anodization protocols adopted that introduce often overlooked sources of

morphological inconsistency, such as bifurcation, lateral spacing, spatial organization and regularity.[15,73,135] To fully harness the potential of NTs to systematically elucidate how cells sense nanotubular substrates, it is thus crucial to fabricate homogeneous, well-defined and spatially uniform topographical features.[128] In this context, a pertinent question is whether the cascade of molecular and cellular events previously ascribed to the beneficial *in vitro* signaling provided to cells by NTs is also contingent upon study-specific variables (e.g. culturing conditions) or is primarily directed by the nature of cell-substrate interactions.[19,63,76,103,128,129,136] It is still unknown whether the differential topography-dependent effects on cellular activity[55,79,134,135,137,138] will be preserved across different biochemical contexts or environmental factors can also contribute, either in synergy or antagonism, to dictating cell fate decisions on nanotubular substrates. This aspect becomes particularly critical in this field not only to call for more cohesive *in vitro* studies and to refine existing mechanistic models[43,78,127,139] but also to ultimately develop the fundamental knowledge towards cell-instructive surfaces for biomedical implants that provide a predictable and consistent response even in the physiologically fluctuating *in vivo* microenvironment[140–142] and/or in pathological conditions, such as hyperglycemia in diabetic patients[19,103,143,144], among others. In this context, comprehensive *in vitro* approaches that integrate and cross-analyze topographical and environmental variables are poised to identify the key design criteria for nanotubular surfaces that either maintain the desired biological performance across dynamic and multifactorial environmental contexts and/or provide adaptable cueing tailored to the specific biochemical conditions of the cellular microenvironment.

In this study, we investigated the differential effects of variable nanotubular morphologies on the activity of human MG63 osteoblastic cells, an immortalized cell line employed for *in vitro* bone research given its similarity to human osteoblasts in terms of growth kinetics, osteocalcin

and Runx2 synthesis and regulation as well as integrin subunits expression.[28,145] Distinctively from previous work,[53,55,138,146] we cross-analyzed both topography-specific cellular responses and relative inter-topography differences in cell behaviour as a function of a variable biochemical environment. To this end, we first implemented a stepwise approach to generate two highly ordered NT arrays with minimal bifurcation characterized by a mean diameter of ~25 nm (NT1) and ~80 nm (NT2). By building on this experimental approach and capitalizing on our previous work,[135] we also considered a two-tiered honeycomb (HC) architecture consisting of smaller NT1-like nanotubes clustered within larger domains, comparable in size to the NT2 nanostructure.

Among the environmental variables which can predictably influence cellular functions, glucose concentration emerged as an optimal option due to its widely studied ability to affect adhesion, proliferation, differentiation and mineralization of MG63 cells.[32–35,107,109,147] The use of a variable glucose content in the culture medium as an environmental modifier is a particularly common *in vitro* protocol to study the effects of hyperglycemia in the context of diabetes research,[147–149] whose application has also extended to the investigation of micro- and nano-structured surfaces for the prospective use under diabetic conditions.[19,103,150–152] Taken together, this large body of literature has established that high glucose has negative effects on migration [32,35,147], proliferation [32–35,103,107,147,150,153], differentiation38,39,50,55,56,60,61,68-71 and mineralization[103,107,147,150,154–159] of MG63 cells and related osteoblastic cell-lines. In this context, when considering glucose as an environmental modifier, adequately preconditioning cells to ensure that they fully adapt their behavior to the altered conditions prior to exposure to the experimental high-glucose culture medium is a fundamental yet often overlooked step. [35,160]

To bridge this gap, we first carried out a functional characterization which included alkaline phosphatase (ALP) and viability/metabolic activity assays as well as cell imaging to establish the

timeframe required for cells to adapt to the high glucose environment. Successively, we evaluated and compared a comprehensive array of cellular processes as a function of the nanotubular substrates in two different cellular environments characterized by a conventional baseline of 5 mM (representative of normal culturing conditions) and a higher content of 25 mM (representative of hyperglycemic conditions).[21,23,34,100,149,153,160,161] To summarize our findings and dissect out the interplay between the environment and the substrate, we devised a correlation table which offers a comparative analysis of the magnitude, variability and directionality of significant differences in order to extract and highlight relevant trends common throughout the various conditions and experiments.

In conclusion, our work investigates the combined effects of environmental conditioning, in the form of exposition to a higher glucose content, and nanotopographical cueing on the response of MG63 cells to nanotubular substrates with variable morphologies. Our results demonstrate that both untreated and nanotubular substrates can provide at various extents and for different cellular processes both "context-indifferent" and "adaptive" cueing for the development of prospective cell-instructive surfaces that are either required to maintain constant potential in dynamic conditions or that can predictively elicit specific cellular functions in response to environmental factors.

1.7 Experimental

1.7.1 Anodization of Titanium

Titanium foil (0.127 mm, 99.9+% purity Alfa Aesar, USA) was cut into 2.5 x 1 cm strips, which were successively submerged in 99.8% anhydrous toluene (Sigma Aldrich, USA), sonicated for 15 minutes to remove any contaminants from the surface, rinsed in deionized water and finally dried in air. The resulting samples were placed into a 3D printed apparatus of UV-hardened resin

and placed in front of a 2.5 cm x 2.5 cm platinum electrode (99.9% purity, Alfa Aesar, USA) by using alligator clips to keep the surfaces levelled and parallel to one another. Anodization was carried out, without contaminating the alligator clips, in a 50 ml Pyrex beaker with anhydrous ethylene glycol (C2H6O2, Sigma Aldrich) containing 0.3 wt% crystalline ammonium fluoride (NH4F, Sigma Aldrich, USA) and 2 wt% deionized water. The anodization was controlled by a PowerPac power supply (Bio-Rad, USA) in constant voltage (DC) and performed in three steps (triphasic anodization process) of variable voltage and duration (Table 2.1), to increase the order and consistency by decreasing the degree of bifurcation in the nanotubular arrays (Figure 2.S1, Table 2.S1). After the first step of anodization, the newly formed anodic layer was removed from both sides using tape and the resulting surface was placed back into the holder to undergo a second round of anodization. Once complete, surfaces were rinsed in deionized water and allowed to dry in air. By varying the experimental parameters of these steps (Table 2.1), the three nanotubular structures used in this study were created, namely: NT1 (~25 nm in diameter), NT2 (~80 nm in diameter) and honeycomb (HC), consisting of clusters of smaller tubes of ~25 nm in diameter (HC-T1) nested within larger domains of ~90 nm in diameter (HC-T2). Calculation of nanotube diameters conservatively utilized a 0.1% Q value to remove outliers.

Table 2.1. Voltage and time parameters for anodization of NT1, NT2 and HC substrates.

	Condition	NT1	NT2	HC
Step 1	Voltage (V)	30	90	60
	Time (Min)	60	5	30
Step 2	Voltage (V)	30	90	20
	Time (Min)	60	5	20
Step 3	Voltage (V)	30	90	/
	Time (Min)	5	5	/

1.7.2 SEM characterization and analysis of nanotubular surfaces

An investigation into the surface morphology of anodized substrates was carried out by using the JEOL JSM-7500F SEM (JEOL, Japan) and Gemini SEM 500 Scanning Electron Microscope (Zeiss, Germany) at a magnification of 50,000 X. Images were processed and analyzed with the analysis software FIJI-ImageJ using a custom smoothing and thresholding pipeline for the quantification of average diameter of the nanotubes, eccentricity, elongation, attachable surface area and the nearest neighbour distance (NND).[162] These values were calculated for each surface using 5 images from 5 independent samples.

1.7.3 Human MG63 osteoblastic cell cultures

Human MG63 osteoblastic cells (CRL-1427, ATCC, USA) were thawed and passaged using 1x TrypLE and DMEM (10567-014, Gibco, USA) in low (5 mM, hereafter referred to as LG) and high (25 mM, hereafter referred to as HG) glucose in complete culture media (CCM) supplemented with 10% fetal bovine serum (FBS). Cells were maintained at 37 °C in 5% CO2. After the CCM was gently aspirated, cells were washed three times in sterile 1x PBS and detached from the surface of the culture flask by using 3 mL of TrypLE. Cells were left in the incubator for 3 minutes until full detachment from the bottom surface. Successively, 7 mL of culture medium were added to the cell suspension and placed into a centrifuge for 8 minutes at 150 rpm. After centrifuging, cells were resuspended in 10 mL of CCM. Finally, 2 mL of the suspension were pipetted into 8 mL of fresh CCM in a filtered 75 cm^2 flask and placed back into the incubator.

1.7.4 Cell Seeding and Fixation

Anodized strips were further cut into 0.5 x 0.5 cm substrates, sterilized in 70% ethanol and washed in sterile 1x PBS. Next, the resulting samples were placed in 48-well plates and a cell suspension of 2,500 cells per well was added. Cells were then cultured for experiment-specific

time periods ranging from 48 hours (h) to 14 days (d) to investigate proliferation, morphology, differentiation and bone mineral deposition. Untreated titanium samples (hereafter referred to as Ti) were used as controls. Experiments were terminated by cellular fixation with 250 µL/well of fresh 4%-paraformaldehyde (PFA, Sigma-Aldrich) for 10 minutes (min) at room temperature (RT). Wells were gently washed three times with 250 µL of PBS to remove the remaining PFA, and filled with a final 250 µL volume of PBS and stored at 4 °C. All experiments were performed with at least 3 samples per condition, per time point, and were completed in triplicate.

1.7.5 Immunofluorescence Staining

Cells were permeabilized with a 0.25% solution of Triton X-100 (TX-100, Sigma-Aldrich) for a duration of 10 min at RT. Nuclei and actin were labeled with DAPI and ReadyProbes Actin Green 488 phalloidin (Thermo Fisher, USA) (2 drops/ml). Samples were blocked with 5% donkey serum (Sigma, USA) at RT for 1 h. Cell proliferation was assessed by staining for anti-Ki67 polyclonal rabbit antibody (Millipore Sigma, USA) at a 1:500 dilution. Ki67 primary stain was followed by secondary labeling with AlexaFluor 647 Donkey-anti-rabbit IgG (Thermo Fisher, USA). The primary antibody incubation was conducted overnight at a temperature of 4 °C, whereas the blocking and secondary antibody incubations were each carried out for 1 h at RT. Post-incubation, the samples were gently washed and then imaged in PBS within a glass-bottomed 24-well plate.

1.7.6 Immunofluorescence Imaging and Analysis

The multi-channel images used for the quantification of nuclei number and the analysis of cytoskeletal morphology were obtained by using a ThermoFisher EVOS FL Auto 2 (inverted) widefield microscope (ThermoFisher, USA). Images of the entire 0.5 x 0.5 cm sample surface were captured with 10X air objective (0.25 NA, Air, PL FL LWD PH), equating to roughly 30

images per sample. The imaging system utilizes LED light sources with specific filters for different wavelengths: Blue (Ex 357/44 nm, Em 447/60 nm), Green (Ex 470/22 nm, Em 510/42 nm), Red (Ex 585/29 nm, Em 624/40 nm), and Far Red (Ex 628/40 nm, Em 692/40 nm). Detection is performed using a monochrome camera. The number of DAPI-stained nuclei and actin morphology on each surface was quantified using custom ImageJ[162] pipelines. The primary morphological parameters considered were the area (μm^2), irregularity index[163], protrusion index and the aspect ratioa robust[135,164] (major axis/minor axis). To form intuitive, positively correlated indexes, irregularity and protrusion were calculated, respectively, by subtracting the form factor and solidity[164,165] (both scales from 0-1) from 1. Form factor is defined by the equation $(4\pi A)/P^2$; where A is the cell area and P is the perimeter. Solidity is defined as the area of the cell divided by the area of its convex hull. The form factor and solidity were inverted to make a perfect circle in both cases equal to 1. Both nuclear and cellular morphology analysis was carried out by stitching, segmenting and processing image in a custom pipeline calculated via particle analysis in ImageJ. For the morphological analysis, a total of 9 samples per condition were analyzed, encompassing three biological replicates from each of the three distinct experimental sets.

Ki67 images were subject to background subtraction and analyzed using a custom ImageJ pipeline. Processed Ki67 images were then subject to Yen auto thresholding to derive %Area metric used to separate cells into mitosis (%Area ≥ 90%) and interphase (%Area < 90%) based on Ki67 phases derived from literature where condensed chromosomes during mitosis phase lead to bright Ki67 signal occupying the majority of the nuclear area.[166] The phase index represents the ratio of cells in mitosis over those in interphase, both phases being divided by total cell count. DAPI images were segmented via custom ImageJ pipeline and used in generating regions of interest (ROIs) for intensity and Area fraction analysis. For Ki67 analysis a minimum of 15

samples per condition were analyzed, encompassing three biological replicates from each of nine distinct experimental sets, discarding damaged samples.

1.7.7 Cell migration Assay

A scratch assay was conducted to assess the migratory capability of MG63 cells on the nanotubular surfaces in the two environments. Cells were seeded at a density of 60,000 cells per well in 12-well plates containing 600 mL of DMEM (10567-014, Gibco, USA) supplemented with 10% FBS and incubated until adequate confluence was achieved after 2 days. The supplemented medium was then replaced with serum-free medium. After 24 h, sterile 200 µL pipette tips were used to create a cell-free area by scraping the cell monolayer across each well. Successively, the cell monolayer was gently washed with PBS to remove detached cells and cell debris. Images of the scratched area were captured at various time points with a ThermoFisher EVOSFL Auto 2 (inverted) widefield microscope (ThermoFisher, USA) at 5X (0.13 NA, Air, PL FL LWD PH) and 10X (0.25 NA, Air, PL FL LWD PH) magnification to quantify the closure of the scratch. The initial scratch area was measured by using a custom ImageJ pipeline to determine the differences between the scratch area at time 0 and the other time points which were segmented via thresholding. Cell migration assays on untreated and anodized 1 x 1 cm^2 titanium surfaces were completed in an identical manner as above at 0, 12 and 24 h. Substrates were moved into a new 12-well plate 24 h after seeding. To visualize migration on the opaque surfaces, cells were stained with CellTracker Red CMTPX Dye (ThermoFisher, USA).

1.7.8 Proliferation Assay

The PrestoBlue Cell Viability Assay (ThermoFisher, USA) was employed to assess cells viability in response to their metabolic activity. Cells were first seeded in a 48-well plate at a density of 2,500 cells per well and cultured at 37 °C. PrestoBlue measurements were taken at 1-,

3- and 7-day intervals. The PrestoBlue reagent was diluted 1:10 in CCM as a working solution. The culture medium was removed from the wells and 250 uL of the prepared PrestoBlue working solution were added to each well. The plate was incubated at 37 °C with 5% CO2 for a duration ranging for 1 h. Following the incubation period, the plate was gently swirled to ensure even distribution of the reagent and cells. Two 100 uL aliquots of solution were transferred to a 96-well plate as technical replicates, while fresh CCM was pipetted back in to the 48-well plate and placed back into the incubator. Fluorescence signal was measured with the Synergy H1 plate reader (BioTek, USA) with excitation and emission wavelengths set at 560 nm and 590 nm, respectively. Data analysis was carried out by subtracting intensity readings of control wells containing only media and the 1:10 PrestoBlue mixture and comparing the relative fluorescence units between anodized and control groups to determine the effect of various treatments on cell viability/metabolism. All experiments were done in triplicate with a minimum of 10 and 6 wells per condition, per plate for preconditioning and NT experiments, respectively.

1.7.9 ALP Assay Protocol

The activity of alkaline phosphatase (ALP) was evaluated at two different time points, namely 7- and 14-days post seeding, by employing the Pierce PNPP Substrate Kit (Thermo Scientific, USA). Following each predetermined incubation period, samples were subjected to lysis and then treated with a solution made from *p*-nitrophenyl phosphate, disodium salt (PNPP) tablets and 1M diethanolamine, as per the guidelines provided by the manufacturer. The reaction was allowed to proceed for 1 h before it was terminated by adding NaOH. Subsequently, ALP activity was quantified by measuring the absorbance at 405 nm using the Synergy H1 plate reader (BioTek, USA). For the purpose of maintaining consistency across multiple time points, all ALP measurements were juxtaposed with a standard curve and converted to standard U/L units by

dividing the p-nitrophenol (pNP) produced (in μmol) by the sample volume multiplied by the reacting time (in minutes). All experiments were done in triplicate with a total of 30 samples, with 10 wells for each experimental condition across 3 independent experiments for the preconditioning and NT experiments.

1.7.10 Alizarin Red Staining and Assay

To assess mineralization occurring on the substrates, an Alizarin Red Staining (ARS) (Sigma, USA) protocol was employed. Initially, the culture medium was carefully discarded from each well, followed by a gentle triple washing step in 1xPBS. Cells were fixed in 4% PFA at RT for approximately 15 min. Following the fixation, the PFA was removed, and the cells were subjected to three thorough washing steps in deionized water. After ensuring the complete removal of deionized water, each well was treated with 1 mL of 40 mM ARS solution. This step involved a RT incubation period of 25 min, during which the plates were subjected to gentle shaking to ensure optimal interaction between the cells and the dye. Post-incubation, the ARS solution was removed, and the cells were washed five times with deionized water to eliminate the unbound dye. As a final step, the plates were tilted for about 2 minutes to facilitate the removal of any residual water, thereby preparing the samples for subsequent procedures and analyses. Representative images were taken with a ThermoFisher EVOS FL Auto 2 inverted widefield microscope with a 10X air objective (0.25 NA, Air, PL FL LWD PH) with small ring phase filter.

After imaging, 200 μL of 10% acetic acid was first added to each well of a 48-well plate and incubation was done at RT for 30 min with shaking. Cells were successively collected using a cell scraper and transferred to a 1.5-mL microcentrifuge tube containing the 10% acetic acid. The samples were then subjected to vortexing for 30 seconds and heated at 85 °C for 10 min. To avoid evaporation, the tubes were sealed with parafilm. After the heating step, the tubes were placed on

ice for a 5-min incubation period until fully cooled. Subsequently, the mixture was centrifuged at 12,000 g for 15 minutes. Post centrifugation, the supernatant was carefully transferred to a new tube. To this, 30 µL of 10% ammonium hydroxide was added to maintain a pH between 4.1 and 4.5. 100 µL of the samples were aliquoted into a 96-well plate and the absorbance was read at 405 nm using the Synergy H1 plate reader (BioTek, USA). An ARS standard curve was plotted using Excel (Microsoft, USA), and the ARS concentration of the samples was calculated. Measurements for the assay were conducted on a total of 27 samples, which included nine wells from each of the three distinct experimental sets.

1.7.11 Western Blots

To isolate the protein content, cells were first harvested from the surface via cell-scraper and subsequently sonicated in cold Radioimmunoprecipitation assay (RIPA) buffer. The lysates were cleared via centrifugation at 12,000 g for 10 min at RT. The Pierce assay (ThermoFisher, 23225) was employed to determine the total protein concentration of the cell lysates. After mixing 2x Laemmli buffer, lysates were boiled for 10 min at 95 °C, and resolve on 10% Sodium Dodecyl Sulfate–Polyacrylamide Gel Electrophoresis (SDS-PAGE) gel (Bio-Rad, USA, Mini Protean TGX Stain Free), with protein bands resolved at 90 V. For protein transfer, resolved proteins were transferred to PVDF membranes for 30 minutes at 20 V using the Transblot Turbo system (Bio-Rad, USA). Following a wash, the membranes were blocked with 5% laboratory grade skim milk (Sigma-Aldrich, USA) for 1 h at RT. Primary antibodies against target proteins, including osteocalcin (OCN), RUNX2 and osteopontin (OPN), were diluted 1:1000 and incubated with the membranes for 18 h at 4 °C. Subsequently, the membranes were incubated with corresponding donkey secondary horseradish peroxidase (HRP)-conjugated antibodies (Invitrogen, PA1-28664, 31458, SA1-100) for 1 h at RT. Finally, the ChemiDoc XRS+ system (Bio-Rad, USA) was used

to image the membranes, and the bands were analyzed using the ImageLab software. Using Bio-Rad's stain-free technology, protein bands were normalized against total protein content, which offers advantages over single-control protein normalization, with improved reliability and interpretability of the Western blot data.[167,168]

1.7.12 Statistical Analysis

The Shapiro-Wilk test was used to evaluate the normal distribution of the data sets. If data sets followed a normal distribution, they were subsequently analyzed using a parametric One-Way ANOVA, and any significant differences in means were identified using Tukey's Honest Significant Difference (HSD) post-hoc test. Data deviating from normal were confirmed by the nonparametric Kruskal-Wallis test, and subject to Dunn's post hoc test. Error bars are displayed as the mean with 95% confidence interval, unless stated otherwise in figure description. A p-value less than 0.05 was considered indicative of statistical significance. The levels of significance were denoted as follows: "*" for $p<0.05$, "**" for $p<0.01$, and "***" for $p<0.001$.

1.8 Results

In the evolving field of biomaterials, the detailed understanding of cell-material interactions is paramount to designing increasingly more effective biomedical technologies. In this context, this study leverages the unique properties of titanium nanotubular surfaces for an exploration of synergistic/antagonistic effects concertedly exerted by nanotopographical features and the biochemical microenvironment on MG63 osteoblastic cells. By integrating analytical techniques with long-term culture observations, the research delineates a multifactorial picture of the cellular dynamics at play.

1.8.1 *Nanotubes Fabrication*

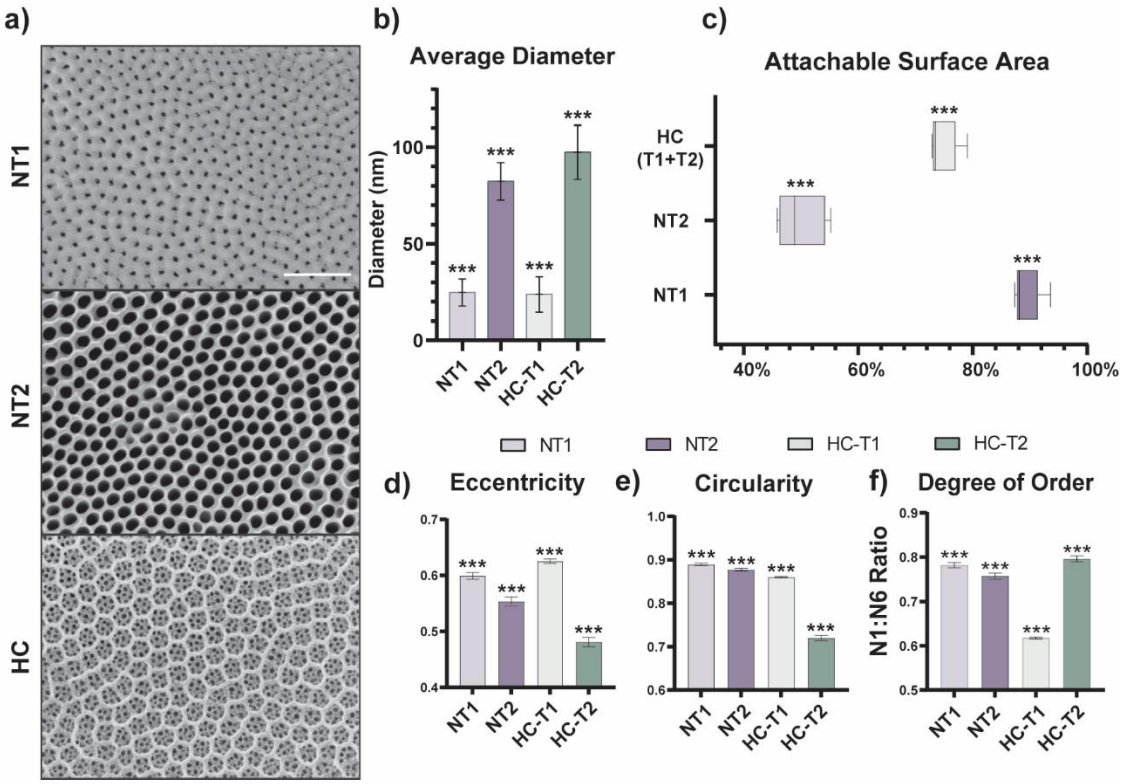

Figure 2.1. Nanotube diameters and geometries. (a) SEM images of NT1, NT2 and HC surfaces, (b) diameters' size distribution (± standard deviation), (c) percent attachable surface area, (d) eccentricity, (e) circularity and (f) degree of order of the nanotubular openings.

Figure 2.1a displays SEM images of NT1, NT2 and the HC substrates, characterized by a diameter of 25 ± 7 nm, 82 ± 11 nm, 24 ± 8 nm (HC-T1) and 92 ± 17 nm (HC-T2), respectively (Figure 2.1b). Notably, architecture-wise, the HC substrate can be regarded as a superimposition of the NT1 (representing the smaller HC-T1 domains) nested within larger 92 nm HC-T2 domains. Significant differences are observable across all surfaces with respect to attachable surface area (Figure 2.1c) and eccentricity (Figure 2.1d). Circular morphology is preserved across all nanotubular openings (Figure 2.1e), except for the larger HC-T2 domains, which assumed a more hexagonal conformation. Finally, the degree of order (Figure 2.1f) for NT1, NT2 and HC-T2 all fell within a narrow range of 0.75-0.80, with the exception of the HC-T1 having the lowest value

of 0.62. This parameter was assessed by calculating the ratio between a tube's nearest neighbor and the average distance between a tube and its six nearest neighbours (N1:N6 ratio) (Figure 2.S1a). This nearest neighbour analysis (NNA) on surfaces obtained by the triphasic anodization protocol used in this study demonstrated a significantly higher ratio value, and lacked the bifurcation peak in their distribution plots, indicating a homogeneous and well-ordered nanotubular array (Figure 2.S1b). Voronoi tessellation[135,169,170] provided a representation of the heterogeneity present in the nanotube structures (Figure 2.S1c), ultimately providing a visual confirmation of the NNA results. In contrast, when surfaces were created via a two-step anodization protocol, two distinct populations appeared (Figure 2.S1b): one representing the majority of the tubular order at the desired diameter and spacing and the other resulting from the presence of bifurcated tubes appearing as closely related nearest neighbors.

1.8.2 Preconditioning

To determine the optimal preconditioning parameters that ensure that cells adapt to the HG environment, we carried out a correlation between the time of exposure to HG conditions in commercial culture flasks and key functional metrics, namely expression of ALP and cell viability/metabolic activity, proliferation and migration. The timeframe for HG preconditioning for the subsequent cellular experiments on the nanotubular substrates was determined based on the stabilization of these metrics. By initiating our cellular assays after this adaptation period, we could more accurately ascribe any variations in behaviour to cell-surface interactions rather than to solely the glucose environment. This methodological approach streamlined the experimental design, reducing external influences and enhancing the clarity of the results regarding the impact of nanotopographical cueing.

To this end, cells were passaged in HG for varying timeframes ranging from 0 to 21 days. At each timepoint, preconditioned cells were transferred and seeded into standard culture plates. Figure 2.2a displays DAPI-stained nuclei count, an indicator of cell proliferation, at different days of preconditioning in HG. A sharp fluctuation in the relative cell counts was observed after 7 days of preconditioning, with stabilization occurring after 10 days. A similar trend was also observed for ALP activity levels, which were measured after an additional seven days of culture (Figure 2.2b). Results show that at 14 days the ALP level plateaus, a finding that confirms previous work on the metabolic changes occurring in patient-derived osteoblasts in HG[160] with similar passaging prior to experimentation.[102,104] This 2-week period was not only required for normalizing proliferation and ALP activity, but was also necessary to stabilize the viability/metabolic activity. In particular, Figure 2.2c displays results from the PrestoBlue (PB) assay (a proxy of cell metabolic activity) in terms of intensity changes collected at day 4 and 7, and expressed in relation to the values collected on day 1 for the respective duration of preconditioning. All three metrics were normalized against the baseline readings measured from cells cultured at day zero (i.e. prior to the beginning of preconditioning) in LG conditions. It can be observed that the impact on cell viability emerged sooner, with substantial changes appearing on both day 4 and day 7 after only 4 days of preconditioning. Therefore, 2 weeks was established as the optimal preconditioning timeframe. Interestingly, this period of time was also found suitable to prevent the imprinting of irreversible modifications into cells (Figure 2.S2a-f), thereby providing the sought-after environmental effects without long-lasting and detrimental consequences, at least within the realm of cellular functions considered in this study, which could introduce additional variables in the comparison of cell behaviour between LG and HG. Therefore, cells utilized for all the functional assays in HG

conditions described in the following sections were pre-conditioned 2-weeks prior to the experiments.

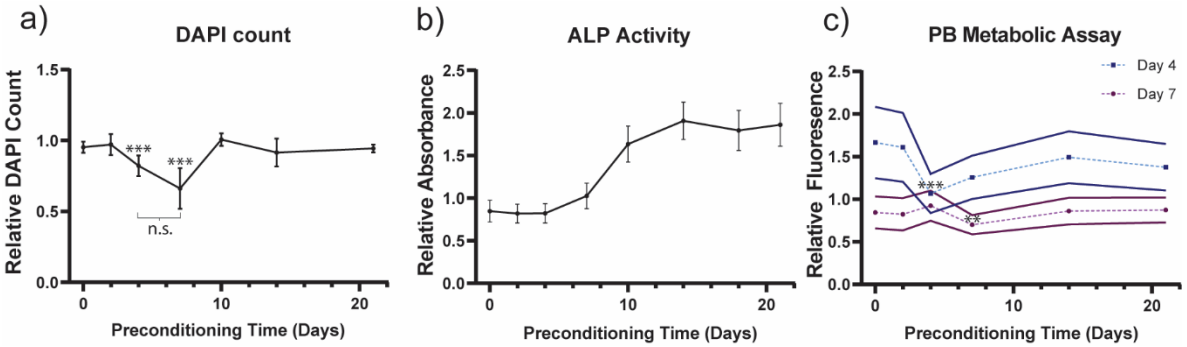

Figure 2.2. Effects of days preconditioned in HG on (a) DAPI count at day 7 (relative to cells grown under normal LG conditions), (b) ALP expression after 7 days post-preconditioning and (c) cell viability/metabolic activity at day 4 and 7 (relative to day 1) expressed as mean PrestoBlue intensity. Timepoints were normalized against baseline readings measured from cells cultured at day zero in LG conditions. Error bars correspond to +/- standard deviation.

1.8.3 *Morphology*

The first step in the evaluation of substrate- and environment-induced variations in the behaviour of cells was a quantitative analysis of their morphology after 2 days of cultures by immunofluorescence microscopy. Figure 2.3a shows that the glucose content had no significant role in affecting cell area. Cells adhering on untreated titanium exhibited the highest degree of cellular spreading while those on NT2 the lowest. A similar trend was observed for cellular irregularity (Figure 2.3b), with all nanotubular surfaces (unlike untreated titanium) displaying no significant differences between LG and HG. Cells on titanium controls showed the highest irregular morphology, while those on NT2 the lowest. In terms of protrusion (Figure 2.3c), the pattern mirrored that of irregularity, with cells on Ti displaying slightly higher levels of protrusion in LG than in HG, and the NT2 surface showing the lowest value. NT1 and HC showed no significant differences from one another in both glucose conditions. Cells on untreated titanium showed the highest elongation in both LG and HG in comparison to the nanotubular surfaces

(Figure 2.3d). Similarly to the degree of protrusion, cells on all nanotubular surfaces showed consistent elongation across both glucose environments and no significant differences were observed between NT1 and HC in either condition. Nuclear area was the largest on Ti in both conditions, uniquely showing no significant differences between LG and HG (Figure 2.3e). Conversely, both NT1 and NT2 were associated with larger areas in HG than in LG, while HC displayed the opposite trend. Cells on NT1 showed the largest area across both conditions compared to the other NT surfaces. Lastly, while cells on untreated titanium and NT1 substrates showed similar degrees of nuclear circularity in both glucose regimes (Figure 2.3f), on NT2 they consistently had the lowest values, particularly in LG.

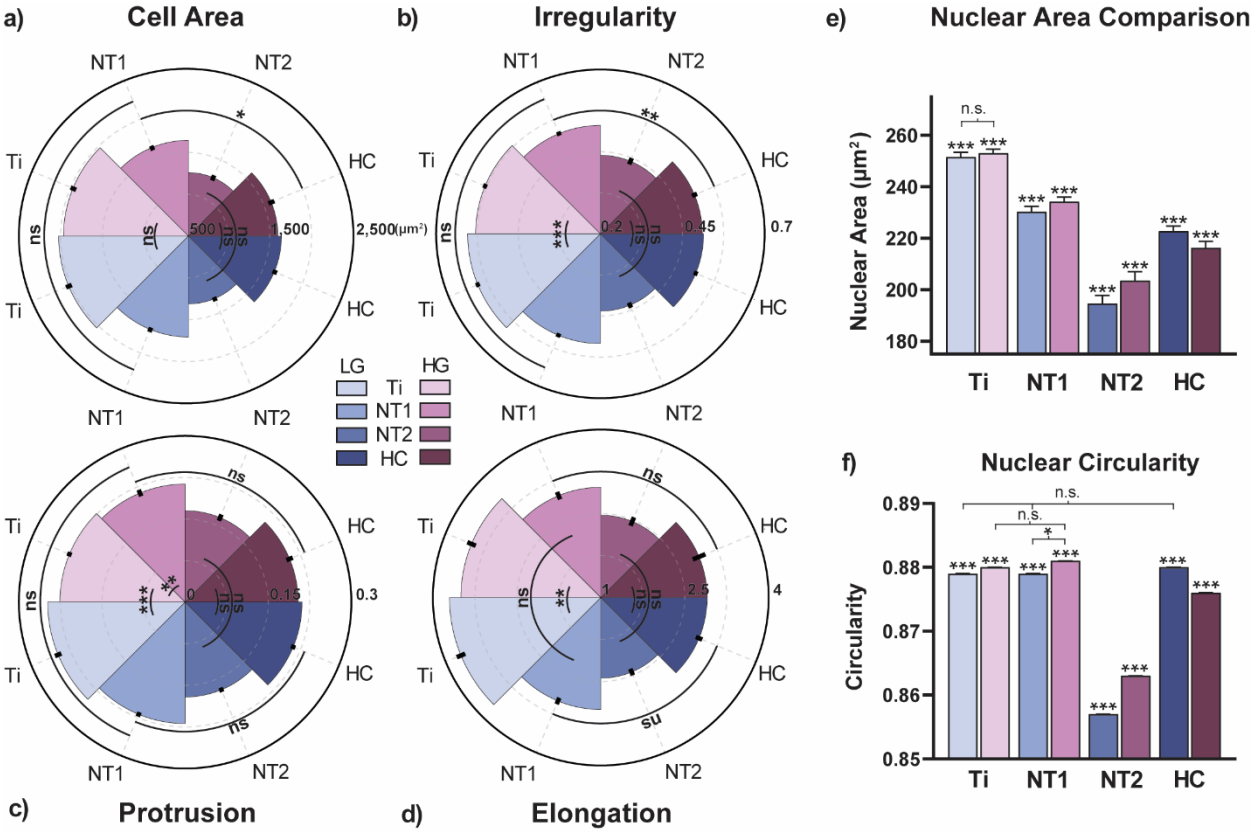

Figure 2.3. Morphological analysis of cells on untreated and anodized substrates after 2 days of cultures in LG and HG conditions: (a) Cell area, (b) irregularity, (c) protrusion and (d) elongation. DAPI-stained nuclei were analyzed for changes in (e) area and (f) circularity, as a function of the substrate and the glucose level.

1.8.4 *Proliferation*

Successively, we transitioned into cellular proliferation metrics, specifically Ki67 positivity and the phase index (i.e. the ratio between mitosis vs. interphase) assessed after 2 days of culture. Larger values of both of these metrics indicate a higher propensity for proliferation.[34,46,49,159,171–175] Figure 2.4a examines the percentage of Ki67 positive cells across the different surfaces in LG and HG. Cells on untreated titanium exhibited the highest Ki67 positivity in both LG and HG. Notably, differences between LG and HG conditions for all substrates were not statistically significant, indicating that surface topography exerts a more pronounced effect than glucose concentration on Ki67 positivity. Successively, we evaluated the phase index (Figure 2.4b), which revealed no differences among surfaces in LG. In HG, cells on NT2 exhibited the highest mean phase index, and those on NT1 the lowest. HC's index in HG did not significantly differ from that of untreated titanium, unlike that for NT1 and NT2. The index associated with these two surfaces in HG also significantly diverged from its counterpart in LG. Cells on all nanotubular surfaces displayed a lower Ki67 intensity when compared to untreated titanium in both glucose conditions (Figures 2.4d). In addition, cells on both Ti and NT2 in HG showed a higher intensity than their LG counterparts, while on NT1, they exhibited a lower value. The HC surface showed no significant intensity variation between the two glucose regimes.

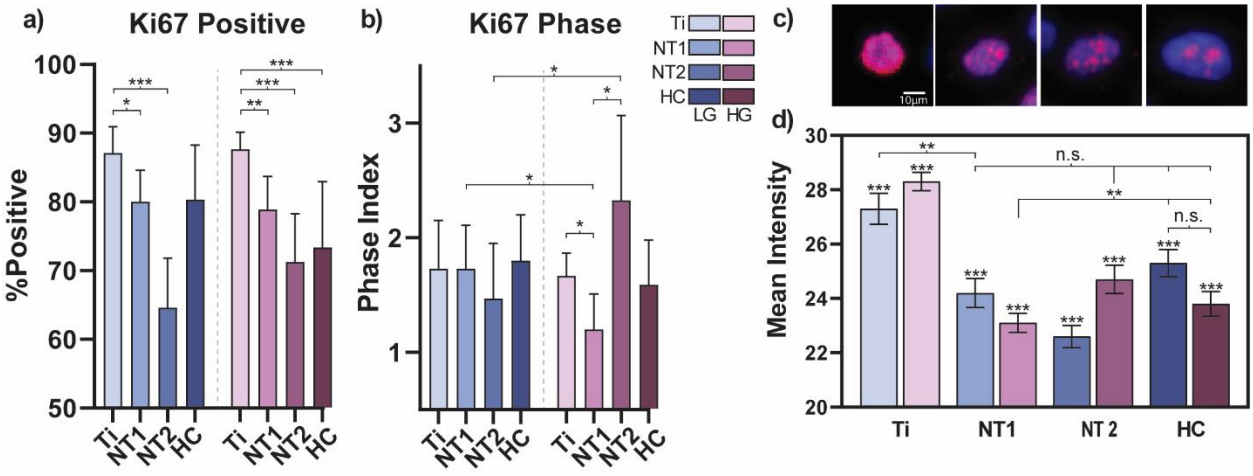

Figure 2.4. (a) Percent of cells testing positive for Ki67 and (b) ratio of cells in mitosis vs. interphase. (c) Representative images of Ki67-stained nuclei in mitosis, and early-, mid- and late-G1 stages. (d) Mean intensity of Ki67 expression.

1.8.5 *Migration*

The analysis of cellular morphology and proliferation was followed by live-cell migration via a scratch assay. It can be readily observed that cell colonization of nanotubular surfaces, and particularly of the NT2 substrates, was more marked than that of titanium across both glucose regimes at both 12 and 24 h intervals (Figure 2.5a). It can be observed that cellular migration across all substrates was unaffected by the glucose environment within the first 12 h. At this time interval, migration was elicited on the NT surfaces when compared to titanium control in both LG and HG. At 24 h, cell migration remained unaffected by the glucose only on Ti. While in HG cells on anodized surfaces maintained a greater migration in respect to controls, in LG this was only valid for the NT2 substrate.

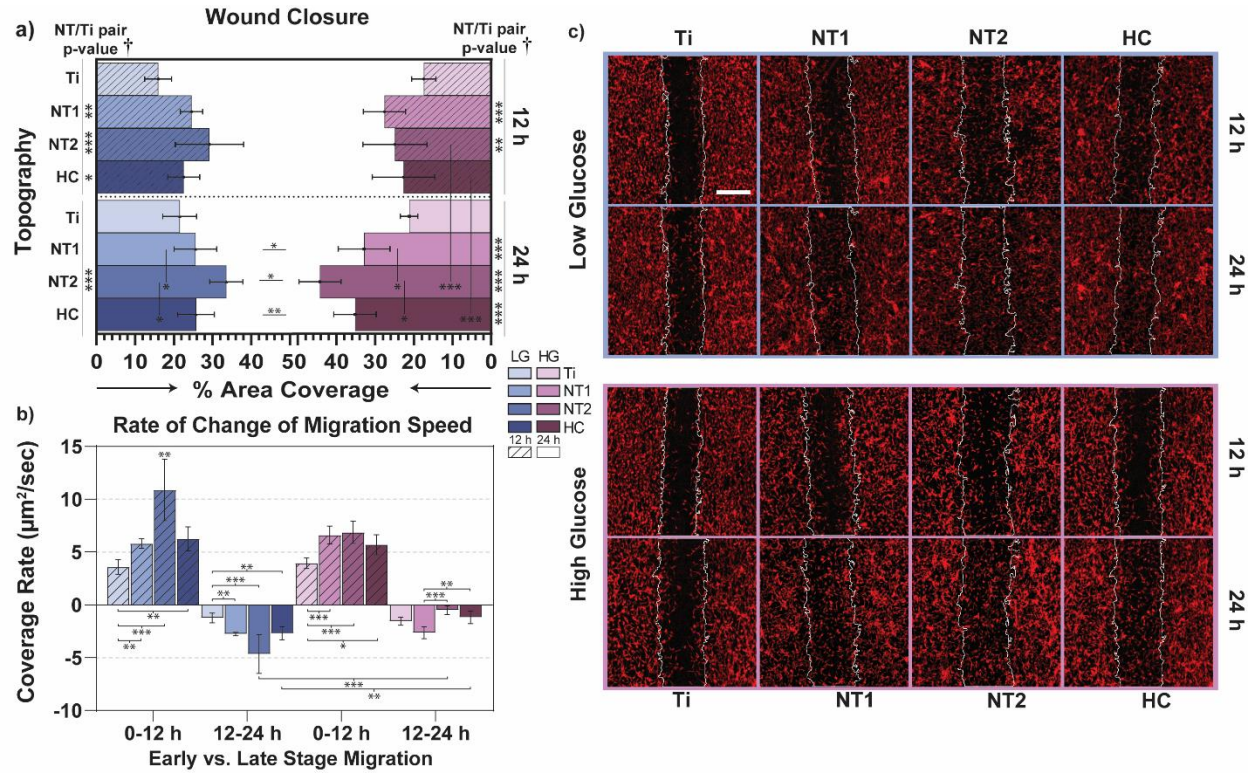

Figure 2.5. (a) Scratch assay of MG63 cells on titanium controls and anodized substrates in HG and LG, showing total area coverage after 12 and 24 h. The "†" symbol on the y-axis denotes the p-value associated with differences between NT surfaces and Ti control, for each time interval and glucose level. (b) Changes in migration rates in early stage (0-12 h) vs late stage (12-24 h) migration. (c) Representative images of cells after 12 h and 24 h migration in LG and HG.

Based on these results, we evaluated variations in migration rates at earlier (0-12 h) and later (12-24 h) stages (Figure 2.5b). An increased migration rate is depicted as a positive value along the y-axis, while a negative number indicates that cells slowed down from one stage to the other. During the earlier stage, all nanotubular surfaces are characterized by higher migration rates compared to untreated controls in both LG and HG conditions. Notably, cells exhibited especially rapid migration on NT2 samples in LG within this initial timeframe. However, all surfaces showed a rate reduction during the later stage. Specifically, migration rates on all nanotubular surfaces decreased relative to untreated titanium in LG. Conversely, migration rates were consistent across all samples in HG. The significant distinction between glucose levels emerged at the later stage,

with cells on NT2 and HC samples in LG displaying slower migration rates than their counterparts in HG. The representative images from the scratch assay in Figure 2.5c qualitatively corroborate these findings, highlighting the rapid migration of cells across the NT surfaces, particularly within the first 12 h.

1.8.6 Viability/Metabolic Activity

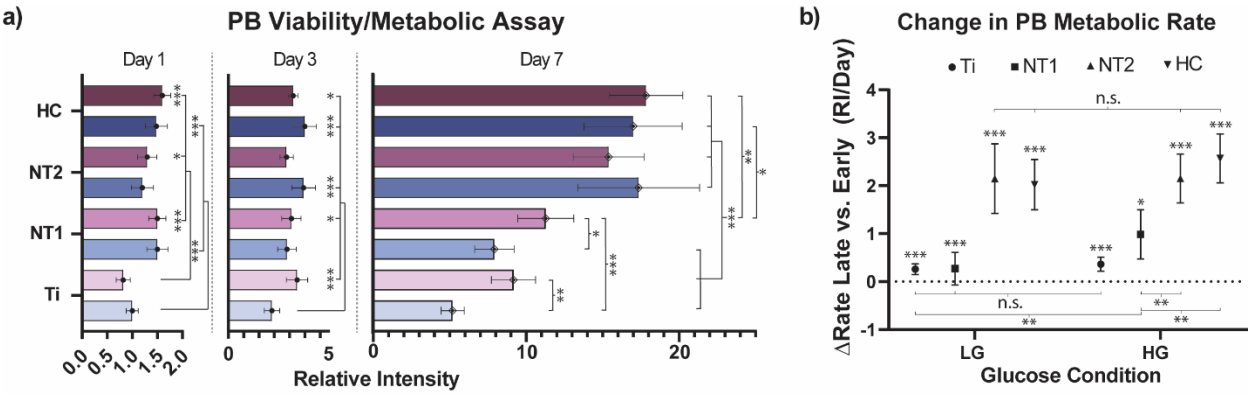

Figure 2.6. PrestoBlue (PB) analysis at day 1, day 3 and day 7 showing (a) overall PB metabolic activity and (b) the differential between PB metabolic rates (Relative Intensity (RI)/Day) during early (days 1-3) and later stage (days 4-7). LG conditions in (a) are represented by shades of blue while HG conditions by shades of red.

Figure 2.6a highlights the differences in cell viability determined by the PrestoBlue assay between the surfaces on day 1, 3 and 7 in LG and HG. NT substrates, with the exception of NT2 in LG, had elevated viability/metabolic activity relative to untreated titanium on Day 1. At day 3, the only significant differences were noted between nanotubular surfaces and titanium control in LG. At this timepoint, cells on titanium in HG, together with NT2 and HC in LG, exhibited the highest levels of viability/metabolic activity. By day 7, cells on NT2 and HC samples demonstrated superior viability/metabolic activity rates in both glucose regimes when compared to NT1 and untreated Ti. Notably, NT1 samples did not significantly deviate from their respective Ti controls in either LG or HG. Although no difference in metabolic activity was observed on the HC or NT2 surfaces between LG and HG conditions, cells both NT1 and Ti samples exhibited higher

viability/metabolism in HG compared to LG. Figure 2.6b explores the differential in metabolic activity rates, calculated as the ratio between day 7 and day 3 data (both normalized to day 1). A positive value suggests that the rate per day was higher in the later stage compared to the earlier stage. In LG conditions, both NT2 and HC showed a much higher differential than Ti and NT1. This pattern was also observed in HG conditions, where NT2 and HC had the highest late-stage rates. Notably, only the NT1 sample exhibited a significant difference between LG and HG with differential being significantly compared to LG counterpart.

1.8.7 Differentiation and Mineralization

Our analysis of the cellular response continued with an investigation into differentiation by considering ALP expression, a pivotal marker for osteoblastic activity and mineralization. Figure 2.7a illustrates the general increase in ALP activity across all substrates from day 7 to 14. All nanotubular surfaces, at both timepoints and glucose levels, exhibited elevated ALP activity when compared to untreated controls. Interestingly, as depicted in Figure 2.7a there were no marked differences in ALP levels between HG and LG conditions by the end of the two-week period on any of the substrates, with the sole exception of the HC surface in HG. However, significant variations in the rate of ALP activity were observed between earlier (day 0-7) and later (day 7-14) stages (Figure 2.7b), particularly when comparing these rates between HG and LG conditions. This was evidenced by a more pronounced increase in ALP activity in HG conditions during days 7-14 on all substrates except for the HC surface.

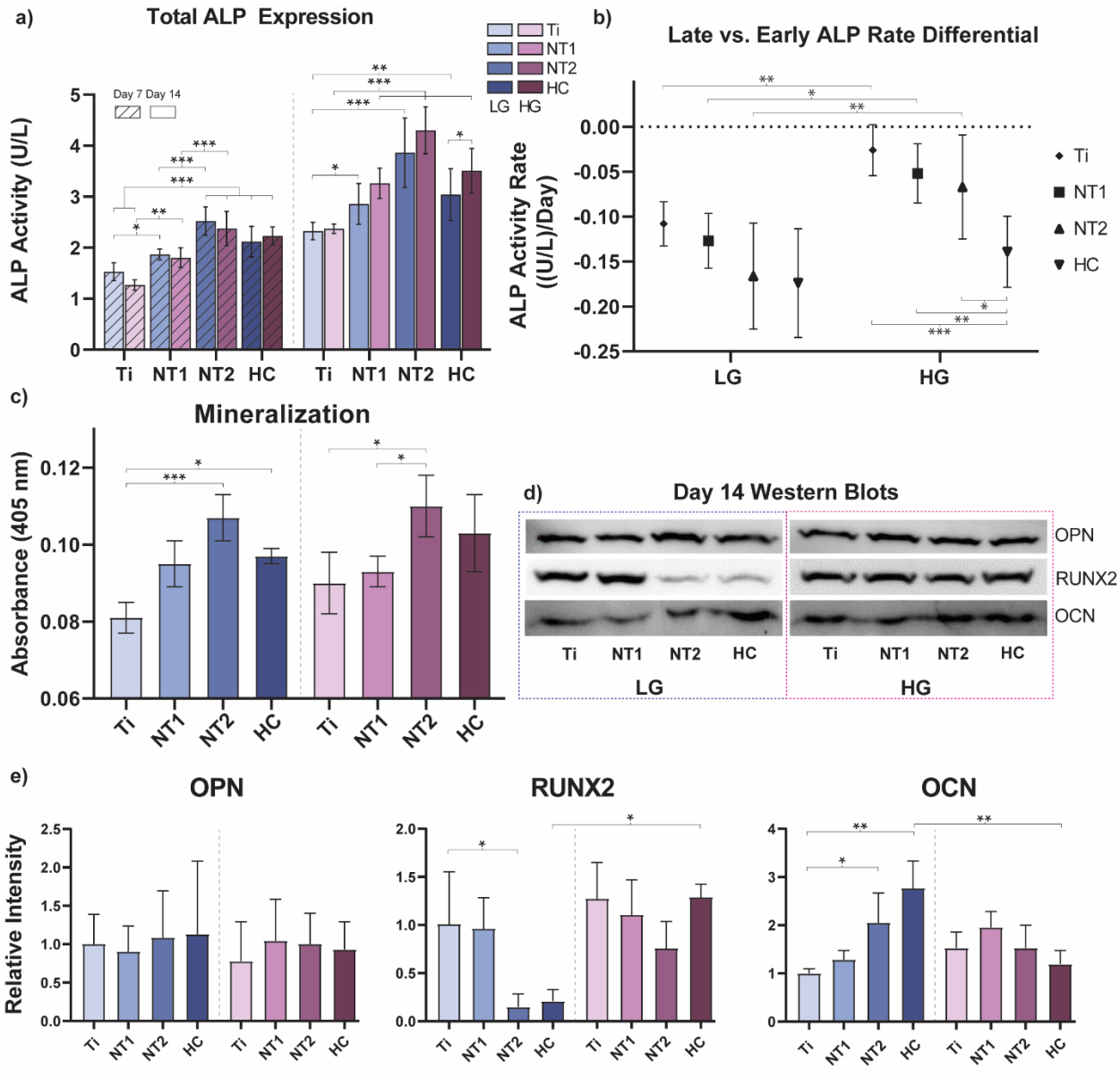

Figure 2.7. Differentiation. (a) Total ALP expression at day 7 and 14 of MG63 cells cultured in LG and HG on untreated Ti, NT1, NT2 and HC surfaces. (b) Differential rates of expression in ALP were calculated by subtracting late-stage ALP rates (Days 7-14) from early stage rates (Days 0-7), and displayed as ALP activity (U/L) divided by the days in culture. (c) Degree of mineralization via Alizarin Red staining assay. (d) Western blot images of OPN, RUNX2 expression in LG and HG at day 14, and e) relative intensities.

When considering the degree of mineralization via Alizarin Red staining assay (Figure 2.7c), NT2 yielded the highest absorbance in both glucose environment. Notably, no surfaces showed significant differences between LG and HG. To complement these analyses, we capitalized on

Western blotting (Figure 2.7d-e) which showed equal expression of OPN across all surfaces and glucose content, with no significant differences. Conversely, the overall expression of RUNX2 was lower on the NT2 and HC surfaces in LG, a trend that reversed when considering OCN. Notably, cells on the NT2 substrate in LG condition exhibited the highest degree of expression out of all samples in both regimes. No significant differences within the HG group were expressed for OPN, OCN or RUNX2.

1.9 Discussion

1.9.1 Nanotubes Fabrication

The creation of uniformly distributed single tubes with highly ordered geometry is critical not only for ensuring that results are consistent and reproducible across different studies but also for the precise correlation of cellular response to nanoscale features for both the design of cell-instructive surfaces and mechanistic models. To this end, in this study we optimized the anodization protocol by adopting a three-step approach that maximizes structural uniformity and minimizes sources of variability, particularly bifurcation (Figure 2.S1). Eccentricity and circularity were considered as quantitative descriptors as they can contribute to the topographical homogeneity, or lack thereof, across nanotubular samples.[135] In our study, eccentricity did not appear to be directly linked to the degree order, as demonstrated by the lack of correlation between these two parameters for NT1, NT2 and HC-T1 topographies. Similarly, circularity, by taking into account both the area and the perimeter of the opening, showed no direct impact on the degree of order in the surfaces with NT1, NT2 and HC-T1 openings all having comparable circularity (within a range of 0.03), and HC-T1 exhibiting the lowest degree of order. The pronounced circularity deviation on the HC-T2 surface can be attributed to its hexagonal geometry, which results in a marked differential between the major and minor axes. This shape augments the perimeter of the

tube relative to the total area of the opening. This attribute in turn influences the metrics by which circularity is measured, producing the seemingly paradoxical result in HC-T2 having both low eccentricity and low circularity. It is for this reason that eccentricity cannot solely be used as proxy for circularity, or vice versa, when assessing the homogeneity across NT surfaces. Ultimately, the diameter, eccentricity and circularity of the NTs affect the percent of attachable surface area available to cells, potentially altering the adhesion strength and focal adhesion complex formation which, in turn, can modulate downstream signaling pathways related to cell survival, growth and differentiation.[55,61,63,127,129,130,134]

Building on the insights garnered from this part of our study, the following takeaways merit emphasis. Firstly, the adoption of a triphasic anodization protocol effectively eliminated bifurcation across the nanotubular structures, enhancing the uniformity and predictability of the nanotube arrays. This strategic adjustment has proven pivotal in creating more consistent and reproducible surfaces for cellular studies. Secondly, our findings revealed no significant correlation between the degree of order and the geometric parameters considered, namely eccentricity and circularity. This dissociation underscores the complexity of nanotopographical cueing, suggesting that these geometric descriptors independently contribute to the surface characteristics without directly impacting each other. The analysis of attachable surface area provided intuitive results; the total attachable area available to cells on the HC substrate effectively represents the sum of the areas available on HC-T1 and HC-T2. This is attributed to the minimal height gap (approximately 30 nm)[135] between these domains, which allows cells to span across and engage with both surfaces simultaneously. In the case of the HC surface, the degree of order in the HC-T1 surface aligns with previous work by our group that demonstrated higher spatial entropy than single-tube substrates, a factor that also plays a role on cellular response.[137] As a

result, although the inner domains are the same size as the NT1 surface, HC -T1 domains have a much lower degree of ordering.

1.9.2 Preconditioning

By considering temporal variations of three functional metrics, we established that 14 days is the required timeframe to modify the behaviour of human MG63 cells by increasing the glucose content in the environment (Figure 2.2). In previous *in vitro* work which investigated micro-and nano-structured titanium surfaces for the prospective use in hyperglycemic patients, [19,101–105,152,176–179] cells were directly cultured in a high-glucose environment without preconditioning (this condition is referred to as LinH in Figure 2.S2). By comparing this commonly used method with our 2-week preconditioning approach (this condition is referred to as HG in Figure 2.S2 a-c) against the same control condition (LG), viability/metabolic activity, ALP activity, mineralization and area coverage follow a similar trend (Figures 2.S2 a-f). However, the adoption of the preconditioning step widens the gap with the LG condition for the functions considered, except for mineralization and area coverage, therefore imparting a significantly more marked environment-driven change in cellular behaviour. Notably, preconditioned cells appear to conserve a certain plasticity by virtue of which they recover, at least in part, their initial functions when cultured in the low-glucose environment (this condition is referred to as HinL in Figure 2.S2 a-c). In fact, ALP activity at day 14, mineralization and area coverage data are comparable, thereby indicating that cells do not permanently diverge from their native state (unlike what was previously demonstrated for MG63 cells in elevated glucose levels).[23,108,109] This factor is particularly critical to ensure a coherent comparison of cellular results between the two glucose environments. Taken together, our results demonstrate that the adoption of the preconditioning step may be a more effective approach to investigate the role of high glucose levels on cell activity by dictating a more

significant change in behaviour without significantly damaging cells. Our analysis also reiterates the importance of adopting coherent culturing conditions in the investigation of cell-surface interactions in the field of osseointegrated implants under hyperglycemic conditions,[19,98,103,179] because the inter-study comparison among putative substrate-driven changes in cell activity will also be affected by the characteristics of the exposure to the specific biochemical environment.

1.9.3 Morphology

Cell area/spreading (Figure 2.3a) indicates the extent of cell attachment and cytoskeletal rearrangement, which are essential for processes like migration, proliferation, and differentiation.[12,31,62,116,135,180,181] Interestingly, cells on untreated titanium exhibited the highest degree of spreading in both glucose conditions, with no significant differences observed across all surfaces in LG and HG environments. This well-spread morphology may be associated with a higher adhesion strength likely due to the greater attachment area of untreated surfaces (Figure 2.1c), given the fact that cellular viability and differentiation (Figure 2.6 and 2.7, respectively), two additional phenomena that are typically associated with a higher spreading,[9,12,180,182] on untreated controls are generally less pronounced than on those on NT surfaces.

In terms of irregularity (Figure 2.3b), while untreated titanium showed greater irregularity than the nanotubular substrates in LG, this trend reversed in HG. This increase in cellular irregularity is most likely due to the absence of nanoscale patters, ultimately allowing unconstrained spreading and potentially a weaker driving force for migration (an effect discussed further for Figure 2.5). The opposite occurs in cells adhering on the NT2 samples, whose low irregularity is due to a more circular shape induced by the larger nanotubes.[135]

Cellular protrusion (Figure 2.3c) followed a similar trend, with untreated titanium displaying slightly higher values in LG than in HG, and NT2 showing the lowest. Notably, NT1 and HC

showed no significant differences from one another in both glucose conditions. Although different, the extent of protrusions on the Ti, NT1 and HC samples is comparable, suggesting that the smaller tube diameters preserve protrusion dynamics that normally occur on untreated titanium. In terms of elongation (Figure 2.3d), cells on Ti displayed the highest levels in both LG and HG compared to the anodized samples, which exhibited consistent values across both glucose environments. Taken together, we can observe consistent trends across all 4 morphological metrics, characterized by the largest values exhibited by cells on titanium controls and the lowest on the NT2 substrates, with a comparable behaviour between NT1 and HC.

Figure 2.3e reveals that the nuclear area of cells on Ti was the largest in both conditions, showing no significant differences between LG and HG. Though nuclear area being higher in HG vs. LG (with the exception of the HC surface) on the NT surfaces, all surfaces exhibited a common correlation between the extent of cell spreading and nuclear size.[183] In addition to the lowest nuclear area, the NT2 substrate also exhibited a notable decrease in nuclear circularity (Figure 2.3f). Though this generally indicates higher rates of cellular stress these changes in irregularity can also be induced by an increase in cell migration and motility[184], which based the results discussed below (Figure 2.4 and 2.5), is more likely. Taken together, morphological results underscore that while glucose environments impose a subtle impact on nuclear morphology, the nature of the surface topography holds a more pronounced influence.

1.9.4 *Proliferation*

The distinct proliferation patterns highlighted by the Ki67 positivity (Figure 2.4a) further emphasize the influence of surface characteristics on cell cycle regulation. The consistency of this metric across LG and HG underscores a baseline proliferative capacity dictated more by the surface interactions than by glucose availability. Notably, the high Ki67 positivity observed on untreated

titanium indicates a reduced proliferation on nanotubular surfaces. Together with a higher elongation (Figure 2.3d) and spreading of cells, this suggests that Ti prioritizes proliferation while having a comparatively limited impact on differentiation (Figure 2.7).[185]

The analysis of the phase index (Figure 2.4b) reveals a critical aspect of cellular proliferation. A higher phase index indicates a greater proportion of cells engaged in division, reflecting a more active proliferative state. Our findings indicate that under LG conditions, the substrate type does not affect this parameter. However, the increase in glucose content enhances the index on NT2 surfaces while decreasing that for NT1 substrates. This shows that under HG conditions, smaller nanotube diameters may not provide the same proliferative advantage as larger ones. The phase index values for the Ti and HC surfaces are consistent in both LG and HG conditions, pointing to nanotopographical effects to explain the glucose-specific fluctuations in NT1 and NT2 values. This is further shown in Figure 2.4c, where NT1 and NT2 have relatively lower and higher Ki67 mean intensities in HG, respectively. This indicates that the HG environment may specifically affect the duration that cells spend in a particular stage of the cell cycle on the NT1 and NT2 surfaces, without altering the overall expression of Ki67, which is significantly different in both LG and HG. It is possible that in HG, NT1's higher proliferation and larger cell surface area lead to crowding and contact inhibition, causing cells to remain longer in early cell cycle stages, whereas NT2, with lower initial proliferation and more space in HG compared to LG, allows more cells to enter mitosis. This suggests that the nanotopographical features of NT1 and NT2 influence cellular metabolic responses and cell cycle dynamics in a glucose-dependent manner, highlighting the complex interplay between cell surface interactions and environmental conditions. The variation in mean intensity across surfaces and glucose conditions (Figure 2.4d) shows similar trends to the Ki67 positive values with the untreated titanium having the greatest mean intensity

but adds nuance particularly in the LG to HG transitions. Notably, both NT1 and NT2 surfaces exhibit consistent directional trends in phase index and mean intensities with NT1 having lower values in HG, while NT2 is higher, again suggesting a higher proliferation rate in HG on the NT2 and a lower rate in HG on the NT1 samples, despites seeing no differences in between glucose regimes in the Ki67 Positive data. In addition, the consistent Ki67 positivity, phase index and mean intensities observed across the two glucose levels indicates that the characteristic nanoscale features of HC mitigate the effects of glucose variability, offering a context-indifferent substrate in terms of proliferation.

1.9.5 Migration

Overall, cells displayed enhanced migration on anodized surfaces compared to untreated titanium across both time intervals and glucose environments (Figure 2.5a). The initial cell area coverage across all surfaces is largely unaffected by glucose levels within the first 12 hours. However, by the 24-hour mark, distinct differences emerged between LG and HG for the nanotubular surfaces, particularly for cells on NT2 substrate. Cells interacting with surfaces featuring larger nanotopographical features exhibited altered migration patterns under higher glucose conditions. While migration rates slowed across all substrates in the 12-24 h timeframe (Figure 2.5b), the bulk of area coverage took place before 12 hours, with only the HC and NT2 surface being significantly higher in HG at 24 h then their counterparts at 12 h. These results indicate that specific surface features may counteract the typically inhibitory effects of high glucose on cell migration (Figure 2.S2 e-f).[20,23,32,35] Furthermore, the marked difference in migratory and closure rate suggests that nanotubular geometry is responsible for a rate increase relative to controls. The influence of nanotopographical cues typically leads to cytoskeletal reorganization that drives greater contraction and tension, causing cells to adopt a more compact

morphology which reduces their overall area.[14,61,78,127] On nanostructured titanium, focal adhesions are smaller, more numerous and more dynamic, a factor which is crucial for efficient migration and that results in reduced cell spreading.[53,127] Complementing the adhesion dynamics that lead to smaller cell areas, this increase in motility may contribute to the lower cell areas observed for the NT2 surface at day 2 (Figure 2.3a) compared to more extensive spreading on the other surfaces.[12] Additionally, in this context, the lower cellular area along with reduced Ki67 positivity and intensity (Figure 2.4a) indicate that at these early timepoints cells may be prioritizing migration over proliferation across the nanotubular surfaces, NT2 in particular.

1.9.6 *Viability/Metabolic Activity*

Viability/metabolic activity assessment (Figure 2.6) complements the proliferation and migration data. At day 1, data normalized against the untreated titanium in LG, PB assay showed much higher levels of metabolic activity across all the NT substrates when compared to untreated Ti in LG and HG. Notably, the lack of impact on viability stands contrary to previous literature[103] that shows a decrease in metabolic activity in HG. This suggests that the preconditioning step allowed cells to adapt and better utilize the elevated levels of glucose. Similar to the morphology and proliferative data, at day 1 measurements are much more effected by nanotopography in respect to glucose levels (Figure 2.6a). Interestingly, although proliferation metrics (Figure 2.4) display lower levels of activity relative to Ti, cells at these early timepoints exhibit significantly higher viability/metabolic activity. It is possible that the cellular response to titanium surfaces is characterized by a more metabolic-intensive behaviour, reducing proliferation. With the exception of Ti in LG, cells exhibit consistent growth at day 3 relative to day 1. The only significant differences occur between Ti in LG and most of the other surfaces. The trends observed on day 1 are largely maintained, with NT surfaces showing elevated metabolic activity compared to

untreated samples. Notably, on day 3 a difference between glucose environments emerges, with Ti samples maintaining an elevated level metabolic activity in HG, while all anodized substrates showing no difference between LG and HG. The initial similarities in metabolic rates across all surfaces on day 3 evolve by day 7, with NT2 and HC demonstrating heightened activities in both glucose environments. This suggests an adaptive increase in metabolic demand as cells acclimate to the surface topographies, potentially reflecting an increased viability due to enhanced proliferation and/or transition to an early differentiative state, where new relative demands for energy are allocated for osteoblast-like functions.

The enhancement in viability/metabolic activity between early and later stages (Figure 2.6b), particularly significant for the NT2 and HC surfaces, combined with the morphological and migratory data, provide a picture of smaller, motile cells with lower proliferation at early time points and, in contrast to untreated titanium, potentially undergoing the bulk of the proliferation after day 3, represented partly by the raised levels of metabolic activity observed on the NT2 and HC substrates on day 7. These results reinforce the concept that the physical microenvironment can significantly impact cellular energy dynamics and proliferation.[32–35,153] Conversely, the consistent activity observed on NT2 and HC surfaces across glucose levels underscores the potential of these nanotopographies to sustain cell functions under varying environmental conditions across early (Day 1-3) and late (Days 4-7) timepoints. For these substrates, such increase in late-stage metabolic activity may not be solely exclusive to higher proliferative rates or a healthy cell population, but also arise due to elevated rates of differentiation within this range of 7 days.

1.9.7 Differentiation

The general increase in ALP activity (Figure 2.7a) from day 7 to 14 across all surfaces indicates a common temporal progression in osteoblastic activity consistent with early-stage differentiation. Notably, all anodized surfaces exhibited elevated ALP activity relative to untreated controls within their respective time points and glucose regimes, suggesting that nanotopography significantly augments early osteogenic signaling and activity. This is in agreement with previous work that demonstrates, using similar NT diameters, early osteogenic markers expression increases as early as day 7 in MC3T3-E1 cells.[127] ALP activity is generally unaffected by the glucose content (with the exclusion of the HC substrate at day 14), suggesting that, as seen in proliferation and migration data (Figure 2.4 and 2.5), that it is mostly driven by the surface nanotopography, a trend clearly represented in Figure 2.8a-c when comparing NTs with Ti. The high degree of proliferation seen in Figure 2.4 and the elongated shape the cells take on the untreated controls (Figure 2.3d), indicate that Ti substrates guide the cells into responses that prioritize proliferation. Conversely, the nanotubular topography is more likely to be characterized by higher level of osteogenic markers in terms of differentiation and mineralization. The elevated ALP activity at day 7 correlates with the higher metabolic activity at the same timepoint (Figure 2.6a) on the NT2 and HC. This further supports the hypothesis that the raised metabolic activity after day 3 is due to a preference for later stage proliferation and a change in differentiative capacity, leading to increased energy consumption.

All conditions, besides the HC surface, had much higher rates of ALP activity expressed at days 7-14 (Figure 2.7a) than those in LG. This late-stage shift in ALP activity under different glucose conditions could indicate a time-dependent cellular adaptation or metabolic shift. The HC surface stands out due to its maintained ALP activity (Figure 2.7b) rate across glucose conditions,

potentially hinting at an intrinsic material property of the HC topography that supports both early and consistent osteogenic signaling and activity. These results indicate that while glucose conditions may transiently affect ALP activity, the long-term osteogenic potential of cells seems to be more profoundly impacted by the substrate's topographical characteristics. However, the differential rate of ALP activity increase between early and late stages, particularly in HG conditions (excluding the HC surface), suggests a nuanced interplay between glucose metabolism and substrate-induced osteogenic differentiation.

Similar to the ALP activity, Alizarin (Figure 2.7c) staining data indicate that mineralization is more dependent on surface nanotopography than on environmental glucose levels (Figure 2.7c). This agrees with previous work which observed no difference in Alizarin levels at day 14 for MC3T3-E1 osteoblastic cells on 80 nm nanotubes under normal and various elevated glucose conditions.[103] Western blots (Figure 2.7d and e) highlighted positive effects on differentiation by both NT2 and HC substrates, but only under LG conditions. While OPN exhibited no significant differences across substrates and glucose levels, both RUNX2 and OCN levels significantly varied on NT2 and HC surfaces in LG. The lowered intensity on the bands in Figure 2.7d, appearing as a downregulation of RUNX2, while having simultaneously elevated levels of ALP, OPN and OCN, can be interpreted as indicative of osteoblastic maturation[28,41] on these two substrates. In addition, OCN levels, which are indicative of late-stage osteoblastic differentiation[41], demonstrated consistent expression across all surface types within HG regimes. This supports the idea of an early transition from a proliferative to a differentiative state, specifically for the HC surface which displayed elevated day 7 metabolic activity (Figure 2.6a) but consistent ALP activity rates between day 7-14 (Figure 2.7a). Conversely, the bulk of the increase of metabolic activity at day 7 on the NT2 substrate (Figure 2.6a), may be due more to proliferation. This state of delayed proliferation

is further supported by the circular morphology, irregular nuclear shape and rapid migration rates, potentially indicating higher cell motility and proliferation beginning at a later stage than the other surfaces. Remarkably, because the OCN levels on the HC surface are elevated in LG compared to HG, a glucose-sensitive response unique to the HC topography can be observed: the osteogenic potential diminishes in the HG environment, while osteoblastic differentiation accelerates under LG conditions. An effect which may be due to the early transition to differentiative state.

When analyzed collectively, while ALP expression and mineralization can be influenced significantly by the surface nanotopography, markers like RUNX2 and OCN may be more sensitive to glucose levels, indicating a dichotomy in metabolic versus differentiation responses. These findings highlight important implications in biomaterials design and surface engineering. For example, behaviors such as that of the HC and NT2 substrates could be harnessed for applications where osteogenic differentiation is desired independent of glucose concentrations. The fact that NT2 and HC surfaces promote distinct differentiation markers' profiles in LG conditions but not in a HG environment, emphasizes the role of environmental conditions in modulating fate decisions regardless of surface cueing.

1.9.8 *Comparative Analysis Table*

To attain a comprehensive view of how MG63 cells adapt and respond to the concomitant influences of substrates and environment, Figures 2.8 provides (a) an analysis table which incorporates all variables presented in this study and their dependence on both the substrate and glucose levels. Experimental results are also presented to (b) show the skew in the variance and (c) provide directional context to trends. The table, and the related discussion, are structured in ways to single out the differential effects exerted by (1) glucose (“HG vs. LG” column), (2)

anodized substrates in comparison to untreated titanium ("NT vs. Ti" column) and (3) NT surfaces in comparison to the HC architecture ("NT vs. HC" column).

1. (a) Untreated titanium and all three anodized surfaces show more than 70% of neutral counts, albeit for different functional readouts. This indicates that, for the metrics known to be affected by the glucose content, both untreated and anodized substrates display the ability to shield specific osteoblastic functions from hyperglycemic conditions. These include migration[32,35,147], Ki67 expression[34,159,172], mineralization[103,107,147,150,154–159], differentiation(ALP activity[19,33,35,99,103,147,154], OPN[19,35,99,103,155], OCN[33,35,94,103,107,147,154,155], RUNX2[35,99,103,143,147,154,155]). In addition, although PrestoBlue assays [157] are limited in studies regarding the *in vitro* response of osteoblasts to titanium surfaces in high glucose, results with PB's proxies (e.g. CCK-8[32,33,35,153] and MTT[34,103,107,147,150]) allow to extrapolate that viability/metabolic activity is also affected by the glucose content, and is therefore similarly restored by both untreated and anodized substrates. Conversely, lack of published comparative data does not allow to differentiate whether the remaining metrics (i.e. morphology, cell phase) are rescued from an inhibited state to a condition typical of a LG environment or are simply not influenced by the glucose in the environment. However, we can infer that among these, cellular area more likely belongs to the second category because all four substrates show a neutral count for this metric. Interestingly, previous literature indicates that all the other cellular functions with four neutral counts across all surfaces, namely Ki67 positive cells [34,159,172], early migration coverage and rates [32,35,147], ALP activity prior to 7 days in culture[19,33,35], mineralization[103,107,147,150,154–159] and OPN expression[19,35,99,103,155], are negatively affected by high glucose. In our case, we ascribe the reported neutrality of these metrics to HG conditions to the preconditioning step which may allow cells to acclimate to their environment prior to seeding onto substrates. Notably, the PB viability/metabolic activity at day 1 also shows four neutral cells, but

results in literature are controversial on whether significant differences appear at this time interval between LG and HG environments.[33–35,103] Taken together, our results demonstrate that untreated titanium can alleviate a hyperglycemia-induced osteogenic inhibition of specific *in vitro* cellular processes comparably to anodized surfaces, thereby providing evidence of a significant role of the native physiochemical properties of the metal regardless of the presence of a surface nanotubular topography. In this way, our observations align more closely with studies involving osteoblastic response to TiO_2 nanotubes in diabetic serum rather than added glucose. For instance, Valdez-Salas *et al*. 2022 reported no significant changes in the expression of OPN, OCN, RUNX2, or mineralization levels when comparing normal media supplemented with FBS to media containing high glucose levels from diabetic serum derived from patients.[103] (b) Similarly, the analysis of variance reveals that when cells on untreated titanium experience a glucose-induced effect, the overall divergence from the neutral state is comparable to that observed on anodized surfaces. (c) However, there is an evident positive directional bias which characterizes the performance of anodized surfaces in HG conditions, especially that of NT2 substrate for which all variations in cellular functions in respect to LG are towards a more beneficial outcome. Taken together, this indicates that the presence of the nanotubular topography, and in particular the one characterized by larger nanotubes, confers the distinctive ability not only to overcome the detrimental effects of HG for specific functions but also to elicit a cellular response that surpasses the one in LG conditions.

2. (a) A clustering of negative differences relative to the morphology and Ki67 positivity can be readily observed for anodized samples. There is in fact an evident early (i.e. day 2) trend indicating that nanotubular surfaces reduce cell area, irregularity, protrusion, elongation and nuclear area (with the exception of nuclear circularity) and Ki67 expression, regardless of the glucose content.

These results demonstrate that while initial cell adhesion and proliferation are favoured on untreated titanium, the benefits of nanotubular surfaces emerge in subsequent events. In fact, grouping of positive differences occurs for PB and ALP readings after 1 and 2 weeks of culture, in particular for the NT2 and HC substrates, showing their potential to enhance osteogenic differentiation and overall cellular health. This enhancement confirms that these rationally designed nanostructures support more beneficial later-stage cell-material interactions than untreated titanium. It also follows that the type of assay and/or the timeframe considered for *in vitro* cellular analyses can provide opposite conclusions on the role of nanotubular structures, with the risk of biasing the conclusions. The investigation of environmental effects, in particular hyperglycemia, should therefore encompass an array of shorter- and longer-term assays to provide a conclusive verdict on the performance of a given substrate. (b) The lower variance observed for the NT1 surface demonstrates that differences from untreated Ti samples are reduced in both LG and HG compared to the effects elicited from the NT2 and HC substrates. In contrast, these two nanostructures show an ability to invoke a stronger cellular response in terms of differentiation, metabolic activity and early differentiation markers. Notably, the comparable variance maintained by all anodized samples across the two culturing conditions indicate an overall "context-indifferent" ability to guide cellular events, thereby pointing at a mainly surface-driven cueing. (c) It can also be observed that the more biased distribution of positive, neutral and negative counts shown in LG conditions tends to even out in HG conditions, indicating that the more extreme nanostructure-induced changes observed in LG are more equally balanced by the HG context.

3. (a) The comparison between the NT1 and NT2 surfaces with the hierarchical HC architecture aims at determining whether the beneficial effects exerted by the latter and reported in previous work by our group[135] are confirmed with a different cell line and variable environmental

conditions. It can be readily observed that a large array of metrics, mainly associated with differentiation and mineralization, are largely neutral regardless of the glucose content. This is in agreement with our previous results obtained with human mesenchymal stem cells, where we determined that comparable nanotubular (i.e. average diameter of ~21 nm and ~90 nm) and HC (i.e. small domains of ~21 nm in diameter, large domains of ~108 nm in diameter) substrates can all induce osteogenic differentiation and mineralization. However, differences arose in the quality of the deposited mineral, a parameter that was not investigated in the present work. In terms of morphology, the NT2 surface is the most different from the HC in both glucose conditions. This in part substantiates our previous conclusions asserting that the larger domains do not significantly influence cytoskeletal organization, which is mainly directed by the order of smaller domains. In fact, morphological metrics tend to be more neutral for the NT1 surfaces, whose structure resembles that of the smaller tubes of the HC architecture. (b) Variance analysis shows that both exhibit similar degrees of variability in cellular responses across LG and HG environments, with that divergence in metrics that is maintained across the culturing conditions. c) The likert plot further highlights the similarities between the surfaces considered, in particular with the NT1 substrate as evidenced by the neutral counts and the more evenly distributed positive and negative counts. Conversely, a distinct negative directional bias is observed for the NT2 surface, particularly in metrics related to proliferation and positive markers of cellular morphology. This contrast could be attributed to the different domain sizes and the elevated disorder in the HC-T1 domains, which are similar in size to the NT1 but not NT2, reiterating that the larger HC domains are more critical for controlling the order of the smaller domains than directly influencing cell behaviour.

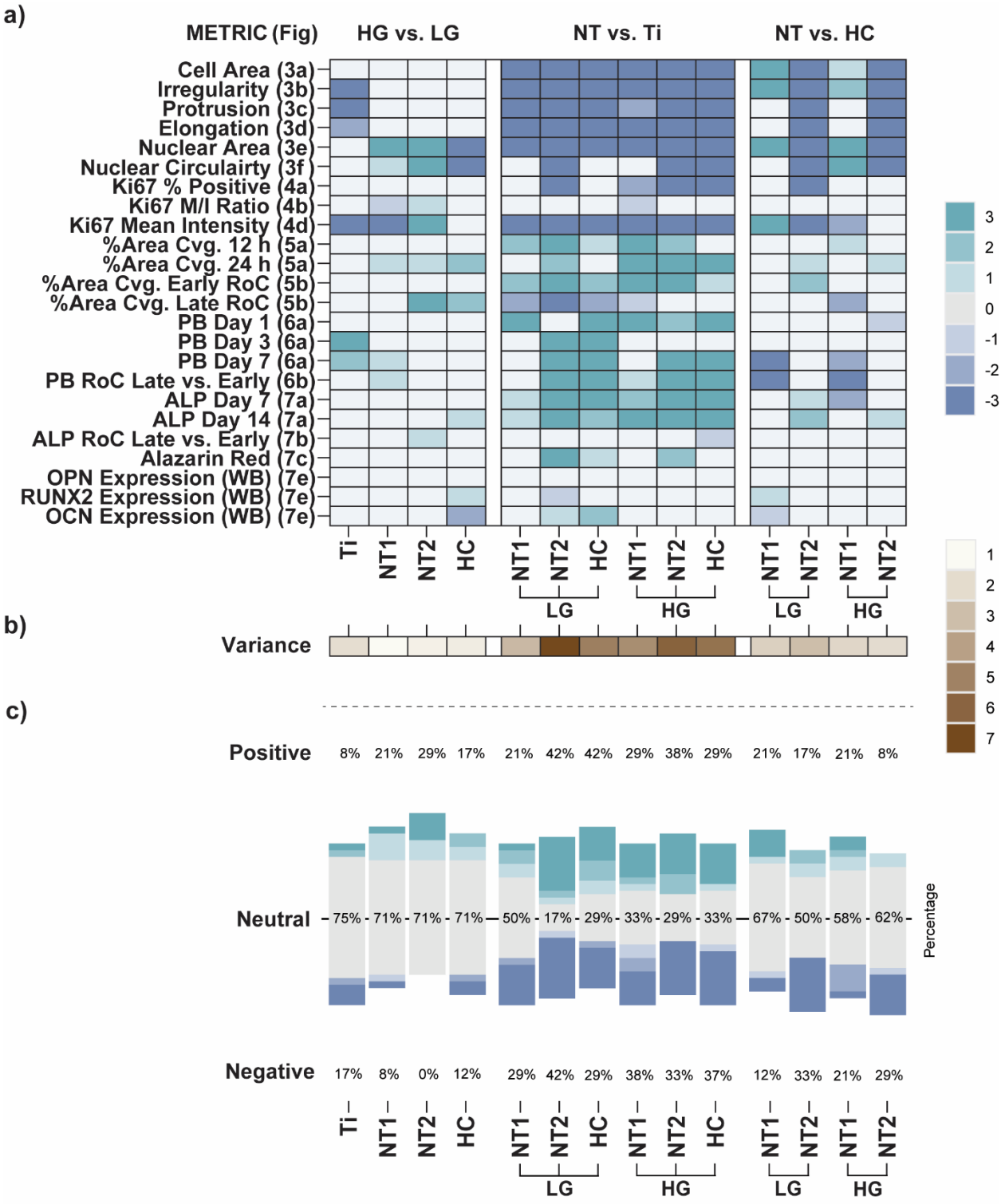

Figure 2.8. Comparative analysis table illustrating a) the relative change in each measurement between: HG vs. LG, NT vs. Ti and NT vs. HC. The direction and degree of significance are represented through a color gradient: Light turquoise (“*”) to dark turquoise (“****”) indicating an increase relative to the comparative variable, and light blue (“*”) to dark blue (“****”) indicating a decrease relative to the comparative variable. The variance b) for each column was computed,

using the scale provided on the right of the variance values to assess the sensitivity to the respective environmental or surface condition across all tests. Data from a) was made into a c) likert (diverging bar) plot, where the top percentages indicate the fraction of responses above 0, the middle percentages are neutral counts and the bottom percentages are the fraction of response below zero for each column.

When analyzing the three main columns of Figure 2.8 against each other, it can also be observed that the variance is notably higher in the “NT vs. Ti” than in the “HG vs. LG”. This shows that the topographical features exert a greater impact on cell behavior and performance than glucose levels. Although surface topography emerged as a dominant factor, the role of glucose conditions cannot be dismissed, as Ti, NT2 and HC showed elevated variability from LG to HG.

Building on our results, the sensitivity of cell responses to different environmental variables beyond glucose levels could offer a broader understanding of cellular adaptation mechanisms, and provide the tools for the development of context-indifferent” and “adaptive” cell-instructive surfaces that either effectively “absorbs” microenvironmental variations without compromising their beneficial effects on cellular functions or predictively elicit desired cellular functions in response to specific environmental changes.

1.10 Conclusion

In conclusion, this study provides an in-depth analysis of the complex interactions between MG63 cells and nanotubular substrates in variable glucose conditions, shedding light on critical aspects relevant to biomaterials surface science. The triphasic anodization process removed bifurcation and improved overall ordering of titanium nanotubes. A 14-day preconditioning period was found optimal for stabilizing ALP expression and cell metabolic activity, highlighting an adaptive mechanism to fluctuating environmental glucose levels and indicating a benchmark for hyperglycemic studies. In the discussion, we have highlighted the differential role of the nanostructured surfaces in respect to untreated titanium in both environments by considering

morphological, proliferative, migration, viability, differentiation and mineralization metrics. To provide a more comprehensive view, we also capitalized on an analysis table which allowed us to achieve more general conclusions. In particular, (i) all surfaces demonstrated an ability to mitigate the negative effects of high glucose for specific functions. However, nanotubular topographies, in particular NT2, elicit a more beneficial outcome in HG than untreated titanium. (ii) the NT1 surfaces are associated with the most stable cellular responses across varying glucose levels, while the NT2 and HC exhibit the strongest enhancement of cell migration, viability/metabolism and differentiation. (iii) Shorter-term processes such as adhesion and proliferation are favored on untreated titanium, while anodized samples support later-term events (iv) The HC surface, while different from both NT1 and NT2, elicited cell responses more similar to NT1, despite having similar variance to both, providing additional support to our previous hypothesis of the role of the smaller and larger domains. (v) The effects from nanotopographical features on anodized surfaces were dominant over the effects of environmental glucose, underscoring the importance of carefully considering nanoscale surface features as well as their geometry, and uniformity in the design and development of cell-instructive titanium surfaces.

1.11 Acknowledgements

This work was supported by the Natural Sciences and Engineering Research Council of Canada (NSERC) through the Discovery grant. RB acknowledges NSERC for financial support throughout the Doctoral Scholarship. The authors acknowledge the Cell Biology and Image Acquisition (CBIA) Core, technical guidance and assistance for imaging and data analysis by Chloë Van Oostende-Triplet and Liyuan Wang.

1.12 Supplementary Information

1.12.1 *Nanotubes Fabrication*

In accordance with the procedures outlined in previous work from our group[36], we carried out a comparison between a 2-step (biphasic) and 3-step (triphasic) anodization process to assess whether the degree of bifurcation can be reduced, thereby generating more consistent nanotubular surfaces. To this end, we considered two sets of parameters, which differed in the initial voltage used and the number of anodization steps. In particular, with the biphasic (-B) procedure, NT30-B samples were fabricated using a constant voltage of 30 V. The initial anodization step lasted for one hour, followed by a second step of five minutes. Conversely, NT60-B samples were subjected to a constant voltage of 60 V, where the first anodization step lasted for 30 minutes and the subsequent step for five minutes. For the triphasic (-T) procedure, the initial anodization step was repeated, resulting in two instances of oxide layer stripping, designated as NT30-T and NT60-T. The experimental parameters adopted for this comparison are summarized in Table 2.1S.

Table 2.S1. Voltage and time parameters for anodization of NT30-B, NT30-T, NT60-B and NT60-T substrates.

	Condition	NT30-B	NT30-T	NT60-B	NT60-T
Step 1	Voltage (V)	30	30	60	60
	Time (Min)	60	60	30	30
Step 2	Voltage (V)	30	30	60	60
	Time (Min)	5	60	5	30
Step 3	Voltage (V)	/	30	/	60
	Time (Min)	/	5	/	5

By leveraging the hexagonal packing of the nanotubes, a ratio was formulated between the NND and the average distance of the first six NNDs (N1:N6 ratio). This ratio was then used to determine

the degree of bifurcation and level of order. In addition, Voronoi tessellation[36,85,86] was applied to the SEM micrographs to create an experimental planar tiling, which served as a qualitative image to compare the change in the degree of order between the bi- and tri-phasic anodization. As evidenced by the N1:N6 ratio, the triphasic samples displayed higher order when compared to their biphasic counterparts (Figure 2.S1a). The distribution plots, illustrated in Figure 2.S1b, highlighted the bifurcation levels of the biphasic surfaces through two distinct clusters of N1:N6 ratios. Notably, the triphasic treatment effectively eliminated the second distribution cluster, thereby augmenting the order and consistency of the triphasic surfaces, as it is also visible from qualitative Voronoi tessellation of SEM images (Figure 2.S1c).

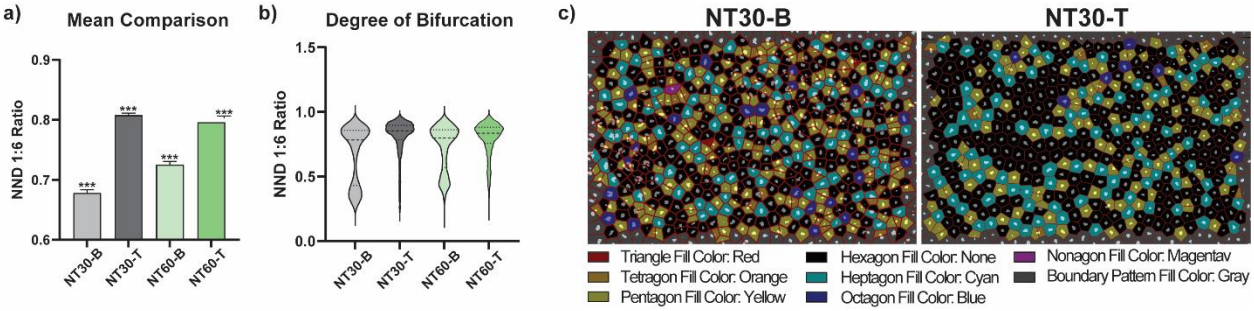

Figure 2.S1. Comparison of NND 1:6 ratios of (a) mean values and (b) distribution plots indicating divergence in degree or order in biphasic samples. Qualitative Voronoi tessellation (c) provides visual representation of this increase in the order of topographical features.

1.12.2 Preconditioning

A noticeable decrease in PrestoBlue intensity (Figure 2.S2a) was observed post-preconditioning in high glucose (HG), in comparison to cells cultured under standard conditions, i.e. pre-conditioned in low glucose (LG) and cultured in low glucose. Interestingly, this effect appears reversible, as metabolic rates for cells grown in LG but seeded in HG (LinH), and cells preconditioned in HG but seeded in LG (HinL), situate between the readings for LG and HG

samples. By day 14, ALP activity (Figure 2.S2b) was substantially elevated compared to LG conditions. LinH samples trended toward the HG samples, while HinL was indistinguishable from the LG samples. The mineralization process was notably influenced under the two different regimes, with a significant uptick in cell mineralization for cells grown in LG versus those in high, via Alizarin assay and staining (Figure 2.S2 c-d). Similar inhibitory effects of HG on behaviour were observed in quantitative results of scratch assays (Figure 2.S2 e-f), with the highest rates of wound closure are present in LG environments, with the greatest reduction in migratory behaviour existing in the HG regimes.

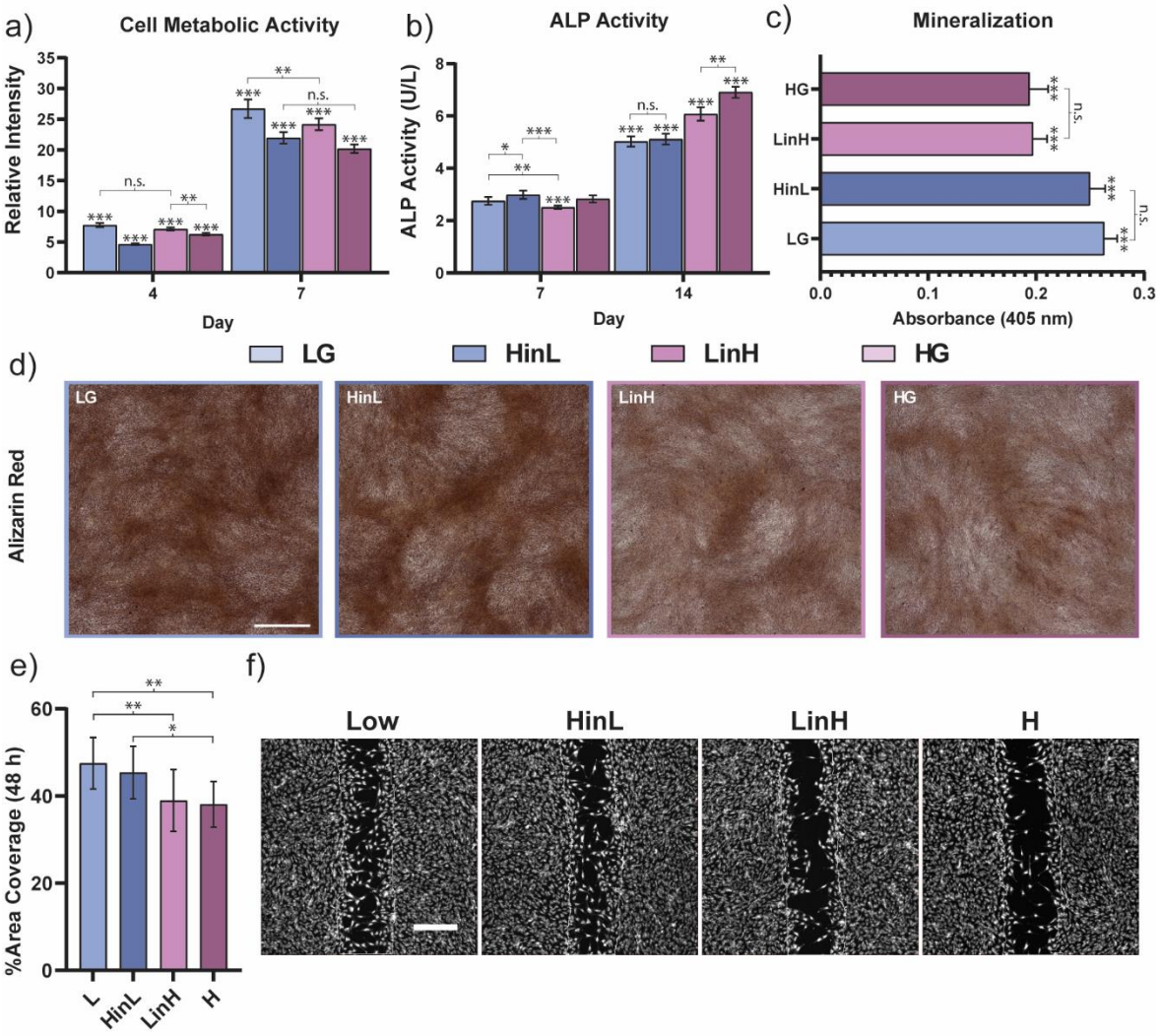

Figure 2.S2. Preconditioned cells were analyzed for changes in (a) metabolic activity (PrestoBlue), (b) ALP Activity and (c) degree of mineralization via Alizarin Red Staining. (d) Widefield images of MG63 cells stained with Alizarin Red Staining. Migration assay analysis for (e) preconditioned MG63 cells grown in culture plates, showing total coverage after 48 h. (f) Representative widefield images of live cells subjected to scratch assay and stained with CellTracker Red CMPTX fluorescent dye and allowed to migrate for 48 h.

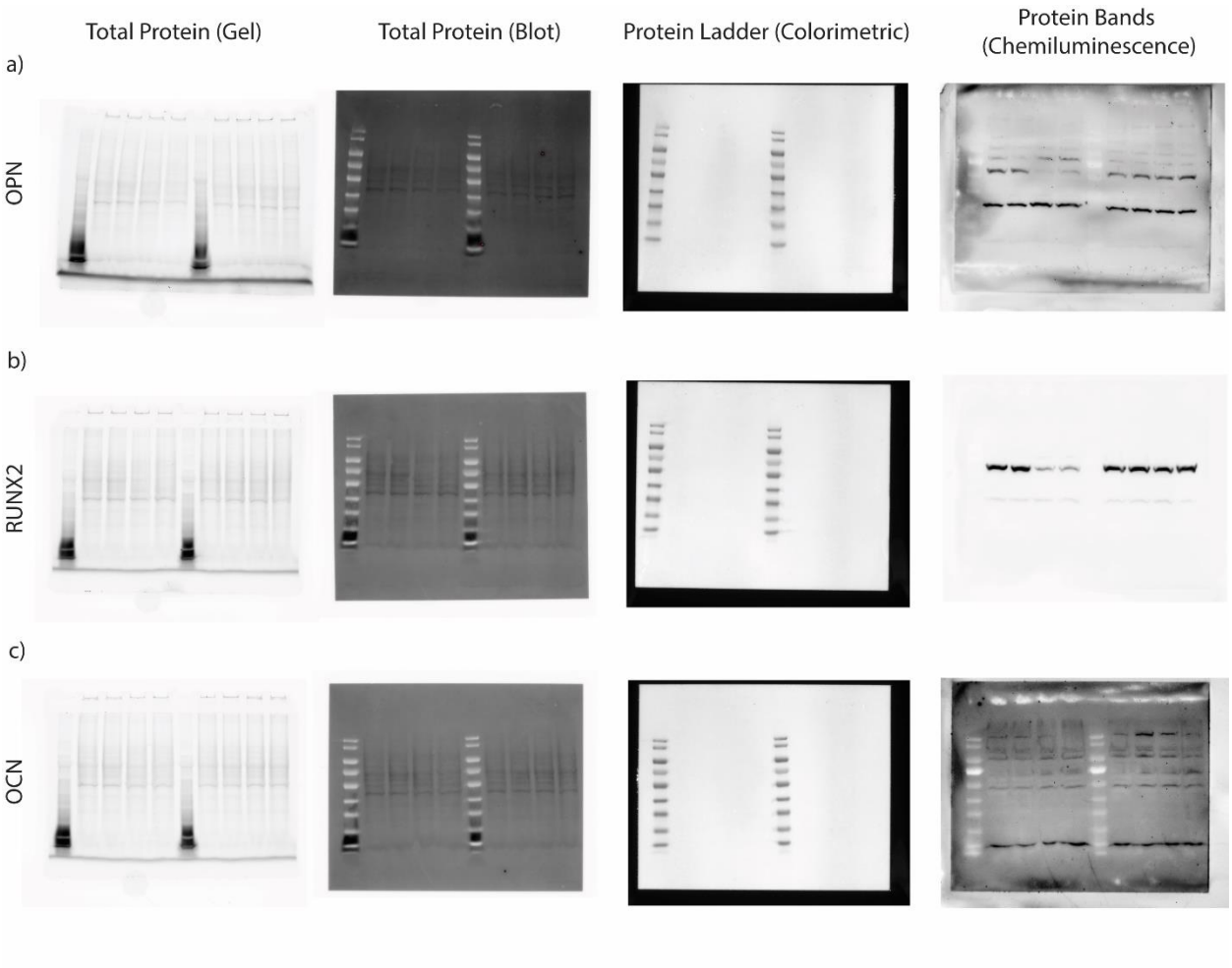

Figure 2.S3. Uncropped and unprocessed images of full gel and blot for Western blot (left to right) total protein (gel), total protein (blot), protein ladder (PL) (colorimetric), protein bands (chemiluminescence) for (a) OPN (~35 kDa), (b) RUNX2 (~60 kDa), and (c) OCN (~15 kDa). Band order for all images (left to right): PL, Ti (LG), NT1 (LG), NT2 (LG), HC (LG), PL, Ti (HG), NT1 (HG), NT2 (HG), HC (HG).

CHAPTER 3: Understanding Nanotopographical Complexity and Its Impact on MG63 Osteoblastic Cells Using Hierarchical Titanium Nanotubular Gradients

Ryan Berthelot [1-2], Fabio Variola[1-4,*]

[1] Faculty of Engineering, Department of Mechanical Engineering, University of Ottawa, Canada

[2] Ottawa-Carleton Institute for Biomedical Engineering (OCIBME), Ottawa, Canada

[3] Department of Cellular and Molecular Medicine, University of Ottawa, Canada

[4] Children's Hospital of Eastern Ontario (CHEO), Ottawa, Canada

2.1 Abstract

Titanium nanotubular surfaces have garnered significant attention for their ability to modulate cellular behavior in biomedical applications, particularly in enhancing osseointegration. Despite extensive research, the influence of nanotopographical complexity on cellular responses is not fully understood, especially in the context of spatially variable surface features. This study systematically investigates the impact of nanotopographical gradients created through a precise 60V anodization process on the behavior of human MG63 osteoblastic cells. Utilizing advanced spatial metrics such as lacunarity, entropy, and fractal dimension, we comprehensively characterized the structural complexity of the nanotubular surfaces. Our findings reveal that the progression across all metrics—including nanotube density, lacunarity, fractal dimension, and entropy—increases consistently from A1 to A7. Among these, A7 exhibited the most beneficial effects on cellular behavior, promoting enhanced cell spreading and morphological irregularity, wider mitochondrial distribution, and elevated expressions of differentiation markers RUNX2 and osteocalcin, while A1 showed the weakest influence. Alizarin staining and assay results confirmed enhanced long-term mineralization on more complex surfaces, suggesting sustained osteogenic potential. While A7 consistently elicited the highest cellular responses, all tested surfaces contributed positively to osteogenesis, emphasizing the nuanced interplay between nanotopographical cues and cellular behavior. The gradient surfaces provide a platform for high-throughput screening, allowing for efficient identification of optimal surface characteristics, beyond just variable diameters, without extensive preliminary trials. Furthermore, with minimal troubleshooting, these gradient-derived parameters can be translated into homogeneous, single-featured surfaces for future applications, though a reduction in voltage is necessary when transitioning to a two-electrode setup. This study underscores the potential of nanotopographical

engineering and surface complexity and entropy in effectively modulating cell behavior, paving the way for advanced applications in tissue engineering and regenerative medicine.

2.2 Introduction

Recent advancements in our understanding of how cells sense and respond to both synthetic and natural substrates have been in part driven by increasingly more effective surface engineering approaches that permit to precisely design the nanotopographical features of substrates at the micro- and nanoscale.[186–198] Achieving spatial and dimensional accuracy in the creation of tailor-made nanotopographies with no interference generating from uncontrolled variability of the substrate features is in fact a fundamental prerequisite to close in on the mechanisms that govern cell-surface interactions.[195–199] This is particularly crucial when considering that the sensing machinery of cells operates at the nanoscale[14,42,43,198–200], and therefore even nanometric variations in the pattern size and/or geometry could potentially affect the resulting cellular behaviour.[4,13,134,186,191,193,201–205] While high-precision techniques, such as e-beam and nanoimprint lithography,[181,195–198] have been successfully applied to materials such as silicon and polymers to achieve highly accurate nanopatterns,[8,40,137,198,206–209] the array of viable techniques that can create these nanostructures onto materials of interest for biomedical implants is limited. This is particularly challenging for biocompatible metals, a factor that has greatly hindered the use of nanopatterned substrates that replicate the physicochemical characteristics of implantable devices such as orthopedic, dental and spinal implants, among others.[198,210,211] To enhance the predictive power of *in vitro* testing in the development of cell-instructive nanostructured surfaces for biomedical applications, it is therefore critical to capitalize on approaches that allow to precisely design the nanoscale topography of clinically approved metals such as titanium, the gold standard in medicine.[9,11,104,182,195,205] To this end, Several studies have explored the application of nanopatterned titanium surfaces to study cellular responses, particularly focusing on osteogenic differentiation.[135,137,198,212–214] For instance, disordered nanotopographies have been shown to

effectively promote integrin clustering and adhesion formation, which are critical for mechanotransduction and subsequent osteogenic differentiation.[1,13,40,135,137,198] One notable study demonstrated that nanoscale disorder could stimulate the differentiation of mesenchymal stem cells (MSCs) into osteoblasts even in the absence of osteogenic supplements.[137] This finding highlights the potential of disordered nanostructures to induce osteogenesis through adhesion-mediated mechanotransductive pathways.[137,206] Studies have demonstrated that vertically aligned yet laterally spaced TiO2 nanotubes on titanium significantly enhance osteoblast adhesion and propagation by promoting organized filopodia interactions with the surface, leading to improved cell attachment and accelerated growth.[214] These observations emphasize the importance of both nanoscale order and disorder in regulating cellular responses.[135,137,200,206,214–217] While these findings are promising, the scalability of nanopatterning techniques for biomedical implants, particularly titanium, remains a significant challenge. Techniques such as micelle nanolithography and block copolymer phase separation, while effective in creating nanopatterns, are often limited to small surface areas.[77,113,115,128,198] This limitation makes it difficult to apply such patterns uniformly across large surfaces, as required for orthopedic and dental implants.[93,193,195,210,211,218,219] As a result, there remains a need for scalable fabrication techniques that can nanopattern titanium at clinically relevant scales without compromising surface accuracy or reproducibility.

In this context, anodization has rapidly emerged as a cost-effective and scalable method not only to maintain the chemistry inherent to titanium implants but also to achieve a high degree of precision in nanopatterning large areas, even of samples with complex geometries.[191,205,220] The surface of anodized titanium is characterized by semi-ordered arrays of hollow cylindrical TiO_2 nanotubes with a lumen diameter ranging from tens to hundreds of nanometers, that can be precisely controlled by adjusting process time and the electrolyte's composition.[15,17,135] This

distinctive characteristic has made anodization a common choice for studies of both fundamental (e.g. cell-surface interactions) and practical (e.g. nanostructured implants) importance.

While the vast majority of studies in this field has largely focused on the role of the lumen diameter on cellular response,[55,61,63,79,83,103,128,134,135,212,221–223] our group has highlighted the importance of complementing geometrical considerations (e.g. size, circularity) with spatial statistics (e.g. degree of order, entropy) in the investigation of interfacial phenomena.[135,224] To this end, we have specifically designed a two-tiered honeycomb-like nanotubular architecture (HC) consisting of smaller nanotubes (~25 nm, HC-T1) nested within larger domains (~90 nm, HC-T2).[2,224] The ~30 nm height gap between HC-T1 and HC-T2 allows cells to span, sense and engage with both tiers. It was theorized that by varying the clustering and spatial arrangement of the HC-T1 nanotubes within the HC-T2 domains both dimensional and spatial parameters can be controlled providing, in turn, tunable nanotopographical cueing to adhering cells.[135]

When studying the cellular response to nanotubes, traditional approaches typically allow the creation of only a single nanostructure within each sample, thereby limiting the scope of analysis to a narrow set of geometrical/spatial parameters, such as lumen diameter and entropy.[18,61,134,135,212,221] However, this strategy carries the risk of overlooking a particular combination of parameters that may provide remarkable insights on cellular response.[137] To address this limitation, it is therefore crucial to develop approaches that will allow researchers to rapidly explore and screen a broader range of nanotube configurations, ultimately accelerating the discovery of high-performing designs for various applications. To this end, the development of a nanotube gradients offers a breakthrough solution by enabling the simultaneous generation of multiple structures within a single sample.[16,17,56–58,70,225,226] When compared to homogenous single-sized nanotubular samples, gradients offer a more comprehensive understanding of cell-

substrate interactions (e.g. identifying critical thresholds in surface properties that elicit significant changes in cellular behavior), as the effects of variable surface topographies continuously span an array of diameters.[70,226]

The mechanism for synthesis of titanium nanotubular gradients was described by Krabbenborg *et al.* 2014[16], who detailed a specific form of electrochemical gradients, which arise from in-plane potential gradients.[16] This approach differs from alternative configurations (e.g. two electrode anodization)[15,126,130,135,180,224,227,228] as it does not involve any conducting connections to either side of the electrode. Instead, the single bipolar electrode simultaneously acts as both the anode and the cathode.[18] What is noteworthy is the presence of a potential gradient in the solution, while the bipolar electrode maintains a roughly uniform potential across its surface.[16,18,58] This setup results in an in-plane varying potential difference between the bipolar electrode's surface and the solution. Once an adequate voltage is applied to the electrolyte solution that contains the bipolar electrode, this potential difference stimulates electrochemical reactions, generating nanotubes at the anodic pole of the bipolar electrode through a standard anodization process.[16,18,58] Over time, this polarization potential reduces, causing a decrease in the dimensions of the nanotubes and leading to the creation of a nanotubular gradient.[58] Interestingly, the size of the nanotubes is influenced by parameters like electrolyte composition, applied potential, anodization duration and electrode size.[18,58,226]

Notably, the creation of well-defined nanotubular gradients requires precise experimental control of anodization parameters, which can be technically demanding and time-consuming. This difficulty has led to a limited number of studies utilizing this approach to investigate cell-surface interaactions,[17,18] with researchers often resorting to homogenous single-sized surfaces due to their simpler fabrication processes.[60] Despite these challenges, pull-stop-pull and electrochemical

anodization methods allowed to investigate the response of mouse MC3T3-E1 cells, bacteria such as *E. coli* and *S. aureus* as well as protein adsorption on structural gradient of titanium nanotubes.[18,70] However, while these previous studies have highlighted the strong potential of gradients for high-throughput screening of nanotubular surfaces according to specific cellular metrics, they did not account for the geometrical complexity as a key driver of cell response.

To bridge this gap, we capitalized on HC hierarchical structures to continuously modulate both the dimension and spatial arrangement of HC-T1 nanotubes by varying their size and spatial distribution within the physical constraints of the HC-T2 domains.[135,224] Distinctively from previous work, these nanoscale architectures offer the ability to design the overall entropy and spatial disorder of the nanotube arrays.

The ability to precisely control the size and spatial statistics of nanotubular gradient across a large surface area enables a multifactorial approach in the study of the complex nature of cell-surface interactions by allowing to investigate multiple nanoscale interactions simultaneously, ultimately increasing experimental efficiency and depth of understanding. To this end, immunofluorescence (IF) imaging of osteogenic markers, such as RUNX2 and osteocalcin (OCN), was employed to determine the differentiation and degree of mineralization of human MG63 osteoblastic cells as a function of their position along the gradient. Osteogenic differentiation was shown to be enhanced on highly entropic regions of the surface, where RUNX2 and OCN expression levels were significantly elevated. Cytoskeletal and Ki-67 staining further demonstrated the influence of surface topography on cell morphology and proliferation, with increased cell spreading, elongation, and nuclear area observed in the more disordered regions. Mitochondrial distribution analysis revealed that surfaces with higher entropy fostered wider mitochondrial spread within the cells, indicative of higher metabolic activity. Finally, scratch

assays were performed to assess cellular migration, showing that nanotopographical features influenced migration speed and closure rates, particularly on the more complex regions of the gradient.

In conclusion, nanotubular gradients offer deeper insights into how surface features influence cell behavior, becoming an invaluable tool for biomaterials research and tissue engineering by generating nanoengineered substrates where multiple parameters, such as nanotube size, spacing and spatial distribution, can be systematically varied across a single surface.[16,18,57,60,70,225] By capitalizing on an original anodization approach and the distinctive HC architectures, we have explored a wide range of interactions relevant to the osseointegration of titanium implants in a high-throughput manner, allowing for the identification of specific topographical/spatial features that drive certain cell responses. Notably, the resulting gradients permit the extraction of homogenous single-sized nanostructures via the interpolation of structural parameters from the relationship between the voltage and the nanotube diameter[15,18,70], thereby also becoming a strategy to instruct the creation of single-sized surfaces for more focused studies. By designing nanotubular arrays with varying entropy, we have integrated the crucial effects of spatial statistics in the study of the mechanisms behind cell proliferation, differentiation, and migration. This not only enhances experimental efficiency but also expand the breadth of cellular studies, ultimately facilitating a more comprehensive investigation of how nanoscale surface features influence cellular behavior.

.

2.3 EXPERIMENTAL

2.3.1 Anodization of Titanium

Titanium foil (0.127 mm, 99.9+% purity Alfa Aesar, USA) was cut into 2.5x1 cm strips. These were successively submerged in 99.8% anhydrous toluene (Sigma Aldrich, USA), sonicated for 15 minutes to remove any contaminants from the surface, rinsed in deionized water and finally dried in air. Samples were placed into a 3D printed apparatus of UV-hardened resin and placed in front of a 2.5 cm x 2.5 cm platinum electrode (99.9% purity, Alfa Aesar, USA) by using alligator clips to keep the surfaces level and parallel to one another. Anodization was carried out, without contaminating the alligator clips, in a 100 ml Pyrex beaker with anhydrous ethylene glycol ($C_2H_6O_2$, Sigma Aldrich) containing 0.3 wt% crystalline ammonium fluoride (NH_4F, Sigma Aldrich, USA) and 2 wt% deionized water. The anodization was controlled by a PowerPac power supply (Bio-Rad, USA) in constant voltage (DC). For voltages lower than 20V, a B&K Precision model 9111 power supply (B&K Precision Corporation, USA) was used. Anodized titanium samples were then stripped of the resulting anodic layer and placed into a custom-built apparatus of 3D printed parts and HF resistant HDPE polymer. Titanium strips were secured to the HDPE platform via APT High Temperature Polymide double sided tape, allowing for each end to be spaced 1 mm from two platinum electrodes on either side, submerged in the electrolyte solutions and subjected to another cycle of anodization. The strips were then rinsed in deionized water and dried in air. All samples were submerged in 70% ethanol prior to culturing within a 60 mm petri dish and left overnight for sterilization. The ethanol was removed with a pipette and each well was washed with 500 uL of PBS three times to remove any remaining ethanol. By varying the experimental parameters of the two anodization steps (Table 3.1), three nanotubular gradients were created: the 30 V HC gradient (HCG30), the 60 V HC gradient (HCG60) and the 90 V HC gradient

(HCG90). For characterization, all gradient samples were divided into seven areas, each measuring 0.5 cm x 1 cm, starting from the anodic edge and labeled A1 through A7 (A1-A7).

Table 3.1. Experimental parameters (voltage and time) for the creation of the hierarchical nanotube gradients.

		HC Structure		
		HCG30	HCG60	HCG90
Step 1	Voltage (V)	30	60	90
	Time (min)	60	30	10
Step 2	Voltage (V)	30	60	90
	Time (min)	30	30	10

After assessing optimal and least effect regions on the gradient, homogenous versions of each characteristic surface were created for experimentation in further studies. For the optimized surfaces, titanium foil (0.127 mm, 99.9+% purity, Thermo Fisher, USA) was cut into strips measuring 2.5 x 1 cm. These strips were then submerged in 99.8% anhydrous toluene (Sigma Aldrich, USA) and sonicated for 15 minutes to eliminate any surface contaminants. The cleaned strips were subsequently rinsed with deionized water and air-dried. Samples were mounted in a 3D-printed apparatus made of UV-hardened resin and aligned parallel to a 2.5 cm x 2.5 cm platinum electrode (99.9% purity, Alfa Aesar, USA) using alligator clips, ensuring the surfaces remained level and undisturbed during the process (Figure 3.1). Anodization took place in a 50 ml Pyrex beaker filled with anhydrous ethylene glycol ($C_2H_6O_2$, Sigma Aldrich) containing 0.3 wt% crystalline ammonium fluoride (NH_4F, Sigma Aldrich, USA) and 2 wt% deionized water. The anodization was performed using a Bio-Rad PowerPac power supply (Bio-Rad, USA) under constant DC voltage. Voltages less than 20V were done on a B&K Precision model 9111 power supply, sourced from (B&K Precision Corporation, USA). After completing the first anodization step, the anodic oxide layer was carefully removed from both sides using adhesive tape, and the

samples were reinserted into the holder for a second anodization cycle. Upon completion, the surfaces were rinsed with deionized water and air dried. By adjusting the parameters of each anodization step (Table 3.2), the three different nanotubular structures examined in this study were produced.

Table 3.2. Voltage and time parameters for optimized HC and single tube surfaces.

		SNT	HCO
Step 1	Voltage (V)	60	60
	Time (min)	30	30
Step 2	Voltage (V)	60	5
	Time (min)	10	5

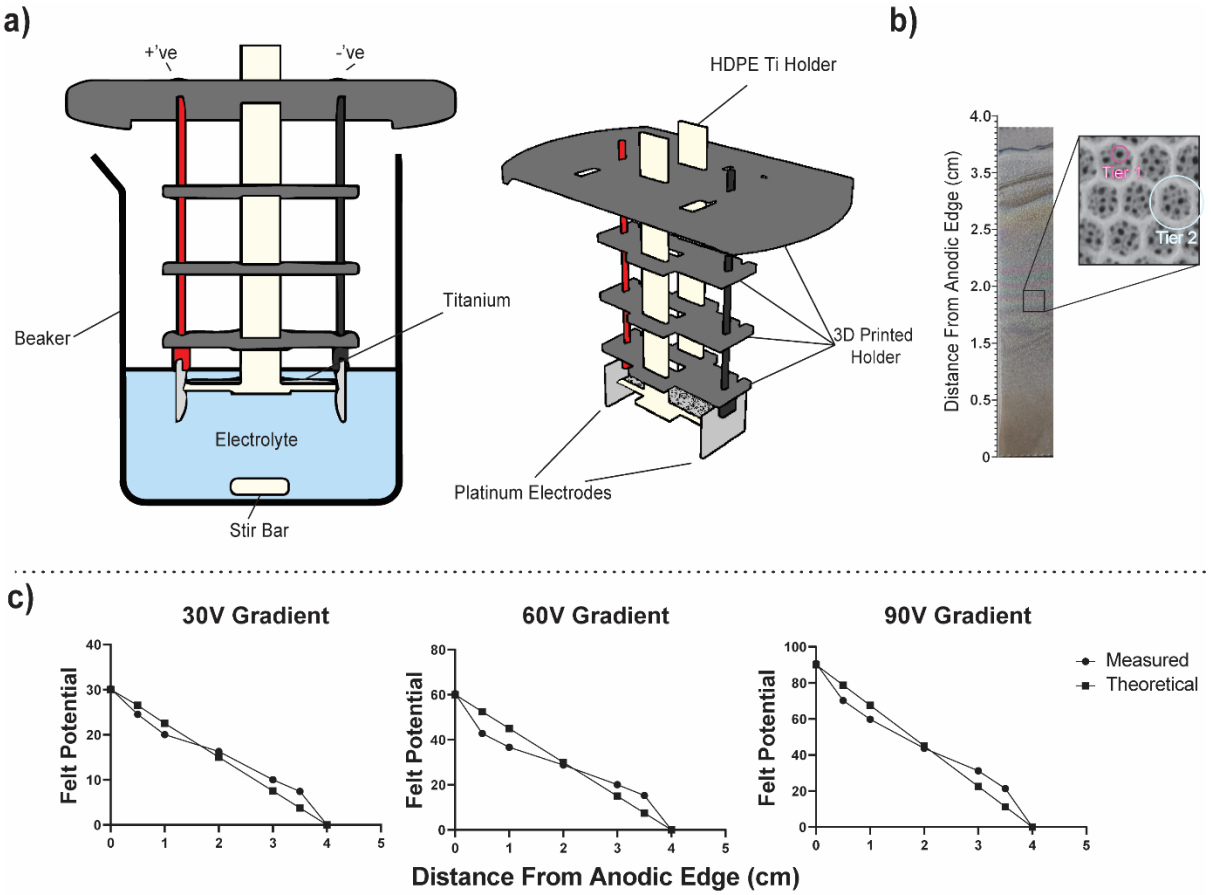

Figure 3.1. Experimental setup for bipolar anodization seen in a) Cross-sectional and 3D/isometric view of the experimental setup for bipolar anodization. The 3D printed holder supports an HF-resistant HDPE scaffold which firmly holds the titanium coupon and keeps it equally spaced from the platinum electrodes. b) Optical image of the titanium coupon showing the distinctive coloration associated with anodization. The inset displays a representative SEM image acquired at a specific location along the gradient, highlighting the T1 and T2 domains. c) Measured and theoretical Felt potential as a function of the distance from the anodic edge for HCG-30, -60 and -90. NOTE: All measured potentials are statistically different from one another by "***".

2.3.2 Characterization and Analysis of Nanotubular Arrays

An investigation into the surface morphology of anodized substrates was carried out by using a Zeiss Gemini SEM 500 Scanning Electron Microscope (SEM) at 50,000X magnification. Images captured via this SEM were processed and analyzed with the image analysis software ImageJ[162] SEM images of the nanotube surfaces were subject to a custom ImageJ pipeline and manually thresholded, segmented and analyzed via the "Particle Analysis" tool. Calculation of nanotube diameters conservatively utilized a 0.1% Q-value to remove outliers. This software allowed for the quantification of various parameters, such as the average diameter of the nanotubes, lacunarity, nanotubular density, fractal dimension, entropy and the N1:N6 ratio (i.e. hexagonal packing metric).[224] Lacunarity was calculated to measure the texture and spatial distribution of gaps within the nanotubular structures. The gliding box method was used, which involves covering the image with a series of boxes of varying sizes and calculating the variance in the number of occupied boxes across scales. This analysis was performed using the MultiFrac[229] plugin in ImageJ, covering a range of box sizes to capture the multi-scale heterogeneity. Entropy was measured to quantify the randomness and complexity of pixel intensity values in the images. To this end, CSIMLab's SampEn2D plugin in ImageJ function was used to evaluate surface entropy.[230,231] The m coefficient was set to 2 while r as a fraction (0.2) of the standard deviation of pixel values.[232] Fractal dimension was computed to quantify the complexity of the nanotubular patterns by using the box-counting method in the MultiFrac plugin. Images Were covered with a grid of boxes of

varying sizes, and the number of boxes containing part of the structure is counted. In this way, the lacunarity, fractal dimension and two dimensional surface entropy are unitless mathematical analysis concerning different types of geometrical complexity of the segmented nanotubular images described above and within the results and discussion section. The hexagonal packing metric was devised to assess the packing efficiency of the nanotubes. It is defined as the ratio of the first nearest neighbor distance (NND) to the average of the six nearest neighbor distances (N1:N6 ratio).[224] This metric provides a quantitative measure of how closely the nanotube arrangements approximate ideal hexagonal packing. Images were processed in ImageJ to convert them into binary format, with nanotubes represented as white pixels on a black background. All calculations were performed on these binary images to ensure consistency in the analysis. Outlier removal was conducted using the ROUT method with a Q value of 0.1% to maintain data integrity while eliminating extreme values.

2.3.3 Human MG63 osteoblastic cell cultures

Human MG63 osteoblastic cells (CRL-1427, ATCC, USA) were thawed and passaged using 1x TrypLE and DMEM (10567-014, Gibco, USA) (5 mM glucose) complete culture medium (CCM) supplemented with 10% fetal bovine serum (FBS). The cells were maintained at 37 °C in 5% CO2. After the CCM was gently aspirated, the cells were washed three times with sterile 1x PBS and detached from the surface of the culture flask by adding 3 mL of TrypLE. The cells were incubated for 3 minutes to ensure full detachment from the flask surface. Subsequently, 7 mL of culture medium were added to the cell suspension, which was successively centrifuged for 8 minutes at 150 rpm. Following centrifugation, the cells were resuspended in 10 mL of CCM. Finally, 2 mL of the cell suspension were transferred into 8 mL of fresh CCM in a filtered 75 cm^2 flask and returned to the incubator.

2.3.4 Cellular Seeding and Fixation

Titanium nanotubular substrates (single diameter and HC gradients) measuring 3.8 x 1 cm were sterilized in 70% ethanol and then washed with sterile 1x phosphate-buffered saline (PBS). Cells were seeded at a density of 5,000 cells/cm² in 60 mm TC-treated petri dishes. Cells were cultured on the nanotubular substrates for experiment-specific durations ranging from 1 to 21 days to study proliferation, morphology, mitochondrial distribution, differentiation, bone mineral deposition, and migration. At the end of the experiments, cells were fixed by adding 4,000 µL of fresh 4% paraformaldehyde (PFA, Sigma-Aldrich) to each well for 10 minutes at room temperature (RT). The wells were then washed three times with PBS to remove residual PFA, filled with a final volume of 5,000 µL of PBS, and stored at 4 °C. All experiments were conducted with at least 3 samples per condition and per time point, with each experiment carried out in triplicate.

2.3.5 Immunofluorescence Staining

MG63 cells were permeabilized using a 0.25% solution of Triton X-100 (TX-100, Sigma-Aldrich) for a duration of 10 minutes at RT. Following permeabilization, samples were blocked with 5% donkey serum (Sigma, USA) at RT for an hour. For both Days 1 and 7, the nuclei and Actin were labeled with DAPI and AlexaFluor 488 Phalloidin (1:400) from Thermo Fisher, USA. Mitochondria and RUNX2 were stained with Mitochondria Antibody (MA5-12017) mAb (Thermo Fisher, USA) at a ratio of 1:100 and RUNX2 polyclonal rAb (Thermo Fisher, USA) at a 1:100 dilution, respectively. These primary stains were then followed by secondary staining using AlexaFluor 594 Donkey-anti-mouse IgG (Thermo Fisher) at a 1:500 dilution. Cell proliferation was assessed by staining for anti-Ki-67 polyclonal rabbit antibody (Millipore Sigma, USA) at a 1:250 dilution, while osteocalcin (OCN) monoclonal antibody (Thermo Fisher, USA) at a 1:100 dilution was used as a second differentiation marker. Both osteocalcin and Ki-67 primary stains

were followed by secondary labeling with AlexaFluor 647 Donkey-anti-rabbit IgG (Thermo Fisher). The primary antibody incubation was conducted overnight at a temperature of 4 °C, whereas the blocking and secondary antibody incubations were each carried out for 1 hour at RT. Post-incubation, the samples were thoroughly washed and then imaged in PBS in 60 mm petri dish. To ensure the reliability of the results, all experiments were conducted in triplicate.

2.3.6 Immunofluorescence Imaging and Analysis

The multi-channel images used for the quantification and analysis of nuclei, cytoskeletal morphology and proliferative and differentiation markers were obtained by using a ThermoFisher EVOS FL Auto 2 (inverted) widefield microscope (ThermoFisher, USA). Day 1 images of the entire 1 x 3.8 cm sample surface were captured with 10X air objective (0.25 NA, Air, PL FL LWD PH), and each analyzed Area on the gradient equated to roughly 12 images per area. Day 7 images were capture using a 20X air objective (20x, 0.40 NA, Air, PL FL LWD PH), and 9 images per area were taken. Day 1 and Day 7 IF experiments were conducted on a total of 14 samples (7 Areas per sample), over 3 distinct, independent experiments. The imaging system utilizes LED light sources with specific filters for different wavelengths: Blue (Ex 357/44 nm, Em 447/60 nm), Green (Ex 470/22 nm, Em 510/42 nm), Red (Ex 585/29 nm, Em 624/40 nm), and Far Red (Ex 628/40 nm, Em 692/40 nm). Detection as performed using a monochrome camera. The number of DAPI-stained nuclei and actin morphology on each surface was quantified using custom ImageJ[162] pipelines. The primary morphological parameters considered were the area (μm^2), irregularity[135,163,164], protrusion (solidity[164,165]) and the aspect ratio[135,164] (major axis/minor axis). Irregularity is defined by the equation $(4\pi A)/P^2$; where A is the cell area and P is the perimeter. Solidity is defined as the area of the cell divided by the area of its convex hull. The irregularity and solidity span 0 to 1, where in both cases a value of 1 represents a perfect circle. Both nuclear

and cellular morphology analysis was carried out by stitching, segmenting and processing image in a custom pipeline calculated via particle analysis in ImageJ. For the morphological analysis, a total of 14 samples per condition were analyzed, encompassing three biological replicates from each of the three distinct experimental sets.

To segment the mitochondria, a threshold was first applied to the DAPI channel to isolate the nuclei, which were then segmented. Next, the red fluorescence channel corresponding to mitochondria was subject to thresholding, and the segmented nuclei were subtracted to ensure only mitochondrial regions were captured. For actin segmentation, the green fluorescence channel was subject to thresholding, and both the segmented nuclei and mitochondria regions were subtracted to isolate the actin structures. Segmented areas were measure using custom ImageJ pipelines and the mitochondrial to DAPI (M/D) and mitochondrial to actin (M/I) ratios were derived be dividing the corresponding areas by one another. Segmented DAPI, actin and mitochondrial areas were subsequently used to generate ROIs to measure the protein expression (integrated density and mean intensity) for Ki67 and RUNX2 (DAPI segment), Mitochondria (Mitochondrial segment), and OCN (Actin segment).

2.3.7 Alizarin Red Staining and Assay

To evaluate mineralization as a function of the position along the substrates, an Alizarin Red Staining (ARS) protocol (Sigma, USA) was utilized. The culture medium was initially removed from each well, followed by gentle washing three times with 1xPBS. Cells were then fixed in 4% PFA at room temperature for approximately 10 minutes. After fixation, the PFA was discarded, and the cells underwent three thorough washes with deionized water. Once all deionized water was removed, 1 mL of 40 mM ARS solution was added to each well, and the plates were incubated at room temperature for 25 minutes with gentle shaking to ensure effective interaction between the

dye and the cells. Following the incubation, the ARS solution was removed, and the cells were washed five times with deionized water to eliminate any unbound dye. The plates were then tilted for about 2 minutes to allow any remaining water to drain, preparing the samples for subsequent analysis.

Using a sharp scalpel and a ruler to mark distances, the gradient monolayer was divided into seven sections. Each A1-A7 section was scraped off using a 1 mL pipette tip and placed into a 1.5 mL microfuge tube. To each tube, 200 µL of 10% acetic acid was added, and the samples were incubated at room temperature for 30 minutes with shaking. The samples were then vortexed for 30 seconds and heated at 85 °C for 10 minutes, with parafilm used to seal the tubes and prevent evaporation. After heating, the tubes were placed on ice for a 5-minute incubation to cool completely. The mixture was then centrifuged at 12,000 g for 15 minutes, and the supernatant was carefully transferred to a new tube. To adjust the pH to between 4.1 and 4.5, 10% ammonium hydroxide was added to the supernatant. Finally, 100 µL of each sample was aliquoted into a 96-well plate, and the absorbance was measured at 405 nm using a Synergy H1 plate reader (BioTek, USA). An ARS standard curve was generated using Excel (Microsoft, USA), and the ARS concentration of the samples was calculated. This assay was performed on a total of 15 samples, comprising 5 samples (each with 7 areas) from each of the three distinct experimental sets.

2.3.8 Scratch Assay

A scratch assay was performed to evaluate the migratory behavior of MG63 cells on nanotubular gradient surfaces. Cells were plated at a density of 20,000 cells/cm² in 60mm TC-treated petri dishes containing 5 ml of DMEM (10567-014, Gibco, USA) supplemented with 10% FBS, and were incubated until they reached confluence, which typically occurred after two days. The culture medium was then switched to DMEM supplemented with 1% FBS. After 24 hours, a

sterile 200 µL pipette tip was used to create a cell-free zone by scraping along the monolayer of MG63 cells across the length of each sample. The cell monolayer was then gently rinsed with phosphate-buffered saline (PBS) to remove any dislodged cells and debris. Images of the scratched areas were taken at various time points using a ThermoFisher EVOS FL Auto 2 inverted widefield microscope (ThermoFisher, USA) at 5X (0.13 NA, Air, PL FL LWD PH) and 10X (0.25 NA, Air, PL FL LWD PH) magnifications to monitor and quantify scratch closure. The initial scratch area was measured using a custom ImageJ pipeline, which segmented the scratch area at different time points through thresholding to determine the extent of closure compared to the initial scratch at time 0. Cell migration assays on untreated and anodized 1 x 3.8 cm^2 titanium surfaces were conducted in a similar fashion, with observations made at 0, 12 and 24 hours. After 24 hours after seeding, substrates were transferred to a new 60 mm petri dish. To aid in visualizing cell migration on opaque surfaces, cells were stained with CellTracker Red CMTPX Dye (ThermoFisher, USA). This assay was conducted on a total of 18 samples, 6 samples ("scratches") representing each of the three distinct experimental groups.

2.3.9 Statistical Analysis

The Shapiro-Wilk test was applied to assess the normality of the data sets. For data sets that followed a normal distribution, a parametric One-Way ANOVA was conducted, with significant differences in means identified using Tukey's Honest Significant Difference (HSD) post-hoc test. Data that did not conform to normality were analyzed using the nonparametric Kruskal-Wallis test, followed by Dunn's post-hoc test. Unless otherwise noted in the figure descriptions, error bars represent the mean with a 95% confidence interval. A p-value of less than 0.05 was considered statistically significant. Significance levels were indicated as follows: * for $p < 0.05$, ** for $p < 0.01$, and *** for $p < 0.001$.

2.4 Results & Discussion

2.4.1 Nanotubes

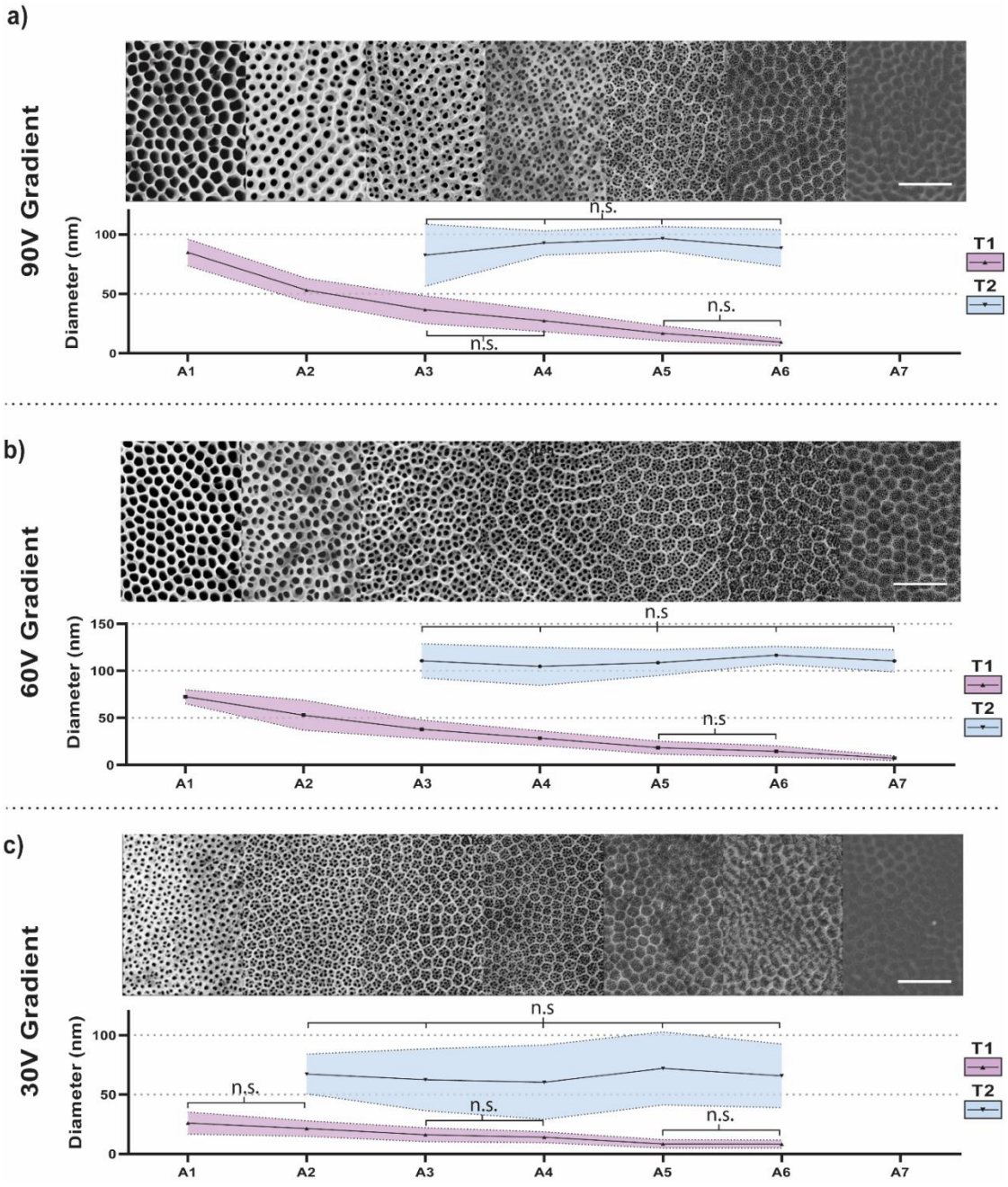

Figure 3.2. SEM images of A1-A7 progression for various gradients. SEM images (top panel) and diameter of the T1 and T2 domains (bottom panel) at specific locations (A1-A7) along the nanotubular gradient obtained by anodization at a) 90 V, b) 60 V and c) 30 V. Scale bar is equivalent to 400 nm. Purple and blue shadowing represent the standard deviation of the diameter for the T1 and T2 domains, respectively. Data are statistically different marked otherwise (n.s.).

The results presented in Figure 3.2 illustrate the comparative analysis of gradient combinations anodized at 30 V, 60 V, and 90 V to form HC structures. Among all tested gradients, HCG60 demonstrated the most stable and consistent formation of the HC structure. This stability was evident in its ability to produce a well-defined and uniform surface in the A7 area, which was not achieved by the other gradients. In contrast, the 90 V gradient encountered challenges due to elevated temperatures during the anodization process. Anodizing beyond 10 minutes led to erosion and delamination in the A1-A2 areas in many cases, compromising the structural integrity of these regions and an additional synthesis to produce the entire gradient for cell response testing. Modifications to the synthesis apparatus that include stringent temperature controls will most likely be necessary to prevent these issues at higher voltages and to achieve a stable HC structure at 90 V and above. Reducing anodization time was also attempted to improve the reliability of the 90 V gradient without altering the anodization setup. Unfortunately, reduced anodization times drastically reduced the span in which nanotopographical features are expressed across the gradient, only having features to A5. However, one interesting aspect of this gradient is a validation of previous work done in our lab theorizing the possibility of controlling the width of the HC structural walls (Figure 3.S1). High voltages with short bipolar anodization allow for synthesis of variable wall thickness and predictable T1 diameters. This combined with the introduction of temperature controls, presents an exciting exploration in future work for a wide variety HC lattices, where larger domains are not just conserved across the gradient, but become entirely tunable. This also suggests that these HC surfaces form from the center outwards, as the tubes synthesized at 90 V for 10 min vs. 5 mins lose this variable wall thickness.

Unlike the HCG60 and HCG90 samples, the HCG30 gradient showed a rapid transition into bifurcation, possibly due to the larger seed points allowing multiple tubes to form within a single

pit from the beginning of the potential gradient. This phenomenon, which was mitigated in previous work using a triphasic anodization process, suggests that repeating the initial anodization step could prevent immediate bifurcation, however if the T2 domain has an inherent fundamental minimum diameter, this bifurcation may be unavoidable. Additionally, the T2 domains in HCG30 were smaller and exhibited a much wider distribution of sizes compared to their HCG60 and HCG90 counterparts. Additional anodization steps may also enhance the structural order of these T2 domains and achieve the desired consistency matching HCG60 and HCG90.

Overall, this comparative analysis underscores the superiority of HCG60 for forming HC nanotube structures. Its stability and consistency, particularly in producing a well-defined surface in the A7 area, all of which is done at room temperature, make it the most reliable choice for gauging cell response across the widest variety of these features, especially in this novel first step in exploring these structures. The challenges observed with HCG90 highlight the necessity of meticulous temperature control to prevent structural degradation, providing meaningful direction for future modifications in the synthesis apparatus. Meanwhile, the fundamental insights gained from the HCG30 suggest that further refinement of the anodization process, potentially increasing the amount of initial anodization steps, is required to prevent rapid bifurcation and improve structural order, if smaller HC features are to be created and explored. Consequently, HCG60 was selected for spatial analysis and cellular studies due to its robustness, reproducibility and ability to form topography in the A7 area, ensuring accurate assessment of cell response across the gradient and providing reliable data for future biomaterial designs and applications.

2.4.2 Spatial Statistics

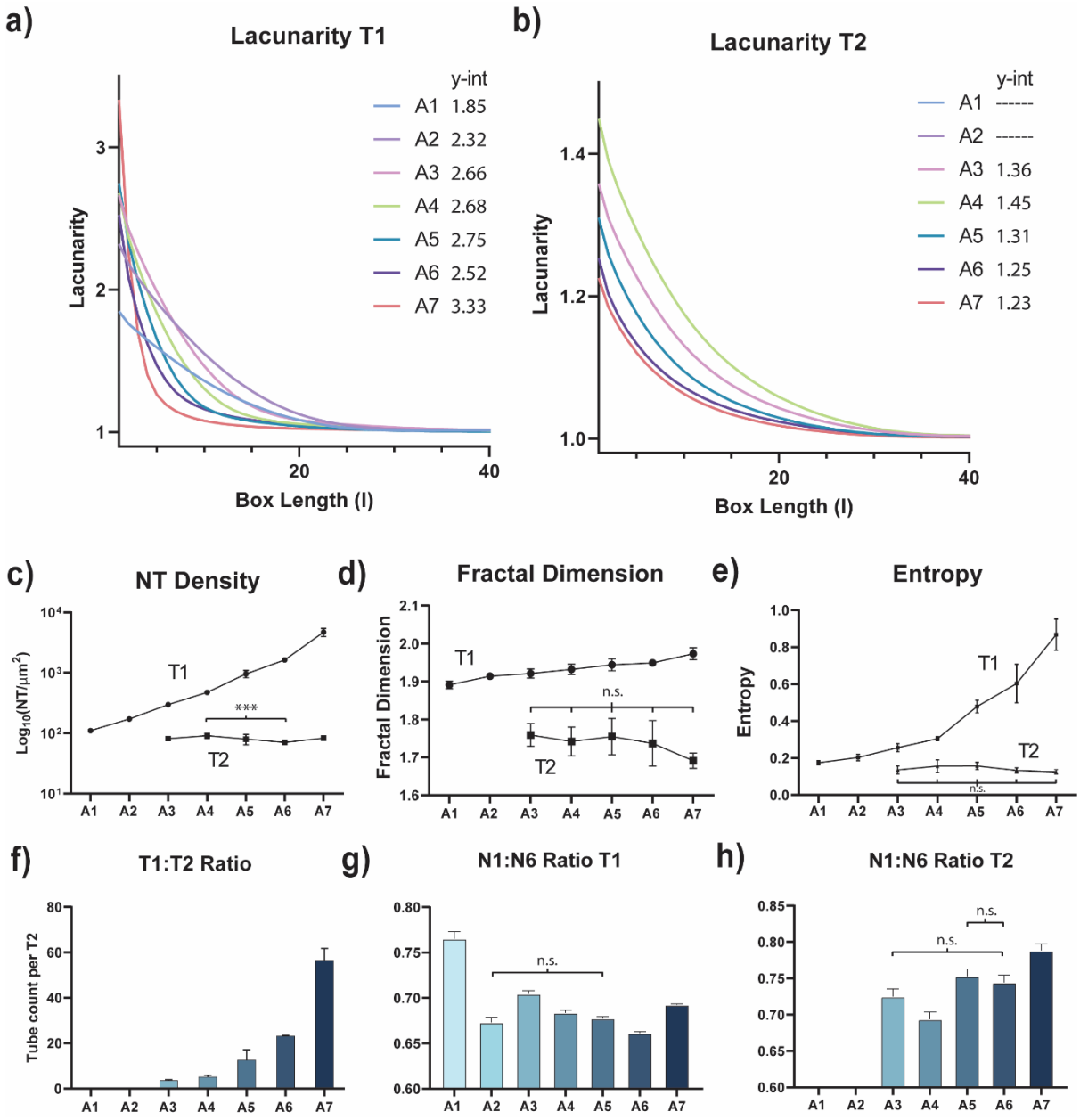

Figure 3.3. HCG60 spatial dynamics for lacunarity for a) T1 and b) T2, c) nanotube density (NT Density), d) fractal dimension and e) entropy values along the gradient. The number of f) T1 tubes within the T2 domains. N1:N6 ratio calculations and a proxy for degree of disorder for g) T1 and h) T2 domains. Data are significantly different from one another unless marked otherwise. All three metrics: Entropy (2D Sample Entropy), Fractal Dimension, and Lacunarity—are unitless, as they describe properties that are independent of the physical dimensions of the analyzed image.

The spatial statistics of our nanotubular gradient surfaces (Figure 3.3) were rigorously analyzed using several key metrics, including lacunarity, entropy, fractal dimension, and a previously

devised hexagonal packing metric. The use of lacunarity to capture texture and variability[233], entropy to measure overall disorder[232], and fractal dimension to quantify geometrical complexity[234] provides multi-faceted approach that paints a comprehensive understanding of the structural complexity and packing efficiency across the gradient. Lacunarity is a critical metric for identifying the degree of clustering within the samples, which increases with the hierarchical complexity of the surfaces, providing insights into the textural heterogeneity.[233] Lacunarity Analysis (Figure 3.3a) was employed to evaluate the texture and spatial distribution of gaps within the nanotubular structures. The peak lacunarity values for the T1 tubes were 1.85, 2.32, 2.66, 2.68, 2.75, 2.52, and 3.33 for samples A1 to A7, respectively. This progression indicates a shift from less clumpy patterns in A1 to more heterogeneous, clumpy structures in A7. In contrast, the Lacunarity values for the T2 domains (Figure 3.3b) lie within a much tighter range, showcasing a consistent trend showing the T1 domains changing while the T2 domains remain consistent across the gradient, reducing the geometrical variables effecting cells. Entropy Measurements quantified the randomness and complexity of pixel intensity values within the images.[230,231] Entropy values increased progressively from A1 (0.18) to A7 (0.87), reflecting growing complexity and disorder in the spatial arrangements of the nanotubes. This trend is consistent with the structural evolution from single nanotubes to intricate hierarchical configurations as indicated from previous work in our lab, demonstrating increasing irregularity and complexity of the patterns.[135] We observed exponential growth of T1 nanotubes (smaller domains) along the gradient, which contrasted with the stable domain sizes of T2 nanotubes (larger domains) (Figure 3.3f). Consequently, the nanotube density scales exponentially as the gradient progresses from A1 to A7 (Figure 3.3c). This exponential increase in T1 nanotubes highlights the dynamic nature of the smaller structures as they proliferate, while the consistent domain size of T2 tubes suggests a stable macrostructure.

This nuanced growth pattern ties into our other spatial metrics by illustrating the increasing complexity and variability of the smaller domains, which are most likely behind the sharp increase in the entropy and lacunarity measurements.

Fractal dimension calculations provided insights into the overall geometrical complexity and scaling properties of the surfaces. The fractal dimension values ranged from 1.83 to 1.96 for the smaller domains, indicating relatively consistent space-filling capacity across these samples. Interestingly, the larger T2 domains in the hierarchical structures (A3 to A7) exhibited a fractal dimension of approximately 1.7-1.75. This lower fractal dimension suggests that while the smaller domains became more complex, the larger framework maintained a less detailed but structurally significant form. The fractal dimension values for A1 to A7 surfaces range narrowly between 1.89 and 1.96, despite significant differences in lacunarity and entropy, suggests that while the surfaces maintain a relatively consistent space-filling capacity (as indicated by fractal dimension), their textural and organizational complexity varies more significantly.[234] Lacunarity reflects the degree of heterogeneity and gap distribution, while entropy measures randomness and disorder.[233] The more pronounced changes in these metrics imply that heterogeneity increase along the gradient, even if the overall geometrical complexity (fractal dimension) changes only slightly. This indicates that the surfaces are becoming more texturally complex and disordered, which might have a more significant impact on cellular responses.[137,206] Hexagonal packing metric (N1:N6 ratio) was devised to assess the efficiency of the nanotube packing arrangement. Interestingly, only the single tube A1 surface has elevated levels above 0.75, where all the other surfaces ranged between 0.65 and 0.7. This means that the packing order does go down which can contribute to higher entropy, however that the level of disorder across the HC surfaces is comparable in a tight range despite the increasing lacunarity, entropy and fractal dimension. The T2 larger domains exhibit higher

N1:N6 ratios as the inner T1 tubes decrease. Most likely due to the tiny tubes propagating from the initial seed point with substantial room for growth and packing within each domain, where the larger domains compete for space and exhibit higher propensities to bifurcate, potentially disrupting the uniform formation of the hexagonally packed T2 domains, characteristic of the HC surfaces. This is especially prominent in the heavily bifurcated A2 and A3 surfaces.

The combination of these metrics offers a detailed analysis of the spatial complexity and packing efficiency of the nanotubular gradient surfaces. The consistent fractal dimension across smaller domains suggests that the initial anodization sets a foundational pattern that persists through subsequent bipolar anodization, resulting in similar fractal structure at a higher level. Increasing entropy and lacunarity values, along with the hexagonal packing metric, reveal the evolution of structural complexity from single to hierarchical nanotube formations.

2.4.3 Morphology

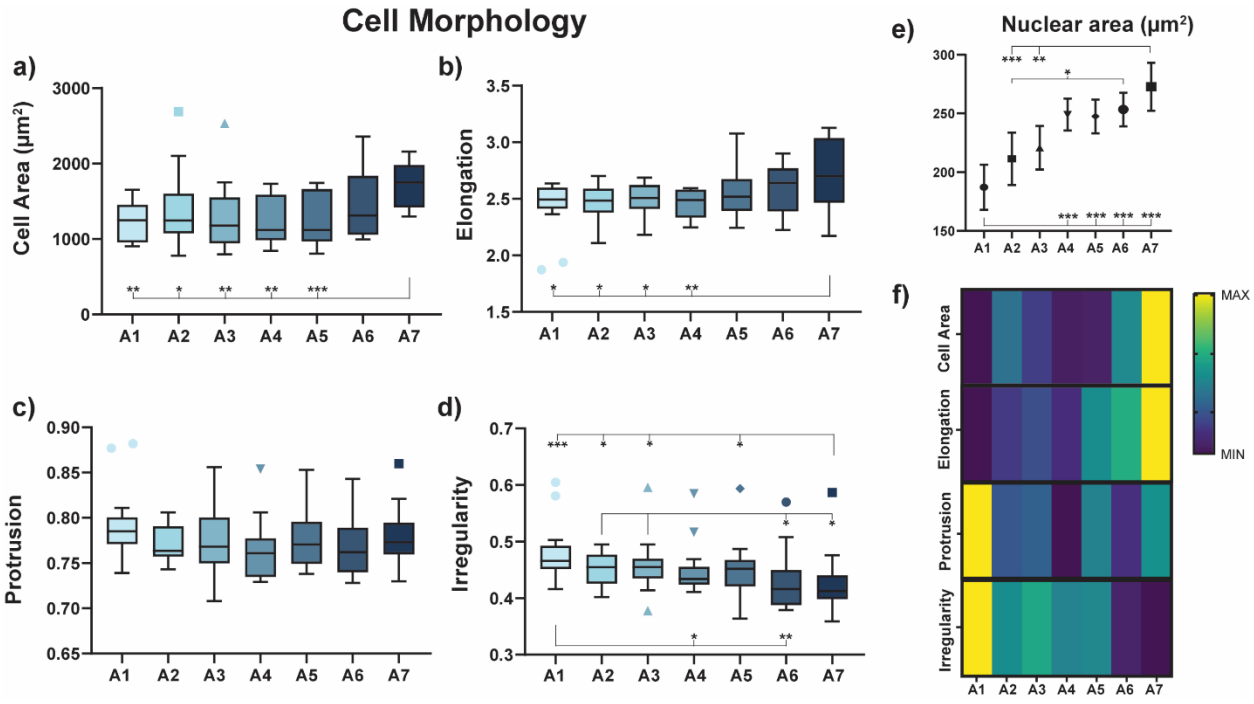

Figure 3.4. Cell morphological measurements. Quantification of cellular a) area, b) elongation, c) degree of protrusion, d) the degree of irregularity and e) the nuclear area at the A1-A7 locations along the HCG60 gradient; f) heatmap of the morphological parameters.

Figure 3.4 presents a comprehensive analysis of cellular morphology across different areas of the nanotubular surfaces. Starting with cell area (Figure 3.4a), the largest differences were observed between area A7 and all other areas. In general, most surfaces exhibited similar cellular areas, except for A7, which displayed significantly larger cell areas than all other regions, besides A6. These results indicate a substantial increase in cell spreading and attachment in area A7, which is characterized by the smallest inner tubes and highest structural complexity. The other areas showed no statistically significant differences in cell area, suggesting a uniform response across the gradient except for the most complex region. The analysis of cellular aspect ratio (Figure 3.4b) revealed that area A7 had a strong influence on cellular elongation. There was a general trend of increasing elongation from A1 to A7, with A7 showing a significantly larger effect on elongation compared to areas A1, A2, A3, and A4. However, areas A5, A6, and A7 did not exhibit significant differences in elongation among themselves. This gradient in elongation suggests that cells are more elongated on surfaces with higher structural complexity, particularly in regions with well-developed HC structures.

When examining cellular irregularity/circularity (Figure 3.4c), it was observed that fully developed HC surfaces had a pronounced effect on increasing cellular irregularity. There was a general trend of increasing irregularity moving from A1 to A7, with the most significant differences occurring between areas A6 and A7 compared to A1. These findings align with previously published results from our lab, which indicated that larger singular tubes tend to induce smaller and more circular cell morphologies, resulting in reduced irregularity.[135,224] Areas A6 and A7, with their further developed irregular geometries, were significantly different from both A2

and A3, indicating a substantial shift in cell morphology on more complex surfaces. Cellular protrusion, as measured by solidity (Figure 3.4d), showed no significant differences across all surfaces along the gradient. This consistency across varying nanotubular structures, indicating that cellular protrusion is not significantly influenced by surface complexity.

Nuclear area (Figure 3.4e) followed a trend as previous studies involving large singular tubes and HC surfaces, with an increase in nuclear area observed on HC surfaces, that correlates directionally with cell area. The largest differences were noted between areas A1 and A2 and the fully formed HC surfaces (A4-A7). This increase in nuclear area, particularly in area A7, coincided with the overall increase in cellular size observed in this region. A7 exhibited the largest nuclear area, significantly larger than areas A1, A2, and A3. The general trend indicated an increase in nuclear area from A1 to A7, mirroring the trend in cell size and elongation, further emphasizing the influence of surface topography on cellular morphology.

Finally, the general trend image heatmap in morphology (Figure 3.4f) consolidates these observations visually, highlighting that most surfaces exhibited similar cell areas except for A7. There was a clear trend of increasing elongation, irregularity, and nuclear area from A1 to A7, with no significant difference in cellular protrusion across the gradient. These findings suggest that the structural complexity and order of the nanotubular surfaces play a crucial role in determining cellular morphology, with more complex HC structures promoting larger, more elongated, and irregular cells with increased nuclear areas. The spatial complexity of the HCG60 surfaces significantly influenced cellular morphology. The increasing lacunarity and entropy from A1 to A7 corresponded with notable changes in cell area, aspect ratio, and irregularity. Specifically, the larger cell areas observed on surface A7 align with its high entropy and lacunarity, indicating that more heterogeneous and disordered surfaces promote greater cell spreading. The enhanced cellular

elongation on surfaces A6 and A7 further emphasizes the role of complex topographies in guiding cellular shape.

The significant influence of surface topography on cellular morphology is well-documented, and our findings further support this relationship. The most complex surface, A7, promoted greater cell area, elongation, and irregularity compared to simpler surfaces like A1. These observations align with studies that demonstrate how intricate topographies can enhance integrin clustering and focal adhesion kinase activation, promoting stronger cell adhesion and signaling pathways that drive differentiation and proliferation.[137,206,215] The increased lacunarity and entropy of A7 likely provide a more stimulating environment for cells, enhancing their spreading and elongation, which is essential for subsequent cellular functions.

2.4.4 *Cellular Metabolism and Proliferation*

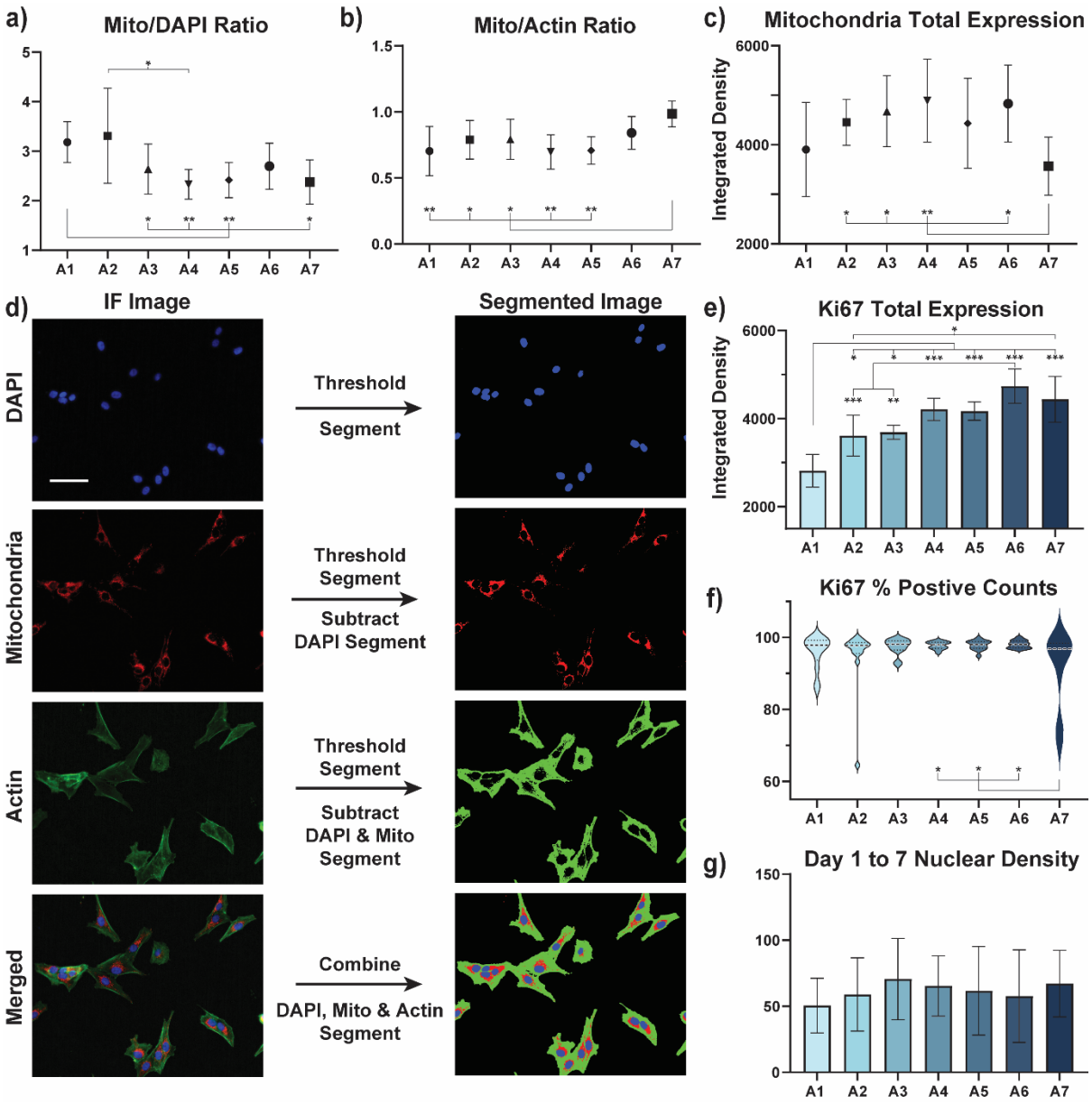

Figure 3.5. Mitochondrial spatial distributions representing the spacing of a) mitochondria relative to the cell nuclei, b) the ratio between the area occupied by the mitochondria and the cell area minus mitochondrial and DAPI segments, and c) the integrated density of mitochondria within the cell. Panel d) represents the segmentation process of how these distributive measurements were analyzed. Cell proliferative metrics are shown in the form of e) Ki67 integrated density, f) distributive violin plots of Ki67 percent positive nuclei, and g) the progressive growth of nuclear density between day 1 and day 7 timepoints.

The mitochondrial analysis presented in Figure 3.5 provides intriguing insights into the distribution and activity of mitochondria relative to cellular and nuclear areas across the nanotubular surfaces. Figure 3.5a shows the mitochondrial distribution relative to nuclear area, revealing the largest differences between the middle of the gradient and the extremes, particularly at the A1 end. Surfaces A3-5 and A7 exhibited a lower value in mitochondrial distribution relative to the nucleus compared to cells on surface A1. This observation can be attributed to the similar cell areas across surfaces A1-6, necessitating comparable levels of energy output relative to mitochondrial activity. The smaller nuclear area in A1 may explain this discrepancy in distribution. Furthermore, this might elucidate why the total mitochondrial area normalized by the number of nuclei showed no significant differences across the gradient, as seen in Figure 3.S2.

In Figure 3.5b, the analysis of mitochondrial distribution within the cell area revealed that surface A7 exhibited the most significant difference, with a much larger mitochondrial-to-cell area (Mito/Actin) ratio than all other areas, significantly surpassing surfaces A1-5. This wider distribution of mitochondria throughout the cells interacting with the A7 surface suggests that the interaction at the cell-surface interface fundamentally affects mitochondrial production and distribution, indicating a potential increase in energy demand. Unlike the distributive difference in the nuclear Mito/DAPI ratio for A1, the notable Mito/Actin ratio on A7, despite the large cell area, suggests an enhanced metabolic activity and energy requirement induced by the complex HC surface. Wider mitochondrial distribution within the cells on A7 suggests a higher metabolic demand, supporting the increased cell area and activity. This distribution pattern might be linked to localized energy requirements and signaling within the cell, as research indicates that mitochondrial dynamics, including fission and fusion, are influenced by cellular stress and the need for localized ATP production.[235,236] Figure 3.5c examines mitochondrial intensity, where

higher integrated density typically indicates more active mitochondria. Contrary to expectations based on distribution, surface A7 exhibited a much lower integrated density compared to surfaces A2-4 and A6. This reduction in intensity does not necessarily imply a decrease in energy consumption but may instead reflect the propensity of the A7 surface to distribute mitochondria more evenly throughout a larger percentage of the cell cytoplasm. This even distribution might dilute/reduce the intensity signal, thereby lowering the integrated density while maintaining or even increasing overall metabolic activity. The analytical segmentation shown in Figure 3.5d illustrates the methodology used to derive mitochondrial area by subtracting segmented DAPI IF channels from the mitochondrial segment and then adding these signals together and subtracting from the actin signal, representing total cell morphology.[235–237] This detailed spatial analysis provided the ratios between these various substructures, offering a comprehensive understanding of cellular and mitochondrial organization.

The Ki67 expression, which serves as a proliferation marker, increases from single tubes on A1 to the more complex A6 and A7 surfaces (Figure 3.5e). The rise of the Ki67 integrated intensity suggests an elevated proliferation rate on surfaces with higher entropy (i.e. A6-A7). in contrast, the Ki67 positive percentage counts (Figure 3.5f) were significantly lower on A7. Overall, Ki67 positive counts remained high across the entire gradient, consistent with previous findings in from our group[224], indicating that cells maintain high proliferation rates after 1 and 2 days of culture. The slightly lower counts on HC architecture such as A7 may indicate a shift in cellular priorities towards early differentiation. Lastly, nuclear density ratios from Day 1 to Day 7 (Figure 3.5g) was used to assess relative growth and cell counts. Although surfaces A2-5 and A7 exhibited elevated values compared to A1, no significant differences were found, indicating that cell proliferation and density changes over time were relatively consistent across the gradient.

Taken together, our findings underscore the significant impact of nanotopographical features on mitochondrial functions. In particular, the mitochondrial distribution analysis revealed that surfaces with higher entropy and lacunarity, particularly A7, exhibited wider mitochondrial spread within the cells. This wider distribution, despite the larger cell area, suggests a fundamental impact of the A7 surface on mitochondrial production and distribution. Conversely, the reduced integrated density of mitochondria on A7, despite the wider spread, implies that the surface topography may enhance energy demands, leading to a more dispersed but less dense mitochondrial network.[235,236] The elevated Ki67 expression on A6 and A7 surfaces further supports this conclusion, indicating increased cellular proliferation on more disordered surfaces, consistent with the increased metabolic activity suggested by the wider mitochondrial distribution.

2.4.5 Differentiation

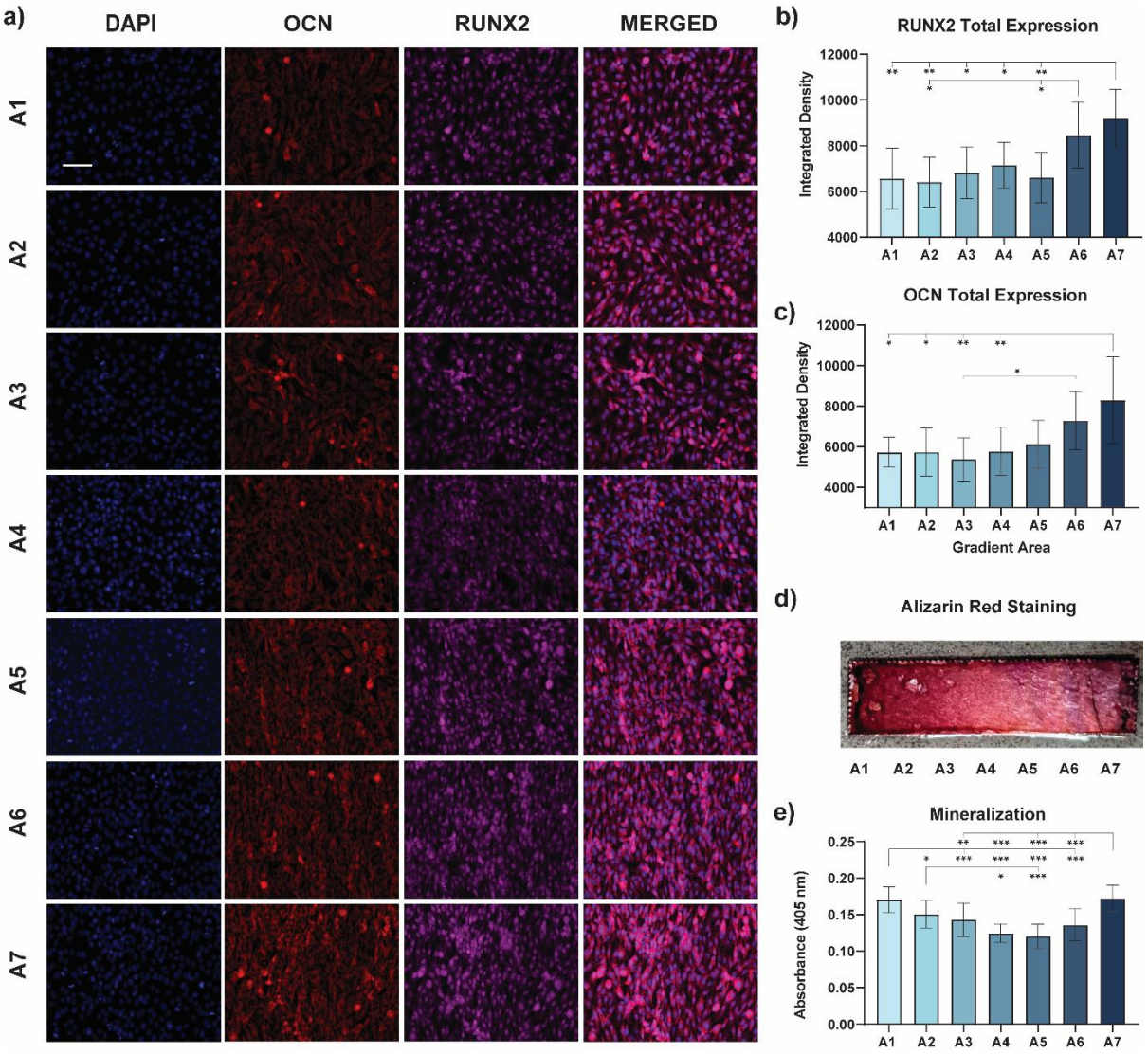

Figure 3.6. IF images at day 7 of a) DAPI (blue), OCN (red), RUNX2 (magenta), and their respective merged images for each of the seven areas (A1-7) along the HCG60. Quantitative analysis is shown for b) RUNX2 and c) OCN integrated densities. The Alizarin stain for each gradient shown photographically in d) and quantified in e) via Alizarin assay.

Figure 3.6 quantifies the expression of two osteoblastic differentiation markers, namely RUNX2 and osteocalcin (OCN), as well as mineralization along the gradient. IF images in Figure 6a illustrate the visible increase in intensity and expression of both osteocalcin (OCN) and RUNX2 as the surface topography progresses from A1 to A7. This increase is particularly pronounced on

the more entropic HC surfaces, suggesting that the complex topography enhances differentiation potential. Figure 3.6b displays the total RUNX2 expression, demonstrating significantly elevated expression on A6 and A7 compared to the other locations examined along the gradient. Similarly, the overall expression of OCN (Figure 3.6c) was significantly higher on A6-A7. Taken together, these results indicate that the increased entropy and lacunarity of these architectures favor early differentiation. This can be attributed to the fact that surface complexity may increase surface energy and wettability, ultimately favoring protein adsorption and cell adhesion.[206,238] In alternative, these findings can potentially be linked to the influence of nanotopography on mechanotransduction pathways. Surface features like those on A7 can affect cytoskeletal tension and nuclear deformation, modulating gene expression through pathways such as YAP/TAZ that are crucial for osteogenic differentiation.[43,49,137,206,222,239]

Mineralization was assessed via Alizarin red staining assay (Figure 3.6d-e) which revealed a divergence from the RUNX2/OCN differentiation results. Specifically, data after 21 days of culture aligned closely with previous findings which demonstrated that nanotubes with a diameter in the 80 nm range elicit higher mineralization levels than HC architectures.[224] A possible explanation is that the HC architectures favor a faster activation of RUNX2 and OCN, while the nanotubular surfaces may activate alternative signaling pathways that lead to mineralization at a later stage, ultimately achieving the same final levels of calcium deposition via different cellular mechanisms. Notably, the expression levels of RUNX2 and OCN does not necessarily determine the absolute amount of mineralization at the end of the process. Cells on nanotubular segments of the gradient (i.e. A1-A2) may in fact eventually produce enough bone matrix to achieve the same amount of mineralization as those on HC architectures (A6-A7), despite their lower early

expression levels. Lastly, it can also be conceived that the influence of the substrates may diminish with time, leading to similar outcomes in terms of mineral deposition in the longer term.

These findings point to a nuanced interplay between surface topography and cellular differentiation. The HC surface, particularly A7, exhibits significant early differentiation, making it an intriguing candidate for further study. This is especially relevant when compared to the A1 surface, which may combine the metabolic advantages of the HC surfaces with the mineralization properties comparable to nanotubular surfaces in this and previous studies[224] with larger diameters in the 80 nm range. However, it is crucial to contextualize these differentiation results within the framework that all tested surfaces are beneficial for cell growth and differentiation. Differences in results indicate relative increases in differentiation and mineralization, rather than any negative impact on cellular function. These observations highlight the potential of the gradients to quickly compare multiple surfaces, extract optimal parameters, and utilize these surfaces efficiently in subsequent experiments despite all having a propensity of positive osteoblastic response.

2.4.6 Migration

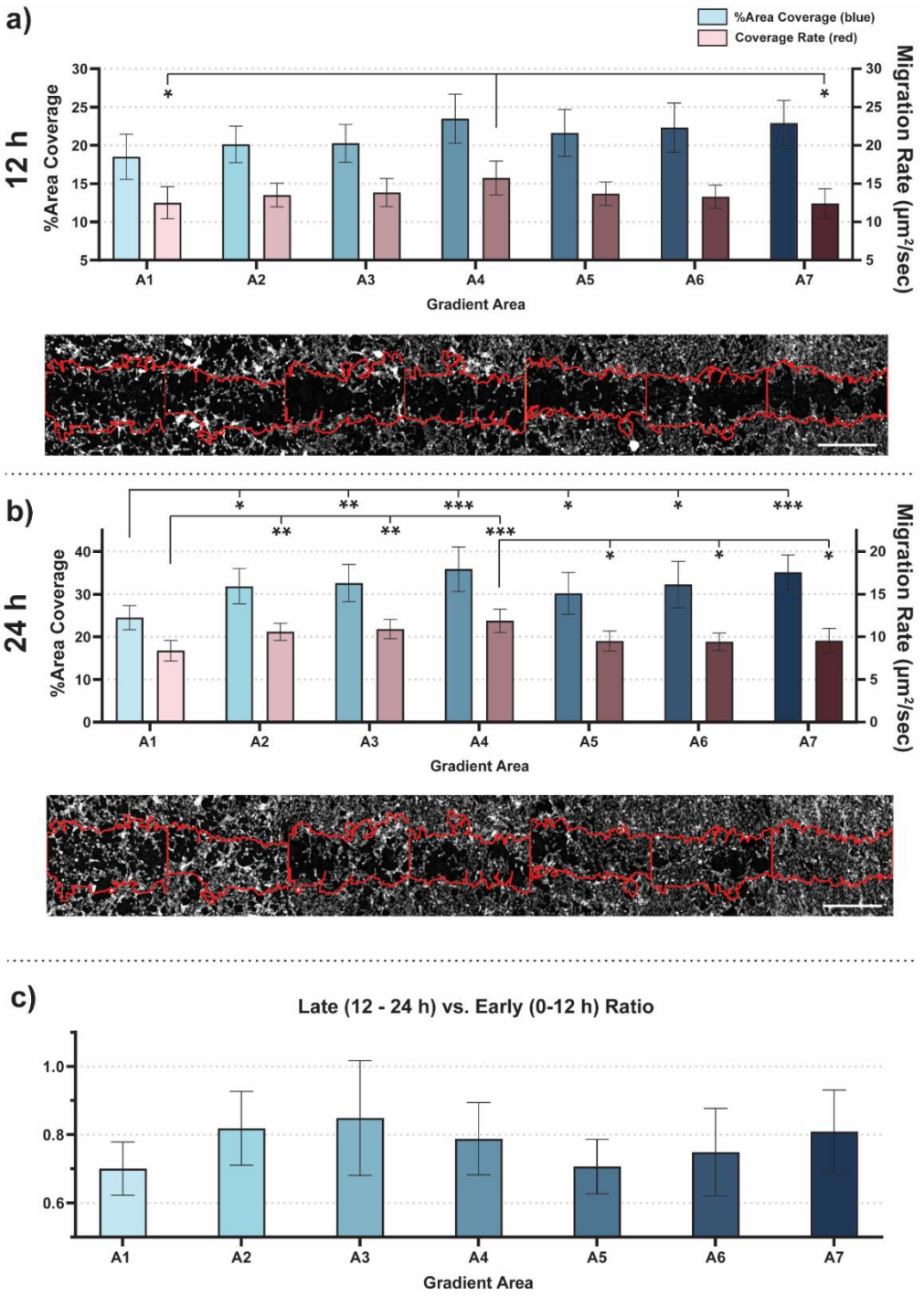

Figure 3.7. Scratch assay percent area coverage and migration speeds. Scratch assay percent area coverage and migration rate (top) and IF images (bottom) at a) 12 h and b) 24 h, relative to the initial scratch (0 hours), represented via the red lines. c) Ratio of "Late" (12-24 hrs) and "Early" (0-12 hrs) migration speeds across all areas.

The analysis of cellular migration via a live-cell scratch assay (Figure 3.7) offers insights into the migratory behavior of MG63 cells across different nanostructures. At the 12 hr mark, there were minimal differences in migration observed across the A1-A7 locations (Figure 3.7a). The only significant differences were noted in the elevated scratch closures on surfaces A4 and A7 compared to A1. This uniformity suggests that the initial cellular migration is not significantly influenced by surface topography, leading to comparable migration rates within the first 12 h. However, differences begin to emerge at the 24 h mark (Figure 3.7b), with most areas exhibiting substantial closure. In particular, cells at locations A2-A7 all showed elevated closure compared to A1, highlighting the impact of bifurcation and lacunarity on cellular migration. The lack of significant differences between the A2-A7 regions indicates that these surface features provide similar topographical cues that affect cellular movement. The migration speeds at 24 hours also revealed that cells at A2-A4 were characterized by increased velocities compared to A1. Cells on A4, in particular, showed the fastest migration rate. Interestingly, there were no significant differences in migration speeds between the 12 h and 24 h timepoints (Figure 3.7c). Despite all areas showing slower speeds at 24 h compared to 12 h, the overall migration rates did not differ significantly between these two timepoints. This consistency may result from a decrease in the initial rapid migration as cells start engaging in other processes such as proliferation and differentiation.

Taken together, the enhanced closure and faster migration rates observed on A2-A4 highlight the critical role of bifurcation, entropy and lacunarity in promoting efficient cellular migration. The significant differences at the 24 h mark, compared to the more uniform responses at 12 h, indicate that topographical features become increasingly important over time as cells interact more extensively with the surface. These findings ultimately demonstrate that the controlled

introduction of spatial irregularity and complexity can enhance cellular migration, which is crucial for wound healing and tissue regeneration processes.[12,31,240]

2.4.7 Optimized Surfaces

The stark contrasts observed between surfaces A1 and A7, with A7 eliciting the highest overall response, highlight the importance of further studies to tease out the mechanisms underlying early differentiation, proliferation, and other cellular processes.

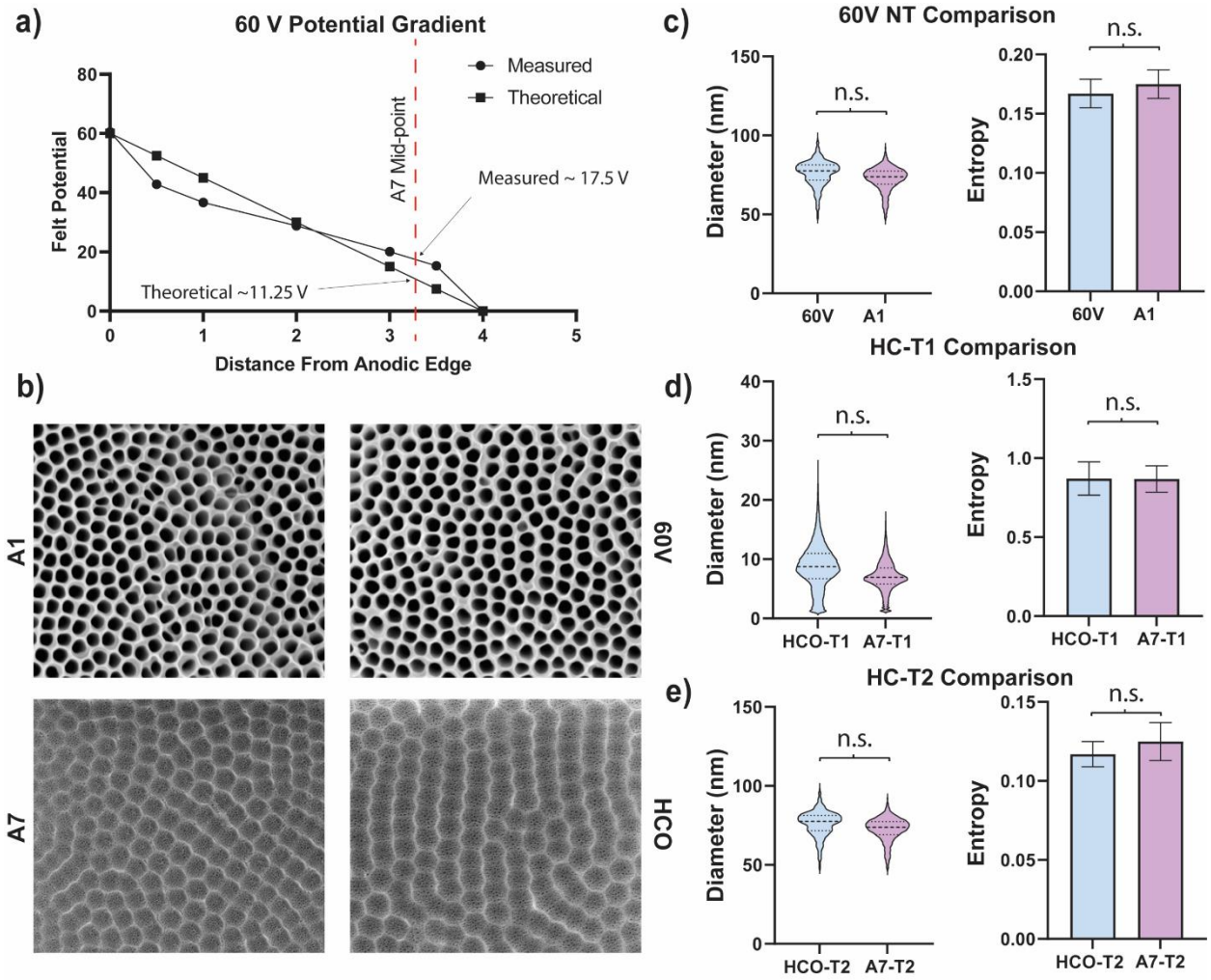

Figure 3.8. Optimized homogeneous surfaces. Potential gradient (a) both measured and theoretical were used in order to replicate the A7 surface created in the bipolar setup on a standard anodization setup with platinum and titanium actin as the two electrodes. Both surfaces were successfully created, shown visually in b) as the SEM images of the A1 and A7 areas on the gradient are compared to the optimized homogenous surfaces 60V and HCO, respectively. Key comparative

metrics of diameter and entropy are shown for a) single nanotubes and A1, b) T1 nanotubes of the optimized surface and T1 of A7 area, and c) T2 nanotubular domains of the optimized surface and T2 of A7 on the gradients.

One distinctive characteristic of the bipolar anodization approach used to fabricate the gradients is that it allows to extract key experimental parameters (i.e. voltage and time) to recreate the nanotopography of a specific location along the gradient as a single-sized nanotubular surface in individual samples with a conventional anodization setup. Following the assessment of the optimal and least effective cellular responses across the nanotubular gradient—specifically surfaces A7 and A1—parameters from the gradient were extracted to create homogenous surfaces for further testing and validation of the observed nanotopographical effects (Figure 3.8). Once successfully created, these surfaces can be used in further studies to determine whether the cellular responses seen in the gradient could be consistently replicated on homogenous surfaces, a critical step often overlooked in related literature.

Potential measurements across the gradient identified the region corresponding to surface A7, which spanned from 3.0 to 3.5 cm on the gradient. This region was associated with a measured voltage of 17.5 V and a theoretical voltage of 11.25 V (over a 30-minute exposure) in the bipolar anodization setup (Figure 3.8a). These parameters were successively applied to a standard two-electrode anodization setup, where titanium served as one electrode and platinum as the cathode. However, the resulting features of T1 were significantly larger than those observed on the gradient, requiring a reduction in voltage to 5 V for 5 minutes to achieve topographical features that closely matched those on the gradient (Figure 3.8b). This adjustment successfully produced a homogenous surface with comparable entropy and diameter, which were not significantly different from those on the gradient (Figures 8c-e). This contrasted with reproducing A1, where identical parameters were used in producing these features at the anodic edge, and no change was required. This may

be due to the potential's non-linear change at the anodic and cathodic edges (Figure 1c), where regions measured directly at each electrode converged with the theoretical values, while areas along the gradient (with the exception of the middle) had significant divergences.

This finding is particularly important because it challenges the common assumption/implication in the literature that parameters used in a gradient setup can be directly translated to create homogenous samples with identical topographical features for high-throughput analysis.[18,241] The need to reduce the voltage in the standard anodization setup likely arises from differences in the distribution of electric fields between the bipolar and two-electrode setups. In the bipolar anodization setup, the non-uniform electric field creates a gradient of nanotube sizes, while the two-electrode setup generates a more uniform field, resulting in larger nanotubes under the same voltage.[17,18] In the bipolar anodization setup, the voltage at the interface between the electrolyte and the titanium, rather than the total applied voltage, controls the anodization process.[17] Because this interface voltage is lower than the total voltage, the resulting titanium nanotubes are smaller in diameter and length compared to those formed in a conventional anodization process using the same voltage.[17] These factors translate into careful fine-tuning of voltage and time when transitioning from a bipolar gradient setup to a standard two-electrode configuration to achieve consistent nanotopographical features.[16–18,227,242]

2.5 Conclusion

In conclusion, our study demonstrates the significant impact of nanotopographical complexity on the behavior of MG63 osteoblastic cells. This study systematically explored the impact of nanotopographical complexity on MG63 osteoblastic cell behavior by examining a gradient of titanium nanotubular surfaces anodized at 60 V. Utilizing spatial statistics such as lacunarity,

entropy, fractal dimension and hexagonal packing metrics provided a quantitative description of the structural complexity and packing efficiency.

Our findings highlighted the influence of surface nanotopography on cellular morphology, with the A7 surface promoting greater cell area, elongation, and irregularity compared to nanotubular arrays such as those in A1. The wider mitochondrial distribution within cells on A7, coupled with elevated Ki67 expression indicate enhanced metabolic activity and proliferation. In terms of differentiation, surfaces A6 and A7 exhibited significantly elevated RUNX2 and OCN expression, indicating that higher entropy and lacunarity favor early osteoblastic differentiation. The mineralization patterns observed further supported the role of topographical features in promoting long-term osteogenic maturation. Migration analysis revealed that surfaces intermediate surfaces such as A4 facilitated faster cellular migration, emphasizing the role of bifurcation and lacunarity in cell movement. Taken together, positive cellular responses generally scaled with entropy and lacunarity, underscoring the importance of surface order, which may be as critical as, if not more so than, nanotube diameter in influencing cell behavior. Our results underscore the potential for high-throughput screening as the gradient allows for efficient identification of cellular response without the extensive use of single sized surfaces. Additionally, gradient-derived parameters can be translated into homogeneous, single-featured surfaces, although adjustments in voltage are necessary when transitioning to a two-electrode setup.

2.6 Acknowledgements

The authors acknowledge financial support from the Natural Sciences and Engineering Research Council of Canada (NSERC) through the Discovery Grant program, Canada Foundation for Innovation (CFI) and the Ontario Ministry of Research and Innovation (MRI) through the Leaders of Opportunity (LOF) fund. R.B. expresses appreciation to NSERC for funding provided

by the Canada Graduate Scholarship. The authors also extend their gratitude to the Cell Biology and Image Acquisition (CBIA) Core Facility for providing access to fluorescence microscopes and to Chloë Van Oostende-Triplet and Liyuan Wang for their technical support and guidance in microscopy.

2.7 Supplementary Information

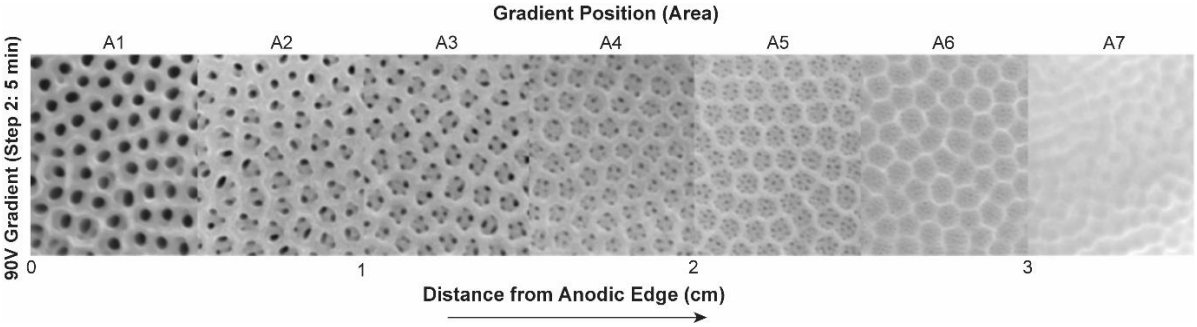

Figure 3.S1. Progression of the 90V gradient, prematurely halted after 5 minutes in the second anodization step. The shortened anodization time results in a honeycomb pattern with noticeably thicker walls and reduced T2 domains and lower diameter tubules.

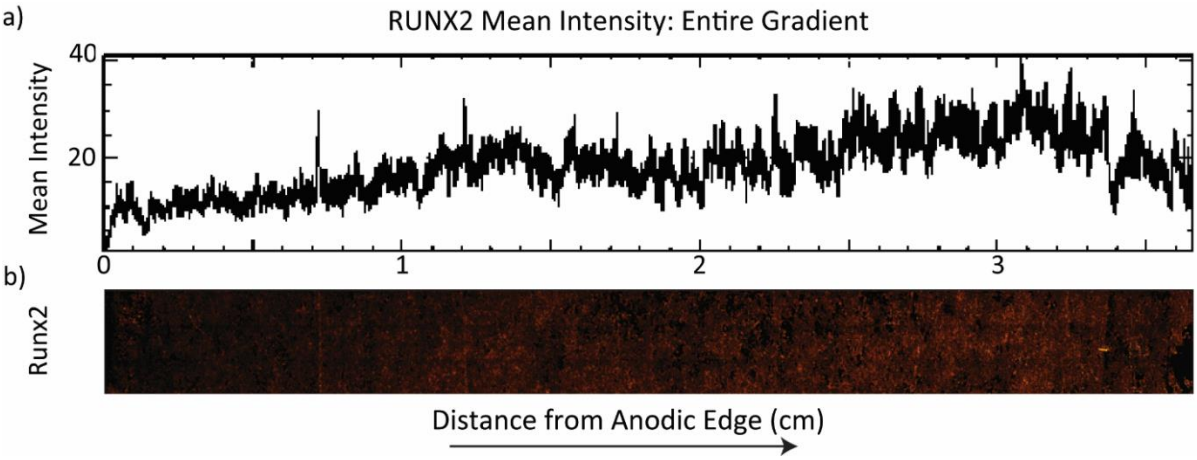

Figure 3.S2. Gradient of mean intensity of RUNX2 expression across the entire gradient surface at day 7. A gradual increase in mean intensity is observed, as shown in a) the slope of mean intensity across the surface (not normalized to nuclei number). Stitched b) IF image of the whole surface, visually demonstrating increasing intensity trend, with lower intensity at A1) and higher intensity at the more complex (A7) end of the gradient.

2.7.1 Spatial Metrics Background

Two-Dimensional Sample Entropy (SampEn2D)

SampEn2D quantifies the irregularity or complexity of pixel patterns in an image. It measures the likelihood that $m \times m$ patterns that are similar will remain similar when extended to $(m+1) \times (m+1)$ patterns.[230,231] The method involves calculating distances between all possible $m \times m$ windows of pixel values in an image and applying a similarity threshold r. Two patterns are considered similar if the maximum absolute difference between corresponding pixel values is less than r. The SampEn2D value is the negative logarithm of the ratio of the number of matches for (m+1) length patterns to the number of matches for m-length patterns (see Equations 3.S1).[230,231] This measure is unitless because it is based on the logarithmic ratio of pattern counts.

Fractal Dimension

The Fractal Dimension (D) provides a measure of structural complexity, describing how detail in an image changes with scale. The MultiFrac plugin employs the Box-Counting Method, where an image is divided into non-overlapping boxes of size ε, and the number of boxes $N(\varepsilon)$ containing part of the structure is counted. By varying ε and plotting $\log(N(\varepsilon))$ against $\log(1/\varepsilon)$, the slope of the resulting linear region gives the fractal dimension (see Equation 3.S2).[229] This unitless measure captures how well the structure fills space, independent of the scale.

Lacunarity

Lacunarity (Λ) measures heterogeneity in the texture and variability of gaps in spatial structures. Using the Gliding Box Algorithm, the image is covered with sliding boxes of size r, and the mass (number of pixels) within each box is determined. This method systematically slides a box of defined size across the image to evaluate structural properties, texture, and gaps within the spatial

distribution of features.[229] A box of size r is defined, where r represents the side length of the square box. The box size is chosen based on the scale of interest, and analyses are often repeated across multiple box sizes to capture multi-scale properties. The box is slid across the entire image in a systematic manner. At each position, the number of pixels (mass) inside the box that belong to the structure of interest is counted. This mass value m is recorded for each box position. For a given box size r, the probability mass distribution $P(m, r)$ is calculated. This distribution represents the frequency of occurrence of boxes containing a given mass m.[229]

Lacunarity is computed as the ratio of the second moment of the probability mass distribution to the square of its first moment. The Gliding Box Method is a powerful tool for characterizing spatial patterns in a wide range of fields, including materials science, biology, and environmental analysis. Its ability to assess texture, heterogeneity, and scaling properties makes it essential for advanced spatial statistical analyses.[229] By providing a flexible framework, the method supports the calculation of robust metrics that describe the complexity and variability of structures. Lacunarity is defined as the ratio of the second moment of this distribution to the square of the first moment (see Equations 3.S3-5). Higher lacunarity indicates greater variability or heterogeneity in the structure, while lower values suggest uniformity.[229]

General Equations:

More information on supporting equations and concepts including explanations and descriptions of SampEn2D, Fractal Dimension and Lacunarity, please refer to the foundational papers (references 229-231) written by the groups that developed and/or derived these ImageJ plugins and analyses.[229-231]

Two-Dimensional Sample Entropy (SampEn2D)[230,231]

$$\text{SampEn2D}(m,r) = -\ln\left(\frac{U_{m+1}(r)}{U_m(r)}\right) \quad (3.S1)$$

Where U is the normalized number of similar patterns of size *m* x *m* within the image, where similarity is determined based on a tolerance *r*, *m* is size of the pixel window and *r* is the tolerance for considering two patterns as similar.

Fractal Dimension (Box-Counting Method)[229]

$$D = \lim_{\epsilon \to 0} \frac{\log(N(\epsilon))}{\log(\epsilon)} \quad (3.S2)$$

Where, ϵ is the box size and N(ϵ) is the number of boxes of size ϵ containing part of the structure.

Lacunarity[229]

$$\Lambda(r) = \frac{M^{(2)}(r)}{(M^{(1)}(r))^2} \quad (3.S3)$$

$$M^{(1)}(r) = \sum_{m=1}^{N} m\, P(m,r) \quad (3.S4)$$

$$M^{(2)}(r) = \sum_{m=1}^{N} m^2\, P(m,r) \quad (3.S5)$$

Where *P(m,r)* = "Probability of a box of scale *r* having mass or number of pixels *m*, and where $M^{(1)}$ and $M^{(2)}$.

CHAPTER 4: Validating Nanotopographical Effects on Osteoblastic Response: Cellular Analysis, Mechanistic Insights and Raman Spectroscopy of MG63 Cells on Optimized Titanium Nanotubular Surfaces of Varying Disorder

3.1 Introduction

Growing recognition of the limitations in traditional *in vitro* models has highlighted the need for more accurate predictions of complex *in vivo* interactions.[113,114,116,224] This shift in focus has driven surface engineering research toward understanding the fundamental mechanisms of surface-cell interactions, leading to the development of precise and tunable substrates that enhance reproducibility.[58,70,135] Although beam-based techniques have shown success in processing materials like silicon and polymers, this study highlights the superior results achieved through anodization when applied to titanium.[195–199] This approach leverages the biocompatibility of titanium surfaces, while also achieving a high degree of precision in modifying surface properties.[124,134,191,205,220,227] Titanium nanotubes, hollow cylindrical structures with diameters ranging from tens to hundreds of nanometers, have garnered significant attention as biocompatible materials for bone implants.[1,9,10,63] These structures are favored in manufacturing due to their reliable and scalable synthesis methods, which produce arrays of nanotubes of varying degrees of order over large surfaces.[124,134,135] Moreover, the diameter of the tube openings can be finely tuned based on anodization times and the composition of the electrolyte solution.[15] Previous studies, both in the literature and within our own lab, have shown that finely tuning spatial dynamics of titanium nanotubes can significantly enhance osseointegration[135,214,224] by promoting mineralization and improving the differentiation and proliferation of osteoblastic cells, which is crucial for the longevity and success of orthopedic implants[11,72,129,195,218,243]. This study builds upon these advancements by utilizing the MG63 cell line, a well-established model for exploring the nuanced

responses of osteoblast-like cells to optimized homogeneous nanotopographical features extracted from previous work on nanotopographical gradients.

Immortalized cell lines such as SAOS-2, MC3T3, or MG63, used in this study, are invaluable tools for researching osteogenic cell-surface responses.[80,136,138,156,226,244–248] MG63 cells are ideal for studying osteoblast-like responses to nanotopographical features due to their ability to synthesize key differentiation markers like osteocalcin and their integrin expression, closely mimicking human osteoblasts.[28,30,31,223,245,249–251] With a high proliferation rate and sensitivity to nanotopographical cues, MG63 cells reliably model early osteoblastic differentiation in response to surface variation.[28,252–255] Central to these interactions is mechanotransduction, the process by which cells convert mechanical stimuli into biochemical signals.[256–259] Integrin-dependent signaling pathways, such as those involving focal adhesion kinase (FAK) and mitogen-activated protein kinase (MAPK), are crucial for regulating essential cellular functions like growth, migration, and differentiation [1,37,38]. The formation of focal adhesions (FAs) and complexes (FCs) that anchor cells to their extracellular matrix (ECM), effectively connect the actin cytoskeleton to the surface, placing tension across the cell and facilitate mechanotransduction.[1,44,47] Vinculin, a critical component of FAs, connects integrins to the actin cytoskeleton, thereby facilitating the transmission of mechanical signals into the cell.[1,14,43,199,257] The size and stability of these adhesions can modulate the activity of downstream signaling pathways, such as FAK and MAPK, which are instrumental in promoting osteogenesis.[8,38,39] These pathways ultimately influence the production of osteogenic markers, including osterix (OSX), osteocalcin (OCN), and osteopontin (OPN), which are vital for bone formation and remodeling.[1,37,38] OSX as well as alkaline phosphatase (ALP) are particularly important as an early-stage transcription factor driving osteoblast differentiation. RUNX2, another critical transcription factor, functions at both early and

early-to-mid stages of differentiation, directing the expression of genes essential for bone development.[1,33,38,40]

Recent research has also highlighted the roles of Yes-associated protein 1 (YAP1) and transcriptional coactivator with PDZ-binding motif (TAZ) in mechanotransduction.[43] These proteins respond to mechanical cues and regulate cell proliferation and differentiation through the Hippo signaling pathway. [43,44] The activation of YAP1/TAZ is influenced by cytoskeletal tension and actomyosin contractility, which are modulated by substrate topography. The interplay between YAP1/TAZ activation and cytoskeletal dynamics underscores the significance of these proteins in translating mechanical stimuli into cellular responses.[43,44] Vinculin and focal adhesions are pivotal in this process, as they directly influence cytoskeletal tension, which in turn regulates YAP1/TAZ activity.[14,43,127] The activation of YAP1, governed by mechanical cues, involves its translocation into the nucleus where it drives gene expression changes essential for cellular proliferation and differentiation.[43,44] This link between mechanical stimuli and YAP1 activation is particularly relevant in the context of nanotopography, where the physical features of the substrate can profoundly impact cell behavior. Recent studies have begun assessing the significant role YAP1 activation plays in osteoblastic response to titanium NT surfaces.[127,199,260–262]

Nanotopographical gradients, featuring continuous variations in surface topography, have garnered significant interest in biomaterials research due to their ability to provide valuable insights into the relationship between surface properties and cellular responses across a wide range of features on a single surface.[17,56–60] Compared to homogenous or single-feature surfaces, nanotopographical gradients offer a more comprehensive understanding of cellular behavior by spanning an array of diameters and other geometrical features within a single sample, reducing batch-to-batch variation.[62] These gradients also address inconsistencies in the literature regarding

the effects of nanotube diameter and other geometrical characteristics on osteoblast behavior.[18] The use of such gradients allows for efficient screening of various surface topographies, accelerating the development of tailored biomaterials that enhance cell-material interactions.[93] However, creating well-defined nanotopographical gradients on materials like titanium can be technically challenging, requiring precise control over surface properties and spatial variation, which has limited the number of studies utilizing this approach. The most relevant studies to this research have emerged only in recent years [17,18], as researchers often focus on homogenous or single-feature surfaces due to their simpler fabrication processes and lesson controlling spatial dynamics an order.[2,3,8] However, the critical secondary step of extracting and synthesizing optimal surface parameters from gradients for practical applications has largely been unexplored with an assumption that cells will behave in the same way. No studies have yet focused on extracting topography from a specific section of the titanium gradient and comparing cellular responses on the newly formed homogeneous surface.[17,18,241] This is a critical step in validating the use of gradients in practical workflow and high throughput screening, as it reduces the time required to test a wide variety of features on a single surface.[241]

This research focuses on two optimized surfaces—HCO and 60V-O—extracted from a hierarchical titanium nanotube gradient in a previous study from our lab (see Section 3.4.7). These surfaces represent distinct extremes in nanotopographical complexity and are used to explore their influence on MG63 osteoblastic cell behavior. The previous gradient study revealed that more complex surfaces within the gradient, particularly those with higher entropy and lacunarity, significantly enhanced the widest variety of cellular responses (proliferation, differentiation, migration etc.) compared to simpler, more ordered surfaces. The honeycomb gradients covered two extremes from “A1” (which 60V-O was modeled on) to “A7” surfaces (which HCO was

modeled on) —as a foundation for creating homogenous surfaces that replicate these effects. A1, with its lower nanotube density, uniform diameters, and lower entropy and lacunarity, offered a highly ordered, less complex topography, resulting in subdued cellular responses. Though still an effective osteoinductive surface, cells on A1 exhibited reduced morphological features (smaller areas and reduced elongation), lower proliferative qualities in centralized mitochondrial structures and reduced nuclear density as a proxy for growth, and suppressed expression of differentiative markers of RUNX2 and OCN by Day 7, in comparison with the A7 honeycomb surface. A7's higher entropy and lacunarity fostered larger cell areas, greater elongation, and increased morphological irregularity. The complex, heterogeneous nature of A7 provided a rich array of cues that stimulated dynamic cellular responses, including more widespread mitochondrial distribution, elevated metabolic activity and upregulated Ki67, RUNX2, and OCN total expressions, enhancing proliferation and driving robust differentiation. In this way, the HCO surface, is characterized by higher spatial metrics such as lacunarity, fractal dimension, and entropy, provides a more complex topography, while the 60V-O surface represents a simpler, single-tube structure. This study presented the whole process of developing a gradient, testing cellular response and extracting and creating the optimized HCO and 60V-O surfaces as a tool for high-throughput *in vitro* material screening, allowing for the efficient identification of optimal surface characteristics without extensive preliminary trials. This study aims to test the validation that cell response, determining whether or not these homogenous surfaces create similar cell responses as their gradient counterparts.

In addition to traditional means of studying these cellular dynamics, this study also aims to establish methods for probing cell-surface interaction between MG63 cells and titanium nanotubes via Raman spectroscopy and confocal imaging.[67,263–270] Raman confocal imaging offers a powerful

method for characterizing the chemical composition and molecular structure of cellular components in a non-destructive, label-free, and non-invasive manner, enabling detailed analysis of interactions between MG63 cells and the substrate.[271] This technique's high spatial resolution facilitates the visualization of fine details, allowing precise mapping of cell-surface interactions and the localization of specific biomolecules at the interface. Such detailed chemical information identifies specific molecular vibrations and chemical bonds, offering deep insights into the mechanisms underlying osseointegration. [67,264,266,268,272] Furthermore, Raman confocal microscopy is compatible with a wide range of substrate materials, promoting direct comparisons of cellular responses to different surfaces and aiding in the development of improved implant designs[265]. Although single-cell Raman spectroscopy has been employed on transparent surfaces, where it has been useful in identifying highly ordered lipid signals within the cell nucleus that provide insights into cellular proliferation and organization, its application on opaque titanium surfaces remains largely unexplored.[263,264,267,270,273] This is partly due to the challenges posed by the top-down microscope setup required for titanium surfaces, which can obscure cellular details and introduce artifacts, depending on the material, such as poor signal-to-noise ratios, photocatalysis or degassing.[179,274,275] Despite these challenges, establishing a protocol for single-cell Raman confocal microscopy on opaque titanium surfaces is crucial, as it could enable researchers to study cellular interactions on these clinically relevant substrates, which has been largely absent in the current literature.

Raman spectroscopy and confocal imaging will be employed to assess and compare the quality of mineral deposits on these surfaces, a critical aspect given that Alizarin assay results were identical across samples.[276–281] Raman spectroscopy's ability to distinguish between different mineral phases allows for a more nuanced understanding of mineral quality, particularly the

balance between amorphous calcium phosphate and crystalline hydroxyapatite, which is essential for long-term bone stability. [282] The integration of confocal Raman spectroscopy and analysis techniques such as PCA, manage the complexity of the high-dimensional spectral data generated, preserving essential variance information while elucidating key biochemical shifts associated with early osteogenic differentiation.[67,264,266,268,272] The primary goal is to show the feasibility of this technique on opaque surfaces and establish a protocol that identifies potential areas of interest, including spectral features that could reveal differences in spatial distribution during early differentiation for future studies for application across multiple studies within our lab.

This study seeks to validate findings observed on the corresponding surfaces within the gradient, specifically A1 and A7, by comparing these with the results obtained on the optimized 60V-O and HCO surfaces, respectively. This comparison will provide a deeper understanding of how well the effects seen in the gradient translate to homogeneous surfaces, further informing surface optimization strategies. Additionally, by integrating confocal Raman spectroscopy, traditional methods, we gain a more accurate, non-invasive understanding of cellular behaviors and transformations. By using conventional tools and establishing new label-free methods of probing cell-surface interactions, information on differentiation and proliferative markers produced by MG63 cells in response to the unique topography of the HCO and 60V-O surfaces will serve as valuable reference tools for future studies. [267,283,284]

3.2 EXPERIMENTAL

3.2.1 Anodization of Titanium

For the optimized surfaces, titanium foil (0.127 mm thickness, 99.9+% purity, Thermo Fisher, USA) was cut into strips measuring 2.5 x 1 cm. These strips were then immersed in 99.8% anhydrous toluene (Sigma Aldrich, USA) and subjected to sonication for 15 minutes to remove

surface contaminants. After sonication, the strips were thoroughly rinsed with deionized water and allowed to air-dry. The prepared samples were then mounted in a 3D-printed fixture made of UV-hardened resin (Figure 3.1), where they were aligned parallel to a 2.5 cm x 2.5 cm platinum electrode (99.9% purity, Alfa Aesar, USA) using alligator clips, ensuring stability and levelness throughout the process. Anodization was carried out in a 50 ml Pyrex beaker filled with anhydrous ethylene glycol ($C_2H_6O_2$, Sigma Aldrich) mixed with 0.3 wt% crystalline ammonium fluoride (NH_4F, Sigma Aldrich, USA) and 2 wt% deionized water. The anodization process was performed using a Bio-Rad PowerPac power supply (Bio-Rad, USA) under constant DC voltage. Voltages below 20V were applied using a B&K Precision model 9111 power supply (B&K Precision Corporation, USA). After the first anodization step, the anodic oxide layer was removed from both sides using adhesive tape, and the samples were re-mounted for a second anodization. Upon completion, the surfaces were rinsed with deionized water and air-dried. By adjusting the parameters of each anodization step (Table 4.1), three distinct nanotubular structures were generated for this study.

Table 4.1. Voltage and time parameters for HCO and 60V-O.

		60V-O	HCO
Step 1	Voltage (V)	60	60
	Time (min)	30	30
Step 2	Voltage (V)	60	5
	Time (min)	10	5

3.2.2 SEM characterization and analysis of nanotubular surfaces

A Surface morphology of the anodized substrates was investigated using a Zeiss Gemini SEM 500 Scanning Electron Microscope at a magnification of 50,000X. The captured SEM images were

processed and analyzed with ImageJ software.[162] The images of the nanotube surfaces were subjected to a custom ImageJ pipeline, where they were manually thresholded, segmented, and analyzed using the 'Particle Analysis' tool. Nanotube diameters were calculated using this tool, with outliers removed by applying a 0.1% Q value. Entropy was quantified to measure the randomness and complexity of pixel intensity values within the images. This was done using 2D Sample Entropy (2DSampEn), which evaluates the probability that sequences of data points that are similar for m points remain similar at the next point within a tolerance r.[230,231] The analysis was performed using the SampEn2D plugin in ImageJ, with m=2 and r set as a fraction (0.2) of the standard deviation of pixel values.[232,285] The hexagonal packing efficiency of the nanotubes was assessed using the N1:N6 ratio, defined as the ratio of the first nearest neighbor distance (NND) to the average of the six nearest neighbor distances.[224] This metric quantitatively measures how closely the nanotube arrangements approximate ideal hexagonal packing. Fractal dimension was calculated to quantify the complexity of the nanotubular patterns. The box-counting method was employed, where the image is covered with a grid of boxes of varying sizes, and the number of boxes containing part of the structure is counted. The fractal dimension was derived from the slope of the log-log plot of the number of boxes versus the box size and was conducted using the MultiFrac[229] plugin in ImageJ.[234] Lacunarity was calculated to measure the texture and spatial distribution of gaps within the nanotubular structures. This was done using the gliding box method, which involves covering the image with a series of boxes of varying sizes and calculating the variance in the number of occupied boxes across scales. The analysis was performed using the MultiFrac[229] plugin in ImageJ, covering a range of box sizes to capture the multi-scale heterogeneity. For an in-depth explanation, please see Section 2.7.1. in the Supplementary Information of Chapter 3. To ensure consistency in the analysis, images were processed in ImageJ

and converted into binary format, with nanotubes represented as white pixels on a black background. Outlier removal was conducted using the ROUT method with a Q value of 0.1% to maintain data integrity while eliminating extreme values.

3.2.3 Human MG63 osteoblastic cell cultures

Human MG63 osteoblastic cells (CRL-1427, ATCC, USA) were thawed and passaged in DMEM (10567-014, Gibco, USA) containing 5 mM glucose, supplemented with 10% fetal bovine serum (FBS), 10mM β-glycerophosphate and 50 µg/mL ascorbic acid. The cells were maintained at 37 °C in a humidified atmosphere of 5% CO2. After gently aspirating the complete culture medium (CCM), the cells were washed three times with sterile 1x PBS. To detach the cells, 3 mL of 1x TrypLE were added to the flask, and the cells were incubated for 3 minutes to ensure complete detachment. The cell suspension was then diluted by adding 7 mL of culture medium and subsequently centrifuged at 150 rpm for 8 minutes. After centrifugation, the cells were resuspended in 10 mL of CCM. A 2 mL aliquot of the cell suspension was then transferred into 8 mL of fresh CCM in a filtered 75 cm² flask, which was returned to the incubator for continued culture.

3.2.4 Cell Seeding and Fixation

Titanium nanotubular substrates (both single diameter and HC gradients), each measuring 1 x 1 cm (IF and Raman experiments) or 0.5 x 0.5 cm (assays), were sterilized in 70% ethanol and subsequently rinsed with sterile 1x phosphate-buffered saline (PBS). Cells for all IF and Raman experiments were seeded onto the substrates at a density of 5,000 cells/cm² in 60 mm TC-treated petri dishes. Surfaces were then removed and placed in 24 well plates and the cells were cultured on the nanotubular substrates for durations specific to each experiment, ranging from 1 to 21 days, to investigate proliferation, morphology, mitochondrial distribution, differentiation and bone

mineral deposition and composition. At the conclusion of the experiments, cells were fixed by adding 500 µL of fresh 4% paraformaldehyde (PFA, Sigma-Aldrich) to each well for 10 minutes at room temperature. The wells were then washed three times with PBS to remove any residual PFA, filled with 500 µL of PBS, and stored at 4 °C. Day 21 mineral samples underwent a separate fixation with methanol. After aspirating the culture medium, cells were rinsed once with cold 1x phosphate-buffered saline (PBS) and then with distilled water. The samples were then immersed in pre-cooled methanol (-20°C) for 10 minutes at room temperature. Following fixation, the methanol was removed, and the samples were allowed to air dry completely. The dried, fixed samples were stored at room temperature until further analysis.

3.2.5 Immunofluorescence Staining

MG63 cells were permeabilized using a 0.25% solution of Triton X-100 (TX-100, Sigma-Aldrich) for a duration of 10 minutes at room temperature (RT). Following permeabilization, samples were blocked with 5% donkey serum (Sigma, USA) at RT for an hour. For both Days 1, 3 and 5, the nuclei and Actin were labeled with DAPI and AlexaFluor 488 Phalloidin (1:400) from Thermo Fisher, USA. Vinculin, active YAP1 and Osterix (OSX) were stained with primary anti-hVin1 mouse mAb (Sigma-Aldrich) at a ratio of 1:500, YAP1 monoclonal antibody (Proteintech, USA) at a ratio of 1:400 and Anti-OSX mAb (SP7 Monoclonal Antibody (2G6)) (Thermo Fisher, USA) at a 1:100 dilution, respectively. These primary stains were then followed by secondary staining using AlexaFluor 594 Donkey-anti-mouse IgG (Thermo Fisher) at a 1:500 dilution. Cell proliferation was assessed by staining for anti-Ki-67 polyclonal rabbit antibody (Millipore Sigma, USA) at a 1:250 dilution, while RUNX2 polyclonal rAb (Thermo Fisher, USA) at a 1:100 dilution was used as a second differentiation marker and YAP1 was stained using phospho-YAP1 (ser127) (Thermo Fisher, USA) at a dilution of 1:100. RUNX2, phosphor-YAP1 and Ki-67 primary stains

were followed by secondary labeling with AlexaFluor 647 Donkey-anti-rabbit IgG (Thermo Fisher). The primary antibody incubation was conducted overnight at a temperature of 4 °C, whereas the blocking and secondary antibody incubations were each carried out for 1 hour at RT. Post-incubation, the samples were thoroughly washed and then imaged in PBS in 60mm.

3.2.6 Immunofluorescence Imaging and Analysis

The multi-channel images used for the quantification of nuclei number and the analysis of cytoskeletal morphology were obtained by using a ThermoFisher EVOS FL Auto 2 (inverted) widefield microscope (ThermoFisher, USA). Images for all IF experiments were captured using a 20X air objective (20x, 0.40 NA, Air, PL FL LWD PH. The imaging system utilizes LED light sources with specific filters for different wavelengths: Blue (Ex 357/44 nm, Em 447/60 nm), Green (Ex 470/22 nm, Em 510/42 nm), Red (Ex 585/29 nm, Em 624/40 nm), and Far Red (Ex 628/40 nm, Em 692/40 nm). Detection is performed using a monochrome camera. For each Day 1 sample, 3 stitched images were analyzed as technical replicates, each consisting of 9 images stitched together (total 27 images). For day 3 and 5 samples 6 images per sample, taken a random locations across each sample. The number of DAPI-stained nuclei and actin morphology on each surface was quantified using custom ImageJ[162] pipelines. Both nuclear and cellular morphology analysis was carried out by stitching, segmenting and processing image in a custom pipeline calculated via particle analysis in ImageJ.

DAPI images were segmented via custom ImageJ pipeline and used in generating regions of interest (ROIs) for measuring nuclear intensities and total expression for Ki67, Active YAP1, OSX and RUNX2. Actin images were also segmented in ImageJ and used in generating regions of interest (ROIs) for measuring nuclear intensities and total expression YAP1 and cytoplasmic OSX. Total protein expression is defined as the integrated density of the ROI. For Ki67 analysis a

minimum of 15 samples per condition were analyzed, encompassing three biological replicates from each of nine distinct experimental sets, discarding one sample to use as a negative control. The active YAP1/YAP1 ratio was calculated by dividing the mean intensities of active YAP1 ROIs by the mean intensities of the YAP1 ROIs. In a similar way, the OSX NucBod Ratio was calculated by dividing the mean intensity of nuclear bound OSX by the OSX mean intensity present in the cytoplasm. Vinculin images were subject to a background subtraction and auto-thresholding via a custom ImageJ pipeline and resulting segmented images were analyzed via the "Particle Analysis" tool in ImageJ. Focal complexes were defined as having a length along the major axis being less than 2 µm and focal adhesions having a major axis length greater than 2 µm, but less than 10 µm.[47,286,287] All Day 1 IF experiments consisted of 14 samples per condition were analyzed, across three separate experiments, with 5 samples being present in each experiment, and 1 damaged sample being discarded. Day 3 and 5 IF experiments consisted of 20 samples per condition being analyzed, across three separate experiments.

3.2.7 Proliferation Assay

The PrestoBlue Cell Viability Assay (ThermoFisher, USA) was employed to assess cells viability in response to their metabolic activity. Cells were first seeded in a 48-well plate at a density of 5000 cells/cm^2 and cultured at 37 °C. PrestoBlue measurements were taken at 1-, 3- and 5-day intervals. The PrestoBlue reagent was diluted 1:10 in CCM as a working solution. The culture medium was removed from the wells and 250 uL of the prepared PrestoBlue working solution were added to each well. The plate was incubated at 37 °C with 5% CO2 for a duration ranging for 1 h. Following the incubation period, the plate was gently swirled to ensure even distribution of the reagent and cells. Two 100 uL aliquots of solution were transferred to a 96-well plate as technical replicates, while fresh CCM was pipetted back in to the 48-well plate and placed

back into the incubator. Fluorescence signal was measured with the Synergy H1 plate reader (BioTek, USA) with excitation and emission wavelengths set at 560 nm and 590 nm, respectively. Data analysis was carried out by subtracting intensity readings of control wells containing only media and the 1:10 PrestoBlue mixture and comparing the relative fluorescence units between anodized and control groups to determine the effect of various treatments on cell viability/metabolism. This assay was completed in triplicate with 10 wells per condition, per plate for NT experiments (30 samples in total).

3.2.8 ALP Assay Protocol

The activity of alkaline phosphatase (ALP) was evaluated at two different time points, namely 3 and 5 days post seeding, by employing the Pierce PNPP Substrate Kit (Thermo Scientific, USA). Cells were first seeded in a 48-well plate at a density of 5000 cells/cm^2 and cultured at 37 °C. Following each predetermined incubation period, samples were subjected to lysis and then treated with a solution made from *p*-nitrophenyl phosphate, disodium salt (PNPP) tablets and 1M diethanolamine, as per the guidelines provided by the manufacturer. The reaction was allowed to proceed for 1 h before it was terminated by adding NaOH. Subsequently, ALP activity was quantified by measuring the absorbance at 405 nm using the Synergy H1 plate reader (BioTek, USA). For the purpose of maintaining consistency across multiple time points, all ALP measurements were juxtaposed with a standard curve. All experiments were done in triplicate with a total of 30 samples, with 10 wells for each experimental condition across 3 independent experiments for the preconditioning and NT experiments.

3.2.9 Alizarin Red Staining and Assay

To assess mineralization occurring on the substrates, an Alizarin Red Staining (ARS) (Sigma, USA) protocol was employed. Cells were first seeded in a 48-well plate at a density of 5000

cells/cm^2 and cultured at 37 °C and grown for 21 Days. Initially, the culture medium was carefully discarded from each well, followed by a gentle triple washing step in 1xPBS. Cells were fixed in 4% PFA at RT for approximately 15 min. Following the fixation, the PFA was removed, and the cells were subjected to three thorough washing steps in deionized water. After ensuring the complete removal of deionized water, each well was treated with 1 mL of 40 mM ARS solution. This step involved a RT incubation period of 25 min, during which the plates were subjected to gentle shaking to ensure optimal interaction between the cells and the dye. Post-incubation, the ARS solution was removed, and the cells were washed five times with deionized water to eliminate the unbound dye. As a final step, the plates were tilted for about 2 minutes to facilitate the removal of any residual water, thereby preparing the samples for subsequent procedures and analyses.

After imaging, 200 µL of 10% acetic acid was first added to each well of a 48-well plate and incubation was done at RT for 30 min with shaking. Cells were successively collected using a cell scraper and transferred to a 1.5-mL microcentrifuge tube containing the 10% acetic acid. The samples were then subjected to vortexing for 30 seconds and heated at 85 °C for 10 min. To avoid evaporation, the tubes were sealed with parafilm. After the heating step, the tubes were placed on ice for a 5-min incubation period until fully cooled. Subsequently, the mixture was centrifuged at 12,000 g for 15 minutes. Post centrifugation, the supernatant was carefully transferred to a new tube. To this, 30 µL of 10% ammonium hydroxide was added to maintain a pH between 4.1 and 4.5. 100 µL of the samples were aliquoted into a 96-well plate and the absorbance was read at 405 nm using the Synergy H1 plate reader (BioTek, USA). Measurements for the assay were conducted on a total of 30 samples, which included nine wells from each of the three distinct experimental sets.

3.2.10 Confocal Raman Spectroscopy and Analysis

All Raman spectra and images were acquired using the alpha 300R confocal Raman Microscope from Witec (Witec, Germany). The imaging system was equipped with a 532 nm laser operating at 40 mW and a 600/mm grating, utilizing a 50 µm diameter optical fiber (pinhole). For spectral acquisition, a variety of Zeiss microscope objectives were employed, including the 50x EC Epiplan air objectives and the 63x W Plan-Apochromat water immersion lenses. Prior to data collection, the Raman microscope system was calibrated using the silicon peak at 520 cm^{-1}. The system was optimized by adjusting the two knobs located on the fiber coupling unit near the optical input of the microscope, maximizing the silicon peak intensity. Day 1 and Day 3 single-cell Raman confocal images were taken in PBS using the 63x water immersion lens with a 532 nm laser at 22 mW, an integration time of 0.45 seconds and a 600 grating. For Day 21 mineral samples, a 633 nm laser with a 1200/mm grating and the 50x objective were used, operating at 32.7 mW.

For the analysis of mineralized MG63 cell samples on Day 21, cells fixed on 60V-O and HCO nanotube surfaces were rehydrated in deionized water, scraped, smeared and dried onto CaF_2 substrates for Raman spectroscopy. Spectra were acquired from the bulk cell layer using a Raman confocal microscope. The spectral regions of interest included the phosphate peak (960 cm^{-1}), the amorphous phase peak (940 cm^{-1}), and the Amide I peak. Data analysis was conducted using Origin Pro (OriginLab, USA). The spectral analysis involved the use of the quick peaks automated peak analyzer, which provided measurements for peak position, maximum intensity, full width at half maximum (FWHM), and integrated area. A straight line baseline was applied during the peak analysis to ensure consistency across measurements. To quantify the relative content of these molecular components, the $\nu_1(PO_4^{3-})$/Amide I and amorphous/$\nu_1(PO_4^{3-})$ ratios were calculated by

dividing the integrated areas of the corresponding peaks, while the $\nu_1(CO_3^{2-})/\nu_1(PO_4^{3-})$ ratio was calculated by dividing the peak intensities.

Raman confocal imaging was performed on single MG63 cells cultured on CaF_2 and HCO titanium nanotube surfaces at Day 1 and Day 3. Raman imaging and data analysis were conducted using WITec Project 4.1 Pro software. To ensure high-quality data, all images underwent spectral subtraction to remove the contributions from PBS and other background spectra. This was followed by Savitzky-Golay smoothing (parameters: 3,3,2,0), cosmic ray removal (CRR) (parameters: 4,4) and a background shape subtraction (parameters: 50,2). Spectral filters were subsequently applied to the reconstructed images to highlight relevant peaks, such as those associated with Amide I, CH wag, and lipids. Spectral averages of the samples were generated using the spectral average tool within Project 4.1 Pro, which provided a representative spectrum for each Raman map after applying the same preprocessing steps (Savitzky-Golay smoothing, cosmic ray removal and background subtraction). The processed images were then subjected to principal component analysis (PCA) using the integrated PCA tool within Project 4.1 Pro. The PCA analysis enabled the identification of principal components that corresponded to specific spectral features and were visually matched with filtered Raman maps. Due to elevated noise in early PCs, PCs were chosen based off clarity and spectral relevance. Selected PCs for Day CaF_2 and HCO were 8, 12 & 15 and 2, 6 and 10, respectively. Respective Eigenvectors displayed in Figure 4.8, displayed wavenumbers between 1000 and 3060 cm^{-1} and had large noise spikes removed.

3.2.11 Statistical Analysis

The Shapiro-Wilk test was used to evaluate the normal distribution of the data sets. For comparisons involving 2 sample conditions, if the data followed a normal distribution, a parametric

Student’s t-test was used to compare means between groups. For data sets that did not meet the normality assumption, the non-parametric Mann-Whitney U test was applied. Levene’s test was conducted to evaluate the equality of variances between groups. In cases where variances were unequal, Welch’s t-test was utilized as a robust alternative to the student’s t-test. Comparisons across timepoints involving more than two variables were analyzed using a parametric One-Way ANOVA, and any significant differences in means were identified using Tukey's Honest Significant Difference (HSD) post-hoc test. Data deviating from normal were confirmed by the nonparametric Kruskal-Wallis test, and subject to Dunn’s post hoc test. Error bars are displayed as the mean with 95% confidence interval, unless stated otherwise in figure description. A p-value less than 0.05 was considered indicative of statistical significance. The levels of significance were denoted as follows: “*” for $p<0.05$, “**” for $p<0.01$, and “***” for $p<0.001$.

3.3 Results & Discussion

The previous study systematically investigated the impact of a nanotopographical gradient on MG63 osteoblastic cell behavior, revealing critical insights into how varying surface complexities influence cellular responses. By utilizing a controlled 60 V anodization process, a gradient was created that spanned from the simplest, most ordered structures to highly complex and disordered surfaces. This gradient allowed for the detailed analysis of spatial metrics such as lacunarity, entropy, and fractal dimension, which provided a comprehensive understanding of how these factors correlate with cell morphology, proliferation, differentiation, and overall cellular activity. This analysis laid the groundwork for developing homogenous versions of these surfaces for this study, namely HCO (modeled from A7) and the single tube 60V-O (modeled from A1) surfaces to further elucidate these effects in controlled contexts.

3.3.1 Nanotubes Fabrication

After evaluating the cellular responses across the nanotubular gradient, focusing on the most and least effective surfaces—HCO and the 60V-O surface—parameters were extracted to create homogenous surfaces for further validation of the observed nanotopographical effects. Potential measurements along the gradient identified the optimal region corresponding to the HCO surface, spanning from 3.0 to 3.5 cm with a measured voltage of 17.5 V and a theoretical voltage of 11.25 V (over 30 minutes) in the bipolar anodization setup. These parameters were applied to a traditional two-electrode anodization system, using titanium and platinum as electrodes. However, the resulting features were significantly larger than those on the gradient, requiring a voltage reduction to 5 V for 5 minutes to closely match the gradient's topographical features. This differed from reproducing A1, where identical parameters were successfully used at the anodic edge without requiring adjustments. This could be attributed to the non-linear potential changes at the anodic and cathodic edges (Figure 3.1c), where measurements taken directly at each electrode aligned with theoretical values, while regions along the gradient, except for the middle, showed significant deviations. This result contradicts the idea that gradient setup parameters can simply be transferred to create uniform samples with the same features.[18,241] It highlights the need for precise adjustments in voltage and timing when moving from a bipolar gradient to a two-electrode system to achieve consistentnanotopography.[17]

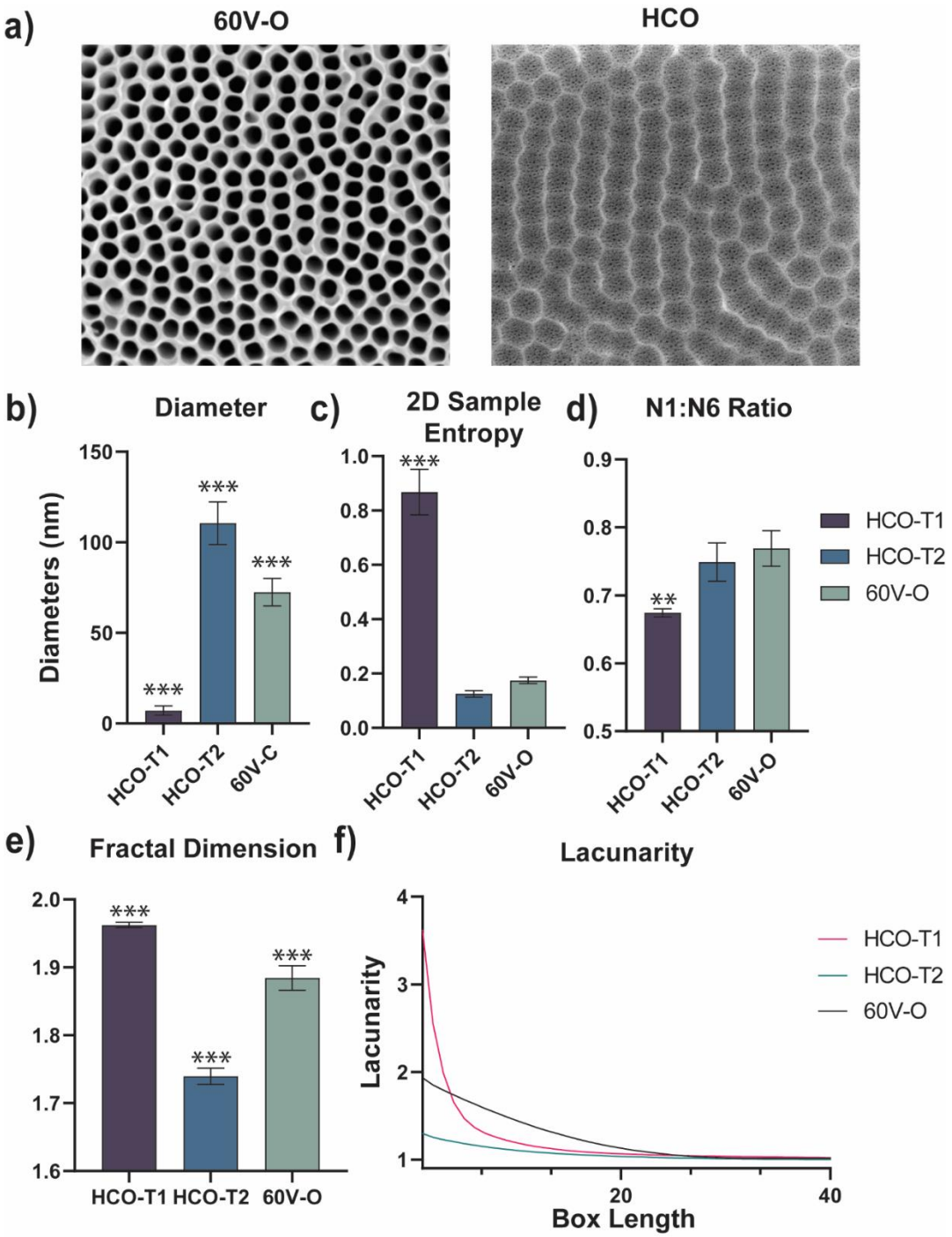

Figure 4.1. SEM images and spatial metrics of the 60V-O and HCO surfaces. Panel a) shows the SEM images of the 60V-O surface (left) and the HCO surface (right). Measured diameters of the nanotubes b) for HCO-T1, HCO-T2, and the 60V-O surface. Spatial statistics are shown in c) 2D Sample Entropy, d) N1:N6 ratio, e) fractal and f) Lacunarity values for each surface.

The analysis of the 60V-O and HCO surfaces, extracted from the nanotopographical gradient, reveals distinct structural and spatial differences, nearly identical to their corresponding locations on the gradient. The SEM images of the 60V-O and HCO surfaces (Figure 4.1a) illustrate the stark contrast between the single nanotube structure of the 60V-O surface and the unique two-tiered architecture of the HCO surface. The 60V-O surface, with an average nanotube diameter of 72 ± 8 nm, presents a more uniform topography compared to the HCO surface, which features two distinct tiers with significantly different diameters: 7 ± 2.5 nm (HCO-T1) and 109 ± 12 nm (HCO-T2), as shown in Figure 4.1b. This variation in diameter is indicative of the increased structural complexity found on the HCO surface and honeycomb surfaces in general, suggesting that these differences may play a role in modulating cell behavior as both tiers are sensed simultaneously by adherent cells.[135,224]

The 2D sample entropy values (Figure 4.1c) highlight the disordered nature of the HCO-T1 domains, which exhibit significantly higher entropy compared to both the HCO-T2 and 60V-O domains. The fact that HCO-T2 domains, despite their larger diameter, do not show a significant difference in entropy from the 60V-O surface suggests that the arrangement of nanotubes, rather than size alone, plays a crucial role in determining the surface's overall complexity. The analysis of hexagonal packing efficiency, as measured by the N1:N6 ratio (Figure 4.1d), further underscores the differences between these surfaces. The HCO-T1 domains, with their less efficient packing and higher disorder, contrast sharply with the more organized packing found in the HCO-T2 and 60V-O domains. This difference in entropy and packing efficiency is crucial as findings in literature emphasize the importance of entropy and disorder in influencing cellular interactions and response, guiding cells more effectively into differentiation.[8,137,198,206] Fractal dimension analysis (Figure 4.1e) provides additional insight into the complexity of these surfaces. The significantly

different fractal dimension values across all surfaces, with the HCO-T1 surface exhibiting the highest value and the HCO-T2 surface the lowest, illustrate the hierarchical nature of the HCO surface. A higher fractal dimension often indicates a more complex surface[234] capable of presenting multiple scales of topographical features to interacting cells, which could enhance cellular responses such as differentiation and proliferation, complimenting the N1:N6 packing metric. In contrast, the lower fractal dimension of the HCO-T2 surface suggests a simpler, more homogenous structure. Lacunarity, which measures the texture and spatial distribution of gaps within the nanotubular arrays, also varies significantly between the surfaces (Figure 4.1f).[233] The highest lacunarity value on the HCO-T1 surface reflects a more heterogeneous and clumpy structure, consistent with its higher entropy and fractal dimension. The lower lacunarity on the HCO-T2 surface suggests a more evenly distributed nanotubular array, which might lead to different, possibly more uniform cellular behaviors.

3.3.2 Cell Viability and Proliferation

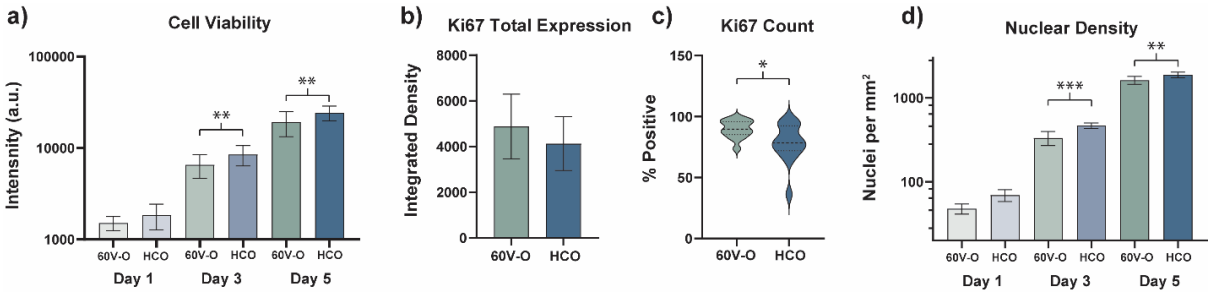

Figure 4.2. Proliferation and viability of MG63 cells on HCO and 60V-O surfaces. Panel a) shows cell viability measured over days 1,3 and 5 on both surfaces. Proliferation dynamics are displayed in b) total Ki67 expression and c) chowing the Ki67 positive cell counts on each surface. Final panel d) shows a comparison of nuclear density between the HCO and 60V-O surfaces.

The proliferation and viability of MG63 cells on the HCO and 60V-O surfaces were evaluated over a five-day period using the PrestoBlue assay for days 1, 3 and 5. Figure 4.2a demonstrates that cell viability on the HCO surface was consistently higher across days 3 and 5 compared to the

60V-O surface. This increased viability on the HCO surface suggests a more favorable environment for cellular metabolism and proliferation, potentially due to its more complex nanotopography and increasing entropy and disorder. These results, derived directly from cellular metabolic activity, align with the mitochondrial dynamics seen in previous work on the nanotubular gradient (Section 3.4.4) where mitochondrial distribution was increased throughout the cellular body as the topographical disorder also increased.

Figure 4.2b further supports this observation by showing a higher total expression of Ki67, a well-established marker for proliferation, on the HCO surface compared to the 60V-O surface. This elevated Ki67 expression suggests that the cells on the HCO surface are in a more active state of proliferation. However, when looking at the Ki67 positive cell counts in Figure 4.2c, an intriguing finding emerges: the 60V-O surface has a higher number of Ki67 positive cells, despite the lower overall Ki67 expression.

Figure 4.2d offers insight into this apparent paradox by showing an increase in nuclear density on the HCO surface. This suggests that the higher total Ki67 expression on the HCO surface could be attributed to the overall greater number of cells rather than an increased proportion of proliferating cells. Faster cellular growth and could mean that cells on the HCO surface may enter a quiescent or differentiated state more readily as they reach confluence, a phenomenon often observed in more complex topographical environments where cell-cell interactions and contact inhibition become more prominent[198,288], potentially keeping elevated rates of Ki67 expression comparatively lower positive counts (though still very high) on the HCO surface.

The differential cellular responses observed on the HCO and 60V-O surfaces highlight the critical role of nanotopographical complexity in modulating osteoblastic behavior. The higher cell viability and total Ki67 expression on the HCO surface suggest that the increased surface

complexity, characterized by higher entropy and lacunarity, provides an environment conducive to enhanced cellular metabolism and growth. This is consistent with previous studies that have shown complex nanotopographies can enhance cell attachment/spreading[200,206,213,289] and subsequent proliferation by providing a more stimulatory environment. [206, 213-215, 217, 238, 289]

3.3.3 Cell Adhesion

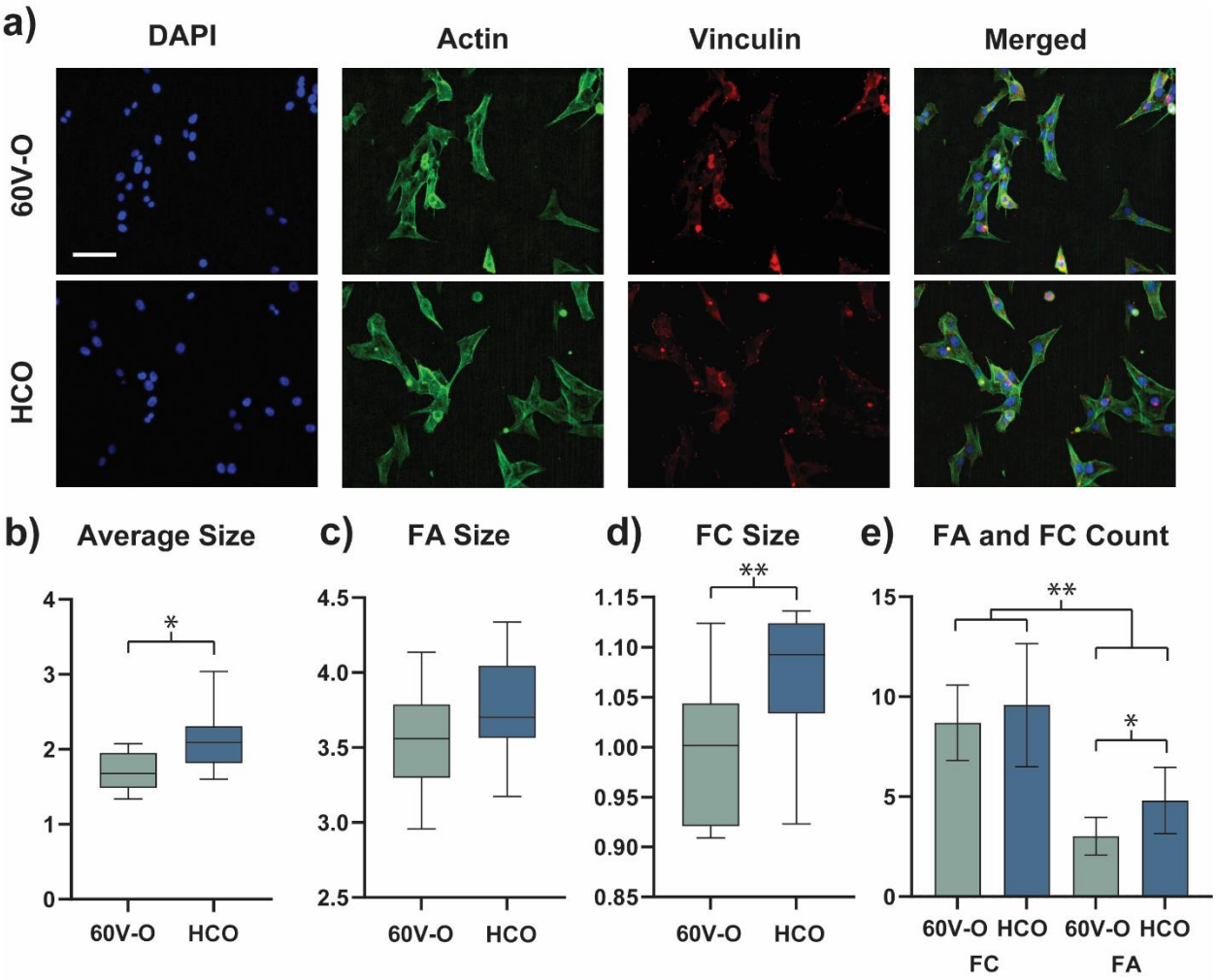

Figure 4.3. Vinculin and focal adhesions on HCO and 60V-O surfaces. Panel a) shows a visual comparison of cells on both surfaces, highlighting differences in focal adhesion formation. Panel b) presents the average size of focal adhesions across both surfaces, with significantly larger adhesions observed on the HCO surface. Adhesion sizes are shown split into c) focal adhesions (2-10 µm) and d) focal complexes (< 2 µm). Focal adhesion and focal complex counts e) between the HCO and 60V-O after one day of attachment. Scale bar corresponds to 100 µm.

The comparative analysis of FA formation and vinculin expression between the HCO and 60V-O surfaces reveals significant differences in cellular adhesion dynamics, crucial for understanding how these nanotopographical features influence cell behavior.[47,286,287] The visual comparisons in Figure 4.3a show immunofluorescence images taken of MG63 cells on the 60V-O and HCO surface on Day 1, highlighting the propensity of both surfaces to successfully form large amounts of focal adhesions and focal complexes. Quantitative analysis in Figure 4.3b shows that the average size of FAs on the HCO surface is significantly larger than on the 60V-O surface, indicating that the HCO surface may better support the formation of more substantial and potentially more stable adhesions. However, when focal adhesions are broken down into specific size categories, Figure 4.3c shows no significant difference in the size of normal FAs (2-10 μm)[286,287] between the HCO and 60V-O surfaces. In contrast, Figure 4.3d highlights a notable difference in the smaller, transient structures known as focal complexes (FCs) (< 2 μm)[286,287], with the HCO surface promoting the formation of larger FCs. The smaller FC sizes observed on the 60V-O surface suggest an adhesion dynamic where the early stages of focal adhesion formation might be less robust. This could indicate a less stable adhesion state, potentially impacting how cells perceive and respond to mechanical stimuli from the substrate, negatively influence various aspects of cell behavior, including spreading.[47,137,200,213,286,287] This suggests that while both surfaces support normal FA formation similarly, the HCO surface may encourage the maturation of FCs into more stable FAs. Further analysis supports this finding as Figure 4.3e reveals that the HCO surface generates a higher number of FAs overall compared to the 60V-O surface. This finding underscores the HCO surface's potential to foster a more stable and mature adhesion environment, which is crucial for effective mechanotransduction, which in turn influences key cellular processes such as proliferation and differentiation. FC counts were significantly higher

than FA counts on both surfaces. The HCO surface demonstrates a clear advantage in promoting stable cell adhesion, as evidenced by the larger and more numerous FAs and FCs. These differences in adhesion dynamics may set the stage for distinct downstream signaling responses, as explored in the analysis of the YAP1/Hippo pathway.[43,239]

3.3.4 YAP1 and Active YAP1

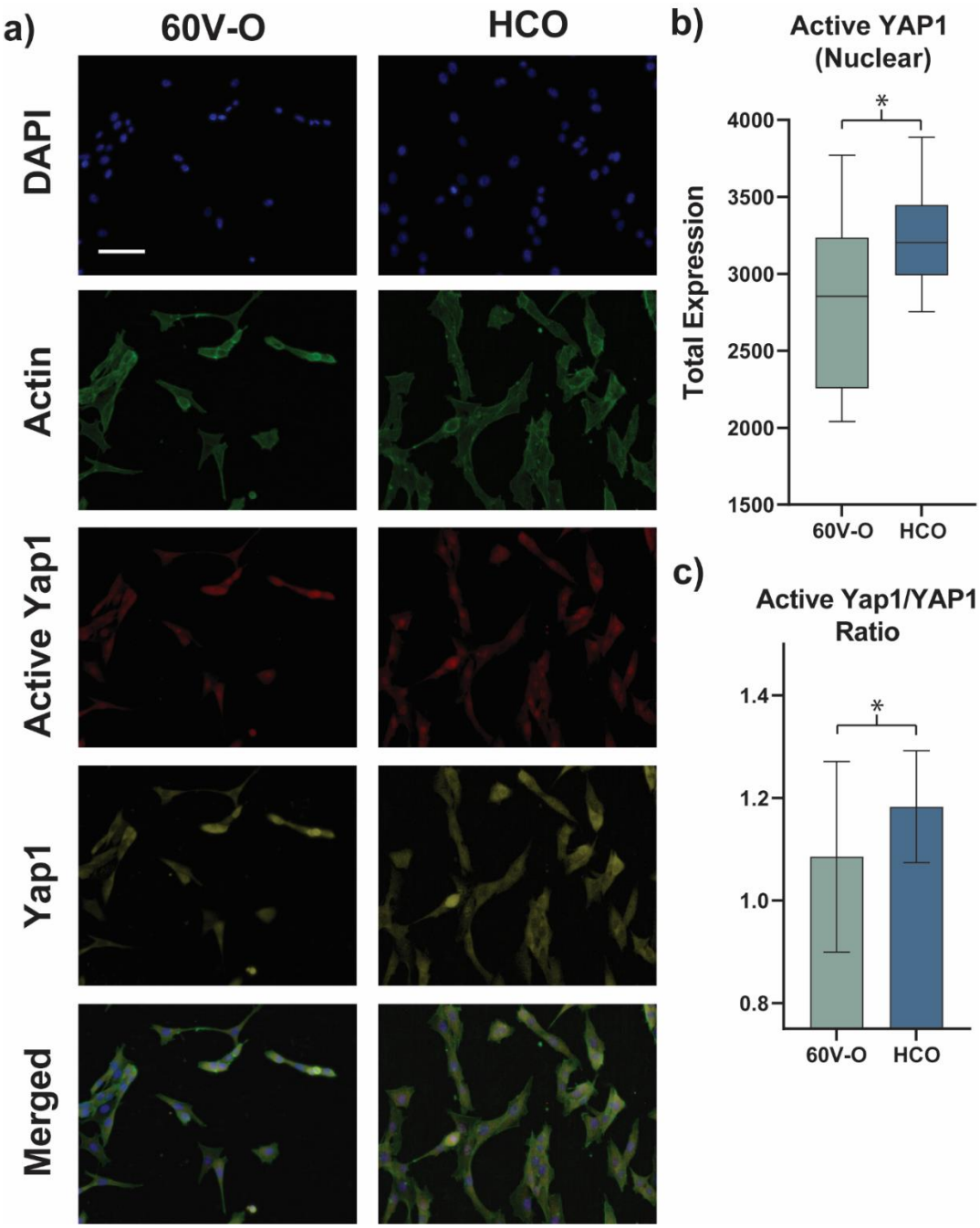

Figure 4.4. Mechanotransduction via the YAP/Hippo pathway on HCO and 60V-O surfaces. Immunofluorescence images of a) actin, active YAP1 and YAP1, highlighting their localization within MG63 cells on both surfaces. Total b) YAP1 expression within cell nuclei and c) average nuclear intensity of active YAP1 to the cytoplasmic intensity of YAP1. Scale bar corresponds to 100 µm.

The analysis of the YAP1/Hippo signaling pathway activation on the HCO and 60V-O surfaces underscores the crucial role of mechanotransduction in the cellular response to these nanotopographies. IF images in Figure 4.4a display YAP1 (Active YAP1) and its phosphorylated form, pYAP1 (YAP1), in MG63 cells, with the presence of YAP1 in the cell nuclei indicating active mechanotransduction. This nuclear translocation of YAP1, a key transcriptional coactivator in the Hippo pathway, suggests that cells are responding to the mechanical cues provided by the underlying nanotopography.[43,222,239] Elevated levels of nuclear expression of active YAP1 can be seen clearly on the HCO surface. Consequently, quantitative analysis in Figure 4.4b reveals that total YAP1 expression within the cell nuclei is higher on the HCO surface compared to the 60V-O surface. This elevated nuclear YAP1 expression suggests that the HCO surface, with its more complex, disordered nanotopographical features, provide a stronger stimulus for early YAP1 activation by day 1. The increased focal adhesion size and complexity observed on the HCO surface, as discussed in the results of Figure 4.3, likely contribute to this enhanced YAP1 activation. Large, stable focal adhesions are known to influence the YAP1 pathway by altering cytoskeletal tension and cell contractility, thereby promoting YAP1 nuclear localization.[239,290–292] The correlation between increased focal adhesion size and higher nuclear active YAP1 levels reinforces the idea that the HCO surface promotes a more robust mechanotransductive response.[43,239]

Further supporting this, Figure 4.4c compares the average intensity of active YAP1 in the cell nuclei to YAP1 in the cytoplasm, showing higher nuclear active YAP1 intensity and lower cytoplasmic phosphorylated YAP1 on the HCO surface. This indicates a more pronounced activation of the YAP1 pathway on the HCO surface, further suggesting that the cells are in a state of heightened mechanotransductive activity, which could accelerate processes such as

differentiation and proliferation.[43,222,239,288,290] This supported by the elevated proliferative levels seen in Figure 4.2. This clear trend of higher YAP1 activation on the HCO surface suggests that this surface may be more effective at promoting early cellular differentiation, the results of which can be seen in Figure 4.5.

These results add to a recent, growing body of literature highlighting the importance of the relationship between nanotopographical features and YAP1/Hippo pathway activation, with particular emphasis on YAP1s impact on osteoblast differentiation.[127,199,260–262] Given the observed trends on Day 1, it is reasonable to hypothesize that the HCO surface would outperform the 60V-O surface in promoting early differentiation due to the rapid mechanotransductive changes observed. Future studies could focus on tracking YAP1 activation over longer periods and across different stages of differentiation to fully elucidate the role of nanotopography in guiding cellular fate through the YAP1/Hippo pathway, as well as utilizing more quantitative experimental methods (Western blots, qPCR etc.) and pathway blockers for greater elucidation into this pathways activation on these surfaces.

3.3.5 Differentiation

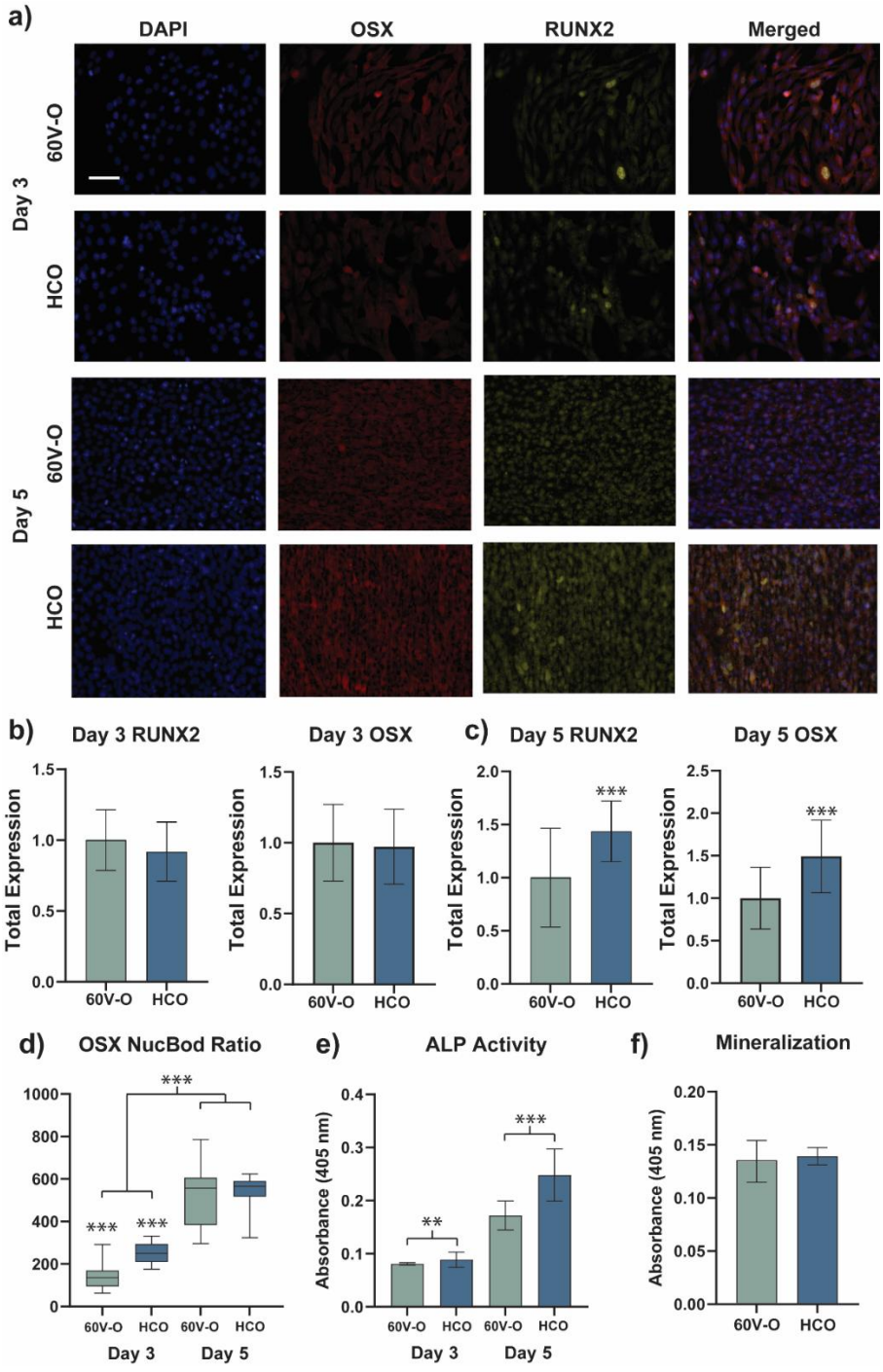

Figure 4.5. RUNX2 and OSX expression, ALP activity, and mineralization on HCO and 60V-O surfaces. IF images of a) RUNX2 and OSX on Days 3 and 5, with visibly brighter staining on the HCO surface. Total expression of nuclear bound RUNX2 and OSX on days b) 3 and c) 5 (expression relative to 60V-O). Panel d) compares the ratio of nuclear to cytoplasmic OSX

expression on Day 3. Assay results for e) ALP activity (days 3 and 5) and f) Alizarin assay (mineralization) after 21 days. Scale bar corresponds to 100 μm.

The expression of key osteogenic markers RUNX2 and OSX, along with the activity of ALP and mineralization, were evaluated to assess the early stages of differentiation of MG63 cells on the HCO and 60V-O surfaces. IF images of RUNX2 and OSX on Days 3 and 5, as shown in Figure 4.5a, reveal visibly brighter staining on the HCO surface, suggesting more robust expression of these markers compared to the 60V-O surface. Despite this visual observation, quantitative analysis of RUNX2 expression on Day 3 shows no significant difference in total expression within the nucleus between the HCO and 60V-O surfaces (Figure 4.5b). Similarly, OSX expression follows an identical trend, with no significant differences in total expression observed until Day 5. By Day 5, however, a significant increase in nuclear expression of both RUNX2 and OSX is evident on the HCO surface (Figure 4.5c). This marked upregulation suggests that the HCO surface promotes a more advanced stage of osteogenic differentiation by Day 5 compared to the 60V-O surface. Further analysis reveals that the ratio of nuclear to cytoplasmic OSX expression on Day 3 is elevated on the HCO surface (Figure 4.5d). This early surge in OSX production, followed by its rapid translocation to the nucleus[293,294], supports the notion that the HCO surface induces a quicker initiation of the differentiation process. By Day 5, this early advantage seems to have normalized, with no significant differences in the nuclear-to-cytoplasmic ratio of OSX between the surfaces, indicating that the cells on the HCO surface may reach a differentiated state more rapidly than those on the 60V-O surface.

The trend of early differentiation is further corroborated by the ALP activity data, where significantly higher ALP activity is observed on both Days 3 and 5 on the HCO surface (Figure 4.5e). ALP is a well-known early marker of osteogenic differentiation, and its elevated activity on the HCO surface suggests that this nanotopography is more effective at inducing early osteoblast

differentiation. Interestingly, despite the accelerated differentiation observed on the HCO surface, mineralization, as measured by the Alizarin assay, shows no distinguishable difference between the HCO and 60V-O surfaces after 21 days (Figure 4.5f).

The differential expression of RUNX2 and OSX, along with the observed ALP activity, provides compelling evidence that the HCO surface promotes a more rapid onset of osteogenic differentiation in MG63 cells compared to the 60V-O surface. RUNX2 and OSX are critical transcription factors in the osteogenic pathway, with RUNX2 initiating the differentiation process and OSX being essential for the maturation of pre-osteoblasts into fully functional osteoblast.[40,105,293,294] The significant increase in their nuclear expression by Day 5 on the HCO surface suggests that this nanotopography provides the necessary cues to accelerate these processes, potentially due to the increased propensity to form large, stable focal adhesions and the enhanced mechanotransductive signaling observed in earlier YAP pathway activation that occurs as a result. These results suggest that the HCO architecture is highly effective in driving early osteogenic differentiation, likely due to the enhanced mechanotransductive signaling and the rapid activation of key transcription factors like RUNX2 and OSX.[8,38,40,41] The elevated nuclear-to-cytoplasmic ratio of OSX on Day 3 on the HCO surface further underscores the early onset of differentiation. This early nuclear localization of OSX is indicative of a rapid transition from a proliferative to a differentiated state, which is consistent with the observed increase in ALP activity. ALP is a key enzyme involved in the early stages of mineralization, and its higher activity on the HCO surface suggests that cells are not only differentiating more quickly but are also preparing for the mineralization phase of bone formation. However, the lack of difference in mineral deposition between the two surfaces after 21 days raises interesting questions about the long-term effects of early differentiation. While the HCO surface clearly promotes rapid

osteoinduction, this does not necessarily lead to a greater accumulation of mineralized matrix over time. This finding aligns with previous studies on interactions with the gradients (Section 3.4.5), suggesting that while early differentiation markers may be upregulated, the ultimate amount of mineralization may be influenced by other factors.

These findings highlight the importance of considering both early and late-stage markers in the design and evaluation of biomaterials intended for bone regeneration. The combined data from Figures 4.2-5 present a comprehensive view of how the nanotopographical features of the HCO and 60V-O surfaces influence MG63 cell behavior, particularly in terms of proliferation, mechanotransduction, and osteogenic differentiation.

3.3.6 Mineral Quality

The following analysis focuses on the key Raman spectral features that are relevant to the study of bone mineralization, ECM composition, and single-cell analysis of MG63 osteoblastic cells. Table 4.2 summarizes the critical Raman peaks observed in this study, including those associated with phosphate, carbonate, amide, and lipid regions, as well as other significant biochemical markers such as proline, hydroxyproline, and phenylalanine. These peaks provide valuable insights into the biochemical environment of the cells and the state of mineralization on the titanium surfaces.

Table 4.2. lists the key Raman peaks identified in this study, including corresponding molecular assignments and significance. The table includes peaks related to bone mineralization, extracellular matrix composition, and specific features relevant to single-cell Raman spectroscopy of MG63 osteoblastic cells.

Peak (cm^{-1})	Assignment	Description/Significance
940[135]	**Amorphous Calcium Phosphate**	Represents amorphous calcium phosphate, indicating less mature mineralization phases.
960[135]	**$\nu_1(1PO_4^{3-})$ (Phosphate)**	The primary phosphate band, associated with the symmetric stretching mode of $\nu_1(1PO_4^{3-})$ in hydroxyapatite, indicating crystalline mineral. Key marker for bone mineralization and crystallinity.
1000[295]	**Phenylalanine**	Associated with the aromatic ring in the amino acid phenylalanine, often used as an internal standard due to its strong and consistent Raman signal.
1070[135]	**$\nu_1(CO_3^{2-})$ (Carbonate)**	Indicates carbonate substitution in hydroxyapatite, commonly associated with bone mineralization and alterations in bone mineral composition.
1245-1270[135]	**Amide III**	Associated with nucleic acids and proteins, specifically the Amide III vibrations, which indicate cellular activity and protein synthesis.
1450[135]	**CH_2 Wagging (Lipids)**	Associated with lipid content, representing cellular membranes and energy storage. Important for identifying lipid distribution in cells.
1660[135]	**Amide I**	Corresponds to the C=O stretching vibrations in proteins, primarily collagen, main organic component of the bone matrix.
2950[295]	**CH Stretching (Lipids)**	Corresponds to C-H stretching vibrations in lipids. Used to identify lipid distribution within cells, particularly in the context of cellular membranes and storage.

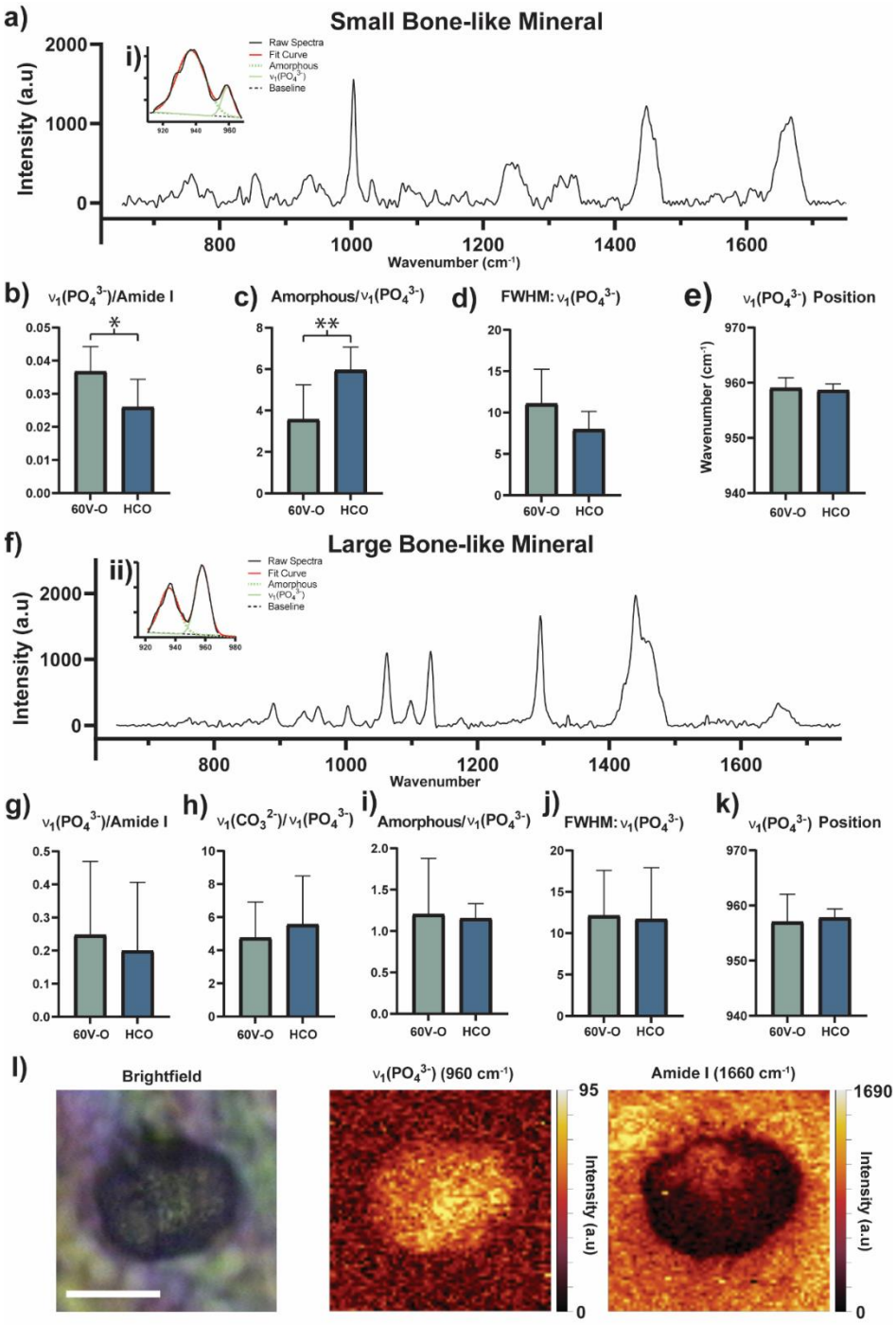

Figure 4.6. Raman analysis of mineralization on HCO and 60V-O surfaces after 21 days in culture. Panel a) shows representative Raman spectra of the small bone-like mineral found in the ECM, with nested panel ai) demonstrating peak deconvolution between the 960 cm^{-1} (calcium phosphate) and 940 cm^{-1} (amorphous calcium phosphate) peaks. Mineral composition analysis compared via b) $\nu_1(PO_4^{3-})$/amide I ratio, c) amorphous calcium phosphate/ $\nu_1(PO_4^{3-})$, d) FWHM (of $\nu_1(PO_4^{3-})$ peak), and e) in the position of the $\nu_1(PO_4^{3-})$ peak between the surfaces. Panel f) shows representative Raman spectra of larger bone-like mineral structures, with nested panel fii)

illustrating peak deconvolution. Panels g-k) compare: $\nu_1(PO_4^{3-})$/amide I ratio, $\nu_1(CO_3^{2-})/\nu_1(PO_4^{3-})$, amorphous mineral/$\nu_1(PO_4^{3-})$, FWHM (of $\nu_1(PO_4^{3-})$ peak), and $\nu_1(PO_4^{3-})$ peak position, respectively. Panel l) provides a representative image of these larger structures, including brightfield, Raman map filtered at 960 cm^{-1}, and Raman map of amide I at 1660 cm^{-1}. Scale bar corresponds to 10 µm.

Probing further into the mineral produced on each of these surfaces, Raman spectroscopy was employed to assess the mineral composition and maturity of the two different mineralized bone-like structures, small (< 5 µm) and large (> 5 µm) produced by MG63 cells cultured on HCO and 60V-O surfaces over 21 days. The samples, after being cultured, were scraped off the surfaces and smeared onto CaF_2 slides for analysis. The spectra obtained from these samples revealed key differences in the mineral content, particularly in the size and composition of the mineral structures. The representative Raman spectra of the small bone-like mineral, shown in Figure 4.6a, highlighted distinct peaks corresponding to calcium phosphate and amorphous calcium phosphate. The deconvolution of these peaks is shown in Figure 4.6ai, specifically the 960 cm^{-1} peak associated with crystalline hydroxyapatite and the 940 cm^{-1} peak associated with amorphous calcium phosphate, provides insights into the mineralization process. A significantly higher $\nu_1(PO_4^{3-})$/amide I ratio was observed on the 60V-O surface compared to the HCO surface (Figure 4.6b), indicating a greater presence of crystalline hydroxyapatite on the 60V-O surface. In contrast, the HCO surface exhibited a higher amorphous calcium phosphate to crystalline hydroxyapatite ratio (Figure 4.6c), suggesting that the mineralization on this surface is less advanced. Interestingly, no significant differences were observed between the surfaces in terms of the full width at half maximum (FWHM) of the phosphate peak or the position of the phosphate peak at 960 cm^{-1} (Figure 4.6d), indicating that the crystallinity of the mineral formed on both surfaces was preserved. This suggests that the 60V-O surface supports more mature mineralization, and the mineral produced on the HCO surface is still in an earlier developmental stage.

Further analysis, however, focused on a limited amount of larger bone-like mineral structures found within the samples, which were also examined using Raman spectroscopy. These bone-like modules are commonly found in MG63 mineral studies at this timepoint.[296,297] The representative spectra from these larger structures (Figure 4.6f) displayed stronger and sharper peaks compared to the smaller structures embedded in the ECM, indicating a higher degree of crystallinity. In contrast with the smaller structures, and despite the stronger signals, no significant differences were found between the HCO and 60V-O surfaces in terms of the $\nu_1(PO_4^{3-})$/amide I ratio (Figure 4.6g), $\nu_1(CO_3^{2-})/\nu_1(PO_4^{3-})$ (Figure 4.6h), amorphous calcium phosphate/phosphate ratios (Figure 4.6i), FWHM (Figure 4.6j), or the position of the phosphate v1 peak (Figure 4.6k). Both of these samples, though comparatively different, have comparable influence on differentiation. If these bone-like structures form in similar windows of time, their composition may become more dependent on the environment than the surface as the majority of the cells are no longer in contact with the material's surface. Finally, the imaging data presented in Figure 4.6l shows a representative image of these larger mineral structures, including brightfield imaging, Raman map spectral filters at 960 cm^{-1} and 1660 cm^{-1}, corresponding with the $\nu_1(PO_4^{3-})$ and amide I peaks, respectively. These images confirm the presence of well-defined and highly crystalline structures throughout the bone-like mineral's structure.

These larger bone-like structures exhibited intense peaks at 1070 cm^{-1}, 1245-1270 cm^{-1}, and 1450 cm^{-1}, along with sharper phosphate peaks, indicating a complex biochemical composition within these mineralized regions. The amide III peak around 1245-1270 cm^{-1}, associated with protein content, further supports the presence of a proteinaceous matrix within these structures. Additionally, the CH_2 bending vibrations at 1450 cm^{-1} indicate the inclusion of lipid content, possibly within cellular membranes or associated with the ECM. These findings suggest that the

mineralized structures observed are not purely inorganic but are rich in organic components, particularly proteins and lipids, which are essential for the formation of a mineralized bone matrix and consistent with results found in literature.[276,282,296,297] The preservation of crystallinity across both surfaces, as evidenced by the consistent FWHM and phosphate peak positions, indicates that the fundamental process of mineral deposition remains robust, regardless of the specific surface characteristics.

The Raman spectroscopy results provide insights into the differences in mineralization between the HCO and 60V-O surfaces after 21 days of culture. The 60V-O surface appears to facilitate more advanced mineralization, as indicated by the higher $\nu_1(PO_4^{3-})$/amide I ratio, which reflects a greater presence of crystalline hydroxyapatite. Additionally, the HCO surface shows a higher proportion of amorphous calcium phosphate relative to crystalline hydroxyapatite, implying that mineralization on this surface is still in a less mature phase.[276,279] It should also be noted that MG63 cells are known for their lack of production of high quality bone mineral in comparison to other immortalized osteoblastic cell lines.[28] This does not invalidate the comparative results; however, it may explain the lack of sharpness and height in the $\nu_1(PO_4^{3-})$ peak along with the early 21 day timepoint. These results provide context to the Alizarin results, showing a more nuanced understanding of mineralization process between these two osteogenic surfaces, slightly favoring the 60V-O surface for long term production of mineral.

3.3.7 Raman Confocal Imaging on Titanium Nanotubular surfaces

Transitioning from bulk mineral analysis, the development and application of a Raman confocal imaging protocol tailored for single-cell analysis on titanium nanotubular surfaces was explored. In this study, a custom 3D-printed cartridge and filter (Figure 4.7) were developed and implemented to address the challenges of Raman imaging on opaque titanium surfaces using the

Witec Alpha 300R Raman microscope. The design of the cartridge and filter, shown in Figure 4.7a, allows for the blocking of direct light and the selective filtering of oblique light, which can be adjusted to optimize the visibility of thin MG63 cells on the highly reflective titanium substrate.[298] This modification was crucial for overcoming the difficulties associated with imaging cells on metallic surfaces, which are often opaque and reflective, making cell visualization under a top-down microscope configuration challenging. Figure 4.7b demonstrates the effectiveness of this custom filter. The unfiltered image (top left) shows an MG63 cell on the HCO surface that is almost indistinguishable due to the lack of contrast and variability against the reflective titanium background. However, when the oblique light filter is applied (top right), the cell's edges, including the nuclei and cell membrane, become visible, allowing for identification of cellular structures for Raman imaging. Due to the difficulty in portraying this imaging pictorially, this improvement is further validated using image processing techniques in ImageJ, where a top-hat and variance filter analysis confirms the ability of the software to detect cell edges only in the filtered image (bottom right), but not in the unfiltered image (bottom left).

After being able to identify single cells adhered to the nanotubular surfaces, Z-stack scans were implanted to troubleshoot imaging heights and technical issues of working with the anodized material. Figure 4.7c illustrates a series of progressive scans of a spherical MG63 cell in division, from the first slice of the top of the cell to the eventual failure of the image, with the last panel displaying the large areas of fluorescence. This highlights the challenges related to laser-induced damage during Raman imaging on titanium surfaces, revealing the risks of using elevated laser powers, which can cause physiochemical reactions with the titanium surface, leading to bubble formation and sample destruction. This issue was mitigated by carefully optimizing laser power and integration times, with subtle adjustments made at the specific height of analysis to avoid

damage. The results show that Z-stack images are clearly possible on the opaque surfaces but underscore the importance of conducting Z-layer scans from the bottom up when optimizing parameters or imaging to prevent bubble formation during prolonged imaging sessions. This method not only preserves the sample but also offers the flexibility to stop imaging early, saving time.

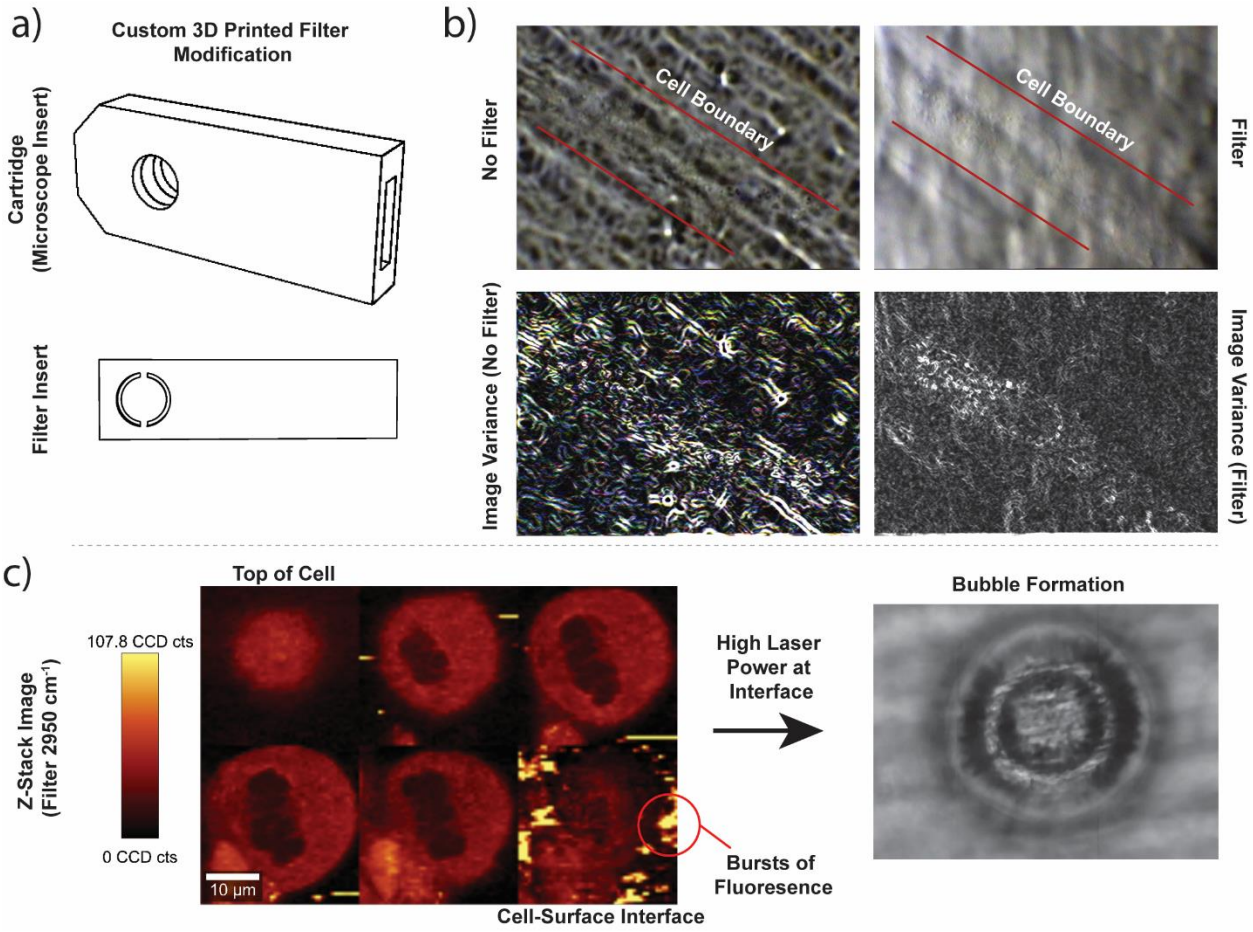

Figure 4.7. Custom 3D-printed cartridge and oblique light filter for Raman imaging on titanium surfaces. Panel a) shows the design of the 3D-printed cartridge (top), the filter (middle), and their assembly (bottom), which fits into the Olympus microscope base to block direct light and filter for oblique light. Panel b) compares unfiltered (top left) and filtered (top right) images of an MG63 cell on the HCO surface, with ImageJ analysis showing edge detection in the filtered image (bottom right) but not in the unfiltered image (bottom left). Panel c) displays progressive scan slices of a dividing MG63 cell on the titanium surface, illustrating the challenges of bubble formation due to laser-induced reactions, and highlighting the optimization of laser power and integration times to prevent sample destruction.

The development of a custom 3D-printed cartridge and oblique light filter represents a significant improvement in the ability to perform Raman imaging on opaque titanium surfaces, which are notoriously difficult to work with using conventional microscopy techniques. Titanium's reflective properties and the limitations of a reflectance-based microscopy setup necessitated this novel approach, which successfully enhanced the visibility of MG63 cells on the HCO surface. Though a more costly solution, it is possible that equipping an imaging system with phase microscopy may also display a similar effectiveness at separating the cellular foreground from the material background. The filter's ability, using oblique light, to reveal cell edges and internal structures, as confirmed by both visual inspection and image processing software, demonstrates its practical utility in overcoming the inherent challenges of imaging on opaque, metallic surfaces.

A second significant challenge encountered during Raman imaging on titanium surfaces was the formation of bubbles, which likely resulted from either heat accumulation, or a photocatalytic reaction induced by the laser. TiO_2 nanotubes are well-known for their photocatalytic properties, and when exposed to UV or visible light, it can generate electron-hole pairs, leading to redox reactions at the surface, potentially forming bubbles.[275] This photocatalytic effect, coupled with localized heating from the laser, could exacerbate the problem, especially at higher laser powers. The challenges associated with laser-induced damage during Raman imaging, as highlighted in the progressive scans (Figure 4.7c), further emphasize the need for careful optimization of imaging parameters, particularly in terms of laser alignment, laser power and integration time. The inability to use full laser power (40mW) with the 532 nm laser, as is often possible or transparent surfaces or in 3D culture systems (ref), necessitates longer integration times to achieve high-quality spectra in future research. However, with these adjustments, it is feasible to perform detailed Raman

imaging on opaque titanium surfaces, providing valuable insights into cell-surface interactions that are otherwise difficult to obtain.

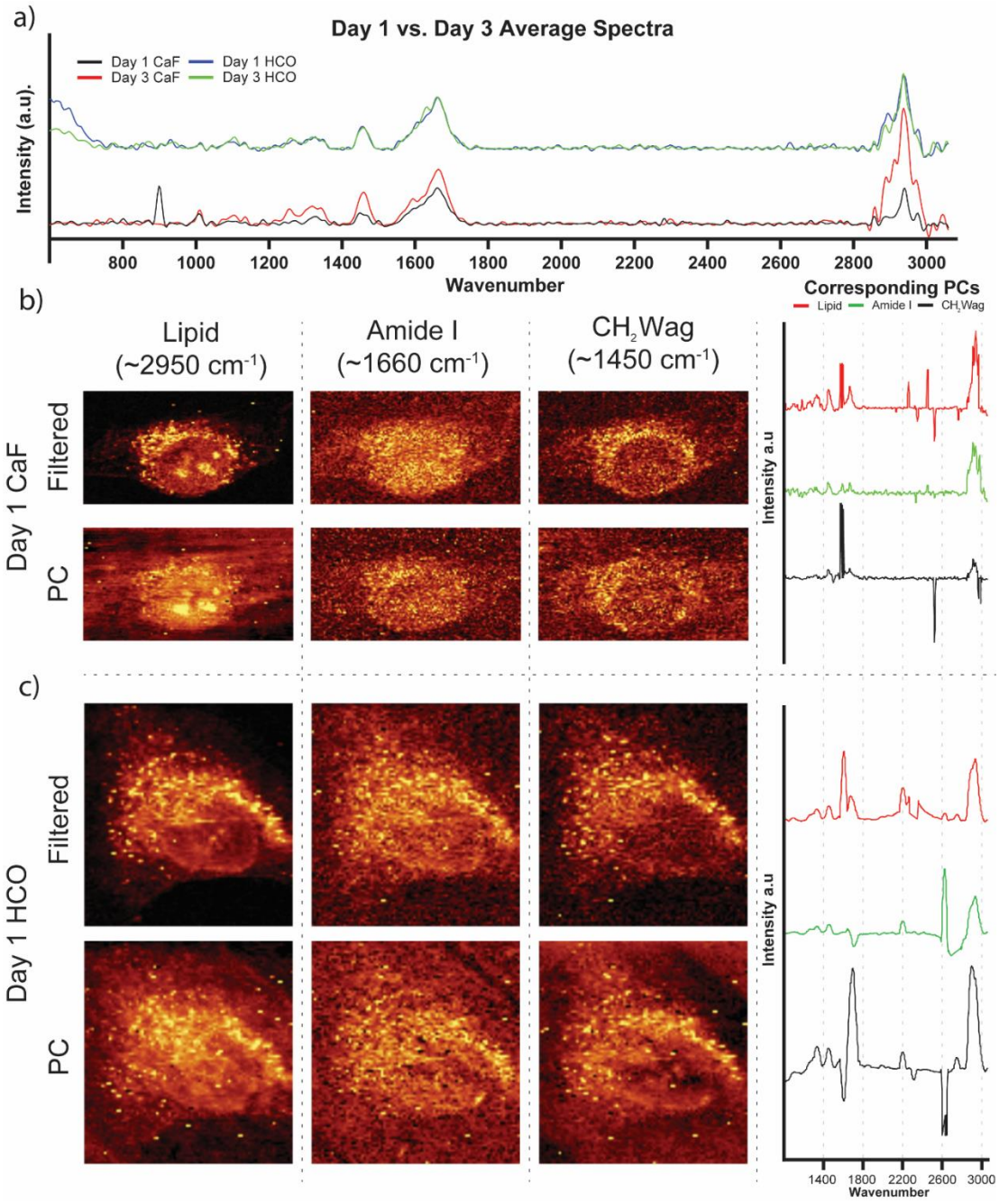

Figure 4.8. Single-cell Raman spectroscopy of MG63 cells on CaF_2 and HCO surfaces. Comparison of a) representative Raman spectra from Day 1 and Day 3 of single cells on CaF_2 slides and HCO. Panel b) presents Raman maps of single MG63 cells on CaF_2 slides for CH_2 wag, amide I, and lipid regions (top), with corresponding principal component analysis (PC) images (bottom) and spectra (right). Panel c) shows similar Raman maps (top), PC images (bottom) and PC spectra (right) for MG63 cells on the HCO surface.

The application of optimized Raman imaging protocols, as developed through the troubleshooting process described above, has made it possible to perform 2D Raman confocal imaging of single cells on titanium surfaces, such as the HCO surface, with significant improvements in signal quality and peak resolution. This section focuses on the qualitative analysis of single MG63 cells on both CaF_2 and HCO surfaces from days 1 to 3.

Figure 4.8a presents a comparative analysis of Raman spectra from MG63 cells on both CaF_2 and HCO slides at Day 1 and Day 3. The spectra from cells on the CaF_2 surface reveal a clear increase in signal intensity and peak definition across several key regions, including the CH_2 wag (~1450 cm^{-1}), Amide I (~1660 cm^{-1}), and lipid (~2950 cm^{-1}) regions. This increase in signal on the CaF_2 surface by Day 3 may suggest that the cells required time to adapt and grow in the supplemented media, resulting in enhanced biochemical activity. Increasing signal in lipid and amide regions apparent in the MG63 cell line on CaF_2 has also been noted in Raman confocal studies of multiple cell lines (MG63[295], NIH3T3, EPH4 and Hepa1–6[299]) in literature as key signal of early differentiation.[295,299–301] However, in contrast, the Raman spectra from cells on the HCO surface showed little difference between Day 1 and Day 3, with a much stronger signal already present at Day 1. This could indicate that the cells are responding more robustly to the HCO surface from the outset, producing more biochemical signals in response to the nanotopography, and potentially suggests that future studies should consider adjusting the timepoints—either by shortening the first timepoint (Day 1) or lengthening the second (Day 3) to capture more nuanced temporal changes.

Figure 4.8b and Figure 4.8c further illustrate the spatial distribution of these Raman peaks in single MG63 cells on CaF_2 and HCO surfaces on day 1. The filtered Raman maps for CH_2 wag, amide I, and lipid regions show distinct spatial patterns, which are complemented by PCA that

highlights the main spectral variations within the cells. Spatial data, particularly from the 2950 cm^{1-} region (Figure 4.8 b and c), on the nucleus and nucleoli allows for cell phase analysis, similar to images generated by Ki67 staining, allowing for identification of whether the cells are in mitosis or G0-2 phases.[224] Complementary filtered Raman images of MG63 cells on CaF_2 and HCO on Day 3 can be seen in Figure 4.S1 in the supplementary material. On the CaF_2 surface, the Day 1 images presented a lot more noise, which translated into the PC images, leading to increased variability that was difficult to eliminate. This variability in the PC images likely reflects the lower signal quality observed in the Day 1 Raman spectra on the CaF_2 surface. By Day 3, as the signal improved, the PC images also showed clearer patterns, albeit with some residual noise that persisted due to the initial lower signal-to-noise ratio. Conversely, on the HCO surface (Figure 4.8c), the noise in the PCs was much lower, consistent with the stronger signal observed in the Day 1 spectra on this surface. The filtered spectral images and PC images from the HCO surface displayed much cleaner and more consistent patterns.

3.4 Conclusion

This study has demonstrated that the HCO surface significantly enhances early cellular responses, particularly in terms of proliferation and early osteogenic differentiation of MG63 cells. The increased cell viability, mitochondrial activity, and upregulation of early differentiation markers on the HCO surface underscore its potential as a superior substrate for promoting initial cellular attachment and growth. These findings highlight the importance of nanotopographical complexity in influencing cell behavior, suggesting that surfaces like HCO could be particularly beneficial in applications requiring rapid cell proliferation and differentiation.

The higher nuclear localization of YAP1 on the HCO surface indicates that mechanotransduction through YAP1 is likely a significant factor in the observed cellular

responses. This pathway's role in responding to mechanical cues provided by the nanotopographical features warrants further investigation, as it may offer new insights into optimizing surface designs for enhanced osteogenic outcomes. Additionally, the HCO surface showed a significantly higher number of FAs compared to the 60V-O surface, further underscoring its potential to support more stable and mature cell adhesion, which is critical for effective mechanotransduction and downstream signaling pathways. Despite the HCO surface's advantages in early cellular activity, the 60V-O single tube surface exhibited robust mineralization, comparable to the HCO surface as measured by the Alizarin assay. Interestingly, the 60V-O surface may produce higher quality mineral deposits, characterized by a greater presence of crystalline hydroxyapatite, which is crucial for long-term bone stability. These findings align with previous research on similar surfaces and suggest that while the HCO surface excels in early stages, the 60V-O surface may be more conducive to producing mature bone tissue. These results serve to validate the successful transition from gradient to homogenous surface, eliciting comparable cell responses across: Ki67 and RUNX2 total expression, metabolic activity and mineralization.

Notably, the HCO surface represents a marked improvement over previous honeycomb structures used in earlier studies, offering a more balanced approach between early cell activity and mineral maturation. A significant contribution of this study is the development of a protocol and modification for performing Raman confocal imaging on opaque titanium surfaces. This overcomes the challenges associated with imaging on such substrates, enabling detailed, non-invasive analysis of single cells on titanium nanotubular surfaces. The successful application of this technique was demonstrated through the capture of representative images of single cells on both HCO and CaF_2 surfaces. Using Raman confocal microscopy in combination with PCA and spectral filtering, several biorelevant chemical signals were extracted, providing a foundation for

future studies and a valuable tool within our lab. These signals can be analyzed both spatially and in terms of intensity and peak changes over time, offering a powerful tool for understanding the biochemical processes involved in osteogenesis.

This research not only advances our understanding of how nanotopographical features influence MG63 cell behavior but also provides new methodologies for studying these interactions in detail. The insights gained from this study pave the way for further exploration into optimizing biomaterial surfaces for enhanced osteogenic outcomes.

3.5 Acknowledgements

The authors acknowledge financial support from the Natural Sciences and Engineering Research Council of Canada (NSERC) through the Discovery Grant program, Canada Foundation for Innovation (CFI) and the Ontario Ministry of Research and Innovation (MRI) through the Leaders of Opportunity (LOF) fund. R.B. expresses appreciation to NSERC for funding provided by the Canada Graduate Scholarship. The authors also extend their gratitude to the Cell Biology and Image Acquisition (CBIA) Core Facility for providing access to fluorescence microscopes and to Chloë Van Oostende-Triplet and Liyuan Wang for their technical support and guidance in microscopy.

3.6 Supplementary Information

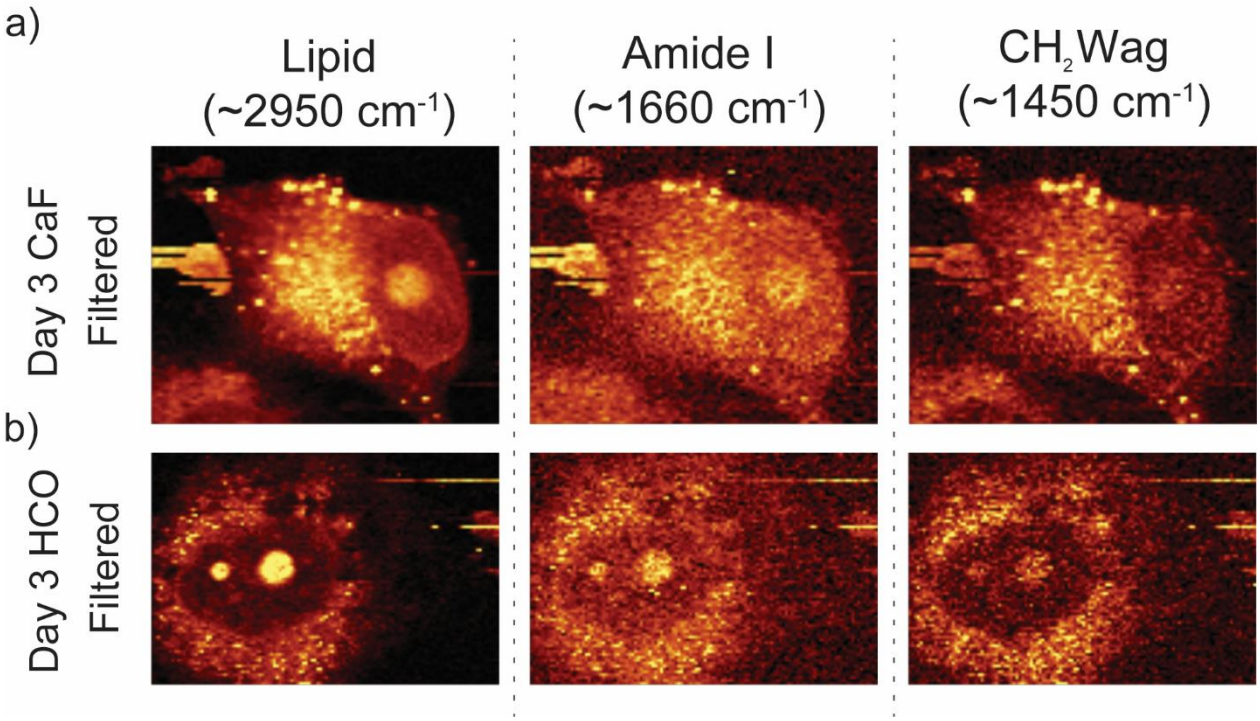

Figure 4.S1. Single-cell Raman spectroscopy of MG63 cells on CaF_2 and HCO surfaces on day 3. Panel a) presents Raman maps of single MG63 cells on CaF_2 slides for CH_2 wag, amide I, and lipid regions, while a cell on b) HCO on day 3 is shown in the bottom row, containing identical regions.

3.6.1 Utilization of Raman confocal Microscopy for the Study of Cell-Surface Interactions

3.6.1.1 Overview of Raman Spectroscopy

In a useful extension of Raman spectroscopy, the spectroscopic data gleaned from Raman spectroscopy can be organized into Raman images using an advanced tool known as Raman Confocal Microscopy. In this process, the Raman scattered light is collected point by point from a sample. By scanning the sample, a spectrum is obtained for each point, and together, these spectra create a "map" of the chemical composition of the sample at a microscopic level. Each pixel in the resulting Raman image corresponds to a full spectrum that reflects the molecular structure at that particular location, creating a comprehensive and detailed visual representation of the sample. To analyze Raman images, hyperspectral datasets undergo a cleaning process to remove noise and auto-fluorescence. These datasets are then analyzed using computational techniques such as principal component analysis, multivariate curve resolution, and clustering analysis to identify and differentiate the Raman spectra of cellular components like the nucleus, cell cytoplasm, and bone mineral. This coupling of Raman spectroscopy with confocal microscopy not only allows for precise spatial resolution but also opens doors to the three-dimensional imaging of samples, pushing the boundaries of molecular analysis to new frontiers.[271]

3.6.1.2 Mineral Analysis

Another crucial aspect in predicting implant osseointegration is the quality of the mineral deposited by osteogenic cells *in vitro*. Recent studies have demonstrated that functionalized surfaces capable of triggering mineral deposition by osteoblastic cells lead to improved osseointegration of the implant.[302] While mineral deposition can be quantified using conventional imaging techniques such as SEM or confocal microscopy, more in-depth analyses may provide insights into the quality of the deposited matrix. Advanced spectroscopic techniques, such as

Raman spectroscopy, can be employed to extract information on the chemical composition and crystallinity of both the mineral and protein matrix deposited by osteoblastic cells.

Primary phosphate (~959 cm^{-1}) band offers a precise quantification of mineral crystallinity, 1070 cm^{-1}, and 1665 cm^{-1} for the Amide I peak that largely represents the amount of collagenous matrix in the sample.[268,280] Several studies have employed specific parameters of Raman peaks, including area, height, and full width at half maximum (FWHM), to gain more insight into the fundamental characteristics of bone, dividing the primary phosphate band by the amide I peak provides a quantification of the mineral-to-matrix ratio, which is indicative of the degree of mineralization and serves as a reliable predictor of bone mechanical properties. Although understanding bone composition and structure is essential for improving fracture risk prediction and prevention, there is a lack of comprehensive studies on mineral deposition on Ti NTs. Future studies should incorporate the characterization of cell mineral deposition, as it provides pivotal knowledge on the osseointegration potential of the tested implant.

In a study by Wang *et al.* 2009, hydroxyapatite mineral crystals were readily detected within extracellular biomineralization foci (BMF) complexes after 76 hours, based on the assignment of the 957–962 cm^{-1} band to the v1 symmetric stretch signal for PO_4^{-3}. These changes were more pronounced when first normalized relative to the signal at 1450 cm^{-1} (N-H bend; methyl deformation; CH_2-wag), which remained relatively constant over the experimental time course. When represented in this way, it appeared that the 1004 and 1660 cm-1 Raman signals first peaked at about 70 hours and then decreased to a minimum at 82 and 88 hours. Interestingly, the mineral-derived phosphate signal near 960 cm^{-1} exhibited a complementary inverse relationship with that for the 1004 band and 1660 cm^{-1} peaks. The band centered at 1340 cm^{-1} also decreased slightly over the mineralization period; this signal has been assigned to protein-helices where its intensity

is sensitive to molecular orientation. However, not all Raman spectral bands, such as the 1243 cm^{-1} and 1307 cm^{-1} bands, underwent substantial changes during the mineralization period. Some control experiments were conducted to rule out the possibility of an artifactual explanation. For instance, direct Raman spectral analyses of UMR 106 cells that were either underlying or adjacent to BMF showed an absence of hydroxyapatite spectrally, as no peak was evident at 957–960 cm^{-1}.[270]

3.6.1.3 Single Cell Analysis

In a study by Ichimura *et al.* 2014., two cell lines were chosen: the murine neuroblastoma cell line, Neuro2a (N2a) (commonly used for studies into neuronal differentiation) and the 3T3L1 cell line, originating from NIH3T3 cells, which can transform into cells resembling adipocytes. Upon initiating the differentiation process, these cells exhibit specific phenotypes. For N2a, this includes a rapid emergence of neurites, whereas for 3T3L1, there is an accumulation of lipid droplets. The differentiation status of a cell is often predicted from its morphology, however, the changes are subtle in some cases and lack a quantifiable aspect. Post-differentiation Raman images highlighted the appearance of large lipid droplets and an increased quantity of cytochrome C in the cytosol across both cell lines. For a more in-depth understanding, Raman spectra were averaged from the nucleus before and after the differentiation of N2a and 3T3-L1. The spectral data displayed noticeable differences post-differentiation, specifically around 1583 cm^{-1} for both cell lines. To scrutinize these spectral changes resulting from differentiation, PCA was applied individually to the two cell lines, with each dataset consisting of 8 to 26 nuclei. [64,113–115]The score plot on the PC1-PC2 plane exhibited minor yet observable differences between the Raman spectra of cells both pre- and post-differentiation for both N2a and 3T3L1. This finding cemented the idea that the combination of Raman spectroscopy and PCA could effectively discriminate between different

cell states.[299] A similar approach to measuring cellular differentiation in single THP-1 monocytes was done by Kallepitis *et al.* 2016. Hyperspectral analysis was done on a z-stack centered on fixed, single THP-1 cell on MgF_2 slides suspended before and after cellular differentiation and datasets were compared. The group identified several lipid components including triglycerides, phospholipids and cholesterol esters, all of which were present in much high quantities after the cells had differentiated

Building off this concept, the ability to side step traditional biochemical labels opens the ability to find new markers of cell proliferation as well. In research conducted by Ramamurthy *et al.* in 2018, Raman spectroscopy was employed to probe the distribution of cellular lipids, specifically within the nuclei of cells. The team discovered that the most organized lipids, as suggested by the 2870/2850 cm^{-1} lipid peak ratios, were located in the nuclei of MG63 cells in interphase. They also observed that these lipids, which often share their location with nuclear chromatin, maintain their association throughout mitosis. A key finding was the identification of phosphatidylinositol as a central component of these highly organized lipids. Unveiling this unique, highly ordered arrangement within the nuclear interior adds a new dimension to our understanding of cellular lipid distribution through mitosis, though the molecular mechanisms driving the organization of these lipids and their potential influence on nuclear activities are not fully understood.[295] The explicit use of MG63 cells (a rarity in Raman confocal), ais in laying the ground work to further investigate the MG63 cell line in more depth and different areas of focus.

Finally, Raman confocal analysis allows for the probing of live, single cell analysis. In work by Li *et al.* 2019, the groundwork was laid for live imaging of single osteosarcoma cells, providing Raman visualization of subcellular features including proteins, lipids and nucleic acids.[267] Using PCA the group was able to distinguish the cell membrane, cytoplasm, cell organelles and the

nucleus from one another in real time, providing both the biochemical signal as well as morphology. A study by Chang *et al.* 2015 performed live single cells analysis on medley of osteosarcoma cells including MG63 cells. The study graded the various cell lines on the amount of hydroxyapatite production and matrix metalloproteinase expression, finding low expression hydroxyapatite to be useful as an indication of malignancy.[266] Cell viability has also been quantified in real time by Notingher *et al.* 2005, using changes at 782, 788 and 1095 cm^{-1} peaks to determine the stage of the cell cycle MBA-MD-231breast cancer cells were currently in, as well as, successfully distinguishing between live and dead cells.[283]

CONCLUSION

Overall, the research presented in this thesis demonstrates:

(Chapter 2) Preconditioning in a high glucose environment significantly modulated the behavior of MG63 osteoblastic cells on nanotubular surfaces, reducing the influence on critical cellular functions such as proliferation and differentiation. Notably, the nanotubular surfaces (and titanium in general) demonstrated an adaptive capacity, largely maintaining their beneficial effects on osteogenesis regardless of glucose levels, being environmentally agnostic to such changes.

(Chapter 3) This study systematically examined the impact of nanotopographical complexity on MG63 osteoblastic cell behavior using a gradient of titanium nanotubular surfaces anodized at 60V. The HC gradients generated through this process effectively showcased a diverse range of nanotubular configurations, with the 60V method proving the most stable. A clear progression was observed from A1 to A7 across metrics like nanotube density, lacunarity, fractal dimension, and entropy, demonstrating that increased nanotopographical complexity enhances cellular responses. The A7 surfaces had the most positive effects on cell morphology, mitochondrial distribution, and proliferation, while A1 had the weakest impact. The influence of spatial metrics (entropy, lacunarity, packing order etc.) on cell behavior provided valuable insights for predicting and optimizing surface properties, enabling high-throughput screening to efficiently identify optimal surface characteristics.

(Chapter 4) The validation of the high-throughput process for creating and optimizing nanotubular surfaces successfully confirmed the findings from the nanotubular gradient studies. This work reinforced the reliability and effectiveness of the gradients in predicting cellular behavior and optimizing surface characteristics for osteogenesis, while additionally providing insights into the mechanisms driven by the HCO surface that effect early differentiation so

profoundly. The successful implementation of Raman confocal single-cell microscopy on opaque titanium, though secondary, provided an additional layer of insight into the molecular interactions at play, laying the groundwork for further exploration into this field of study.

Taken together, these studies highlight the development of engineered nanotubular surfaces with tailored physicochemical properties that effectively elicit specific osteoblastic responses. The adaptive nature of these surfaces, coupled with their ability to function across varying environmental conditions, offers valuable insights into the design and application of biomaterials for bone tissue engineering.

CHAPTER 5: FUTURE DIRECTIONS

Future research should focus on experiments exploring the mechanisms of preconditioning in MG63 osteoblastic cells, particularly how preconditioning in high glucose environments affect mechanisms surrounding cell viability, proliferation and differentiation. Proteomic comparisons between preconditioned and non-preconditioned cells could shed light on subtle mechanistic changes within the cell, providing deeper insights into how preconditioning modulates cellular behavior in response to nanotopographical cues. Expanding these studies to include different time frames and varying levels of glucose could help delineate the boundaries between temporary and permanent cellular adaptations.

To further advance the development of optimized nanotubular surfaces, future work should focus on refining the gradient anodization setup with precise temperature control. This will allow for sustained exposure to elevated voltage levels, enabling the formation of larger HC-T2 domains with variable wall thickness and controlled T1 spacing. Additionally, the exploration of single nanotube gradients using low initial voltages followed by higher voltages in a second anodization step should be pursued, despite the high disorder observed. Research on these gradients could lead to surfaces that effectively control disorder for both honeycomb and single-tube structures, enhancing their applicability in biomedical contexts.

Moreover, the application of coatings to these gradient surfaces presents a promising area of study. Previous work in our lab has shown that catecholamines like norepinephrine can elicit beneficial cellular responses. Combining these biochemical effects with the nanotopographical benefits of the surfaces could yield synergistic outcomes. Investigating the interactions between

these coatings and the nanotubular gradient surfaces could open new avenues for enhancing cell response in rapid fashion.

Further exploration of the YAP1/Hippo signaling pathway on nanotubular surfaces is also a viable next step. Employing robust techniques such as Western blotting or qPCR, combined with the use of blocking compounds like verteporfin, could provide more detailed insights into the pathways and mechanisms that influence osteoblast proliferation and differentiation. Understanding which pathways are most dominant in response to specific nanotopographies could guide the design of more targeted biomaterials.

Now that the experimental protocol for Raman confocal single-cell microscopy has been established, this technique should be applied more broadly to study cell-surface interactions on both metallic opaque surfaces and transparent polymers. Future work should focus on developing more robust noise removal methods to improve the quality of Raman spectra. Accessing MATLAB libraries for handling Witec spectra, as recommended by experts like Dr. Mads Bergholt, could significantly enhance background subtraction, smoothing, and data processing capabilities. The current Witec Project 4.1 Pro software is limited in these aspects, and developing custom methods will be essential.

Additionally, reducing noise through higher integration times and increased sample size is recommended, though this approach is time intensive. Modifying the alpha 300r microscope with a temperature control stage capable of both cooling and heating may allow for higher laser power usage by potentially reducing localized heating. Such a setup may prevent the formation of heat related bubbles, and by exclusion, potentially determining whether the titanium nanotubes exhibit photocatalytic properties or if the observed bubbles and surface interferences are due to heating and degassing. If the former is true, quantifying the photocatalytic sensitivities of these materials

could lead to new applications, expanding the utility of nanotubular surfaces in various biomedical contexts.

REFERENCES

1. Biggs, M. J. P., Richards, R. G. & Dalby, M. J. Nanotopographical modification: A regulator of cellular function through focal adhesions. *Nanomedicine* **6**, 619–633 (2010).
2. Steeves, A. J. *et al.* The implication of spatial statistics in human mesenchymal stem cell response to nanotubular architectures. *Int J Nanomedicine* **15**, 2151–2169 (2020).
3. J, D. M. Nanostructured surfaces : cell engineering and cell biology E ditorial. *Nanomedicine* **4**, 247–248 (2009).
4. de Peppo, G. M. *et al.* Osteogenic response of human mesenchymal stem cells to well-defined nanoscale topography in vitro. *Int J Nanomedicine* **9**, 2499–2515 (2014).
5. Perez, J. E., Ravasi, T. & Kosel, J. Mesenchymal stem cells cultured on magnetic nanowire substrates. *Nanotechnology* **28**, (2017).
6. Kuo, S. W. *et al.* Regulation of the fate of human mesenchymal stem cells by mechanical and stereo-topographical cues provided by silicon nanowires. *Biomaterials* **33**, 5013–5022 (2012).
7. US FDA. Biological Responses to Metal Implants. *Food and Drug Admistration (FDA)* 1–143 (2019).
8. Dalby, M. J., Gadegaard, N. & Oreffo, R. O. C. Harnessing nanotopography and integrin-matrix interactions to influence stem cell fate. *Nat Mater* **13**, 558–569 (2014).
9. Kulkarni, M. *et al.* Titanium nanostructures for biomedical applications. *Nanotechnology* **26**, (2015).
10. Amin Yavari, S. *et al.* Bone regeneration performance of surface-treated porous titanium. *Biomaterials* **35**, 6172–6181 (2014).
11. Sidambe, A. T. Biocompatibility of advanced manufactured titanium implants-A review. *Materials* **7**, 8168–8188 (2014).
12. Zhukova, Y. *et al.* The Role of Titanium Surface Nanostructuring on Preosteoblast Morphology, Adhesion, and Migration. *Adv Healthc Mater* **6**, 1–13 (2017).
13. Biggs, M. J. P. & McNamara, L. E. The modulation of skeletal stem cell function through nanoscale topography. *Stem Cells and Bone Tissue* 125–144 (2013) doi:10.1201/b14590.
14. Dalby, M. J. *et al.* Nanotopographical stimulation of mechanotransduction and changes in interphase centromere positioning. *J Cell Biochem* **100**, 326–338 (2007).
15. Gulati, K., Santos, A., Findlay, D. & Losic, D. Optimizing anodization conditions for the growth of titania nanotubes on curved surfaces. *Journal of Physical Chemistry C* **119**, 16033–16045 (2015).
16. Krabbenborg, S. O. & Huskens, J. Electrochemically generated gradients. *Angewandte Chemie - International Edition* vol. 53 9152–9167 Preprint at https://doi.org/10.1002/anie.201310349 (2014).

17. Zhang, Q. *et al.* Fabrication and formation mechanism of gradient TiO2 nanotubes via bipolar anodization. *Journal of Electroanalytical Chemistry* **915**, 116337 (2022).

18. Li, Y. *et al.* Effect of size and crystalline phase of TiO2 nanotubes on cell behaviors: A high throughput study using gradient TiO2 nanotubes. *Bioact Mater* **5**, 1062–1070 (2020).

19. Yang, J. *et al.* Tio2 nanotubes alleviate diabetes-induced osteogenetic inhibition. *Int J Nanomedicine* **15**, 3523–3537 (2020).

20. Basmaeil, Y. *et al.* Preconditioning of Human Decidua Basalis Mesenchymal Stem/Stromal Cells with Glucose Increased Their Engraftment and Anti-diabetic Properties. *Tissue Eng Regen Med* **17**, 209–222 (2020).

21. Pastukh, V. *et al.* Reversal of hyperglycemic preconditioning by angiotensin II: role of calcium transport Downloaded from. *Am J Physiol Heart Circ Physiol* **288**, 1965–1975 (2005).

22. Guan, J. *et al.* Oxygen-glucose deprivation preconditioning protects neurons against oxygen-glucose deprivation/reperfusion induced injury via bone morphogenetic protein-7 mediated ERK, p38 and Smad signalling pathways. *Clin Exp Pharmacol Physiol* **43**, 125–134 (2016).

23. Xuan, Y. H. *et al.* High-glucose inhibits human fibroblast cell migration in wound healing via repression of bFGF-regulating JNK phosphorylation. *PLoS One* **9**, (2014).

24. McGarvey, J. J. & Renwick Beattie, J. Raman microscopy: A versatile approach to bio-imaging. *Springer Series in Optical Sciences* **168**, 219–242 (2012).

25. Robey, P. G. & Bianco, P. The Collagenous and Noncollagenous Proteins of Cells in the Osteoblastic Lineage. in *Molecular and Cellular Biology of Bone* vol. 5 565–589 (Elsevier, 1998).

26. Ryaby, J. T., Fitzsimmons, R. J., Mohan, S. & Baylink, D. J. Coupling of Bone Formation and Bone Resorption: A Model. in *Molecular and Cellular Biology of Bone* vol. 5 101–122 (Elsevier, 1998).

27. Kartsogiannis, V. & Ng, K. W. Cell lines and primary cell cultures in the study of bone cell biology. *Molecular and Cellular Endocrinology* vol. 228 79–102 Preprint at https://doi.org/10.1016/j.mce.2003.06.002 (2004).

28. Czekanska, E. M., Stoddart, M. J., Ralphs, J. R., Richards, R. G. & Hayes, J. S. A phenotypic comparison of osteoblast cell lines versus human primary osteoblasts for biomaterials testing. *J Biomed Mater Res A* **102**, 2636–2643 (2014).

29. Shapira, L. & Halabi, A. Behavior of two osteoblast-like cell lines cultured on machined or rough titanium surfaces. *Clin Oral Implants Res* **20**, 50–55 (2009).

30. Staehlke, S., Rebl, H. & Nebe, B. Phenotypic stability of the human MG-63 osteoblastic cell line at different passages. *Cell Biol Int* **43**, 22–32 (2019).

31. Wang, J., Zhang, L., Qu, R. & Zhang, L. Rho A Regulates Epidermal Growth Factor-Induced Human Osteosarcoma MG63 Cell Migration. (2018) doi:10.3390/ijms19051437.

32. Zhang, Z. *et al.* AMD3465 (hexahydrobromide) rescues the MG63 osteoblasts against the apoptosis induced by high glucose. *Biomedicine and Pharmacotherapy* **138**, 111476 (2021).

33. Shao, X., Cao, X., Song, G., Zhao, Y. & Shi, B. Metformin rescues the MG63 osteoblasts against the effect of high glucose on proliferation. *J Diabetes Res* **2014**, (2014).

34. Linxi, Z., Guirong, Z., Xue, W. & Gang, S. The effect of high glucose on proliferation and expression of correlation factors of MG63 osteoblasts. *J Hard Tissue Biol* **24**, 143–146 (2015).

35. Chen, X. *et al.* Xianling Gubao attenuates high glucose-induced bone metabolism disorder in MG63 osteoblast-like cells. *PLoS One* **17**, (2022).

36. Yang, J. *et al.* Tio2 nanotubes alleviate diabetes-induced osteogenetic inhibition. *Int J Nanomedicine* **15**, 3523–3537 (2020).

37. Lee, L. C. Y. *et al.* Nanotopography controls cell cycle changes involved with skeletal stem cell self-renewal and multipotency. *Biomaterials* **116**, 10–20 (2017).

38. Burger, E. H., Klein-Nulend, J. & Cowin, S. C. Mechanotransduction in Bone. in *Molecular and Cellular Biology of Bone* vol. 5 123–136 (Elsevier, 1998).

39. Barcelona-Estaje, E., Dalby, M. J., Cantini, M. & Salmeron-Sanchez, M. You Talking to Me? Cadherin and Integrin Crosstalk in Biomaterial Design. *Adv Healthc Mater* **10**, (2021).

40. Davison, M. J., McMurray, R. J., Smith, C. A., Dalby, M. J. & Meek, R. D. Nanopit-induced osteoprogenitor cell differentiation: The effect of nanopit depth. *J Tissue Eng* **7**, (2016).

41. Tsao, Y. T. *et al.* Osteocalcin mediates biomineralization during osteogenic maturation in human mesenchymal stromal cells. *Int J Mol Sci* **18**, (2017).

42. Chen, J. C., Castillo, A. B. & Jacobs, C. R. *Cellular and Molecular Mechanotransduction in Bone*. *Osteoporosis: Fourth Edition* (Elsevier, 2013). doi:10.1016/B978-0-12-415853-5.00020-0.

43. Arvind, V. & Huang, A. H. Mechanobiology of limb musculoskeletal development. *Ann N Y Acad Sci* **1409**, 18–32 (2017).

44. Tsimbouri, P. Adult Stem Cell Responses to Nanostimuli. *J Funct Biomater* **6**, 598–622 (2015).

45. Miller, I. *et al.* Ki67 is a Graded Rather than a Binary Marker of Proliferation versus Quiescence. *Cell Rep* **24**, 1105-1112.e5 (2018).

46. Galea, G. L. *et al.* Estrogen receptor α mediates proliferation of osteoblastic cells stimulated by estrogen and mechanical strain, but their acute down-regulation of the Wnt antagonist Sost is mediated by estrogen receptor β. *Journal of Biological Chemistry* **288**, 9035–9048 (2013).

47. Tolbert, C. & Burridge, K. Focal Adhesions. *Cellular Domains* 285–302 (2011) doi:10.1002/9781118015759.ch17.

48. Bologna-Molina, R., Mosqueda-Taylor, A., Molina-Frechero, N., Mori-Estevez, A. D. & Sánchez-Acuña, G. Comparison of the value of PCNA and Ki-67 as markers of cell proliferation in ameloblastic tumors. *Med Oral Patol Oral Cir Bucal* **18**, (2013).

49. Hülter-Hassler, D. *et al.* Biomechanical strain-induced modulation of proliferation coincides with an ERK1/2-independent nuclear YAP localization. *Exp Cell Res* **361**, 93–100 (2017).

50. Patents; 'Modified Surfaces for Attachment of Biological Materials' in Patent Application Approval Process (USPTO 20170112962). 936 Article at (2017).

51. Gaviria, L., Salcido, J. P., Guda, T. & Ong, J. L. Current trends in dental implants. *J Korean Assoc Oral Maxillofac Surg* **40**, 50 (2014).

52. Park, S. Y. *et al.* Carbon nanotube monolayer patterns for directed growth of mesenchymal stem cells. *Advanced Materials* **19**, 2530–2534 (2007).

53. Kuo, C. W., Chueh, D. Y. & Chen, P. Investigation of size-dependent cell adhesion on nanostructured interfaces. *J Nanobiotechnology* **12**, 1–10 (2014).

54. Sjöström, T. *et al.* Fabrication of pillar-like titania nanostructures on titanium and their interactions with human skeletal stem cells. *Acta Biomater* **5**, 1433–1441 (2009).

55. Park, S. & Im, G. Il. Stem cell responses to nanotopography. *J Biomed Mater Res A* **103**, 1238–1245 (2015).

56. Simon, K. A. *et al.* Enhancing cell adhesion and confinement by gradient nanotopography. *J Am Chem Soc* **129**, 4892–4893 (2007).

57. Wang, P. Y. *et al.* Screening mesenchymal stem cell attachment and differentiation on porous silicon gradients. *Adv Funct Mater* **22**, 3414–3423 (2012).

58. Ni, J. H. *et al.* Fabrication of gradient TiO2 nanotubes on Ti foil by anodization. *Adv Eng Mater* **15**, 464–468 (2013).

59. Wang, P. Y. *et al.* Screening mesenchymal stem cell attachment and differentiation on porous silicon gradients. *Adv Funct Mater* **22**, 3414–3423 (2012).

60. Kunzler, T. P., Drobek, T., Schuler, M. & Spencer, N. D. Systematic study of osteoblast and fibroblast response to roughness by means of surface-morphology gradients. *Biomaterials* **28**, 2175–2182 (2007).

61. Park, J., Bauer, S., Von Der Mark, K. & Schmuki, P. Nanosize and vitality: TiO2 nanotube diameter directs cell fate. *Nano Lett* **7**, 1686–1691 (2007).

62. Wang, P. Stem Cell Response to Surface Micro- and Nanotopography Part 4 Control of Stem-Cell Fate by Engineering of Microenvironment. in *Stem-Cell Nanoengineering* 187–203 (John Wiley & Sons, Inc. Published, 2015).

63. Su, E. P. *et al.* Effects of titanium nanotubes on the osseointegration, cell differentiation, mineralisation and antibacterial properties of orthopaedic implant surfaces. *Bone and Joint Journal* **100B**, 9–16 (2018).

64. Sousa, A. A. & Kruhlak, M. J. Introduction: Nanoimaging techniques in biology. *Methods in Molecular Biology* **950**, 1–10 (2013).

65. Eaton, P. Jonathan. & West, Paul. *Atomic Force Microscopy*. (Oxford University Press, 2010).

66. Ferraro, J. R., Nakamoto, K. & Brown, C. W. *Introductory Raman Spectroscopy: Second Edition*. *Introductory Raman Spectroscopy: Second Edition* (2003). doi:10.1016/B978-0-12-254105-6.X5000-8.

67. Bergholt, M. S., Serio, A. & Albro, M. B. Raman Spectroscopy: Guiding Light for the Extracellular Matrix. *Front Bioeng Biotechnol* **7**, 1–16 (2019).

68. Cortés-Jácome, M. A. *et al.* In situ thermo-Raman study of titanium oxide nanotubes. *Catal Today* **126**, 248–255 (2007).

69. Niilisk, A. *et al.* Structural study of TiO2 thin films by micro-Raman spectroscopy. *Central European Journal of Physics* **4**, 105–116 (2006).

70. Song, R. *et al.* Facile construction of structural gradient of TiO2 nanotube arrays on medical titanium for high throughput evaluation of biocompatibility and antibacterial property. *ACS Appl Bio Mater* **1**, 1056–1065 (2018).

71. Goto, T. *[Osseointegration and Dental Implants]*. *Clinical calcium* vol. 24 (2014).

72. Subramani, K., Ahmed, W. & Pachauri, P. *Titanium Nanotubes as Carriers of Osteogenic Growth Factors and Antibacterial Drugs for Applications in Dental Implantology*. *Emerging Nanotechnologies in Dentistry: Second Edition* (Elsevier Inc., 2018). doi:10.1016/B978-0-12-812291-4.00007-8.

73. Gulati, K. *et al.* Anodized 3D–printed titanium implants with dual micro- and nano-scale topography promote interaction with human osteoblasts and osteocyte-like cells. *J Tissue Eng Regen Med* **11**, 3313–3325 (2017).

74. Tan, A. W., Pingguan-Murphy, B., Ahmad, R. & Akbar, S. A. Review of titania nanotubes: Fabrication and cellular response. *Ceram Int* **38**, 4421–4435 (2012).

75. Berger, D. R., Popat, K. & Prasad, A. Nanotopography Driven Mesenchymal Stem Cell Differentiation and Proliferation. *Biophys J* **102**, 705a–706a (2012).

76. Brammer, K. S., Oh, S., Gallagher, J. O. & Jin, S. Enhanced cellular mobility guided by TiO2 nanotube surfaces. *Nano Lett* **8**, 786–793 (2008).

77. Arnold, M. *et al.* Activation of integrin function by nanopatterned adhesive interfaces. *ChemPhysChem* **5**, 383–388 (2004).

78. Bauer, M. S. *et al.* Structural and mechanistic insights into mechanoactivation of focal adhesion kinase. *Proc Natl Acad Sci U S A* **116**, 6766–6774 (2019).

79. Park, J. *et al.* TiO2 nanotube surfaces: 15 nm - an optimal length scale of surface topography for cell adhesion and differentiation. *Small* **5**, 666–671 (2009).

80. Orimo, H. & Shimada, T. Regulation of the human tissue-nonspecific alkaline phosphatase gene expression by all-trans-retinoic acid in SaOS-2 osteosarcoma cell line. *Bone* **36**, 866–876 (2005).

81. Oh, S. *et al. Stem Cell Fate Dictated Solely by Altered Nanotube Dimension*. www.pnas.org/cgi/content/full/ (2009).

82. Popat, K. C., Leoni, L., Grimes, C. A. & Desai, T. A. Influence of engineered titania nanotubular surfaces on bone cells. *Biomaterials* **28**, 3188–3197 (2007).

83. Das, K., Bose, S. & Bandyopadhyay, A. TiO2 nanotubes on Ti: Influence of nanoscale morphology on bone cell-materials interaction. *J Biomed Mater Res A* **90**, 225–237 (2009).

84. He, Y. *et al.* Nanotopographical cues for regulation of macrophages and osteoclasts: emerging opportunities for osseointegration. *J Nanobiotechnology* **20**, 1–22 (2022).

85. Kshitiz, Afzal, J., Kim, S. Y. & Kim, D. H. A nanotopography approach for studying the structure-function relationships of cells and tissues. *Cell Adh Migr* **9**, 300–307 (2015).

86. Jesus, D., Pinho, A. R., Gomes, M. C., Oliveira, C. S. & Mano, J. F. Emerging modulators for osteogenic differentiation: a combination of chemical and topographical cues for bone microenvironment engineering. *Soft Matter* **18**, 3107–3119 (2022).

87. Cao, S. & Yuan, Q. An update of nanotopographical surfaces in modulating stem cell fate: a narrative review. *Biomaterials Translational* **3**, 55–64 (2022).

88. Xiao, L., Sun, Y., Liao, L. & Su, X. Response of mesenchymal stem cells to surface topography of scaffolds and the underlying mechanisms. *J Mater Chem B* **11**, 2550–2567 (2023).

89. Nazemi, M. & Rainero, E. Cross-Talk Between the Tumor Microenvironment, Extracellular Matrix, and Cell Metabolism in Cancer. *Front Oncol* **10**, 1–7 (2020).

90. Kim, H. N. *et al.* Nanotopography-guided tissue engineering and regenerative medicine. *Adv Drug Deliv Rev* **65**, 536–558 (2013).

91. Potapova, I. Functional Imaging in Diagnostic of Orthopedic Implant-Associated Infections. *Diagnostics* **3**, 356–371 (2013).

92. Gulati, K. *et al.* Drug-releasing nano-engineered titanium implants: therapeutic efficacy in 3D cell culture model, controlled release and stability. *Materials Science and Engineering C* **69**, 831–840 (2016).

93. Shah, F. A., Nilson, B., Brånemark, R., Thomsen, P. & Palmquist, A. The bone-implant interface - nanoscale analysis of clinically retrieved dental implants. *Nanomedicine* **10**, 1729–1737 (2014).

94. Yusop, N., Moseley, R. & Waddington, R. J. Hyperglycemia exerts disruptive effects on the secretion of TGF-β1 and its matrix ligands, decorin and biglycan, by mesenchymal sub-populations and macrophages during bone repair. *Frontiers in Dental Medicine* **4**, (2023).

95. Gopalakrishnan, V., Vignesh, R. C., Arunakaran, J., Aruldhas, M. M. & Srinivasan, N. Effects of glucose and its modulation by insulin and estradiol on BMSC differentiation into osteoblastic lineages. *Biochemistry and Cell Biology* **84**, 93–101 (2006).

96. Chen, N. X., Duan, D., O'Neill, K. D. & Moe, S. M. High glucose increases the expression of Cbfa1 and BMP-2 and enhances the calcification of vascular smooth muscle cells. *Nephrology Dialysis Transplantation* **21**, 3435–3442 (2006).

97. Suzuki, Y., Kim, H. W., Ashraf, M. & Haider, H. K. Diazoxide potentiates mesenchymal stem cell survival via NF-κB-dependent miR-146a expression by targeting Fas. *Am J Physiol Heart Circ Physiol* **299**, (2010).

98. Feng, Y. F. *et al.* Effect of reactive oxygen species overproduction on osteogenesis of porous titanium implant in the present of diabetes mellitus. *Biomaterials* **34**, 2234–2243 (2013).

99. Guan, C. chao *et al.* Sonic hedgehog alleviates the inhibitory effects of high glucose on the osteoblastic differentiation of bone marrow stromal cells. *Bone* **45**, 1146–1152 (2009).

100. Al-Qarakhli, A. M. A., Yusop, N., Waddington, R. J. & Moseley, R. Effects of high glucose conditions on the expansion and differentiation capabilities of mesenchymal stromal cells derived from rat endosteal niche. *BMC Mol Cell Biol* **20**, (2019).

101. Tan, N. *et al.* The influence of direct laser metal sintering implants on the early stages of osseointegration in diabetic mini-pigs. *Int J Nanomedicine* **12**, 5433–5442 (2017).

102. Yu, Y. *et al.* Osteogenesis potential of different titania nanotubes in oxidative stress microenvironment. *Biomaterials* **167**, 44–57 (2018).

103. Valdez-Salas, B. *et al.* Recovering Osteoblast Functionality on TiO2 Nanotube Surfaces Under Diabetic Conditions. *Int J Nanomedicine* **17**, 5469–5488 (2022).

104. Dong, S. *et al.* Sandblasted/Acid-Etched Titanium Surface Modified with Calcium Phytate Enhances Bone Regeneration in a High-Glucose Microenvironment by Regulating Reactive Oxygen Species and Cell Senescence. *ACS Biomater Sci Eng* **9**, 4720–4734 (2023).

105. Jiang, H. *et al.* The Effects of Hierarchical Micro/Nano-Structured Titanium Surface on Osteoblast Proliferation and Differentiation under Diabetic Conditions. *Implant Dent* **26**, 263–269 (2017).

106. Takeno, A. *et al.* High glucose promotes mineralization via bone morphogenetic protein 4-Smad signals in early stage of osteoblast differentiation. *Diabetol Int* **12**, 171–180 (2021).

107. Wang, W., Zhang, X., Zheng, J. & Yang, J. High glucose stimulates adipogenic and inhibits osteogenic differentiation in MG-63 cells through cAMP/protein kinase A/extracellular signal-regulated kinase pathway. *Mol Cell Biochem* **338**, 115–122 (2010).

108. Ottawa: Diabetes Canada. Diabetes in Canada: Backgrounder. 1–7 (2022).

109. Chen, C. H. *et al.* Thrombomodulin Functional Domains Support Osteoblast Differentiation and Bone Healing in Diabetes in Mice. *Journal of Bone and Mineral Research* **35**, 1812–1823 (2020).

110. Dhanasekaran, M., Indumathi, S., Rajkumar, J. S. & Sudarsanam, D. Effect of high glucose on extensive culturing of mesenchymal stem cells derived from subcutaneous fat, omentum fat and bone marrow. *Cell Biochem Funct* **31**, 20–29 (2013).

111. Kim, Y. H., Heo, J. S. & Han, H. J. High glucose increase cell cycle regulatory proteins level of mouse embryonic stem cells via PI3-K/Akt and MAPKs signal pathways. *J Cell Physiol* **209**, 94–102 (2006).

112. Sato, K. *et al.* Hyperglycemia enhances pancreatic cancer progression accompanied by elevations in phosphorylated STAT3 and MYC levels. *PLoS One* **15**, (2020).

113. Saini, M. Implant biomaterials: A comprehensive review. *World J Clin Cases* **3**, 52 (2015).

114. Kazimierczak, P. & Przekora, A. Osteoconductive and Osteoinductive Surface Modifications of Biomaterials for Bone Regeneration: A Concise Review. *Coatings* **10**, 971 (2020).

115. Yan, X., Cao, W. & Li, H. Biomedical alloys and physical surface modifications: A mini-review. *Materials* **15**, (2022).

116. Dobbenga, S., Fratila-Apachitei, L. E. & Zadpoor, A. A. Nanopattern-induced osteogenic differentiation of stem cells – A systematic review. *Acta Biomater* **46**, 3–14 (2016).

117. Rajendran, A. K. *et al.* Trends in mechanobiology guided tissue engineering and tools to study cell-substrate interactions: a brief review. *Biomater Res* **27**, 1–24 (2023).

118. Zhang, Y. *et al.* Investigation of nanotopography on SOCE mediated cell migration via live-cell: Imaging on opaque implant surface. *J Nanobiotechnology* **21**, 1–12 (2023).

119. Zhianmanesh, M., Gilmour, A., Bilek, M. M. M. & Akhavan, B. Plasma surface functionalization: A comprehensive review of advances in the quest for bioinstructive materials and interfaces. *Appl Phys Rev* **10**, (2023).

120. Kargupta, R. *et al.* Coatings and surface modifications imparting antimicrobial activity to orthopedic implants. *Wiley Interdiscip Rev Nanomed Nanobiotechnol* **6**, 475–495 (2014).

121. Florea, D. A., Albuleț, D., Grumezescu, A. M. & Andronescu, E. Surface modification – A step forward to overcome the current challenges in orthopedic industry and to obtain an improved osseointegration and antimicrobial properties. *Mater Chem Phys* **243**, 122579 (2020).

122. Wen, X., Liu, Y., Xi, F., Zhang, X. & Kang, Y. Micro-arc oxidation (MAO) and its potential for improving the performance of titanium implants in biomedical applications. *Front Bioeng Biotechnol* **11**, 1–23 (2023).

123. Fialho, L. & Carvalho, S. Surface engineering of nanostructured Ta surface with incorporation of osteoconductive elements by anodization. *Appl Surf Sci* **495**, 143573 (2019).

124. Batool, S. A., Salman Maqbool, M., Javed, M. A., Niaz, A. & Rehman, M. A. U. A Review on the Fabrication and Characterization of Titania Nanotubes Obtained via Electrochemical Anodization. *Surfaces* **5**, 456–480 (2022).

125. Fei, D., Chen, L. & Zhang, Y. Nanostructured titanium regulates osseointegration via influencing macrophage polarization in the osteogenic environment. *Int J Nanomedicine* **13**, 4029–4043 (2018).

126. Bjursten, L. M. *et al.* Titanium dioxide nanotubes enhance bone bonding in vivo. *J Biomed Mater Res A* **92**, 1218–1224 (2010).

127. Zhang, H. *et al.* Titanium nanotubes induce osteogenic differentiation through the FAK/RhoA/YAP cascade. *RSC Adv* **6**, 44062–44069 (2016).

128. Cheng, Y. *et al.* Progress in TiO2 nanotube coatings for biomedical applications: A review. *J Mater Chem B* **6**, 1862–1886 (2018).

129. Cheng, Y.-L. *et al.* Titanium Dioxide Nanotube Arrays for Biomedical Implant Materials and Nanomedicine Applications. *Intech* **11**, 13 (2018).

130. Păun, A. G. *et al.* Y-Branched Titanium Dioxide Nanotubes as a Potential Antimicrobial Coating for Implants. *Crystals (Basel)* **13**, (2023).

131. Bartlet, K., Movafaghi, S., Prasad, L., Kota, A. K. & Popat, K. C. Colloids and Surfaces B : Biointerfaces Antibacterial activity on superhydrophobic titania nanotube arrays. *Colloids Surf B Biointerfaces* **166**, 179–186 (2018).

132. Cowden, K., Dias-netipanyj, M. F. & Popat, K. C. Effects of titania nanotube surfaces on osteogenic differentiation of human adipose-derived stem cells. *Nanomedicine* **17**, 380–390 (2019).

133. Savargaonkar, A. V., Munshi, A. H. & Soares, P. Antifouling Behavior of Copper-Modified Titania Nanotube Surfaces. *J Funct Biomater* **14**, 413 (2023).

134. Park, J. *et al.* Nanoscale Topography of Anodic TiO 2 Nanostructures Is Crucial for Cell − Surface Interactions. *ACS Appl Mater Interfaces* **16**, 4430–4438 (2024).

135. Steeves, A. J. *et al.* The implication of spatial statistics in human mesenchymal stem cell response to nanotubular architectures. *Int J Nanomedicine* **15**, 2151–2169 (2020).

136. Yu, W. Q., Jiang, X. Q., Zhang, F. Q. & Xu, L. The effect of anatase TiO2 nanotube layers on MC3T3-E1 preosteoblast adhesion, proliferation, and differentiation. *J Biomed Mater Res A* **94**, 1012–1022 (2010).

137. Dalby, M. J. *et al.* The control of human mesenchymal cell differentiation using nanoscale symmetry and disorder. *Nat Mater* **6**, 997–1003 (2007).

138. Filova, E. *et al.* The diameter of nanotubes formed on Ti-6Al-4V alloy controls the adhesion and differentiation of Saos-2 cells. *Int J Nanomedicine* **10**, 7145–7163 (2015).

139. Wang, C., Gao, S., Lu, R., Wang, X. & Chen, S. In Vitro and In Vivo Studies of Hydrogenated Titanium Dioxide Nanotubes with Superhydrophilic Surfaces during Early Osseointegration. *Cells* **11**, (2022).

140. Gasik, M. Understanding biomaterial-tissue interface quality: combined in vitro evaluation. *Sci Technol Adv Mater* **18**, 550–562 (2017).

141. Al-Shalawi, F. D. *et al.* Biomaterials as Implants in the Orthopedic Field for Regenerative Medicine: Metal versus Synthetic Polymers. *Polymers (Basel)* **15**, (2023).

142. Cometta, S., Hutmacher, D. W. & Chai, L. In vitro models for studying implant-associated biofilms - A review from the perspective of bioengineering 3D microenvironments. *Biomaterials* **309**, 122578 (2024).

143. Chen, Y. *et al.* Investigation for GSK3β expression in diabetic osteoporosis and negative osteogenic effects of GSK3β on bone marrow mesenchymal stem cells under a high glucose microenvironment. *Biochem Biophys Res Commun* **534**, 727–733 (2021).

144. Oliveira, P. G. F. P. *et al.* Histological and nanomechanical properties of a new nanometric hydroxiapatite implant surface. An in vivo study in diabetic rats. *Materials* **13**, 1–17 (2020).

145. Goreham, R. V., Mierczynska, A., Smith, L. E., Sedev, R. & Vasilev, K. Small surface nanotopography encourages fibroblast and osteoblast cell adhesion. *RSC Adv* **3**, 10309–10317 (2013).

146. Xie, Y. *et al.* Beta1-integrin/Hedgehog-Gli1 signaling pathway fuels the diameter-dependent osteoblast differentiation on different TiO2 nanotubes: The optimal-diameter nanotubes for osteoblast differentiation. *International Journal of Biochemistry and Cell Biology* **137**, 106026 (2021).

147. Li, Y. *et al.* Impact of diabetes mellitus simulations on bone cell behavior through in vitro models. *J Bone Miner Metab* **38**, 607–619 (2020).

148. Yuan, G., Zhao, Y., Wu, D. & Gao, C. Mir-150 Up-regulates glut1 and increases glycolysis in osteosarcoma cells. *Asian Pacific Journal of Cancer Prevention* **18**, 1127–1131 (2017).

149. An, F. *et al.* Reprogramming of glucose metabolism: Metabolic alterations in the progression of osteosarcoma. *J Bone Oncol* **44**, 100521 (2024).

150. Ramenzoni, L. L., Bösch, A., Proksch, S., Attin, T. & Schmidlin, P. R. Effect of high glucose levels and lipopolysaccharides-induced inflammation on osteoblast mineralization over sandblasted/acid-etched titanium surface. *Clin Implant Dent Relat Res* **22**, 213–219 (2020).

151. Vijay, R. *et al.* Carbon nanomaterials modified biomimetic dental implants for diabetic patients. *Nanomaterials* **11**, (2021).

152. Bai, Q. *et al.* Potential applications of nanomaterials and technology for diabetic wound healing. *Int J Nanomedicine* **15**, 9717–9743 (2020).

153. Yang, L., Liu, J., Shan, Q., Geng, G. & Shao, P. High glucose inhibits proliferation and differentiation of osteoblast in alveolar bone by inducing pyroptosis. *Biochem Biophys Res Commun* **522**, 471–478 (2020).

154. Kato, H. *et al.* High Glucose Concentrations Suppress the Proliferation of Human Periodontal Ligament Stem Cells and Their Differentiation Into Osteoblasts. *J Periodontol* **87**, 1–20 (2016).

155. Liu, S., Yang, X., Zhong, X., Li, L. & Zhang, X. Involvement of miR-337 in high glucose–suppressed osteogenic differentiation in bone marrow mesenchymal stem cells via negative regulation of Rap1A. *In Vitro Cell Dev Biol Anim* **57**, 350–358 (2021).

156. Medeiros, C. & Wallace, J. M. High glucose-induced inhibition of osteoblast like MC3T3-E1 differentiation promotes mitochondrial perturbations. *PLoS One* **17**, 1–22 (2022).

157. Brown, P. M., Hutchison, J. D. & Crockett, J. C. Absence of Glutamine Supplementation Prevents Differentiation of Murine Calvarial Osteoblasts to a Mineralizing Phenotype. *Calcif Tissue Int* **89**, 472–482 (2011).

158. Rezaei, A. *et al.* Hypoxia mimetics restore bone biomineralisation in hyperglycaemic environments. *Sci Rep* **12**, 1–16 (2022).

159. Aya, B. *et al.* High Glucose in Culture Media of Adipose Derived Mesenchymal Stem Cells – Gene Expression Alteration and Early Senescence. *Stem Cell and Regenerative Medicine* **4**, (2020).

160. Donat, A. *et al.* Glucose metabolism in osteoblasts in healthy and pathophysiological conditions. *International Journal of Molecular Sciences* vol. 22 Preprint at https://doi.org/10.3390/ijms22084120 (2021).

161. Yang, P., Chen, X., Kaushal, S., Reece, E. A. & Yang, P. High glucose suppresses embryonic stem cell differentiation into cardiomyocytes: High glucose inhibits ES cell cardiogenesis. *Stem Cell Res Ther* **7**, (2016).

162. Schindelin, J. *et al.* Fiji: An open-source platform for biological-image analysis. *Nat Methods* **9**, 676–682 (2012).

163. Kikukawa, K., Sato, R., Iwamoto, M. & Higaki, T. Wide-range segmentation of cotyledon epidermal cells for morphometrical analysis and mechanical simulation. *Cytologia* vol. 86 189–194 Preprint at https://doi.org/10.1508/cytologia.86.189 (2021).

164. Phillip, J. M., Han, K. S., Chen, W. C., Wirtz, D. & Wu, P. H. A robust unsupervised machine-learning method to quantify the morphological heterogeneity of cells and nuclei. *Nat Protoc* **16**, 754–774 (2021).

165. Vadori, V., Peruffo, A., Graïc, J.-M., Finos, L. & Grisan, E. Automated Classification of Cell Shapes: A Comparative Evaluation of Shape Descriptors. (2024).

166. Sun, X. & Kaufman, P. D. Ki-67: more than a proliferation marker. *Chromosoma* **127**, 175–186 (2018).

167. Pillai-Kastoori, L., Schutz-Geschwender, A. R. & Harford, J. A. A systematic approach to quantitative Western blot analysis. *Anal Biochem* **593**, (2020).

168. Kirshner, Z. Z. & Gibbs, R. B. Use of the REVERT ® total protein stain as a loading control demonstrates significant benefits over the use of housekeeping proteins when analyzing brain homogenates by Western blot: An analysis of samples representing different gonadal hormone states. *Mol Cell Endocrinol* **473**, 156–165 (2018).

169. Yang, R. Y., Zou, R. P. & Yu, A. B. Voronoi tessellation of the packing of fine uniform spheres. *Phys Rev E Stat Phys Plasmas Fluids Relat Interdiscip Topics* **65**, 8 (2002).

170. Barthélemy, M. Spatial networks. *Phys Rep* **499**, 1–101 (2011).

171. Lanng, M. B. *et al.* Quality assessment of Ki67 staining using cell line proliferation index and stain intensity features. *Cytometry Part A* **95**, 381–388 (2019).

172. Zhang, B. *et al.* High glucose microenvironments inhibit the proliferation and migration of bone mesenchymal stem cells by activating GSK3β. *J Bone Miner Metab* **34**, 140–150 (2016).

173. Brown, J. R., Digiovanna, M. P., Killelea, B., Lannin, D. R. & Rimm, D. L. Quantitative assessment Ki-67 score for prediction of response to neoadjuvant chemotherapy in breast cancer. *Laboratory Investigation* **94**, 98–106 (2014).

174. Scavo, M. P. *et al.* Exosome Released FZD10 Increases Ki-67 Expression via Phospho-ERK1/2 in Colorectal and Gastric Cancer. *Front Oncol* **11**, 1–15 (2021).

175. Montreekachon, P. *et al.* Proliferative effect of cannabidiol in human gingival fibroblasts via the mitogen-activated extracellular signal-regulated kinase (MEK) 1/2. *J Periodontal Res* **58**, 1223–1234 (2023).

176. Huang, Y. Z. *et al.* Nanostructured titanium surfaces fabricated by hydrothermal method: Influence of alkali conditions on the osteogenic performance of implants. *Materials Science and Engineering C* **94**, 1–10 (2019).

177. Gomes, A. M., da Silva, D. F., Bezerra, F. J. & Zambuzzi, W. F. Nanohydroxyapatite-Coated Titanium Surface Increases Vascular Endothelial Cells Distinct Signaling Responding to High Glucose Concentration. *J Funct Biomater* **14**, (2023).

178. Yamawaki, I., Taguchi, Y., Komasa, S., Tanaka, A. & Umeda, M. Effects of glucose concentration on osteogenic differentiation of type II diabetes mellitus rat bone marrow-derived mesenchymal stromal cells on a nano-scale modified titanium. *J Periodontal Res* **52**, 761–771 (2017).

179. Kheur, S. *et al.* In-Vitro Evaluation of Photofunctionalized Implant Surfaces in a High-Glucose Microenvironment Simulating Diabetics. *J Funct Biomater* **14**, (2023).

180. Sjöström, T., Lalev, G., Mansell, J. P. & Su, B. Initial attachment and spreading of MG63 cells on nanopatterned titanium surfaces via through-mask anodization. *Appl Surf Sci* **257**, 4552–4558 (2011).

181. Lamers, E. *et al.* The influence of nanoscale grooved substrates on osteoblast behavior and extracellular matrix deposition. *Biomaterials* **31**, 3307–3316 (2010).

182. Fraioli, R. *et al.* Mimicking bone extracellular matrix: Integrin-binding peptidomimetics enhance osteoblast-like cells adhesion, proliferation, and differentiation on titanium. *Colloids Surf B Biointerfaces* **128**, 191–200 (2015).

183. Efremov, A. K., Hovan, L. & Yan, J. Nucleus size and its effect on nucleosome stability in living cells. *Biophys J* **121**, 4189–4204 (2022).

184. Mhatre V. Ho, Ji-Ann Lee, and K. C. M. & Craik, C. Nuclear mechanics during cell migrations. *Bone* **23**, 1–7 (2012).

185. Rabel, K. *et al.* Controlling osteoblast morphology and proliferation via surface micro-topographies of implant biomaterials. *Sci Rep* **10**, 1–14 (2020).

186. Karazisis, D. *et al.* The effects of controlled nanotopography, machined topography and their combination on molecular activities, bone formation and biomechanical stability during osseointegration. *Acta Biomater* **136**, 279–290 (2021).

187. Mastrangelo, F. *et al.* Effects of Novel Laser Dental Implant Microtopography on Human Osteoblast Proliferation and Bone Deposition. *Int J Oral Maxillofac Implants* **35**, 320–329 (2020).

188. Barlian, A. & Vanya, K. Nanotopography in directing osteogenic differentiation of mesenchymal stem cells: Potency and future perspective. *Future Sci OA* **8**, (2022).

189. Bighetti-Trevisan, R. L. *et al.* Effect of osteoblasts on osteoclast differentiation and activity induced by titanium with nanotopography. *Colloids Surf B Biointerfaces* **229**, 113448 (2023).

190. Souza, P. G. *et al.* Effects of Modulation of the Hedgehog and Notch Signaling Pathways on Osteoblast Differentiation Induced by Titanium with Nanotopography. *J Funct Biomater* **14**, (2023).

191. Hou, C. *et al.* Surface Modification Techniques to Produce Micro/Nano-scale Topographies on Ti-Based Implant Surfaces for Improved Osseointegration. *Front Bioeng Biotechnol* **10**, 1–16 (2022).

192. Zhang, Y. *et al.* Effect of microtopography on osseointegration of implantable biomaterials and its modification strategies. *Front Bioeng Biotechnol* **10**, 1–14 (2022).

193. Petrini, M. *et al.* Influence of nano, micro and macro topography of dental implant surfaces on human gingival fibroblasts. *Int J Mol Sci* **22**, (2021).

194. Luo, J. *et al.* TiO2Nanotopography-Driven Osteoblast Adhesion through Coulomb's Force Evolution. *ACS Appl Mater Interfaces* **14**, 34400–34414 (2022).

195. Greer, A. I. M. *et al.* Nanopatterned Titanium Implants Accelerate Bone Formation in Vivo. *ACS Appl Mater Interfaces* **12**, 33541–33549 (2020).

196. Huethorst, E. *et al.* Customizable, engineered substrates for rapid screening of cellular cues. *Biofabrication* **12**, (2020).

197. Cuahtecontzi Delint, R. *et al.* Nanotopography Influences Host-Pathogen Quorum Sensing and Facilitates Selection of Bioactive Metabolites in Mesenchymal Stromal Cells and Pseudomonas aeruginosa Co-Cultures. *ACS Appl Mater Interfaces* (2024) doi:10.1021/acsami.4c09291.

198. Luo, J. *et al.* The influence of nanotopography on cell behaviour through interactions with the extracellular matrix – A review. *Bioact Mater* **15**, 145–159 (2022).

199. Cuahtecontzi Delint, R. *et al.* Mechanotransducive surfaces for enhanced cell osteogenesis, a review. *Biomaterials Advances* **160**, (2024).

200. Xie, W. *et al.* Static and Dynamic: Evolving Biomaterial Mechanical Properties to Control Cellular Mechanotransduction. *Advanced Science* **10**, 1–37 (2023).

201. Di Cio, S. & Gautrot, J. E. Cell sensing of physical properties at the nanoscale: Mechanisms and control of cell adhesion and phenotype. *Acta Biomater* **30**, 26–48 (2016).

202. Wheeldon, I., Farhadi, A., Bick, A. G., Jabbari, E. & Khademhosseini, A. Nanoscale tissue engineering: Spatial control over cell-materials interactions. *Nanotechnology* **22**, (2011).

203. Aminuddin, N. I., Ahmad, R., Akbar, S. A. & Pingguan-Murphy, B. Osteoblast and stem cell response to nanoscale topographies: a review. *Sci Technol Adv Mater* **17**, 698–714 (2016).

204. Zhang, Y., Gordon, A., Qian, W. & Chen, W. Engineering Nanoscale Stem Cell Niche: Direct Stem Cell Behavior at Cell-Matrix Interface. *Adv Healthc Mater* **4**, 1900–1914 (2015).

205. Gulati, K., Zhang, Y., Di, P., Liu, Y. & Ivanovski, S. Research to Clinics: Clinical Translation Considerations for Anodized Nano-Engineered Titanium Implants. *ACS Biomater Sci Eng* **8**, 4077–4091 (2022).

206. Allan, C. *et al.* Osteoblast response to disordered nanotopography. *J Tissue Eng* **9**, 1–7 (2018).

207. Damiati, L. A. *et al.* Materials-driven fibronectin assembly on nanoscale topography enhances mesenchymal stem cell adhesion, protecting cells from bacterial virulence factors and preventing biofilm formation. *Biomaterials* **280**, (2022).

208. Francone, A. *et al.* Impact of surface topography on the bacterial attachment to micro- and nano-patterned polymer films. *Surfaces and Interfaces* **27**, 101494 (2021).

209. Li, M., Xi, N. & Liu, L. Hierarchical micro-/nanotopography for tuning structures and mechanics of cells probed by atomic force microscopy. *IEEE Trans Nanobioscience* **20**, 543–553 (2021).

210. Wähnert, D. *et al.* Strategies to improve bone healing: Innovative surgical implants meet nano-/micro-topography of bone scaffolds. *Biomedicines* **9**, 1–20 (2021).

211. Berger, M. B. *et al.* A Review of Biomimetic Topographies and Their Role in Promoting Bone Formation and Osseointegration: Implications for Clinical Use. *Biomimetics* **7**, (2022).

212. Yu, X. *et al.* Size-Dependent Effect of Titania Nanotubes on Endoplasmic Reticulum Stress to Re-establish Diabetic Macrophages Homeostasis. *ACS Biomater Sci Eng* **10**, 4323–4335 (2024).

213. Wang, X. *et al.* Effect of RGD nanospacing on differentiation of stem cells. *Biomaterials* **34**, 2865–2874 (2013).

214. Oh, S. *et al.* Significantly accelerated osteoblast cell growth on aligned TiO2 nanotubes. *J Biomed Mater Res A* **78**, 97–103 (2006).

215. Luo, J. *et al.* The influence of nanotopography on cell behaviour through interactions with the extracellular matrix – A review. *Bioactive Materials* vol. 15 145–159 Preprint at https://doi.org/10.1016/j.bioactmat.2021.11.024 (2022).

216. Putra, V. D. L., Kilian, K. A. & Knothe Tate, M. L. Biomechanical, biophysical and biochemical modulators of cytoskeletal remodelling and emergent stem cell lineage commitment. *Commun Biol* **6**, 1–24 (2023).

217. Chen, X. *et al.* Scaffold structural microenvironmental cues to guide tissue regeneration in bone tissue applications. *Nanomaterials* **8**, 1–15 (2018).

218. Bressan, E. *et al.* Nanostructured surfaces of dental implants. *Int J Mol Sci* **14**, 1918–1931 (2013).

219. Dearnley, P. A. A brief review of test methodologies for surface-engineered biomedical implant alloys. *Surf Coat Technol* **198**, 483–490 (2005).

220. Chopra, D., Gulati, K. & Ivanovski, S. Understanding and optimizing the antibacterial functions of anodized nano-engineered titanium implants. *Acta Biomater* **127**, 80–101 (2021).

221. Matsuura, T., Komatsu, K., Cheng, J., Park, G. & Ogawa, T. Beyond microroughness: novel approaches to navigate osteoblast activity on implant surfaces. *Int J Implant Dent* **10**, (2024).

222. Kong, K. *et al.* TiO2 Nanotubes Promote Osteogenic Differentiation Through Regulation of Yap and Piezo1. *Front Bioeng Biotechnol* **10**, 1–13 (2022).

223. Haghjoo, R., Sadrnezhaad, S. K. & Nemati, N. H. The effect of TiO2 nanotubes on the biological properties of porous titanium foam by anodization technique for orthopedic application. *Journal of Ultrafine Grained and Nanostructured Materials* **56**, 99–107 (2023).

224. Berthelot, R. & Variola, F. Investigating the interplay between environmental conditioning and nanotopographical cueing on the response of human MG63 osteoblastic cells to titanium nanotubes. *Biomater Sci* in press (2024).

225. Loget, G., So, S., Hahn, R. & Schmuki, P. Bipolar anodization enables the fabrication of controlled arrays of TiO2 nanotube gradients. *J Mater Chem A Mater* **2**, 17740–17745 (2014).

226. Luo, X. *et al.* Effect of Gradient Nanostructured Ti on Behaviours of MG63 Cells in Vitro. *J Nanomater* **2020**, (2020).

227. Fan, R. & Wan, J. Electrode distance regulates the anodic growth of titanium dioxide (TiO2) nanotubes. *Nanotechnology* **28**, (2017).

228. Klimas, J., Łukaszewicz, A., Szota, M. & Nabiałek, M. Modification of the structure and properties of the titanium alloy Ti6Al4V in biomedical applications. *Archives of Metallurgy and Materials* **60**, 2013–2018 (2015).

229. Torre, I. G., Heck, R. J. & Tarquis, A. M. MULTIFRAC: An ImageJ plugin for multiscale characterization of 2D and 3D stack images. *SoftwareX* **12**, 100574 (2020).

230. Silva, L. E. V., Filho, A. C. S. S., Fazan, V. P. S., Felipe, J. C. & Murta, L. O. Two-dimensional sample entropy: Assessing image texture through irregularity. *Biomed Phys Eng Express* **2**, (2016).

231. Virgilio Da Silva, L. E., Da Silva Senra Filho, A. C., Fazan, V. P. S., Felipe, J. C. & Murta, L. O. Two-dimensional sample entropy analysis of rat sural nerve aging. *2014 36th Annual International Conference of the IEEE Engineering in Medicine and Biology Society, EMBC 2014* 3345–3348 (2014) doi:10.1109/EMBC.2014.6944339.

232. Richman, J. S., Randall Moorman, J., Randall, J. & Physi, M. Physiological time-series analysisusing approximate entropy and sample entropy. *Am J Physiol Heart Circ Physiol* **278**, 2039–2049 (2000).

233. Plotnick, R. E., Gardner, R. H., Hargrove, W. W., Prestegaard, K. & Perlmutter, M. Lacunarity analysis: A general technique for the analysis of spatial patterns. *Phys Rev E Stat Phys Plasmas Fluids Relat Interdiscip Topics* **53**, 5461–5468 (1996).

234. Smith, T. G., Lange, G. D. & Marks, W. B. Fractal methods and results in cellular morphology - Dimensions, lacunarity and multifractals. *J Neurosci Methods* **69**, 123–136 (1996).

235. Detmer, S. A. & Chan, D. C. Functions and dysfunctions of mitochondrial dynamics. *Nat Rev Mol Cell Biol* **8**, 870–879 (2007).

236. Shi, P. *et al.* Research article arp2/3-branched actin regulates microtubule acetylation levels and affects mitochondrial distribution. *J Cell Sci* **132**, (2019).

237. Hirose, E., Noguchi, M., Ihara, T. & Yokoya, A. Mitochondrial Metabolism in X-Irradiated Cells Undergoing Irreversible Cell-Cycle Arrest. *Int J Mol Sci* **24**, (2023).

238. Anselme, K., Ponche, A. & Bigerelle, M. Relative influence of surface topography and surface chemistry on cell response to bone implant materials. Part 2: Biological aspects. *Proc Inst Mech Eng H* **224**, 1487–1507 (2010).

239. Dupont, S. *et al.* Role of YAP/TAZ in mechanotransduction. *Nature* **474**, 179–184 (2011).

240. Lamers, E. *et al.* Dynamic cell adhesion and migration on nanoscale grooved substrates. *Eur Cell Mater* **23**, 182–194 (2012).

241. Mu, P. *et al.* High-Throughput Screening of Rat Mesenchymal Stem Cell Behavior on Gradient TiO2 Nanotubes. *ACS Biomater Sci Eng* **4**, 2804–2814 (2018).

242. Galstyan, V., Comini, E., Faglia, G. & Sberveglieri, G. TiO2 nanotubes: Recent advances in synthesis and gas sensing properties. *Sensors (Switzerland)* vol. 13 14813–14838 Preprint at https://doi.org/10.3390/s131114813 (2013).

243. Zhu, Y. *et al.* Regulation of macrophage polarization through surface topography design to facilitate implant-to-bone osteointegration. *Sci Adv* **7**, 1–14 (2021).

244. Sakai, D. & Minkin, C. The Osteoclast Molecular Phenotype. in *Molecular and Cellular Biology of Bone* vol. 5 385–421 (Elsevier, 1998).

245. Campagna, R. *et al.* In Vitro Study of the Proliferation of MG63 Cells Cultured on Five Different Titanium Surfaces. *Materials* **17**, (2024).

246. Hong, Y. J., Chun, J. S. & Lee, W. K. Association of collagen with calcium phosphate promoted osteogenic responses of osteoblast-like MG63 cells. *Colloids Surf B Biointerfaces* **83**, 245–253 (2011).

247. Lee, S. J. *et al.* Response of MG63 osteoblast-like cells onto polycarbonate membrane surfaces with different micropore sizes. *Biomaterials* **25**, 4699–4707 (2004).

248. Sjöström, T., Lalev, G., Peter, J. & Su, B. Applied Surface Science Initial attachment and spreading of MG63 cells on nanopatterned titanium surfaces via through-mask anodization. **257**, 4552–4558 (2011).

249. Kim, C. S. *et al.* Proteomic analysis of the biological response of MG63 osteoblast-like cells to titanium implants. *Odontology* **102**, 241–248 (2014).

250. Martins de Sousa, K. *et al.* Modulation of MG-63 Osteogenic Response on Mechano-Bactericidal Micronanostructured Titanium Surfaces. *ACS Appl Bio Mater* **6**, 1054–1070 (2023).

251. Li, H. *et al.* Bioactive surface modified Ti with titania nanotube arrays to design endoprosthesis for maxillofacial surgery: Structural formation, morphology, physical properties and osseointegration. *Mater Today Proc* **22**, 16–20 (2019).

252. Gui, N. *et al.* The effect of ordered and partially ordered surface topography on bone cell responses: A review. *Biomater Sci* **6**, 250–264 (2018).

253. Park, S. & Im, G. Il. Stem cell responses to nanotopography. *J Biomed Mater Res A* **103**, 1238–1245 (2015).

254. Wang, W. *et al.* The role of the Wnt/β-catenin pathway in the effect of implant topography on MG63 differentiation. *Biomaterials* **33**, 7993–8002 (2012).

255. Jafarkhani, S. *et al.* Exploring the effects of micro-nano surface topography on MG63 osteoblast-like cell responses: An in vitro study. *Colloids Surf A Physicochem Eng Asp* **675**, 131872 (2023).

256. Wang, W. *et al.* The role of integrin-linked kinase/β-catenin pathway in the enhanced MG63 differentiation by micro/nano-textured topography. *Biomaterials* **34**, 631–640 (2013).

257. Dalby, M. J. Topographically induced direct cell mechanotransduction. *Med Eng Phys* **27**, 730–742 (2005).

258. Rougerie, P., dos Santos, R. S., Farina, M. & Anselme, K. Molecular mechanisms of topography sensing by osteoblasts: An update. *Applied Sciences (Switzerland)* **11**, 1–17 (2021).

259. Liu, Q. *et al.* Involvement of N-cadherin/β-catenin interaction in the micro/nanotopography induced indirect mechanotransduction. *Biomaterials* **35**, 6206–6218 (2014).

260. Sun, Y. *et al.* Nanotube topography rejuvenates the senescence of mesenchymal stem cells by activating YAP signalling. *J Mater Chem B* **12**, 6917–6926 (2024).

261. Tong, Z. *et al.* F-actin Regulates Osteoblastic Differentiation of Mesenchymal Stem Cells on TiO2 Nanotubes Through MKL1 and YAP/TAZ. *Nanoscale Res Lett* **15**, (2020).

262. Li, L. *et al.* Nanotopography on titanium promotes osteogenesis via autophagy-mediated signaling between YAP and β-catenin. *Acta Biomater* **96**, 674–685 (2019).

263. Hedegaard, M. A. B., Bergholt, M. S. & Stevens, M. M. Quantitative multi-image analysis for biomedical Raman spectroscopic imaging. *J Biophotonics* **9**, 542–550 (2016).

264. Kallepitis, C. *et al.* Quantitative volumetric Raman imaging of three dimensional cell cultures. *Nat Commun* **8**, (2017).

265. Ember, K. J. I. *et al.* Raman spectroscopy and regenerative medicine: a review. *NPJ Regen Med* **2**, (2017).

266. Chiang, Y. H. *et al.* Raman spectroscopy for grading of live osteosarcoma cells. *Stem Cell Res Ther* **6**, 1–8 (2015).

267. Li, J. *et al.* Label-free Raman imaging of live osteosarcoma cells with multivariate analysis. *Appl Microbiol Biotechnol* **103**, 6759–6769 (2019).

268. Mandair, G. S., Steenhuis, P., Ignelzi, M. A. & Morris, M. D. Bone quality assessment of osteogenic cell cultures by Raman microscopy. *Journal of Raman Spectroscopy* **50**, 360–370 (2019).

269. McManus, L. L. *et al.* Raman spectroscopic monitoring of the osteogenic differentiation of human mesenchymal stem cells. *Analyst* **136**, 2471–2481 (2011).

270. Wang, C. *et al.* Confocal Laser Raman microspectroscopy of biomineralization foci in UMR 106 osteoblastic cultures reveals temporally synchronized protein changes preceding and accompanying mineral crystal deposition. *Journal of Biological Chemistry* **284**, 7100–7113 (2009).

271. Microscopy, C. R. Confocal Raman Configuration for Automated Measurements. 1–26 (1923).

272. Bergholt, M. S., Serio, A., Albro, M. B. & Albro, M. B. Raman Spectroscopy : Guiding Light for the Extracellular Matrix. *Front Bioeng Biotechnol* **7**, 1–16 (2019).

273. Hsu, C. C. *et al.* A single-cell Raman-based platform to identify developmental stages of human pluripotent stem cell-derived neurons. *Proc Natl Acad Sci U S A* **117**, 18412–18423 (2020).

274. Suhaimy, S. H. M., Lai, C. W., Tajuddin, H. A., Samsudin, E. M. & Johan, M. R. Impact of TiO2 nanotubes' morphology on the photocatalytic degradation of simazine pollutant. *Materials* **11**, 1–15 (2018).

275. Jiang, T. *et al.* Carbon nanotubes/TiO2 nanotubes composite photocatalysts for efficient degradation of methyl orange dye. *Particuology* **11**, 737–742 (2013).

276. Stammeier, J. A., Purgstaller, B., Hippler, D., Mavromatis, V. & Dietzel, M. In-situ Raman spectroscopy of amorphous calcium phosphate to crystalline hydroxyapatite transformation. *MethodsX* **5**, 1241–1250 (2018).

277. Ulian, G., Moro, D. & Valdrè, G. Hydroxylapatite and related minerals in bone and dental tissues: Structural, spectroscopic and mechanical properties from a computational perspective. *Biomolecules* **11**, (2021).

278. Unal, M., Ahmed, R., Mahadevan-Jansen, A. & Nyman, J. S. Compositional assessment of bone by Raman spectroscopy. *Analyst* **146**, 7444–7470 (2021).

279. Ghita, A., Pascut, F. C., Sottile, V. & Notingher, I. Monitoring the mineralisation of bone nodules in vitro by space- and time-resolved Raman micro-spectroscopy. *Analyst* **139**, 55–58 (2014).

280. Morris, M. D. & Mandair, G. S. Raman assessment of bone quality. *Clin Orthop Relat Res* **469**, 2160–2169 (2011).

281. Shah, F. A. Towards refining Raman spectroscopy-based assessment of bone composition. *Sci Rep* **10**, 1–8 (2020).

282. Ghita, A., Pascut, F. C., Sottile, V. & Notingher, I. Monitoring the mineralisation of bone nodules in vitro by space- and time-resolved Raman micro-spectroscopy. *Analyst* **139**, 55–58 (2014).

283. Notingher, I. & Hench, L. L. Raman microspectroscopy: A noninvasive tool for studies of individual living cells in vitro. *Expert Rev Med Devices* **3**, 215–234 (2006).

284. Verrier, S., Zoladek, A. & Notingher, I. Raman Micro-Spectroscopy as a Non-invasive Cell Viability Test. in *Methods in Molecular Biology* vol. 740 179–189 (Humana Press Inc., 2011).

285. Delgado-Bonal, A. & Marshak, A. *Approximate Entropy and Sample Entropy: A Comprehensive Tutorial*. *Entropy* vol. 21 (2019).

286. Xiao, L. *et al.* A novel culture platform for fast proliferation of human annulus fibrosus cells. *Cell Tissue Res* **367**, 339–350 (2017).

287. Horzum, U., Ozdil, B. & Pesen-Okvur, D. Step-by-step quantitative analysis of focal adhesions. *MethodsX* **1**, 56–59 (2014).

288. Gumbiner, B. M. & Kim, N. G. The Hippo-YAP signaling pathway and contact inhibition of growth. *J Cell Sci* **127**, 709–717 (2014).

289. Luo, J. *et al.* The influence of nanotopography on cell behaviour through interactions with the extracellular matrix – A review. *Bioact Mater* **15**, 145–159 (2022).

290. Aragona, M. *et al.* A mechanical checkpoint controls multicellular growth through YAP/TAZ regulation by actin-processing factors. *Cell* **154**, 1047–1059 (2013).

291. Zhang, Y. *et al.* Tunable Hybrid Matrices Drive Epithelial Morphogenesis and YAP Translocation. *Advanced Science* **8**, 1–16 (2021).

292. Sero, J. E. & Bakal, C. Multiparametric Analysis of Cell Shape Demonstrates that β-PIX Directly Couples YAP Activation to Extracellular Matrix Adhesion. *Cell Syst* **4**, 84-96.e6 (2017).

293. Yang, G., Yuan, G., MacDougall, M., Zhi, C. & Chen, S. BMP-2 induced Dspp transcription is mediated by Dlx3/Osx signaling pathway in odontoblasts. *Sci Rep* **7**, 1–11 (2017).

294. Tai, G., Christodoulou, I., Bishop, A. E. & Polak, J. M. Use of green fluorescent fusion protein to track activation of the transcription factor osterix during early osteoblast differentiation. *Biochem Biophys Res Commun* **333**, 1116–1122 (2005).

295. Ramamurthy, B., Cohen, S., Canales, M. & Coffman, F. D. Three-dimensional cellular raman analysis: Evidence of highly ordered lipids within cell nuclei. *Journal of Histochemistry and Cytochemistry* **66**, 889–902 (2018).

296. Hong, Y. J., Chun, J. S. & Lee, W. K. Association of collagen with calcium phosphate promoted osteogenic responses of osteoblast-like MG63 cells. *Colloids Surf B Biointerfaces* **83**, 245–253 (2011).

297. Choi, Y. S. *et al.* Bone nodule formation of MG63 cells is increased by the interplay of signaling pathways cultured on vitamin D3- entrapped calcium phosphate films. *Anim Cells Syst (Seoul)* **13**, 363–370 (2009).

298. Sanchez, C. *et al.* Oblique illumination in microscopy: A quantitative evaluation. *Micron* **105**, 47–54 (2018).

299. Ichimura, T. *et al.* Visualizing cell state transition using raman spectroscopy. *PLoS One* **9**, (2014).

300. D'Acunto, M., Trombi, L., D'Alessandro, D. & Danti, S. Raman spectroscopy of osteosarcoma cells. *Phys Biol* **16**, (2019).

301. Marzi, J. *et al.* Non-Invasive Three-Dimensional Cell Analysis in Bioinks by Raman Imaging. *ACS Appl Mater Interfaces* **14**, 30455–30465 (2022).

302. Klymov, A. *et al.* Increased acellular and cellular surface mineralization induced by nanogrooves in combination with a calcium-phosphate coating. *Acta Biomater* **31**, 368–377 (2016).